Normandie Université

THESE

Pour obtenir le diplôme de doctorat

Spécialité Physique

Préparée au sein de l'Université de Caen Normandie

Nuclear structure studies with neutron-induced reactions: Fission fragments in the N=50-60 region, a fission event tagger for FIPPS, and production of the isomer Pt-195m

Présentée et soutenue par

Dennis WILMSEN

Thèse soutenue publiquement le 21 décembre 2017 devant le jury composé de		
Mme Alison BRUCE	Professor, University of Brighton	Rapporteur
M. Waldemar URBAN	Professor, University of Warsaw	Rapporteur
Mme Fanny FARGET	Chargé de recherche, HDR, LPC Caen-IN2P3 Paris	Examinateur
Mme Silvia LEONI	Professor, Università degli Studi di Milano	Examinateur
M. Jean-Marc RÉGIS	Postdoctoral fellow, Universität zu Köln	Examinateur
M. Ulli KÖSTER	Professeur associé des universités, Université Grenoble Alpes	Examinateur
Mme Francesca GULMINELLI	Professeur des universités, Université de Caen Normandie	Examinateur
M. Gilles DE FRANCE	Directeur de recherche CNRS, GANIL Caen	Directeur de thèse

Thèse dirigée par M. Gilles DE FRANCE, laboratoire GANIL

UNIVERSITÉ CAEN NORMANDIE

ED 591 PSIME

GANIL laboratoire commun CEA/DSM spiral2 CNRS/IN2P3

Nuclear structure studies with neutron-induced reactions:

Fission fragments in the N=50-60 region, a fission event tagger for FIPPS, and production of the isomer ^{195m}Pt

Abstract

Within the scope of atomic nuclear structure studies with neutron-induced reactions, this work presents the results of a fission fragment study in the $N = 50 - 60$ region, the development of a fission event tagger, and the production of the isomer ^{195m}Pt.
Each of the different sub-topics has its origin in the 2012/13 EXILL campaign, where nuclear structure studies have been carried out with neutron-induced reactions, and explored with a γ-efficient detector array.
In the first part of this thesis, the neutron-rich region around neutron number $N = 50 - 60$ has been investigated with neutron-induced fission reactions on the fissile targets ^{235}U and ^{241}Pu. γ spectroscopy methods have been applied for the identification of the respective fission fragments, the assignment of γ transitions, and the analysis of lifetimes of excited states. The well-known slope fit method as well as the recently developed *generalized centroid difference method* have been used for the analysis of lifetimes in the low picoseconds to sub-nanoseconds range. Lifetimes for the nuclei ^{92}Kr, ^{93}Kr and ^{101}Zr are presented.
In the second part, first results of the development of a new detector for the discrimination of fission fragments are presented. This fission event tagger is intended to use at the *FIssion Product Prompt γ-ray Spectrometer* (FIPPS) at ILL. Within the scope of this study, two different detector designs, based on a solid plastic scintillator and an organic liquid scintillator, respectively, have been tested.
In the third part the possibility of the specific population of the spin-isomer in ^{195}Pt is discussed with special regard to its use as radioisotope in nuclear medicine. Such a specific activation could be realized via certain "doorway states" in photo-excitation reactions. The search for these doorway states was initiated within a neutron capture experiment at EXILL where potential states have been found. The activation of the isomer via these states has afterwards been tested in photo-excitation with the high intense γ beam of the HIGS facility.

Resumé

Ce travail s'inscrit dans le cadre d'études de structures nucléaires réalisées en utilisant des réactions de fission induites par neutrons froids. Il décrit successivement les résultats d'une étude sur des noyaux ayant un nombre de neutrons $N = 50 - 60$, sur le développement d'un marqueur d'événements de fission et enfin sur la production de l'isomère ^{195m}Pt.
Chacun des différents sous-thèmes trouve son origine dans la campagne EXILL qui s'est déroulée en 2012-2013 et durant laquelle un spectromètre de grande efficacité pour la détection des rayonnements γ (EXOGAM) a été utilisé auprès du réacteur à haut flux de neutrons de l'Institut Laue-Langevin (ILL). Dans la première partie de cette thèse, les noyaux d'intérêt ont été produits par fission induites par des neutrons sur les cibles fissiles ^{235}U et ^{241}Pu. Des méthodes de spectroscopie γ ont été appliquées pour l'identification des fragments de fission, l'attribution des transitions γ à un noyau et l'analyse des durées de vie moyenne des états excités. L'analyse des durées de vie moyenne des états excités dans la plage de quelques picosecondes à quelques nanosecondes a été réalisée en utilisant deux méthodes complémentaires. Dans les deux cas, il s'agit de réaliser un spectre en temps construit à partir de la coincidence entre une transition qui alimente le niveau mesuré et une transition qui le désexcite. La première méthode consiste à analyser la pente de décroissance exponentielle de ce spectre (méthode d'ajustement de la pente de décroissance). Dans la deuxième méthode, on inverse les deux partenaires de la coincidence et on mesure la différence en temps entre les centroides deux distributions ainsi obtenues. C'est la méthode dite de la différence de centroide généralisée. Les durées de vie moyenne pour les noyaux ^{92}Kr, ^{93}Kr et ^{101}Zr sont présentées.
Dans la seconde partie, les premiers résultats du développement d'un nouveau détecteur pour la discrimination des fragments de fission sont présentés. Ce marqueur d'événements de fission est destiné à être utilisé sur le spectromètre *FIssion Prompt Product γ-ray Spectrometer* (FIPPS) de l'ILL. Dans le cadre de cette étude, deux conceptions de détecteurs différentes,

basées sur un scintillateur en plastique solide et un scintillateur liquide organique, ont été testées. Dans la troisième partie, la possibilité de la population spécifique de l'isomère de spin dans ^{195}Pt est examinée au regard particulièrement de son utilisation en tant que radio-isotope en médecine nucléaire. Une telle activation spécifique pourrait être réalisée grâce à l'existence d'états excités dont la structure permettrait une population ciblée dans le cas de l'utilisation de réactions de photo-excitation. La recherche de tels états a été initiée lors d'une expérience de capture de neutrons à EXILL dans laquelle des états potentiels ont été identifiés. L'activation de l'isomère par ces états a ensuite été testée avec des réactions photonucléaires à l'aide du faisceau haute intensité disponible auprès de l'installation γ HIGS de TUNL (Triangle Universities Nuclear Laboratory, Duke, USA).

Foreword

The present thesis was written between November 2014 and October 2017, jointly supervised in a bilateral cooperation between the *Grand Accélérateur National d'Ions Lourds* (GANIL) in Caen and the *Institut Laue-Langevin* (ILL) in Grenoble, France.
As deducible from the title of this document, the thesis covers three topics which are embedded into the framework of *"Nuclear structure studies with neutron-induced reactions"*. However, the intended preparation of one single, coherent document would not have led to the benefit of didactic comprehensibility. Accordingly, the thesis is subdivided into three parts, each related to the respective subtitle.
The outline of each part tries to follows the structure of an introductory chapter, a chapter about the applied experimental and analytical methods, a results chapter, and a discussion. This way, each part was intended to keep as self-consistent as possible. Due to certain overlap in content however, the reader is from time to time referred to previous chapters or sections.
The first part - *"Fission fragments in the* $\mathrm{N} = 50 - 60$ *region"*- refers to the study of neutron-rich nuclei in the mass region around neutron number $\mathrm{N} = 50 - 60$ which were produced in cold neutron induced fission of ^{235}U and ^{241}Pu within the frame of the EXILL campaign. The first chapter briefly reviews the structural characteristics of nuclei in this mass region followed by the second chapter which introduces the EXILL campaign and the analytical methods which were carried out for the identification of fission fragments, and the analysis of lifetimes of excited atomic nuclei. Special attention is given to the *Generalized Centroid Difference Method* for the determination of lifetimes in the lower picoseconds range. The results of this work are presented in the third chapter and discussed afterwards in the fourth chapter.
The second part - *"A fission event tagger for FIPPS"*- follows directly from the experimental boundaries of the first part and presents preliminary considerations and first results for the use of a detector which discriminates fis-

sion events from β-decay. This "fission event tagger" is intended to be used at the recently developed germanium spectrometer FIPPS at the ILL. The fifth chapter gives an introduction to the FIPPS spectrometer and presents some basic design considerations for the use of a fission event tagger under neutron exposure. In the sixth chapter two fission event tagger designs are presented, one is based on a thin scintillating plastic foil, the other one on an organic scintillating liquid. The results of a first test at the *Lohengrin* mass separator, and for the decay of ^{235}U are presented and discussed in chapter seven and eight, respectively.
The last part of this thesis - *"Production of the isomer* ^{195m}Pt*"*- discusses the production of the isomer ^{195m}Pt and the possibility of its specific activation for the use as a radioisotope in nuclear medicine. This part is related to two experiments. In the first experiment, ^{195m}Pt was produced via neutron capture on enriched ^{194}Pt targets within the EXILL campaign. The analysis was focused on the assignment of states which populate the isomer. These states have been irritated with a narrow-band γ beam produced via Compton backscattering of eV photons on relativistic electrons at the HIGS facility in the second experiment. The ninth chapter gives a brief introduction to a potential use of ^{195m}Pt as radioisotope in nuclear medicine. The HIGS facility and the technique of Compton backscattering are described in chapter ten. The results of both experiments are presented in the eleventh chapter and discussed afterwards in chapter twelve.

Préface

La présente thèse a été réalisée entre novembre 2014 et octobre 2017, dans le cadre d'une collaboration entre entre le Grand Accélérateur national d'Ions Lourds (GANIL) à Caen et l'Institut Laue-Langevin (ILL) à Grenoble, France.
Comme le titre de ce document l'indique, la thèse couvre trois sujets qui sont intégrés dans le cadre générique d'études de structure nucléaire avec des réactions induites par neutrons. En conséquence, la thèse est subdivisée en trois parties distinctes, autoconsistantes et construites selon un même schéma. Ainsi chaque partie suit la structure d'un chapitre introductif, un chapitre sur les méthodes expérimentales et analytiques appliquées, un chapitre sur les résultats et une discussion. Cependant, en raison de certains chevauchements de contenu, le lecteur est parfois appelé à se référer aux chapitres ou sections précédents.
La première partie - *"Fragments de fission dans la région* $\mathrm{N} = 50 - 60$*"*- concerne l'étude des noyaux riches en neutrons dans la région de masse autour du nombre de neutrons $\mathrm{N} = 50 - 60$ qui ont été produits dans la fission induite par des neutrons froids des noyaux ^{235}U et ^{241}Pu dans le cadre de la campagne EXILL. Le premier chapitre passe brièvement en revue les caractéristiques structurelles des noyaux dans cette région de masse. Le deuxième chapitre présente la campagne EXILL et les méthodes analytiques utilisées pour l'identification des fragments de fission et l'analyse des durées de vie moyenne des noyaux atomiques excités. Une attention particulière est accordée à la méthode dite de différence de centroide généralisée pour la détermination des durées de vie moyenne dans la gamme de temps inférieure à la picoseconde. Les résultats de ce travail sont présentés dans le troisième chapitre et discutés ensuite dans le quatrième chapitre.

La seconde partie - *"Un marqueur d'événement de fission pour FIPPS"*- fait directement suite aux limites expérimentales observées dans la première partie et présente des considérations préliminaires et des premiers résultats pour l'utilisation d'un détecteur qui distingue des événements de fission par l'emission bêta. Ce "marqueur d'événement de fission" est destiné à être utilisé auprès du spectromètre *FIPPS* dont la première phase constituée d'un ensemble de huit détecteurs germanium a été récemment installé à l'ILL. Le cinquième chapitre donne une introduction au spectromètre FIPPS et présente quelques considérations de conception de base pour l'utilisation d'un marqueur d'événement de fission sous exposition aux neutrons. Dans le sixième chapitre, deux modèles d'un marqueur d'événement de fission sont présentés, dont l'un est basé sur une mince feuille de plastique scintillante, l'autre sur un liquide scintillant organique. Les résultats d'un premier test au séparateur de masse *Lohengrin*, et de la désintégration de ^{235}U, sont présentés et discutés dans les chapitres sept et huit, respectivement.
La dernière partie de cette thèse - *"Production de l'isomère* ^{195m}Pt*"*- discute la production de l'isomère ^{195m}Pt et la possibilité de son activation spécifique pour l'utilisation comme radio-isotope en médecine nucléaire. Cette partie est liée à deux expériences. Dans la première expérience, ^{195m}Pt a été produit par capture de neutrons sur des cibles ^{194}Pt enrichies dans le cadre de la campagne EXILL. L'analyse était axée sur l'attribution d'états qui peuplent l'isomère. Dans une deuxième experience menée auprès de l'installation HIGS de TUNL (Triangle Universities Nuclear Laboratory, USA), ces états ont été excités avec un faisceau γ à bande étroite produit par rétrodiffusion Compton de photons d'énergie de l'ordre de l'électronvolt sur des électrons relativistes. Le neuvième chapitre donne une brève introduction à l'utilisation potentielle de ^{195m}Pt comme radio-isotope en médecine nucléaire. L'installation HIGS et la technique de rétrodiffusion Compton sont décrites au chapitre dix. Les résultats des deux expériences sont présentés dans le onzième chapitre et discutés ensuite dans le chapitre douze.
Cette thèse a été préparée en anglais. À la fin de chaque partie, le lecteur peut trouver un bref résumé de la section correspondante dans la langue française. Il convient toutefois de mentionner que ces résumés ne couvrent qu'une partie et ne sont donc pas suffisants pour la compréhension détaillée de ce travail.

Contents

I Fission Fragments in the N=50-60 region **15**

1 Introduction **16**

2 Applied Experimental Methods **19**
2.1 The EXILL and FATIMA@EXILL Campaign 19
2.1.1 Experimental Environment 20
2.1.2 The EXILL detector array 21
2.1.3 The FATIMA@EXILL detector array 23
2.2 Analysis of Fission Spectra 25
2.2.1 Data Processing 26
2.2.2 On Fission 26
2.2.3 Identification of Fission Fragments 29
2.3 Analysis of Time Spectra 33
2.3.1 Electronic fast-timing 34
2.3.2 The Slope Fit and the Convolution Method 36
2.3.3 The Generalized Centroid Difference Method 38
2.3.4 Applicability to Fission Fragments 45
2.3.5 Data Processing 46

3 Results **47**
3.1 Krypton 48
3.1.1 ^{92}Kr 48
3.1.2 ^{93}Kr 53
3.1.3 ^{94}Kr 59
3.2 Zirconium 61
3.2.1 ^{101}Zr 61

4 Summary **70**

II A Fission Event Tagger for FIPPS 75

5 Introduction 76
5.1 The FIPPS Spectrometer 77
5.1.1 FIPPS Phase I - The Germanium Array 77
5.1.2 FIPPS Phase II - The Mass Spectrometer 79
5.2 A Conceptual Fission Event Tagger for FIPPS 80
5.2.1 Silicon Detector 81
5.2.2 Gas Detector 81
5.2.3 Active Target based on a Liquid Scintillator 82
5.2.4 Solid Plastic Scintillator 82

6 Applied Experimental Methods 84
6.1 Thin Plastic Scintillating Layers 84
6.1.1 Production of a Thin Plastic Scintillator 84
6.1.2 The Lohengrin Spectrometer 86
6.1.3 The Experimental Setup 88
6.2 Active Scintillating Liquid Targets 89
6.2.1 Vessel Capability 89
6.2.2 Production of Active Scintillating Liquid Targets . . . 91

7 Results 93
7.1 A Thin Plastic Scintillating Layer 93
7.1.1 Scintillator Response 93
7.2 Active Scintillating Liquid Targets 96
7.2.1 Vessel Compatibility 96
7.2.2 Particle Discrimination Performance 97

8 Discussion 99

III Production of the isomer ^{195m}Pt 105

9 Introduction 106
9.1 ^{195m}Pt for Medical Use 106
9.1.1 Radioisotopes in Medicine 107
9.1.2 ^{195m}Pt for Medical Use 109
9.1.3 Production Routes 111

10 Applied Experimental Methods **114**
10.1 The EXILL Experiment 114
10.1.1 Neutron Capture 114
10.1.2 Data Processing 120
10.2 The HIGS Experiment 122
10.2.1 The HIGS Facility 122
10.2.2 Compton Backscattering 124
10.2.3 Experimental Conditions 127

11 Results **128**
11.1 ^{194}Pt(n,γ) with EXILL 128
11.1.1 Isomer Populating Transitions 129
11.1.2 Doorway States 133
11.2 ^{195}Pt(γ,γ') with HIGS 138
11.2.1 Irradiation Process 138
11.2.2 Activity Measurement 142

12 Discussion **146**

13 Final Conclusions **153**

A Light Fission Fragment Distribution **159**

B Selenium Analysis **162**
B.1 Selenium 163
B.1.1 ^{83}Se 165
B.1.2 ^{84}Se 166
B.1.3 ^{85}Se 169

C Tabulated EXILL Results **173**

D Activity Measurement Spectra from HIGS **180**

Part I

Fission Fragments in the N=50-60 region

Chapter 1

Introduction

The neutron-rich nuclei in the A = 100 mass region are a very active field of nuclear structure studies for many years already, experimentally and theoretically [1–3]. The attention to this mass region emerges from particular features of single nuclei therein, but even more from the structural evolution along isotopic and isotonic chains, respectively. In this context, especially the mass region around neutron number N = 60 is constantly subject of discussion when it comes to deformation or shape transitions. Today, there are several indications which provide evidence of a behavior which is often described as a "sudden onset of deformation" or "sudden onset of collectivity", respectively. A prominent example of this shape change is the dramatic drop in energy of the first excited 2^+ states in even-even Sr and Zr isotopes from 1 MeV to 200 keV when N = 60 is reached, which can be interpreted as a large and sudden increase in collectivity for these nuclei. Another example is likewise the sudden increase of the respective $B(E; 2_1^+ \rightarrow 0_1^+)$ values or the $4^+/2^+$ energy ratio $R_{4/2}$. However, these observables account only for even-even nuclei. A deduction for odd-A or odd-odd nuclei is thus often more complicated. A similar picture is however also drawn for the evolution of the mean square charge radii $\delta < r^2 >$ and the two neutron separation energies S_{2n} in this region as presented in figure 1.1 for the isotopes with the proton numbers Z = 36 − 42.

The microscopic origin of deformation is often interpreted by the residual proton-neutron interaction as the main driving mechanism. Accordingly, especially at mid-shell regions, where the influence of the stabilizing effect of shell-closures becomes less pronounce, the majority of deformed nuclei are observed. With regard to a discussion within the deformed nuclear shell model (e.g. in [17]) this concerns particularly the interplay of the $\nu g_{7/2}$ and

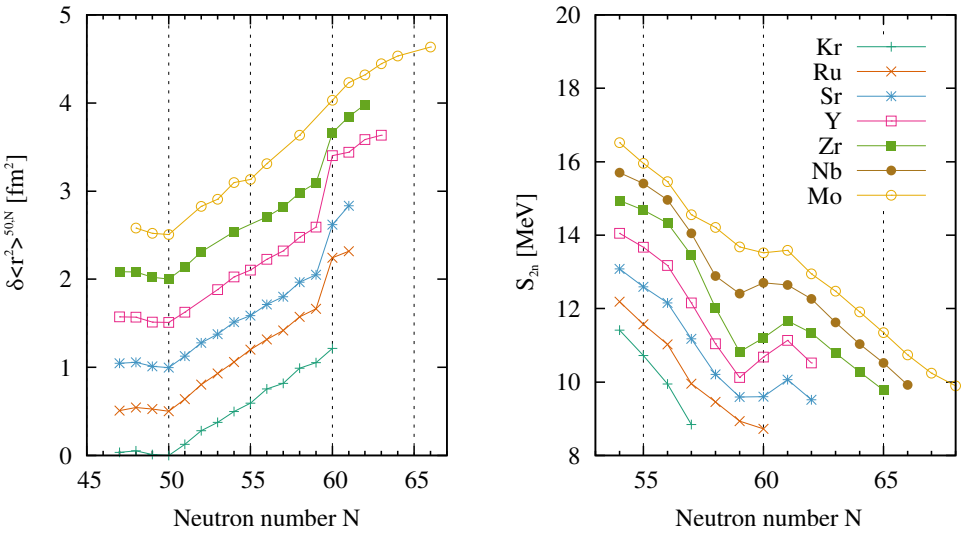

Figure 1.1: Evolution of nuclei with Z = 36 − 42 as a function of the neutron number N in the N = 60 region (from [4]). Left: Difference in mean square charge radii relative to N = 50 [5–10]. Right: Two neutron separation energies [11–16].

$\nu h_{9/2}$ neutron orbits, and the $\pi g_{9/2}$ and $\pi h_{11/2}$ proton orbits in the neutron-rich region around N = 60.

Another interesting phenomenon is the existence of shape coexistence scenarios which arise from a similar argumentation: On one side there is the stabilizing effect of closed shells and sub-shells, respectively, which retain nuclei within the vicinity in rather spherical shapes. And on the other side there is the residual proton-neutron interaction, mentioned above, which drives nuclei into deformation [18]. As a consequence, nuclei where the proton-number is at mid-shell and the neutron-number is around closed-shells, or vice versa, are often prone to this effect. Regarding the N = 50 − 60 region shape coexistence was e.g. observed for the even-even N = 58 isotones ^{96}Sr and ^{98}Zr, as well as for the odd-mass N = 59 isotones ^{97}Sr and ^{99}Zr [19–21], though lying in the open-shell region between proton magic number 28 and 50, and neutron magic number 50 and 82, could be interpreted with respect to a possible interaction with the N = 40 sub-shell closure.

However, the detailed origin of the above introduced phenomena, either for the sudden shape change, or for the appearance of shape coexistence, is still not fully understood and call for further investigation.

A convenient way to study excited states of a large number of nuclei in this

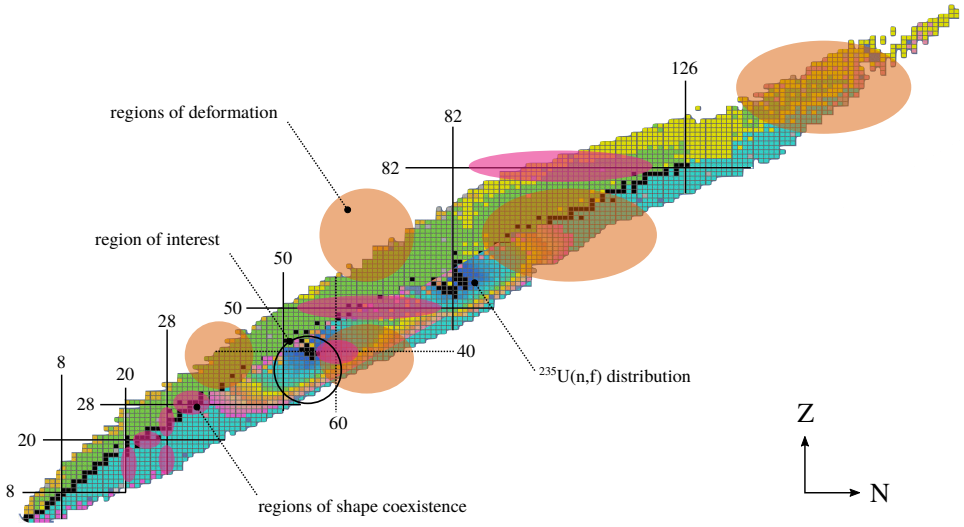

Figure 1.2: Nuclide chart. Closed shells are indicated. Approximate regions of deformation are shown in orange, approximate regions of shape coexistence are shown in red. The fission yield distribution for thermal neutron induced fission of ^{235}U is indicated.

region is via nuclear fission reactions. The light fission fragment distribution of many of the commonly used fissile targets covers this region at least partly. The nuclei presented in this work were produced via the cold neutron induce fission reaction for ^{235}U and ^{241}Pu. A schematic illustration of the nuclide chart is presented in figure 1.2 indicating the fission yield distribution of ^{235}U(n, f) as well as the regions where deformation and shape coexistence is expected.

Chapter 2

Applied Experimental Methods

This chapter gives an overview about the EXILL/FATIMA campaign, the characteristic properties of the EXILL and FATIMA@EXILL setups as well as about the experimental and analytical methods and techniques which were used within the framework of this thesis. Therefore, in section 2.1, the EXILL/FATIMA campaign is introduced with special regard to its main objective and the description and classification of the detector array and its components. Section 2.2 refers to the EXILL detector configuration and is dealing with the γ-spectroscopic analysis of fission spectra. A brief introduction to fission is given and a method for the assignment of γ transitions to a nucleus for an EXILL-like spectrometer is presented. Section 2.3 refers to the FATIMA@EXILL configuration. The fast-timing technique is discussed as well as different analytical methods for the determination of nuclear lifetimes. Special attention is given to the recently developed picosecond sensitive *Generalized Centroid Difference Method*.

2.1 The EXILL and FATIMA@EXILL Campaign

From November 2012 until April 2013 the EXILL and FATIMA@EXILL γ detector array was installed for a duration of two reactor cycles, i.e. 100 days at the cold neutron beam line PF1B at the Institut Laue-Langevin in Grenoble, France. The purpose of the campaign was the γ-spectroscopic investigation of nuclei produced by cold neutron capture at high rates with an efficient gamma detector array (EXILL), i.e. a combined germanium/ lanthanum-bromide detector array (FATIMA@EXILL) which was optimized

for lifetime measurements of excited states in atomic nuclei. Researchers from more than 20 laboratories were participating in this campaign performing experiments of a broad spectrum of physics cases in the field of fundamental nuclear physics, e.g. [22], astrophysics or nuclear related applications. In order to cover all the requirements for the different experimental proposals the campaign was scheduled for an n-γ measurement on 17 stable targets in total, to investigate nuclei near the valley of stability [23] and a neutron induced fission part for the actinides ^{235}U and ^{241}Pu for measurements on the corresponding fission products in the β^- unstable region around neutron number 50-60 for the light fission fragments and around neutron number 80-90 for the heavy fission fragments respectively.

2.1.1 Experimental Environment

This section intends to give a brief overview about conditional framework for the EXILL campaign [24, 25]. In the following the basic properties of the ILL reactor are discussed as well as the experimental workspace PF1B where the EXILL array was operating.

The ILL Reactor

The Institut Laue-Langevin is an international research center of neutron science and technology with a research focus primarily on fundamental science in a variety of fields such as condensed matter physics, chemistry, biology, nuclear physics and materials science [26]. The heart of ILL is its high-flux reactor operating at a thermal power of 58 MeV and driven by a highly enriched fuel element of ^{235}U which is producing a thermal neutron flux of $1.5 \cdot 10^{15}\,\mathrm{cm^{-2}s^{-1}}$. Besides thermal neutrons (25 meV) three components within the reactor vessel (one hot source and two cold sources) produce neutrons of different temperature; hot neutrons (≈ 200 meV), cold neutrons (≈ 3 meV) and ultracold neutrons (≈ 200 neV). These neutrons are guided through beam lines to around 40 different instruments, while other instruments are directly located in the reactor hall. In total 7 instruments are dedicated to nuclear and particle physics (NPP) experiments such as the recoil mass spectrometer Lohengrin (see section 6.1.2), the newly developed fission product prompt γ-ray spectrometer FIPPS (see section 5.1) or the cold neutron beam facility PF1B which is discussed in more detail in the following section.

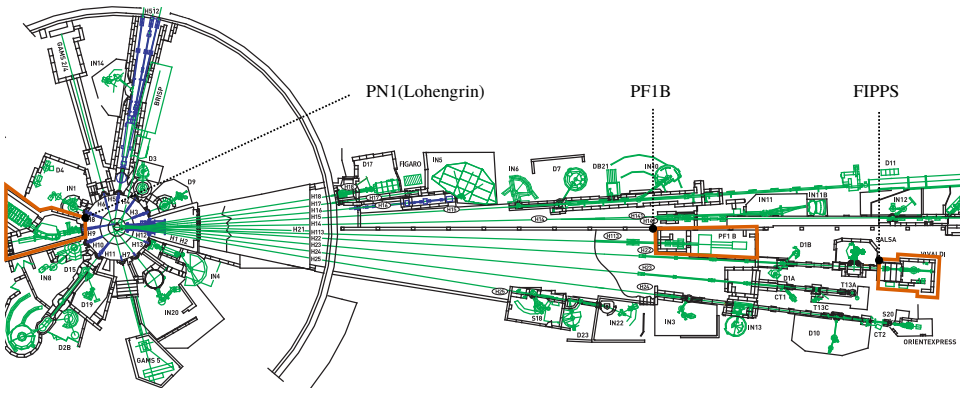

Figure 2.1: Schematic partial top view of the ILL reactor building (left side) and the neutron guide hall ILL7 (right side). The instruments are connected through neutron beam guides (straight green lines) with the reactor vessel. The NPP instruments PN1, PF1B and FIPPS are highlighted.

The PF1B Experimental Area

The PF1B experimental area is connected to the H113 super mirror beam line guiding cold neutrons from the reactor's cold source and providing a neutron flux of density of $2.2 \cdot 10^{10}\,\mathrm{cm^{-2}s^{-1}}$. It is described as the simplest but most flexible instrument at the ILL [27]. However, PF1B is rather an experimental zone than an instrument providing a workspace for the installation of complementary instruments as in the case of the EXILL array. The experimental zone of about 3 m width and 10 m length in beam direction is equipped with a proper shielding for the reduction of γ and neutron background from the surrounding beam lines. A casemate situated before the experimental zone provides the possibility for the installation of additional devices dedicated to the neutron beam (e.g. polarizers). For the EXILL campaign a 4 m long collimation system [24] was installed for γ and neutron suppression with a thermal equivalent neutron flux of $1 \cdot 10^{8}\,\mathrm{cm^{-2}s^{-1}}$ and a FWHM beam profile of 12 mm.

2.1.2 The EXILL detector array

The EXILL array was a HPGe detector cluster array designed for the use of detecting rare γ events taking place in neutron induced fission reactions of ^{235}U and ^{241}Pu and in neutron capture reactions on stable nuclei. Similar arrays such as EUROGAM/EUROBALL [28, 29] and Gammasphere [30] were already established in the past for spontaneous fission reactions of

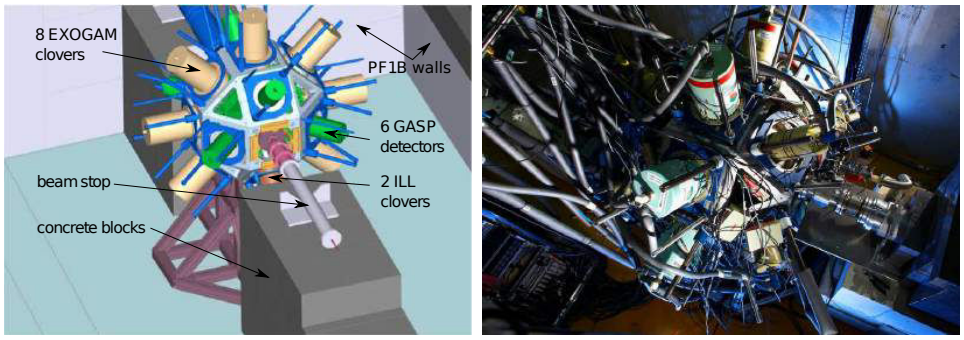

Figure 2.2: The EXILL detector array at the cold neutron beam area PF1B, schematically (left from [24]) and in real (right). See text for further information.

^{252}Cf and ^{248}Cm. The array itself is of rhombicuboctahedron geometry with HPGe detectors placed on 16 of 18 square faces. Two square faces remained open for the entry and the exit of the beam tube which ended about one meter outside the array in a neutron absorbing ^{6}LiF beam stop. Additional boron shielding along the beam tube prevented the detectors from activation by scattered neutrons, and a lead shielding from the detection of unwanted secondary γ events. The targets were placed under vacuum in the center of the array. In order to reduce unwanted γ events Teflon bags were used as supporting material for all stable targets due to its low neutron capture cross section. For the fission experiments 99.7% enriched ^{235}U and 78% enriched ^{241}Pu targets were used. One of the main requirements to the fission targets was the stopping of the corresponding fission fragments to occur within picoseconds in the target in order to reduce Doppler broadening of the emitted γ-rays. The actinide layers were thus covered by two layers of either beryllium or zirconium on both sides[1] resulting in a set of two targets, for ^{235}U and ^{241}Pu.

Detectors

In total 16 HPGe detectors were mounted to the EXILL frame[2]. The main plane - perpendicular to the beam direction - is equipped with 8 clover[3]

[1] often referred to as "sandwiched".
[2] or 46 germanium crystals.
[3] 4 crystals sharing the same cryostat.

detectors of the EXOGAM[4] instrument [31] from the GANIL laboratory in Caen, France. Due to the geometry of the array each one of them encloses an angle of 45° to its neighboring EXOGAM detector with a target-to-detector distance of 14.5 cm [32]. The efficiency of each single clover crystal is about 38% (relative to a standard NaI crystal) leading to a combined efficiency for the reconstruction of internally Compton scattered full energy peak (FEP) events in the add-back mode of about 220% [24]. Besides each EXOGAM clover is surrounded by a bismuth germanate scintillator crystal (BGO) shielding for the active suppression of Compton events. Six large volume coaxial germanium detectors of 80% efficiency each from the Legnaro National Laboratories from the GASP instrument[5] [33] were mounted under 45° relative to the beam direction in forward angle and backward angle respectively. Like the EXOGAM detectors the GASP detectors were also equipped with a BGO shielding. Two additional clover detectors from the ILL's Lohengrin instrument[6] were placed under 45° with respect to beam direction from below. They provide a γ-ray efficiency of 25% for each crystal or 130% for the combined clover in add-back mode [24].

Data Acquisition and Event Structure

The data processing for the EXILL campaign was completely realized by a digital data acquisition system. Therefore, the analog output signals from the detector preamplifier were sampled by ten V1724 CAEN 8-channel digitizers. The digitizers were synchronized with a 100 MHz common clock, resulting in a theoretical nominal time uncertainty of 10 ns. Each signal was stored triggerless in a hexadecimal representation of 32 bits containing the information on the crate, the card number, the associated channel number, the energy and an absolute time stamp of the signal. A subdivision of the data stream to files of a size of 2 GB each results, for typical count rates of 10-20 kHz per channel, in runs of 7-15 min.

2.1.3 The FATIMA@EXILL detector array

The FATIMA@EXILL detector array [32] was basically an extended configuration of the EXILL setup dedicated to lifetime measurements in the low picoseconds to nanoseconds range of nuclear excited states by using the tech-

[4] often referred to as the EXOGAM detectors and the reason for the name EXILL. EXOGAM is usually located at GANIL but went into "exile" at ILL.

[5] therefore often referred to as GASP detectors.

[6] Lohengrin detectors

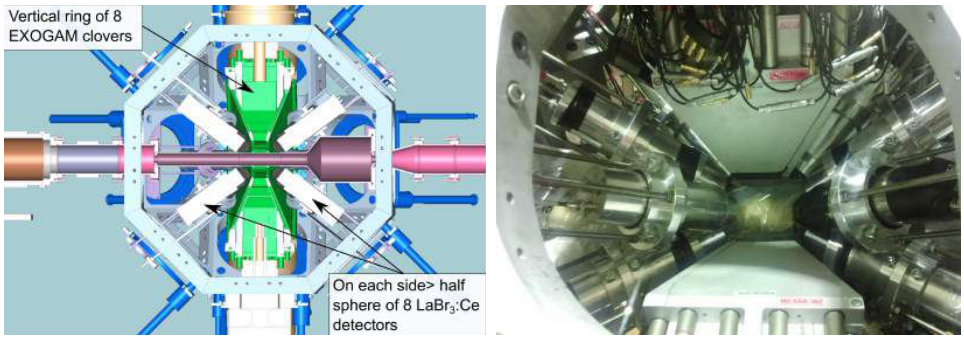

Figure 2.3: The FATIMA configuration of the EXILL setup: Left: Schematically open top view showing the EXOGAM clovers (in green) and the LaBr detectors (in white) [24]. The beam is coming from the right side. Right: Close-up view showing the inner reaction chamber for the actinide targets (middle), the LaBr detectors pointing to it (left and right side) and two BGO suppression shieldings of the EXOGAM detectors (coming from above and below).

nique of delayed coincidences. In order to access such lifetimes germanium detectors provide an insufficient time response. Therefore the six GASP detectors as well as the two Lohengrin detectors were removed and replaced by 16 fast $LaBr_3(Ce)$[7] detectors with a distance of 8.5 cm to the target. Although the time response of such LaBr detectors is much superior to the time response of germanium detectors their energy resolution is far worse. Especially for reactions of high γ density like for the fission reaction of ^{235}U and ^{241}Pu a simple γ-γ coincidence analysis with LaBr detectors becomes insufficient at best. Additional γ constraints provided by high resolution germanium detectors are therefore indispensable for a proper truncation of the unwanted coincidence events and thus requiring the need of the EXOGAM detector ensemble (see also section 2.3.4). The FATIMA@EXILL array is hence consisting of 24 detectors; the 8 BGO shielded EXOGAM HPGe clovers in the main plane and the 16 LaBr detectors in forward and backward direction enclosing angles of 40° and 140° with respect to the beam direction.

[7] in the following just called LaBr.

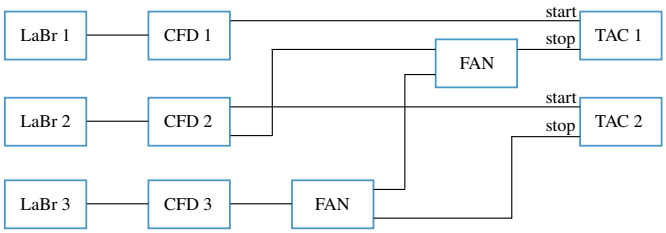

Figure 2.4: Schematic illustration of an analog fast-timing circuit as it was used for the FATIMA@EXILL campaign, simplified for a three detector setup as it was. If detector 1 starts, detector 2 and 3 are allowed to stop, if detector 2 starts, only detector 3 can stop, detector 3 cannot start at all.

Data Acquisition

In contrast to the germanium detectors of the EXILL array the LaBr detectors of the FATIMA array undergo an analog electronic fast-timing circuit before fed in the CAEN V1724 digitizers of the EXILL DAQ and thus synchronized with the overall data stream. Therefore each LaBr preamplifier's output signal is first processed by a constant fraction discriminator (CFD) picking up its time information. A time-to-amplitude converter module (TAC) then converts the time information from two independent CFDs into an equivalent amplitude of an output signal by being started and stopped respectively by two nearly coincident signals. However, since the FATIMA array consists of 16 timing detectors a sophisticated fan-in/fan-out logic (see figure 2.4) is connected in between the CFDs and the TACs in a way that any signal provided by a "parent" detector can start its associated TAC which is then stopped by a coincident signal of any other "daughter" detector[8]. By doing so the possible combination of detector-detector timing combinations calculates to N(N-1)/2 by excluding double counting, e.g. TAC_{12}=-TAC_{21} [34] (cf. figure 2.4).

2.2 Analysis of Fission Spectra

Basically, the γ spectroscopic observables of the EXILL array may be summarized as the energy, the location of detection, i.e. detector number, and the time of detection of a γ event. Especially the latter offers an important information for the assignment of such events to a nucleus when implemented

[8] often denoted as common stop technique.

into a coincidence circuit[9]. This section will briefly introduce the data processing regarding the EXILL fission experiments $^{235}\mathrm{U}(\mathrm{n},\gamma)$ and $^{241}\mathrm{Pu}(\mathrm{n},\gamma)$ and discuss the applied methods for the identification of fission fragments afterwards.

2.2.1 Data Processing

The total amount of recorded raw data, i.e. listmode data for the two fission experiments was about 10 TB referring to a 22 days measurement of $^{235}\mathrm{U}(\mathrm{n},\gamma)$ (6.1 TB) and a 14 days measurement of $^{241}\mathrm{Pu}(\mathrm{n},\gamma)$ (3.4 TB). In order to recombine the uncorrelated raw data signals to correlated events a sorting algorithm was applied to the listmode files. This procedure was performed with the event building code lst2root [36]. Therefore at least two signals[10] being detected by any Ge-detector of the EXILL array within a coincidence window of 200 ns were considered as an event which was chosen with respect to the overall Ge-Ge time alignment. In a further step the events were calibrated in energy by using a ^{152}Eu source for the low energy range up to ≈ 1.4 MeV and an in-beam measurement of a $BaCl_2$ for the high energy range. Energy shifts in time were corrected within an adjustment of the different run files. Events occurring in single crystals of a clover detector were merged to clover events by implementing an add-back routine and coincident BGO-Ge events following a Compton out-scattering were rejected as invalid γ events. The gaspware package [37] was then used to create a γ-γ matrix and a γ-γ-γ cube. It allows also the creation of quadruple events i.e. γ-γ-γ-γ 4-folded events which were used within this work.

2.2.2 On Fission

In general nuclear fission is a process in which a heavy nucleus splits into smaller nuclei usually accompanied by the emission of neutrons and the release of energy. In a semi-classical approach this process can by understood by comparing the associated binding energies. A heavy nucleus in the uranium region has a binding energy of about 7.6 MeV per nucleon while the binging energy of corresponding tighter bound fission fragments is of the order of about 8.5 MeV per nucleon. The extra amount of energy is being primarily released in the fission process as kinetic energy of the fission fragments. As an example following thermal fission of ^{235}U with an release energy of about 203 MeV, then approximately 89% of the energy is released

[9] for the development of which Walther Bothe received the Nobel prize in 1954 [35].
[10] γ multiplicity 2.

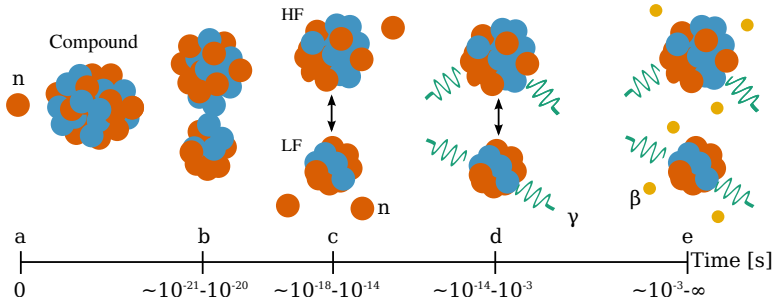

Figure 2.5: Schematic illustration of the evolution of neutron induced fission with time: a) The compound nucleus e.g. ^{235}U or ^{241}Pu is capturing a neutron. b) The fissioning system e.g. ^{236}U or ^{242}Pu is driving towards instability reaching the scission point. c) The fission fragments are overcoming their Coulomb barrier, thus repelling each other and releasing a portion of their energy by the emission of neutrons. d) The residual energy is released by γ emission (prompt γ). e) The fission fragments β decay until stability is reached. This process also goes along with the emission of γ-rays (delayed γ).

instantaneously via the kinetic energy of the fission fragments (169 MeV (84%)), prompt neutrons (5 MeV (2%)) and prompt γ emission (7 MeV (3%)). The remaining 11% are released in via the decay of fission products in β-decay (7 MeV (3%)), its accompanied anti-neutrino decay (9 MeV (4%)) and delayed γ emission (6 MeV (3%)).

However, not every heavy nucleus has - with respect to a statistical relevance - the capability to fission as it can be assumed as being energetically stable within its potential well, classically prevented by the Coulomb barrier from fissioning. In order to overcome the Coulomb barrier for ^{236}U an activation energy which is calculated to be 6.2 MeV is necessary. In its ground state ^{236}U has an energy - following the mass-energy equivalence $E = mc^2$ - of $E = 219877.9$ MeV. However, an excited compound state of ^{236}U produced by adding a single neutron of negligible kinetic energy to ^{235}U calculates to $E = 219883.5$ MeV leading to an excitation energy of 6.6 MeV[11]. The neutron induced fission reaction ^{235}U(n, f) can be seen as a compound reaction following neutron capture on ^{235}U. It is worth to stress that the above calculation was assuming the kinetic neutron energy to be zero. In fact, the cross sections for neutron-induced fission are strongly depending on the energy of the neutron. For thermal neutron energies and below the cross section

[11] following the example in [38].

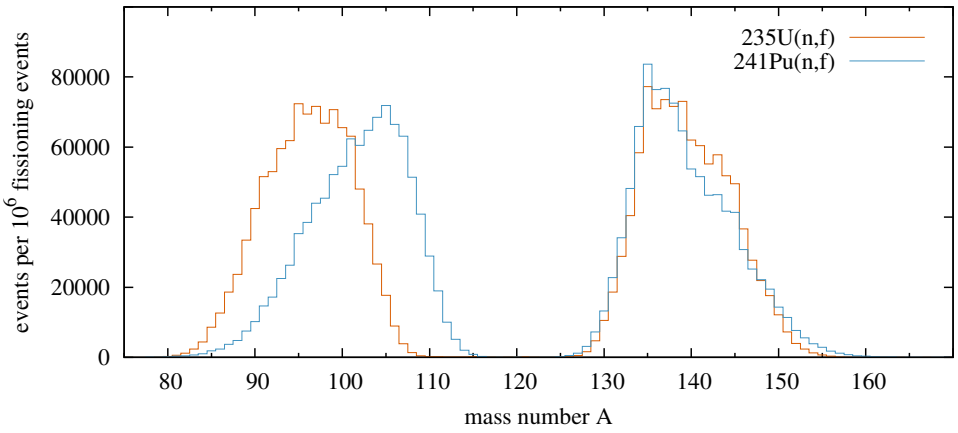

Figure 2.6: GEF [39] simulation of fission fragment yields for neutron induced fission of ^{235}U and ^{241}Pu. The simulation was performed for 10^6 fissioning events and a (cold) neutron energy of 5 meV.

is showing a 1/v dependence implying a higher fission probability for lower the neutron energy. However, for experimental conditions the benefit of the higher cross section for cold neutrons with regard to e.g. thermal neutrons evens out with a reduced flux.

The production yields for fission fragments in neutron induced fission of ^{235}U and ^{241}Pu are schematically presented in figure 2.6. For both fissioning systems it shows the fission fragment yields with respect to the mass number. It is important to point out that a representation like this does not take into account of specific nuclei with a given Z and N but only an aggregation of nuclei with the same mass number A which means that each data point in 2.6 summarizes the cumulative yield of any nuclei with A=Z+N. In particular nuclei with the same A but a different N or Z might thus not be represented sufficiently with this yield. It gives however an interesting information about the yield distribution of such fissioning systems in general as well as about the difference of ^{235}U and ^{241}Pu in particular. Thus, fig. 2.6 is showing the well known asymmetric double hump structure as well as a differing maximum for the light fission fragment distribution which peaks around mass number 95 for ^{235}U and around mass number 105 for ^{241}Pu. That implies ^{241}Pu to be more favorable for light fission fragments heavier than mass A $\approx$ 102 with respect to its fission fragment yield in neutron induced fission.
Another aspect of fission which is especially important with regard to the following section is the distribution of emitted neutrons (cf. figure 2.5c).

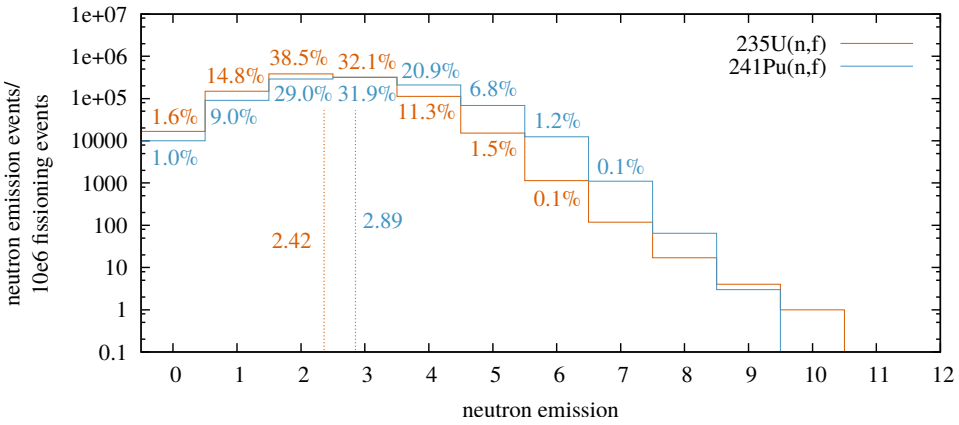

Figure 2.7: GEF [39] simulation of the prompt neutron distribution for neutron induced fission of ^{235}U and ^{241}Pu. The simulation was performed for 10^6 fissioning events and a (cold) neutron energy of 5 meV.

These so called prompt neutrons have been intensively studied in the 1950s and 1960s by J. Terrell and others [40–44] to which the reader is referred to for more detailed information. Within the scope of this work the focus is rather set to the overall prompt neutron emission. One of the main features of prompt neutron emission in compound fission reactions is the almost Gaussian prompt neutron multiplicity distribution for all of the common fissioning systems with a constant full width half maximum σ=1.08 while the average maximum varies approximately between 2.41 for neutron induced fission of ^{235}U and 3.77 for spontaneous fission of ^{252}Cf [45, 46]. An illustration is shown in figure 2.7 for ^{235}U and ^{241}Pu.

2.2.3 Identification of Fission Fragments

The identification of fission fragments is one of the major aspects for a γ spectroscopy analysis for an EXILL-like Ge array. Since there is no device within the EXILL array for the direct identification of fission fragments a proper assignment of detected γ transitions to its corresponding nucleus becomes challenging. As mentioned earlier the coincidence technique is basically the only method which can be applied to such data by truncating the quantity of nuclei. Therefore, - as starting point - some initial information about known γ transitions assigned to a nucleus is necessary.
The performance of such a coincidence analysis is discussed with regard to figure 2.8. The different spectra are showing the evolution from a γ-γ projec-

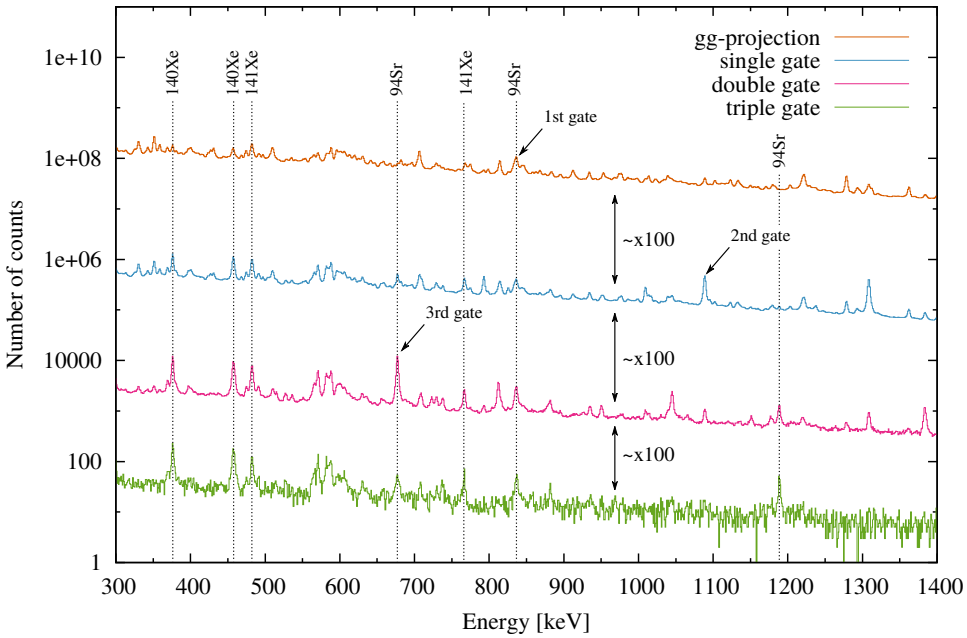

Figure 2.8: Germanium spectra for muliple coincidences in ^{94}Sr: Orange: Ungated γ-γ projection. Blue: Single gate at 837 keV. Red: Double gate on 837 keV and 1089 keV. Green: Triple gate at 837 keV, 1089 keV and 677 keV. The appearance of the peaks referring to previous gates is due to random coincidences caused by high count rates and a relatively large coincidence window.

tion through a single gated, a double gated and a triple gated spectrum for known transitions in ^{94}Sr for the ^{235}U(n, f) data set. One can clearly see an increase in selectivity by adding additional gates. However, each additional requested γ coincidence is also decreasing the statistics by about a factor of 100. While ^{94}Sr is among the strongest produced nuclei in neutron induced fission of ^{235}U, especially for less produced nuclei respectively weaker γ transitions a more selective γ restriction does not necessarily lead to a better identification. It is also worth to mention that the coincidence analysis of a purely ^{94}Sr gated events is attended by the occurance of γ transitions in the spectra which can be assigned to different xenon nuclei. This is due to the fact that each ^{94}Sr fission fragment is emitted together with a ^{A}Xe isotope where $A = 236 - 94 - \nu$ (ν = number of emitted neutrons). Such pairs are called “complementary”.

For a γ coincidence analysis this means that mainly two stages of the

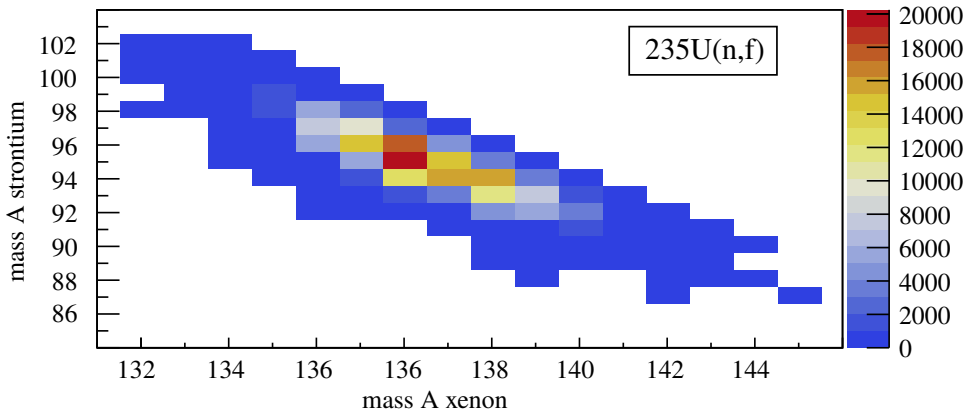

Figure 2.9: GEF [39] simulation of the yield distribution for given strontium-xenon pairs performed for 10^6 fission events and a neutron energy of 5 meV.

fission process are of importance which, a priori, can not be distinguished by the EXILL setup: 1) prompt γ-rays (fig. 2.5d) and 2) delayed γ-rays (fig. 2.5e). While the latter appear to be in coincidence only with other γ transitions from the same nucleus, prompt γ transitions are in addition always coincident with γ transitions of the complementary fission fragment. For the statistical ensemble of fission partners however, and with regard to the neutron emission distribution there is never one but always several fission partners of the same Z but a different neutron number with respect to a defined partner fragment. A case example for different reactions of ^{94}Sr in neutron induced fission of ^{235}U and ^{241}Pu is shown exemplary in eq. (2.1) and eq. (2.2). An assignment of the light fission fragments to their corresponding heavy fission fragments is presented in table 2.1:

Table 2.1: Complementary fission fragments in uranium and plutonium fissioning systems.

	light fission fragments										
Element	Zn	Ga	Ge	As	Sc	Br	Kr	Rb	Sr	Y	Zr
	complementary heavy fission fragments										
U	Sm	Pm	Nd	Pr	Ce	La	Ba	Cs	Xe	I	Te
Pu	Gd	Eu	Sm	Pm	Nd	Pr	Ce	La	Ba	Cs	Xe

$$^{235}\mathrm{U} + \mathrm{n} \rightarrow {}^{94}\mathrm{Sr} + \begin{cases} 0\mathrm{n} + {}^{142}\mathrm{Xe} \\ 1\mathrm{n} + {}^{141}\mathrm{Xe} \\ 2\mathrm{n} + {}^{140}\mathrm{Xe} \\ \vdots \end{cases} \tag{2.1}$$

$$^{241}\mathrm{Pu} + \mathrm{n} \rightarrow {}^{94}\mathrm{Sr} + \begin{cases} 0\mathrm{n} + {}^{148}\mathrm{Ba} \\ 1\mathrm{n} + {}^{147}\mathrm{Ba} \\ 2\mathrm{n} + {}^{146}\mathrm{Ba} \\ \vdots \end{cases} \tag{2.2}$$

For a coincidence analysis it is thus of major interest to have an estimation about which complementary fragments are produced to which yield with respect to a selected nucleus, respectively its corresponding γ transitions. Figure 2.9 illustrates a simulation of different isotopes of the strontium-xenon pair for the ^{236}U fissioning system. Although this simultaneous appearance of γ transitions from different nuclei limits a proper assignment to the nucleus, it also offers some spin-off. It is hence possible to intentionally use partner gated spectra in order to assign γ transitions of the corresponding complementary fission fragments by their intensity ratio. For illustration an example of this technique is shown with respect to figure 2.10.
The purpose of this analysis is the assignment of γ transitions of strontium isotopes by gating on xenon isotopes. With respect to the prompt neutron distribution and figure 2.9 it is evident that ^{139}Xe and ^{140}Xe are the most suited fission partner for the analysis of ^{94}Sr produced within the 2n and 3n reaction channel. Therefore two coincidence spectra were sorted with double gates on 571 keV and 492 keV in ^{139}Xe and 376 keV and 475 keV in ^{140}Xe (cf. 2.10, upper panel). Ideally all transitions of these two spectra which appear in both spectra should either belong to a strontium isotope or are of random coincidence origin. Transitions which appear in only one spectrum on the other hand are either in coincidence with the chosen gates within the xenon nucleus (either ^{139}Xe or ^{140}Xe) or coming from a similar transition pair of any other nucleus resp. fission fragment pair. The lower panel of figure 2.10 is thus showing the peak volume ratio (PVR) of those transitions which are present in both coincidence spectra deduced by fitting a Gaussian function to the corresponding peaks and building the ratio Vol(^{139}Xe)/Vol(^{140}Xe). Additional transitions which are well known and can be clearly assigned to a strontium isotope (^{93}Sr,^{94}Sr,^{95}Sr) were used as calibration in order to determine the PVR which is assigned to the strontium isotope and is indicated

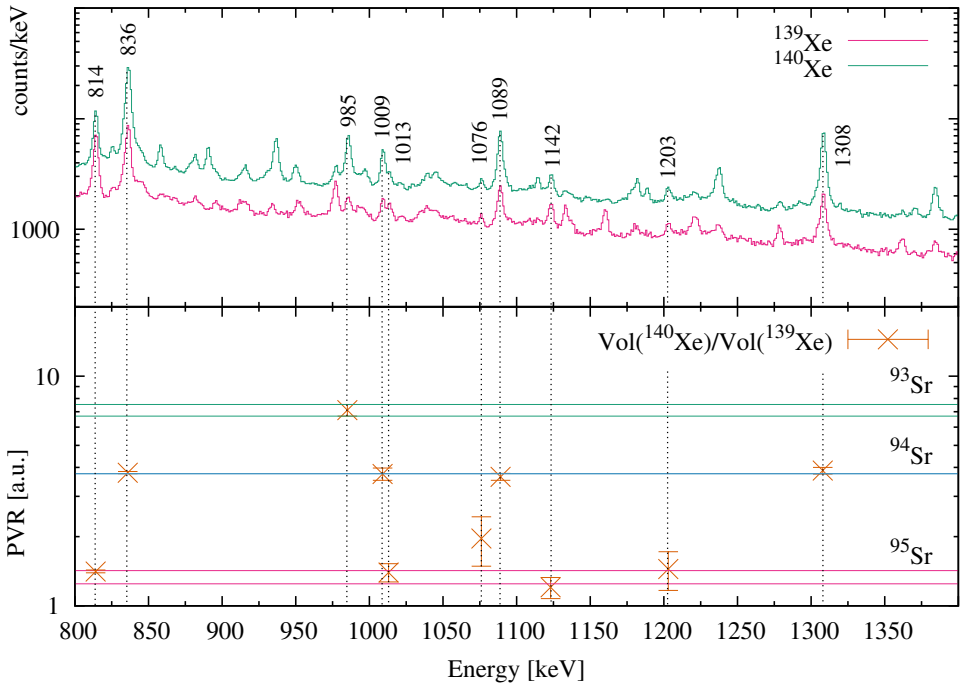

Figure 2.10: PVR representation for the experimental identification of fission fragments in the strontium region around mass 94, respectively the assignment of γ transitions to its nucleus. See text for further information.

as horizontal lines. The basic idea of this technique was first presented by M.A.C Hotchkis *et al.* [47, 48]. Since then it was consequently adopted to γ optimized fission experiments like for the EXOGAM array [49] or more recentely for the EXILL campaign [50, 51].

2.3 Analysis of Time Spectra

The precise knowledge of the lifetime of excited nuclear states is of uttermost importance in nuclear structure physics. The mean lifetime τ of such an excited state Ψ_i before decaying into a lower lying state Ψ_f is directly correlated with it's transition probability $\lambda{=}1/\tau$ which gives direct information about the interaction that causes the transition (i.e. matrix elements) between the involved states. It is thus a main observable in the description and explanation of complex nuclei as well as in testing and developing new nuclear structure models. However, the range of different lifetimes can be

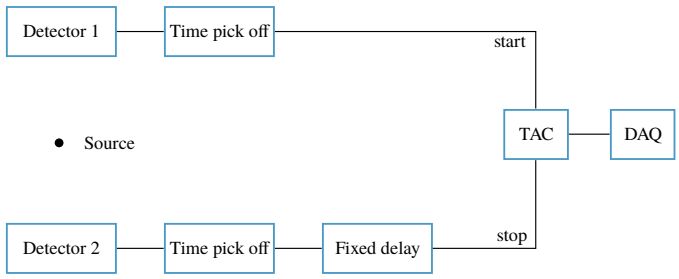

Figure 2.11: Schematic illustration of a fast-timing circuit [53]. See text for further information.

very broad, reaching from 10^{15} years for some natural occurring radioisotopes to a few femtoseconds or less for short-lived excited states [38]. Hence, various techniques have been developed, each of which is adapted to a specific lifetime regime and experimental conditions. A complete description of these techniques can be found in [52].
The following section will give an overview of different methods which were used to determine lifetimes of γ decaying excited states from the low picoseconds to the nanoseconds range of excited nuclei produced via neutron induced fission of ^{235}U within this work. A brief introduction to the main features of experimental electronic fast-timing as well as its associated analyzing techniques such as the slope method, the deconvolution method and the recently developed *Generalized Centroid Difference Method* is given.

2.3.1 Electronic fast-timing

In the most general meaning electronic fast-timing means the measurement of "short" nuclear lifetimes with electronic acquisition systems by using the method of delayed coincidences. It is thus to differentiate from other techniques accessing short lifetimes such as the *Recoil Distance Method* (RDM) or the *Doppler-Shift Attenuation Method* (DSAM) [52]. The word "fast" refers to both, the "fast" decay to be measured as well as the fast electronic acquisition system. However, throughout the development of this technique and the associated development of faster detector systems, the fast-timing technique is nowadays crucial to lifetimes within the nanosecond regime down to a few picoseconds.

The general idea behind experimental fast-timing is based on the measurement of the time difference of two signals which are in delayed coincidence; that is, the population of a state of interest and its depopulation.

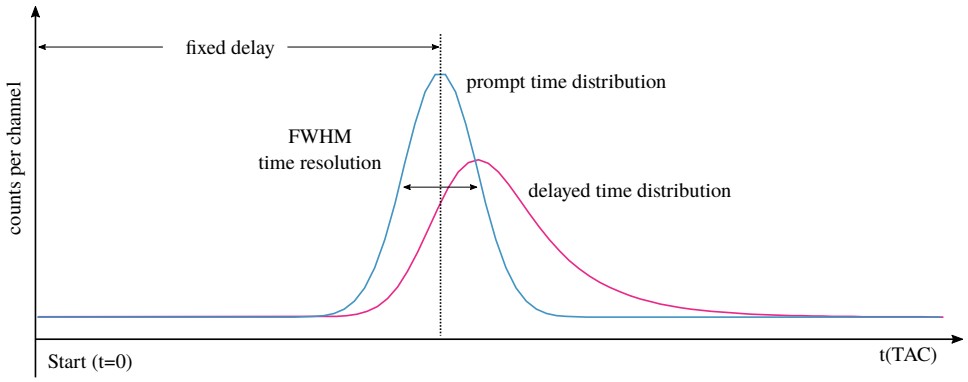

Figure 2.12: Schematic illustration of prompt and delayed time distributions for a fast-timing setup as it is presented in figure 2.11 [53]. See text for further explanations.

With regard to figure 2.11 both signals are processed by two independent time branches of the same setup. In the most comprehensible situation the populating transition is detected by detector 1 which is connected with the start branch. A time pick-off module is then converting the detector pulse with regard to its time dependence, which is then starting the time measurement by triggering the Time-to-Amplitude Converter (TAC). The decaying transition however is detected by detector 2 and thus stopping the time measurement. The reason of the implemented delay in the stop branch, as quoted in e.g. [53], is for delaying the time spectrum in order to avoid cutting it off; if there was no delay between the two branches, a prompt time distribution would be centered around zero time and thus only half of its shape would be measured. For the measurement of the lifetime of an excited state a source is indicated exemplary for any coincident radiation emitting system. Hence, any measurable event can serve as such a signal. However, β-γ timing where the β decay serves as start event and the γ decay as stop and γ-γ timing where the feeding γ decay starts and the decaying γ-decay stops the measurement are among the most commonly used. An important characteristic of a fast-timing setup is its time resolution. The time response of the involved detectors and electronics is usually of the same order as the lifetimes to measure. It is thus of major importance to define the time uncertainty of such a setup. This is particularly true for the lower time limit which is given by so-called prompt events; that is the time distribution of two signals which are in delayed coincidence in a way that they can not be resolved by the setup and are thus indistinguishable from a real prompt

event. This property is given by the Prompt Response Function (PRF). For modern fast-timing setups using fast scintillating detectors a time resolution of about 100 ps is feasible which allows lifetime measurements down to about 5 ps with e.g. centroid difference analysis. The upper limit however is often quoted as to be in the microseconds range. There is actually no general reason for this limit, but a practical one which is due to the fundamental idea of delayed coincidences namely coincident events which are belonging to the same deexcitation process. The correct assignment of such signals becomes evidently uncertain with raising decay rates. With regard to figure 2.11 a typical time spectrum of such a fast-timing measurement is presented in figure 2.12 for a real prompt time distribution as well as for a time distribution of measurable lifetime. Mathematically such time distributions D(t) are described by equation (2.3); that is a convolution of a non-zero prompt response function $P(t')$ and an exponential decay $e^{-\lambda(t-t')}$,

$$D(t) = \lambda N_0 \int_{-\infty}^{t} P(t')e^{-\lambda(t-t')}dt'. \tag{2.3}$$

Different methods to analyze such a time distribution are presented in the following sections.

2.3.2 The Slope Fit and the Convolution Method

The time distribution of a delayed coincidence measurement of nuclear excited states is described by equation (2.3). For states whose lifetime is considerably longer than the setup's resolution given by $P(t')$ the lifetime can be either determined by fitting an exponential function to the exponentially decaying part of the time distribution or by fitting the whole spectrum with the convolution method [54]. For the use of the slope fit method the time distribution can be seen as the statistical process of an exponential decay as it is known for the radioactive decay. Such a process is described by the differential equation (2.4) which is solved by equation (2.5):

$$\frac{dN(t)}{dt} = -\lambda N(t), \tag{2.4}$$

$$N(t) = N_0 e^{-\lambda t}, \tag{2.5}$$

where N(t) is the quantity of excited states at a time t, N_0 the initial quantity of excited states and λ the exponential decay constant which is connected with the mean lifetime τ via $\lambda=1/\tau$ or with the half-life $T_{1/2}$ via $\lambda=\ln(2)/T_{1/2}$ respectively. The representation in a semi-logarithmic plot

thus leads to a straight line with the slope constant $-\lambda$. The use of this method has clearly a great advantage due to its simple application. However, especially for a γ-γ-γ or fission analysis the results of this method have to be interpreted carefully. This is especially true for the treatment of background events; For populating and/or depopulating transitions of excited states at low energy these transitions are usually superimposed with a large Compton background which is usually not in true coincidence with the involved transitions but can however contribute with random coincidences to an artificial broadening of the resolution (cf. figure 4.23). For the actual fit limits of the slope fit it is therefore of importance to consider not only the convoluted prompt response function but also the transition-Compton coincidences in a time spectrum. An active background subtraction by means of a subtraction of coincident background events in the coincidence matrix would generally lead to a clear time spectrum but is practically showing some minor inconsistencies depending on the chosen gate. The origin of these inconsistencies is not always obvious but due to the broad energy resolution of the involved LaBr timing detectors the actual Compton background is often "contaminated" with other coincident transitions which contribute to the time spectrum. Therefore, in this thesis, background events were determined analytically and subtracted from the lifetime within the analysis.
In contrast to the fit slope method not only the slope but the entire time distribution is fitted within the convolution fit method. The reconstruction of the mean lifetime is thus based on the deconvolution of equation (2.3) i.e. its prompt response function and the exponential decay part. Assuming the PRF to be approximately of Gaussian shape the convolution is described by equation (2.6):

$$\mathrm{D(t)} = \frac{\mathrm{N_0}}{2\tau} \mathrm{e}^{\frac{\sigma^2}{2\tau^2} - \frac{\mathrm{t}-\mathrm{t_0}}{\tau}} \ \mathrm{erfc}(\sigma/\sqrt{2}\tau - (\mathrm{t}-\mathrm{t_0})/\sqrt{2}\sigma), \tag{2.6}$$

with the position $\mathrm{t_0}$ of the PRF, its width σ and the Gaussian complementary error function erfc. This method is reported to yield in more precise results than the slope fit method [54–56]. It is however also more sensitive to misinterpretations due to its 4 fitting parameters. Especially when the calculated prompt curve is not representing the actual setup's resolution because the time spectrum is superimposed with background or unwanted coincident events the resulting lifetime could be overestimated by eq. (2.6).

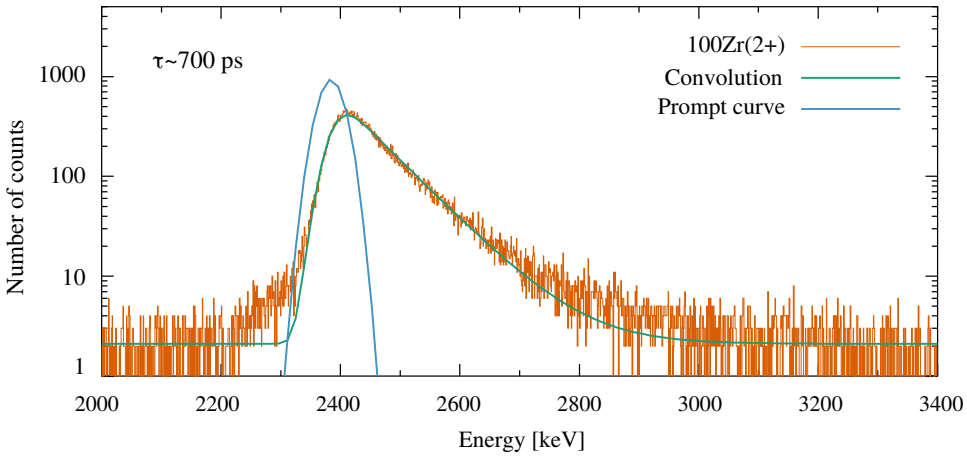

Figure 2.13: Illustration of the convolution fit method applied to the first 2^+ state of ^{100}Zr. The prompt curve was reconstructed with respect to the fit parameters of the convolution. See text for further explanations.

2.3.3 The Generalized Centroid Difference Method

For lifetimes which are smaller than the FWHM of the setup's PRF or which are too short to extract the exponential information from the convolution the above presented methods are not applicable anymore or lead to increased uncertainties. Centroid shift methods however are more sensitive to such "short" lifetimes. This section reports on the *Generalized Centroid Difference Method* which was applied to picoseconds and sub-nanoseconds lifetime determination within this work. For the purpose of comprehensibility the method is introduced with the *Centroid Shift Method* and the related *Mirror Symmetric Centroid Difference Method*, respectively.

The Centroid Shift Method

The basic idea of measuring decay times with coincidence techniques was proposed analytically by Z. Bay in 1950 [57] where he introduced a method for the calculation of any delayed time spectrum from the moments of two curves, a prompt curve of negligible time delay with respect to the setup's time resolution which is thus characterizing it, and the actual time delay curve from the coincidence measurement of two transitions. In the case of single decay processes (i.e. feeding transition starts, decaying transition stops) these two curves can each be expressed by their first moment which is given by the center of gravity of the respective centroid. In the following

the centroids are indicated as C(P) for the centroid of the prompt curve and C(D) for the centroid of the delayed curve (cf. also figure 2.12) generally defined for any time distribution F(t) as

$$C(F(t)) = \frac{\int tF(t)}{\int F(t)}. \tag{2.7}$$

It is obvious that this method is mainly sensitive to lifetimes which are smaller than the setup's PRF but can also be applied to lifetimes in the sub-nanosecond regime where the slope fit method or the convolution fit method are no longer feasible. Either way for a delayed time distribution which is a convolution of a prompt curve and a delayed curve the mean lifetime τ is defined by

$$\tau = C(D_{\text{d.stop,f.start}}) - C(P_{\text{d.stop,f.start}}), \tag{2.8}$$

when the feeding transition is giving the start signal and the decaying transition is giving the stop signal, respectively,

$$\tau = C(P_{\text{d.start,f.stop}}) - C(D_{\text{d.start,f.stop}}), \tag{2.9}$$

when the decaying transition is giving the start signal and the feeding transition serves as stop. From the analysis point of view the centroid C(D) of the delayed curve can be easily determined by integrating over the experimentally observed time distribution of a γ-γ coincidence measurement. The prompt curve however has to be determined in a separate calibration measurement of prompt events due to its energy dependence (i.e. the PRF changes for different energies of the two gammas). The centroid shift method has since then been experimentally developed and intensively adopted to β-γ-γ experiments, e.g. by H. Mach and Moszyński [54, 58, 59] and more recently by J.-M. Régis with the *mirror symmetric centroid difference* (MSCD) [60] and its generalization for multi detector fast-timing systems the *generalized centroid difference* [34] which are introduced in the following section (see also [32, 34, 61–63]).

The Generalized Centroid Difference Method

There are basically two ways of determining the lifetime of a nuclear state with the centroid shift method for a two detector fast-timing system. Either one starts the time measurement with the feeding transition and stops with the decaying transition which would lead to a delayed time distribution with the slope on the right hands side. Or vice versa by starting the fast-timing

measurement with the decaying transition and stopping it with the feeding transition which is generally possible by implementing a relatively long delay in the stop branch. This would lead to an anti-delayed time distribution with a slope on the left hand side. However for both scenarios one has to calibrate the corresponding PRF as the timing characteristics differs for both branches in real setups [60]. Thus, especially for multi-detector systems with various start-stop options an analysis can become very complex. The mirror symmetric centroid difference method is therefore defining a new quantity which is the centroid difference ΔC(F) of any time distribution F(t) defined for a γ_{feeder}-γ_{decay} cascade as

$$\Delta\text{C}(\text{F}_{\text{decay}}) = \text{C}(\text{F}_{\text{d.stop,f.start}}) - \text{C}(\text{F}_{\text{d.start,f.stop}}), \tag{2.10}$$

where $\text{C}(\text{F}_{\text{d.stop,f.start}})$ refers to the centroid of the F(t) where the feeding transition γ_{feeder} starts the time measurement and the decaying transition stops, and $\text{C}(\text{F}_{\text{d.start,f.stop}})$ refers to the centroid where the decaying transition decay starts and the feeding transition stops. Since $\text{F}_{\text{d.stop,f.start}}$ is a delayed time distribution (tail on right hands side) its centroid $\text{C}(\text{F}_{\text{d.stop,f.start}})$ is of positive sign, and since $\text{F}_{\text{d.start,f.stop}}$ is of anti-delayed nature its centroid $\text{C}(\text{F}_{\text{d.start,f.stop}})$ is of negative sign. Accordingly, with respect to equation (2.10) it is thus evident that the resulting centroid difference ΔC(F) is also of positive sign. Applying this to the the idea of the centroid shift method defines in turn two quantities. The actual centroid difference ΔC(D),

$$\Delta\text{C}(\text{D}_{\text{decay}}) = \text{C}(\text{D}_{\text{d.stop,f.start}}) - \text{C}(\text{D}_{\text{d.start,f.stop}}), \tag{2.11}$$

corresponding to the lifetime of the observed state which is analog to the centroid shift C(D), and a prompt response difference PRD,

$$\text{PRD}_{\text{decay}} = \text{C}(\text{P}_{\text{d.stop,f.start}}) - \text{C}(\text{P}_{\text{d.start,f.stop}}), \tag{2.12}$$

which is corresponding to the prompt time response of the fast-timing setup and which is analog to the PRF of the centroid shift method. Rearranging equation (2.11) and (2.12) for $\text{C}(\text{D}_{\text{d.stop,f.start}})$ and $\text{C}(\text{P}_{\text{d.stop,f.start}})$ and applying it to equation (2.8) then leads to

$$\tau = \Delta\text{C}(\text{D}_{\text{decay}}) - \text{PRD}_{\text{decay}} - \text{C}(\text{D}_{\text{d.start,f.stop}}) + \text{C}(\text{P}_{\text{d.start,f.stop}}), \tag{2.13}$$

which results - after applying equation (2.9) - to an expression for τ as a function of the centroid differences $\mathrm{PRD_{decay}}$ and $\Delta\mathrm{C(D_{decay})}$ of the form

$$\Delta\mathrm{C(D_{decay})} = 2\tau + \mathrm{PRD_{decay}} \tag{2.14}$$

$$\Leftrightarrow \tau = \frac{1}{2}\Big(\Delta\mathrm{C(D_{decay})} - \mathrm{PRD_{decay}}\Big). \tag{2.15}$$

With special regard to the analysis it is important to stress that the above derivation was done for the decay transition to be the reference energy gate. The actual meaning of a reference gate is introduced within the discussion of the prompt response difference curve in the following section.

The Prompt Response Difference Curve

The prompt response difference is a quantity which defines the energy dependence of a fast-timing setup for a given pair of prompt γ transitions. The overall prompt time response as a function of energy is thus described with the prompt response difference curve. In contrast to a prompt response for a given start-stop detector pair however, the PRD is symmetric with regard to whether the start detector was triggered by the feeding transition or by the decaying transition. For its calibration it was shown that the ^{152}Eu source is preferentially suited with a relatively broad energy range, and even more important with transitions of well known lifetime. Therefore it is not necessarily required that the calibration transitions have to be prompt when corrected with respect to equation (2.15) when τ is precisely known. For the purpose of demonstration the procedure leading to the PRD is shortly sketched for a two detector system:

Considering the ^{152}Gd decay branch of ^{152}Eu which is decaying by a 344 keV transition into the ground state. Several other transitions between 411 keV and 1300 keV are feeding this state. By triggering the stop detector with the 344 keV transition and thus starting the measurement with any of the other transitions leads to a prompt response dependency $\mathrm{C(P_{d.stop,f.start})}$ for a fixed decay of 344 keV and a feeder of the corresponding energy of the populating transition after correcting for τ with equation (2.15). On the other hand, when triggering the start detector with the 344 keV transition and stopping the time measurement with the feeding transitions one obtains the corresponding prompt time response $\mathrm{C(P_{d.start,f.stop})}$ of the inverse detector pair. In both cases the corresponding prompt response curve is a function of energy with respect to the decaying transition of 344 keV, and with equation (2.12) it follows the prompt response difference for a decay

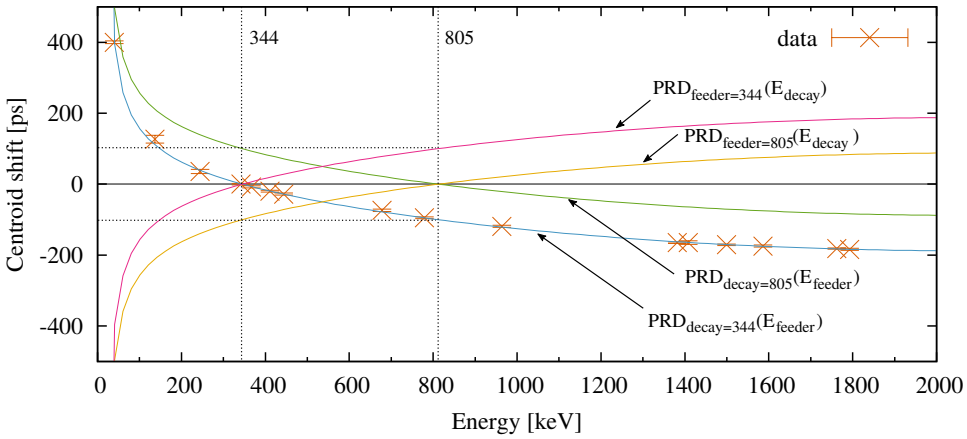

Figure 2.14: The fitted PRD curve of the FATIMA@EXILL array for a 344 keV reference energy (in blue) and possible variation of it. See text for further explanations.

reference energy of 344 keV. Since only the energy difference of the two transitions are of importance the actual calibration reference is independent of the PRD for a given pair of transitions[12]. For a multi-detector system and with respect to figure 2.4 this procedure leads to N(N-1)/2 detector combinations each with its associated PRD. For the FATIMA@EXILL array with its 16 LaBr timing detectors this leads to 120 combinations respectively 120 PRDs. It is however shown that a mean PRD curve for such an array can be deduced from the sum of all combinations. The procedure of which is described in [63] within the framework of the *generalized centroid difference method*. The mean PRD of the FATIMA@EXILL array is shown in 2.14. The data points in 2.14 are referring to centroids of prompt (or prompt corrected) transitions of the ^{152}Eu source with the 344 keV transition as the decay reference energy. As mentioned earlier the PRD can be shifted vertically to a given reference energy. This property is illustrated exemplary with the $\mathrm{PRD}_{\mathrm{decay=805}}(\mathrm{E}_{\mathrm{feeder}})$ curve for a decay reference energy of 805 keV for which the PRD is of positive sign for a feeding transition of an energy less than 805 keV and of negative sign for a feeding transition bigger than 805 keV. However the major characteristic of the *mirror symmetric centroid difference* or the *generalized centroid difference* respectively is shown with

[12]For reasons of clarity the PRD is always shown with respect to its corresponding reference energy within this work. This can be easily achieved by shifting the PRD vertically until it is crossing the zero centroid shift line at the given reference energy.

respect to the indicated PRD curve $PRD_{feeder=344}(E_{decay})$ with the reference energy

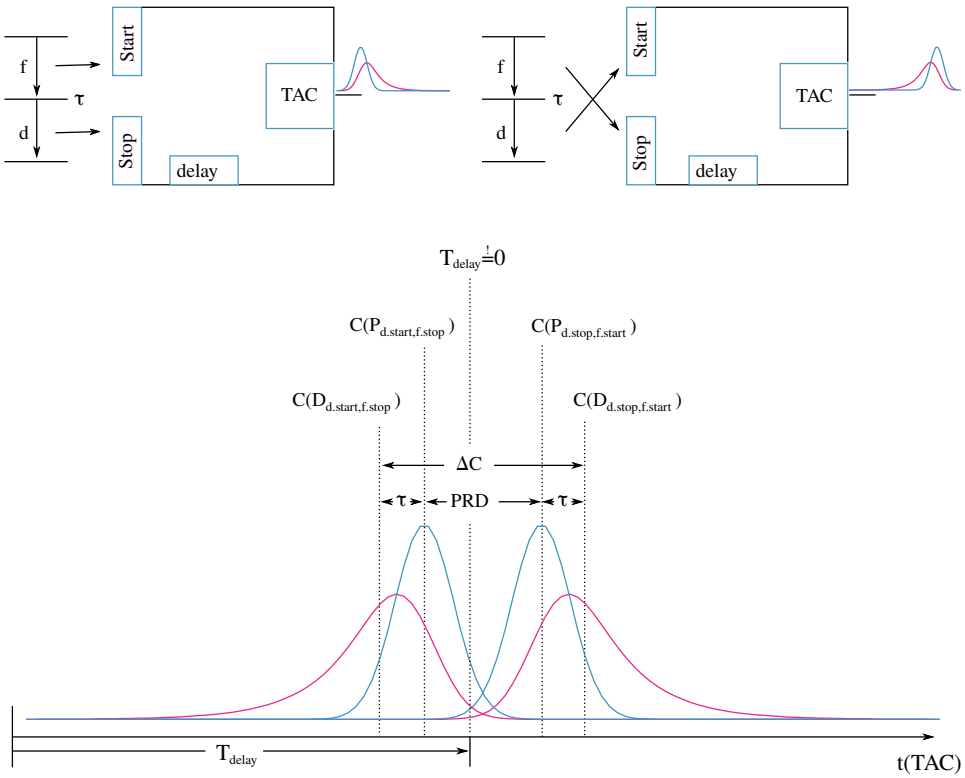

Figure 2.15: Schematic illustration of the GCDM for a two detector fast-timing circuit: Upper part: The feeding transition triggers the start detector and the decaying transition stops (left). The decaying transition triggers the start detector and the feeding transition stops (right). Lower part: The resulting spectra for both options illustrated in the upper part for a prompt transition (in blue) and for a delayed transition corresponding to the lifetime τ of the the state. The delay is shifted to t=0. The centroid differences ΔC and PRD are indicated. Note the asymmetry of the centroids C(P) and and C(D) with respect to t=0 coming from the different time responses of the two branches. The difference is however not affected by this.

on a hypothetically feeding transition of 344 keV as a function of the energy of the decaying transition. With regard to equation (2.12) PRD_{feeder} with the energy reference gate on the feeder is described as

$$\mathrm{PRD_{feeder}} = \mathrm{C(P_{f.stop,d.start})} - \mathrm{C(P_{f.start,d.stop})}, \tag{2.16}$$

which leads for a given reference energy (i.e. $\mathrm{E_{ref=feeder}} = \mathrm{E_{ref=decay}}$) to the actual spin-off of this technique , the mirror symmetry,

$$\mathrm{PRD_{decay}} = -\mathrm{PRD_{feeder}}. \tag{2.17}$$

Subsequently the $\mathrm{PRD_{feeder}}$ in figure 2.14 with the reference energy on the feeding transition were obtained by mirroring the corresponding $\mathrm{PRD_{decay}}$. However equation (2.17) is true for a given reference energy. For a given γ_{feeder}-γ_{decay} cascade the relation can be immediately extracted with respect to figure 2.14. Consider a γ_{feeder}-γ_{decay} cascade with a feeder energy of 805 keV and a decay energy of 344 keV. By choosing the decay as reference energy gate one observes a negative $\mathrm{PRD_{decay=344}(E_{feeder=805})} = -100\mathrm{ps}$. The result does not change due to the mirror symmetry when setting the reference energy gate on the feeding transition $\mathrm{PRD_{feeder=805}(E_{decay=344})} = -100$ ps. For an inverted γ_{feeder}-γ_{decay} cascade with a feeder energy of 344 keV and a decay energy of 805 keV however the resulting PRDs change their signs. In other words, the prompt response difference for a γ_{feeder}-γ_{decay} cascade is of negative sign if $\mathrm{E_{feeder}} > \mathrm{E_{decay}}$, and of positive sign if $\mathrm{E_{feeder}} < \mathrm{E_{decay}}$. The relation for such a given γ_{feeder}-γ_{decay} pair is shown in equation (2.18):

$$\mathrm{PRD_{decay=E_{ref}}(E_{feeder})} = \mathrm{PRD_{feeder=E_{ref}}(E_{decay})}. \tag{2.18}$$

Following the above calculation for the decay reference energy, $\Delta\mathrm{C_{feeder}}$ changes accordingly and is thus defined as

$$\Delta\mathrm{C(D_{feeder})} = \mathrm{C(D_{f.stop,d.start})} - \mathrm{C(D_{f.start,d.stop})}, \tag{2.19}$$

which results analogously to (2.15) for a γ_{feeder}-γ_{decay} cascade connected by a mean lifetime τ with a feeder energy gate to

$$\Delta\mathrm{C(D_{feeder})} = 2\tau + \mathrm{PRD_{feeder}} \tag{2.20}$$

$$\Leftrightarrow \tau = \frac{1}{2}\Big(\Delta\mathrm{C(D_{feeder})} - \mathrm{PRD_{feeder}}\Big). \tag{2.21}$$

The data points of the mean PRD were fitted with the function (2.22) which is proposed in [60]. PRD data points were determined within the energy range from 40 keV to 6.8 MeV. For the purpose of this work the PRD function eq. (2.22) was fitted to the energy range from 0 to 1.5 MeV:

$$\mathrm{PRD}_{\mathrm{decay}}(\mathrm{E}_{\mathrm{feeder}}) = \frac{\mathrm{a}}{\mathrm{E}+\mathrm{b}} + \mathrm{cx}^2 + \mathrm{dx} + \mathrm{e}. \tag{2.22}$$

2.3.4 Applicability to Fission Fragments

The above discussion about the mirror symmetric centroid difference method or generalized centroid difference method respectively is only valid under optimal circumstances. This especially involves the absence of any background contributions. In particular there are two major effects to point out in more detail: With respect to the discussion about the identification of fission fragments in section 2.2 it became evident that an analysis using double coincidences often does not lead to a sufficient selection. This is especially true for a coincidence measurement using LaBr detectors which suffer from a relatively bad energy resolution. Thus, coincidence gates have to be chosen broader in comparison with e.g. germanium detectors in order to cover a sufficient amount of events within the peak. Obviously, this also increases the contribution of unwanted events from peaks nearby. It is therefore of importance to be aware of the "cleanliness" of a gate. This can be easily verified with the coincidence spectra of the corresponding germanium γ gates. Practically however delayed coincidence time measurements for a LaBr-LaBr double gate, especially for less strong transitions, are insufficiently selective. For this purpose additionally coincident γ gates provided by the germanium clover of the EXILL array were used to truncate the γ space of randomly coincident transitions. With regard to figure 2.8 a triple coincidence of two LaBr detectors and one germanium detector (Ge-LaBr-LaBr) turned out to be the only feasible combination. Ge-Ge-LaBr-LaBr quadruple events resulted in very low statistics and could not be used for lifetime determinations even when summed up over multiple germanium combinations[13].
The second major effect is concerning the Compton background. Each peak of a coincidence spectrum is, with respect to the chosen coincidence window, a composition of real coincident events and Compton events. The relative Compton contribution differs with energy which especially becomes noticeable in the low energy range below 1 MeV. However, for the correction of Compton events within the GCDM a correction term is proposed in [34]. Accordingly, the centroid difference $\Delta\mathrm{C}$ is described by eq. (2.23),

$$\Delta\mathrm{C} = \frac{\Pi\Delta\mathrm{C}_{\mathrm{FEP}} + \Delta\mathrm{C}_{\mathrm{Compton}}}{1+\Pi}, \tag{2.23}$$

[13] this is only true for the lifetime determination of states analyzed within this work.

with the peak-to-background ratio Π, the centroid difference of the corresponding reference transition with the Compton background $\Delta C_{Compton}$ and the actual real centroid difference of the full energy peak ΔC_{FEP} which rewrites to eq. (2.24),

$$\Delta C_{FEP} = \Delta C + \frac{\Delta C - \Delta C_{Compton}}{\Pi}. \tag{2.24}$$

Applied to equation (2.15), the corrected mean lifetime τ is then described by eq. (2.25):

$$\tau = \frac{1}{2}\left(\Delta C + \frac{\Delta C - \Delta C_{Compton}}{\Pi} - PRD\right). \tag{2.25}$$

A refinement of this correction suggests a Compton correction for a combined background correlation with regard to the reference energy of the feeder and the decay, respectively.

2.3.5 Data Processing

The total amount of listmode data recorded within the FATIMA@EXILL experiments was 3.6 Tb for the ^{235}U measurement referring to 13 days of beam time and a 10 days measurement (3.2 Tb) of ^{241}Pu. The further data processing was completely performed with the C++ software package *SOCOv2* [64]. Therefore calibration parameters were excluded from the rawdata files and implemented into a second pre-sorting process. This event building process was performed with a coincidence window of 120 ns for triple- and quadruple events with a fixed LaBr γ multiplicity of 2 (i.e the start- and the stop signal) and a variable clover multiplicity between 1 and 4 for triple events and 1-8 for quadruple events respectively to allow for add-back corrections. For the further analysis of actual lifetimes γ-time matrices were sorted for a given LaBr gate and coincident selected germanium gate(s) with respect to the presorted Ge-Ge-LaBr-LaBr quadruple- or the Ge-LaBr-LaBr triple events. The gate width was each adapted to the FWHM of the corresponding peak. The time distribution is then obtained by an additional energy gate referring to the other state connected populating respectively depopulating transition in the γ-time matrix. The sorting routine thus offers two ways for the determination of lifetime with respect to whether the feeding transition was set as reference gate or as the decaying transition.

Chapter 3

Results

In total 26 nuclei from the β^- unstable side between neutron number 50 and 60 were subject of investigation within this work. However, for most of these nuclei it was not possible to gather new information within the scope of its particular analysis; either spectroscopic or in terms of a lifetime analysis. The reasons for this are diverse. For some nuclei the production yield for the neutron induced fission reaction of either ^{235}U or ^{241}Pu was just too low or insufficient for a coincidence analysis like for ^{79,80,81,83}Zn and ^{80,81,82}Ga. For other nuclei however the analysis could not additionally contribute to the currently available data, e.g. for ^{98}Sr. In either case a proper coincidence analysis had to be done. For the reason of clarity these results are summarized in Appendix C.
This chapter presents some new results which were found for ^{92,93,94}Kr in the first section and for ^{101}Zr in the second part.

3.1 Krypton

The krypton isotopes ^{92,93,94}Kr were analyzed; ^{93,94}Kr spectroscopically and ^{92,93}Kr within the scope of lifetime measurements for the fissioning system ^{236}U. For the purpose of a better understanding of the presented coincidence plots within this section schematic level schemes of the most dominant transitions for the relevant complementary barium fission partner are presented in figure 3.1.

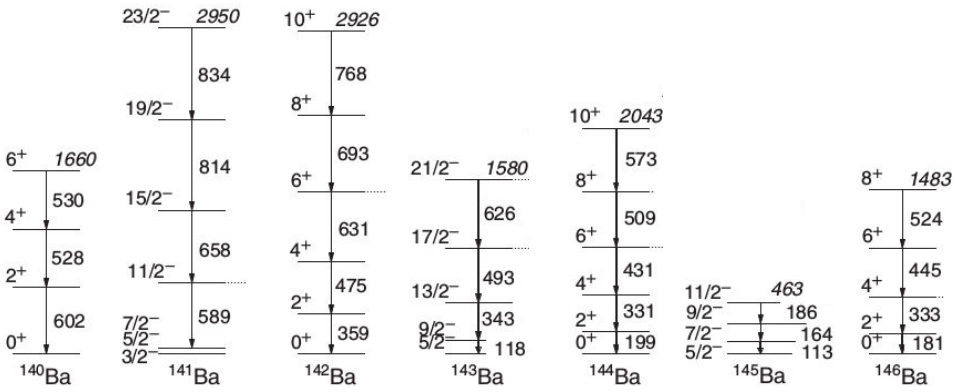

Figure 3.1: Partial level schemes of the barium isotopes $^{140-146}$Ba as the complementary fission partner of krypton for an uranium fissioning system deduced from neutron induced fission of ^{235}U (from [65]).

3.1.1 ^{92}Kr

The first excited 2^+ state of ^{92}Kr was studied in a fast-timing analysis from neutron induced fission of ^{235}U. The lifetime of this state was recently deduced from B(E2) values by Albers *et al.* in a Coulomb excitation measurement [66]; they indicate a mean lifetime of $\tau = 9.0^{+2.7}_{-1.5}$ ps. The level scheme of ^{92}Kr was intensively studied earlier mainly in β^- decay studies of ^{92}Br, e.g. by [67], [68] and later by Rzaca-Urban *et al.* in spontaneous fission of ^{248}Cm [69] who are suggesting a strong ground state transition of 769 keV depopulating the first excited 2^+ state. A coincidence analysis of this state is indicating a 1034 keV transition to be the strongest feeding transition as well as ^{142}Ba to be the most abundant complementary fission partner. The associated coincidence spectra are presented in figure 3.2. The corresponding γ-energies are listed in table 3.1.

From the results of the spectroscopic investigation two transitions which are populating the 2^+ state were considered to be efficiently produced for

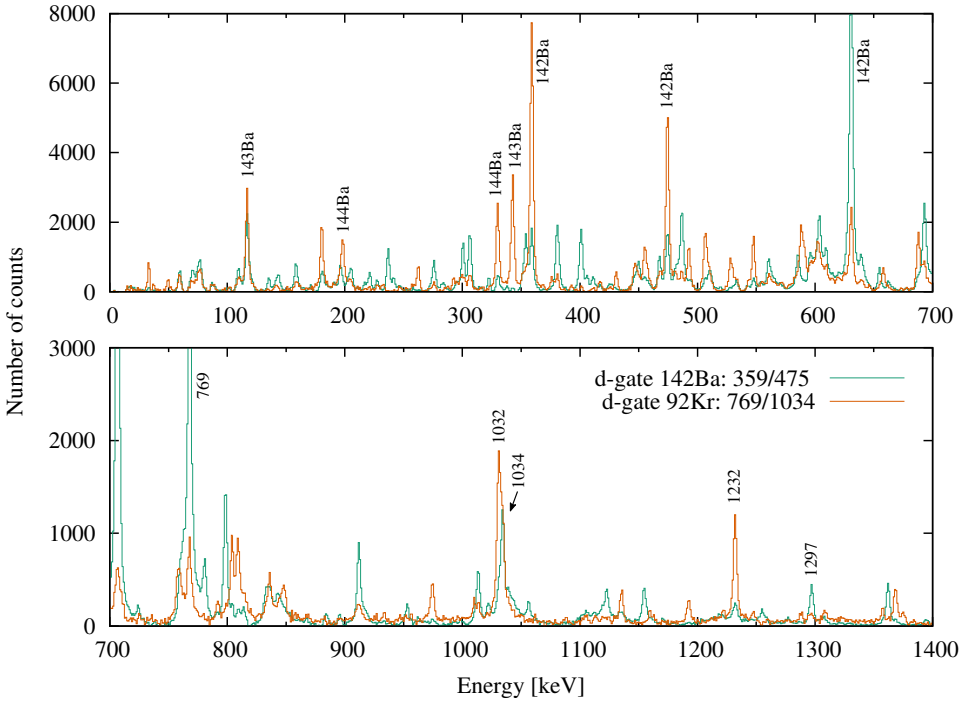

Figure 3.2: Background subtracted double coincidence spectrum of 359 and 475 keV for ^{142}Ba reduced by a factor of 5 for better comparison (green), and of 769 and 1034 keV for ^{92}Kr (orange). See text for further explanations.

a delayed coincidence lifetime analysis of which the strong $4^+ \rightarrow 2^+$ transition of 1034 keV is the more favoured one. However, as quoted in [69] this transition occurs as a doublet in coincidence with 769 keV. A hint of this energy to be a doublet can be found in figure 3.2 which agrees with [69] to be placed above the 4^+, most probably as its direct feeder. For a fast-timing analysis with LaBr scintillators this doublet cannot be resolved in energy. Also no efficiently produced coincident transition in ^{92}Kr could be found to purify further the lifetime measurement. Thus, for the purpose of estimating its contribution the relative intensity was measured in a combined coincidence spectrum using triple gates of 769 keV from ^{92}Kr and 359 keV and 475 keV from ^{142}Ba leading to a ratio of $R_{(I_\gamma(1032)/I_\gamma(1034)}$=0.49(22). The corresponding fit and level scheme are presented in figure 3.3. Since there are no relevant branchings for the 4^+ state known the ^{92}Kr gate is justifying this procedure. However, similar results were observed for a coincidence spectrum of ^{142}Ba gates only. For the fast-timing analysis presented in figure

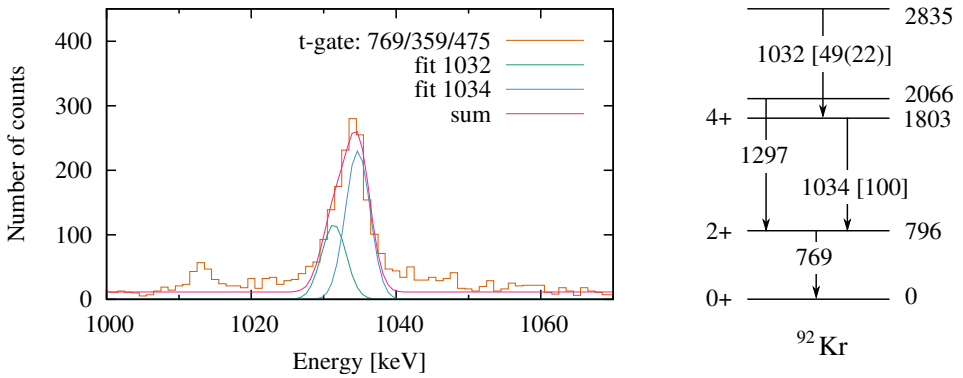

Figure 3.3: The 1032/1034 keV doublet in ^{92}Kr. Left side: "Mixed" triple gated coincidence plot with a 769 keV gate in ^{92}Kr and a 359 keV and 475 keV gate in ^{142}Ba. The summed peak was reconstructed with a fixed FWHM corresponding to the resolution for this energy. Right side: Partial level scheme for the relevant transition in ^{92}Kr. The value in square brackets is given the relative intensity of the transition normalized to the 1034 transition with an error indicated in round brackets.

3.4 a 20 keV wide gate on the 1034 keV feeding doublet was used as reference energy. Due to the large fragmentation above the 4^+ level three partner transitions from ^{142}Ba were used as selection gates; 359, 475 and 631 keV, each separately. The LaBr projection in the upper panel of figure 3.4 is thus a summation of γ-γ matrices LaBr-gated on 1034 keV with the above mentioned Ge-gated barium transitions. The corresponding Ge-projections are indicated underneath in order to check for cleanness. With a centroid shift difference of ΔC = -17(7) ps, a $\Delta C_{Compton}$ = -40(10) ps, a PRD = -35(10) ps and a peak-to-background ratio P/BG = 0.64(6) the mean lifetime calculates with eq. 2.25 to τ = 27(13) or $T_{1/2}$ = 18(9) ps.
Due to the above pointed out contamination of the feeding gate an additional feeder-decay combination was analyzed using the populating 1297 keV transition as reference gate, which is however clearly less populated than the previous one. Here, the resulting half-life leads to a value of $T_{1/2}$ = 22(12) ps which calculates with the previous result to a mean half-life of $T_{1/2}$ = 20(14) ps.

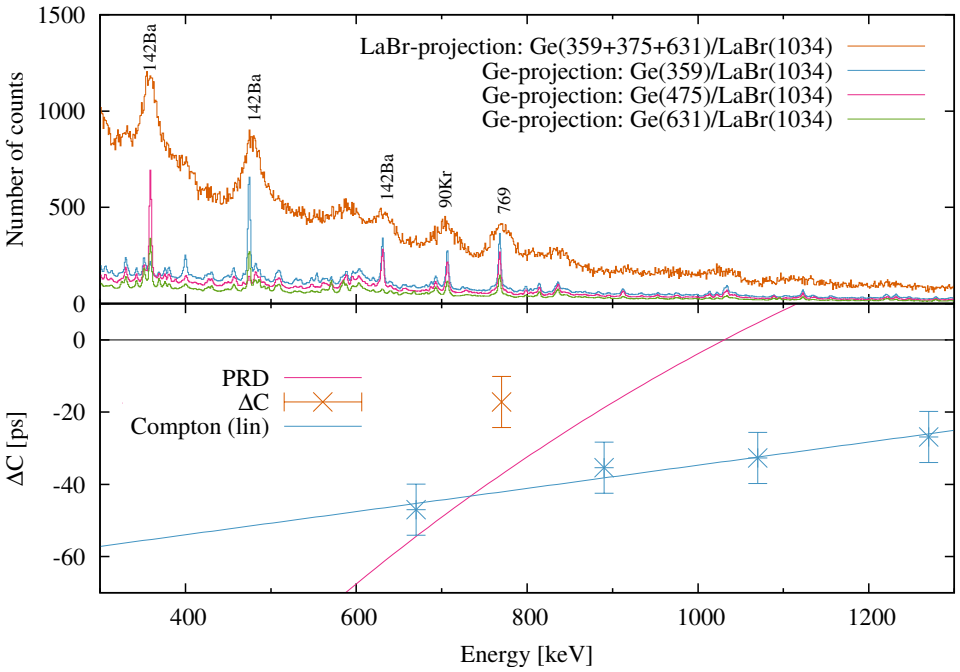

Figure 3.4: Lifetime determination of the first 2^+ state in ^{92}Kr. Upper panel: Double gated germanium projections of the three selective γ transitions in ^{142}Ba with the LaBr gated 1034 keV transition in ^{92}Kr (in blue, red and green) for the verification of the "cleanness" of the spectrum, and the corresponding summed LaBr projection (in orange). Lower panel: The centroid difference representation for the 769-1034 transition pair with respect to the 1034 keV reference energy. The PRD is indicated in red, the centroid difference in orange, and the Compton background centroid shift and its linear fit is indicated in blue. See text for further explanations.

Table 3.1: Energies assigned to ^{92}Kr within this work

$\mathbf{E_{level}}$ keV	$\mathbf{J_\Pi}^\dagger$	$\mathbf{E_\gamma}$ keV	**Final level** keV	$\mathbf{J_\Pi}^\dagger$
0	0^+			
768.4(2)	2^+	768.4(2)	0	0^+
1803.1(2)	4^+	1034.7(2)	768.4(2)	2^+
1984.2(23)		181.1(1)	1803.1(2)	4^+
2065.8(2)	4	1297.4(1)	768.4(2)	2^+
2077.0(2)		1308.7(1)	768.4(2)	2^+
2491.6(3)		507.4(1)	1984.2(3)	
		688.3(1)	1803.1(2)	4^+
2834.5(3)		1031.4(2)	1803.1(3)	4^+
3035.7(3)		1232.6(1)	1803.1(3)	4^+
3171.8(23)		1368.7(2)	1803.1(3)	4^+
3178.1(3)		1112.3(1)	2065.8(2)	4
3593.9(4)		759.5(2)	2834.5(3)	
3627.4(4)		1135.9(1)	2491.6(3)	
		455.5(1)	3171.8(3)	
3845.4(4)		809.8(1)	3035.7(3)	
4175.7(4)		548.3(1)	3627.4(4)	
4980.3(4)		804.6(1)	4175.7(4)	

† Spin and parity assignment was adopted from [69].

3.1.2 ^{93}Kr

The presented analysis of ^{93}Kr was focused on a lifetime analysis of low lying states of the positive parity band. The existence of the band was first proposed by Hwang *et al.* as a result of a spontaneous fission measurement of ^{252}Cf with the Gammasphere set-up [70]. Within that work they also performed a lifetime measurement by comparing different transition strengths for various coincidence time windows. As a result they propose the $(7/2^+)$ state of this band to have an isomeric half-life of $T_{1/2} = 10(2)$ ns. As a spin-off of that analysis they quoted an upper limit for the half-life of the $(3/2^+)$ state below to be $T_{1/2} \leq 4$ ns. However, the isomeric character of the $(7/2^+)$ was already observed earlier by Lhersonneau *et al.* within a centroid shift analysis of a β-decay study of ^{83}Br which resulted in a half-life of $T_{1/2} = 22(12)$ ns.

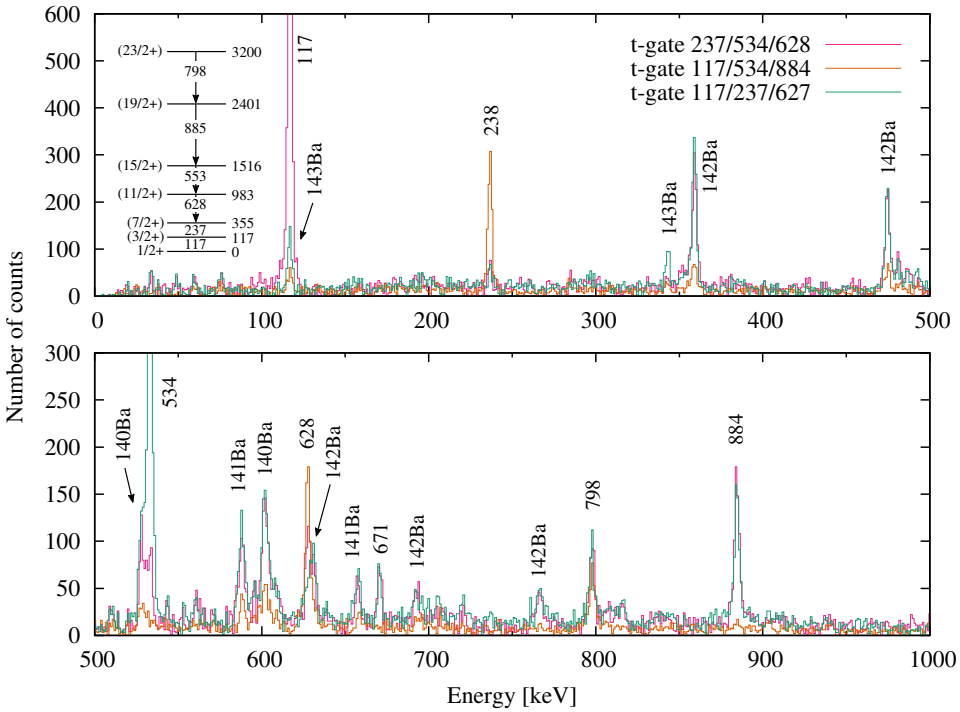

Figure 3.5: Triple coincidence spectra for various combinations of the positive parity band in ^{93}Kr. The inlay shows the level scheme of this band. See text for further explanations.

The present spectroscopy study for neutron induced fission of ^{235}U confirms well the band as shown in figure 3.5. Therefore, a coincidence analysis of the involved transitions was performed. The study implies a new transition of 671 keV which was seen in coincidence with the lower four transitions of this band but not with 885 keV (cf. figure 3.6). It is thus reasonable to propose a new level at 2187 keV which decays by this transition into the $(15/2^+)$ at 1516 keV. It is also worthy to mention that a transition of 670 keV in coincidence with 117 keV was already observed by [71] but was placed differently in the level scheme; in fact none of those transitions other than 117 keV and 237 keV could be observed within this work.

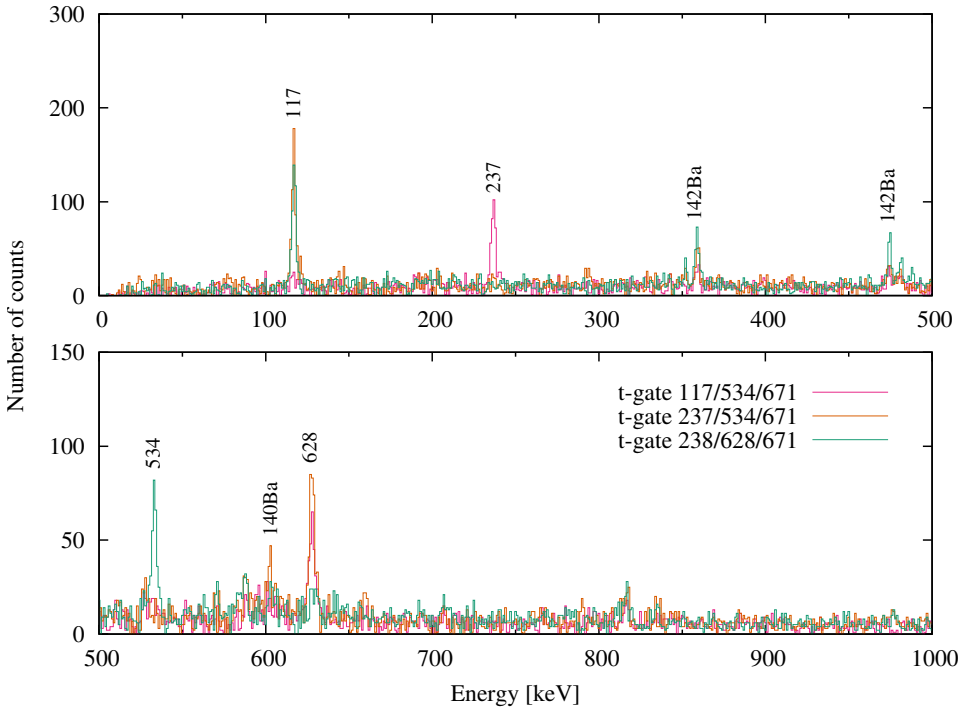

Figure 3.6: Triple coincidence spectra of transitions in ^{93}Kr with the newly found 671 keV transition. See text for further explanations.

Table 3.2: Energies assigned to ^{93}Kr within this work.

$\mathbf{E_{level}}$ keV	$\mathbf{J_\Pi}^\dagger$	$\mathbf{E_\gamma}$ keV	Final level keV	Final level $\mathbf{J_\Pi}^\dagger$
0	$1/2^+$			
117.4(1)	$(3/2^+)$	117.4(1)	0	$1/2^+$
354.7(2)	$(7/2^+)$	237.3(1)	117.4(1)	$(3/2^+)$
982.8(2)	$(11/2^+)$	628.1(2)	354.7(2)	$(7/2^+)$
1516.4(3)	$(15/2^+)$	533.7(2)	982.8(2)	$(11/2^+)$
2187.4(3)		671.0(1)	1516.4(3)	$(15/2^+)$
2401.4(3)	$(19/2^+)$	885.0(1)	1516.4(3)	$(15/2^+)$
3199.6(3)	$(23/2^+)$	798.2(2)	2401.4(3)	$(19/2^+)$

† Spin and parity assignment is taken from [70]

$3/2^+$ (117 keV) :

Based on this strongly populated band, a centroid shift analysis was performed to determine the lifetime of the $(3/2^+)$ state at 117 keV. Therefore, two matrices for the 237 keV feeder gate as the reference energy were built with a narrow germanium selection gate for the above 628 keV transition. The LaBr projection of this matrix is shown in the upper panel of figure 3.7 with its corresponding Ge projection. The centroid shifts of the 237/117 keV pair are indicated in the panel below; they were generated by scanning 5 keV wide gates through the evolution of the 117 keV peak. One should mention that the 117 keV peak is slightly contaminated with the 117 keV ground state transition of ^{143}Ba. However, with regard to figure 3.5 its contribution was not included for correction since the 0n-channel is only weakly populated as can be estimated from the intensity ratios for the barium transitions 117 keV and 343 keV of $R_{(I_\gamma(117)/I_\gamma(343)}$=0.05 as it was measured in spontaneous fission of ^{252}Cf and ^{248}Cm [72]. With a centroid shift difference of $\Delta C = 1695(100)$ ps, a $\Delta C_{Compton} = 1104(100)$ ps, a PRD = -111(10) ps and a peak-to-background ratio P/BG = 0.51(5) the mean lifetime calculates with eq. 2.25 to $\tau = 1476(185)$ ps or $T_{1/2} = 1023(128)$ ps, respectively.

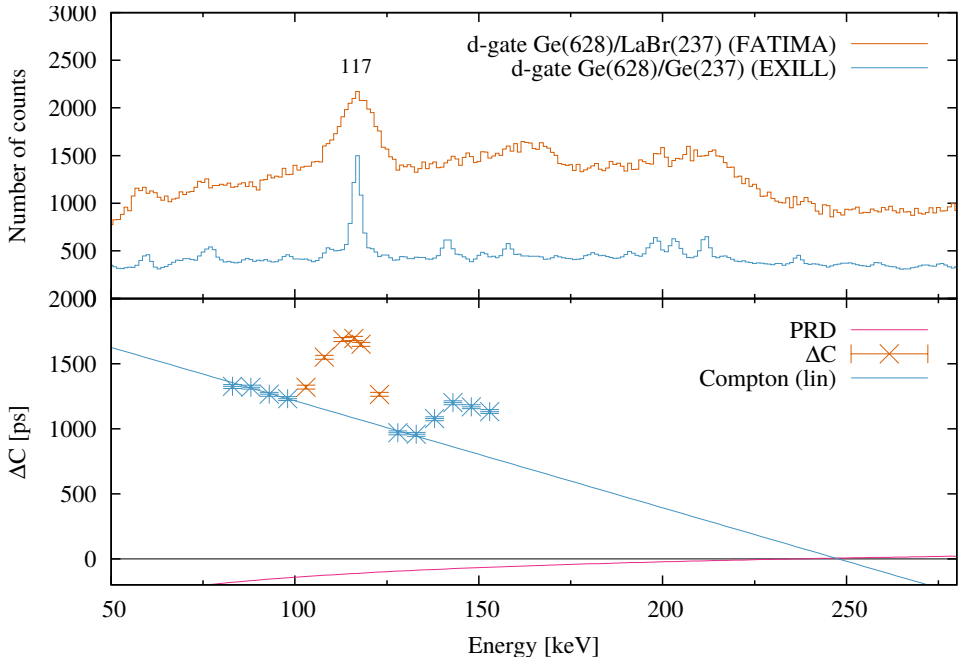

Figure 3.7: Lifetime determination of the $3/2^+$ state at 117 keV in ^{93}Kr. Upper panel: Double gated germanium projections of the 628 keV and the 237 keV transitions, and the corresponding LaBr projection (in blue). Lower panel: The centroid difference representation for the 117-237 transition pair with respect to the 237 keV reference energy. The centroid difference of the transition pair and the Compton background was determined by "scanning" through the relevant energy range. The Compton centroid difference was fitted with a linear function to the data points in the close vicinity to the transition peak. See text for further explanations.

$7/2^+$ (355 keV) :

The $(7/2^+)$ state was analyzed using the slope fit method. However, in consideration of the strongly down-sloping Compton background in the region around 237 keV a direct measurement involving this transition is due to a lack of pure FEP events strongly constrained. Hence a delayed coincident lifetime measurement LaBr gated on the 117/628 keV transition pair with a narrow selection Ge gate on the 237 keV transition was performed. The 628 keV transition was therefore set as the timing stop signal which is started by a 10 keV wide gate for the 117 keV peak. For the estimation of the underlying background an additional time spectrum was produced for the

neighboring 135 keV region of the same gate width. The slope fit was applied to the background subtracted time spectrum leading to a mean lifetime of $\tau = 8.7(14)$ ns. The inverse transition pair (feeder provides start signal, decay provides stop signal) gives a comparable mean lifetime of $\tau = 9.5(14)$ ns which results in a mean value of $\tau = 9.1(14)$ ns respectively a half-life of $T_{1/2} = 6.3(10)$ ns.

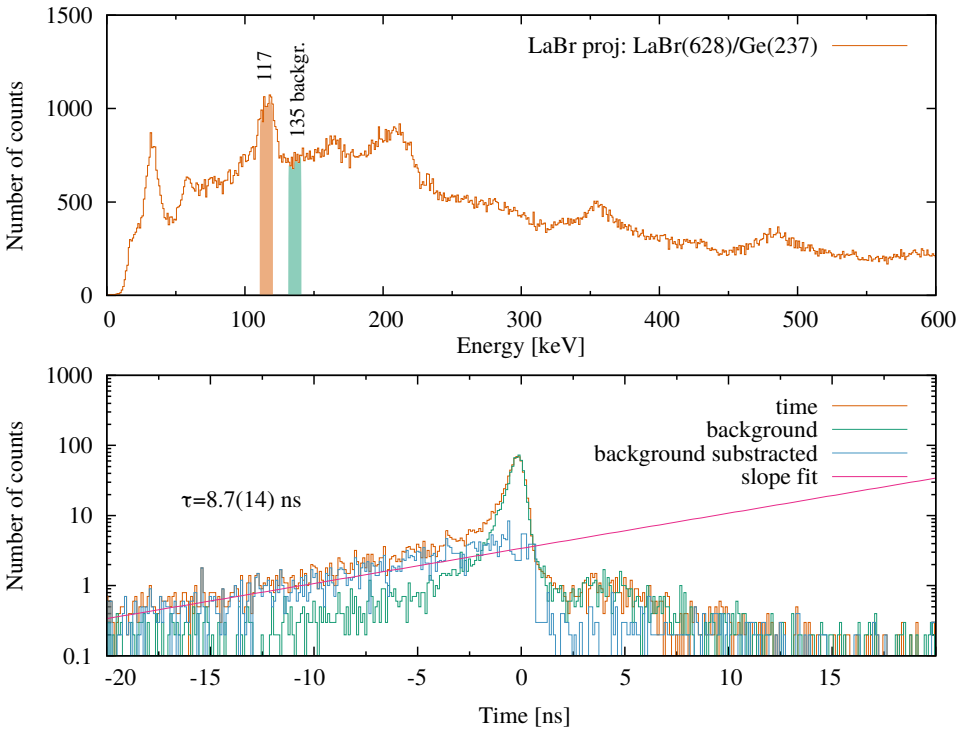

Figure 3.8: Lifetime determination of the $7/2^+$ state at 355 keV in ^{93}Kr. Upper panel: Double gated LaBr projection for a 628 keV LaBr gate and a 237 keV Ge gate. Lower panel: Time distribution of the 117-628 LaBr gate pair with the additional selective 237 keV Ge gate (in orange), and a corresponding 135-628 LaBr transition-background gate pair (in green), and the subtraction of both (in blue). The colors are referring to the gates in the upper panel. The fit function was fitted to the slope of the background subtracted time spectrum. See text for further explanations.

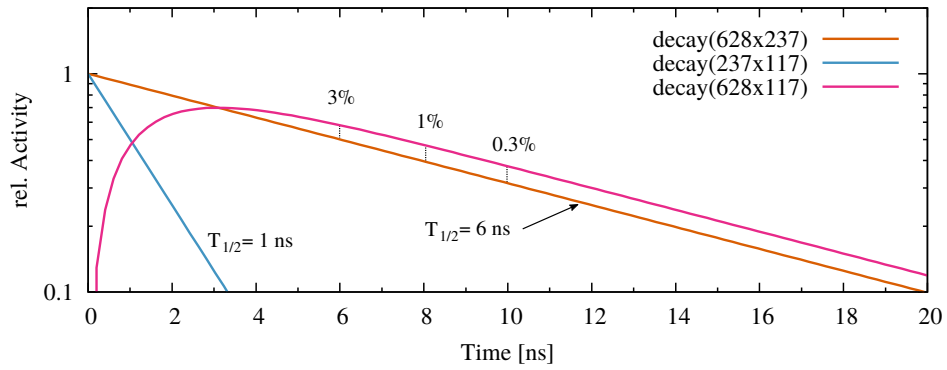

Figure 3.9: Theoretical representation based on the Bateman equation of the convoluted time distribution for the enclosing gate pair (decay(628x117) in red) referring to 3.8, and its components for the 1 ns 117 keV state (decay(237x117) in blue) and the 6 ns 237 keV state (decay(628x237) in orange). The resulting lifetime of decay(628x117) is only varying with a derivation of 1% with respect to an unperturbed 6 ns lifetime after 8 ns. The fit range in 3.8 was chosen from the results of this plot. Note also the visual similarities to the experimental time distribution shown in 3.8. See text for further explanations.

Since the delayed coincidence measurement for the $(7/2^+)$ state was applied to the 628 keV feeding and the 117 keV decaying transition the time distribution shown in figure 3.8 is not only the one of the $(7/2^+)$ state but a cumulated time spectrum of both, the $(7/2^+)$ state and the $(3/2^+)$ state below. It is thus of importance to evaluate the interplay of both lifetimes for the resulting time distribution of a decay chain. The behavior of such is mathematically described by the Bateman equation. For a two state system as the present one, where the detection of the 628 keV transition gives the start signal of population of the parent state P (here: $7/2^+$) and the 117 keV transition provides the stop signal for the depopulation of the daughter state D (here: $3/2^+$) the time distribution, respectively the activity of the daughter state A_D as a function of $T_{1/2}$ is given by

$$A_D = \frac{\lambda_D}{\lambda_D - \lambda_P}(e^{-\lambda_P T_{1/2}} - e^{-\lambda_D T_{1/2}}), \tag{3.1}$$

with the decay constants λ_D and λ_P for the daughter respectively parent state. Relation 3.1 is plotted in figure 3.9 for a $(3/2^+)$ daughter half-life of $T_{1/2} = 1$ ns and a $(7/2^+)$ parent half-life of $T_{1/2} = 6$ ns. One can see that the parallel behaviour of the resulting activity for the 628/237 keV transition

pair with regard to the 6 ns half-life of the $(7/2^+)$ converges after a few ns. After 8 ns the deviation remains only 1% with decreasing tendency, which means that the total time distribution is strongly dominated by the 6 ns lifetime of the $(7/2^+)$ after 8 ns in which the activity of both states reaches an equilibrium, often referred to as a transistent equilibrium in which the parent state has a longer but not negligable lifetime than the daughter state. This was taken into account for the slope fit ranges for distribution in figure 3.8 covering the region from 8-20 ns (respectively -20-(-8) ns for inverse time picking).

3.1.3 ^{94}Kr

The currently available nuclear data for the krypton isotope ^{94}Kr is rather limited. Latest spectroscopic results were published by Rzaca-Urban *et al.* in 2000 from spontaneous fission of ^{248}Cm from the EUROGAM2 campaign [69].

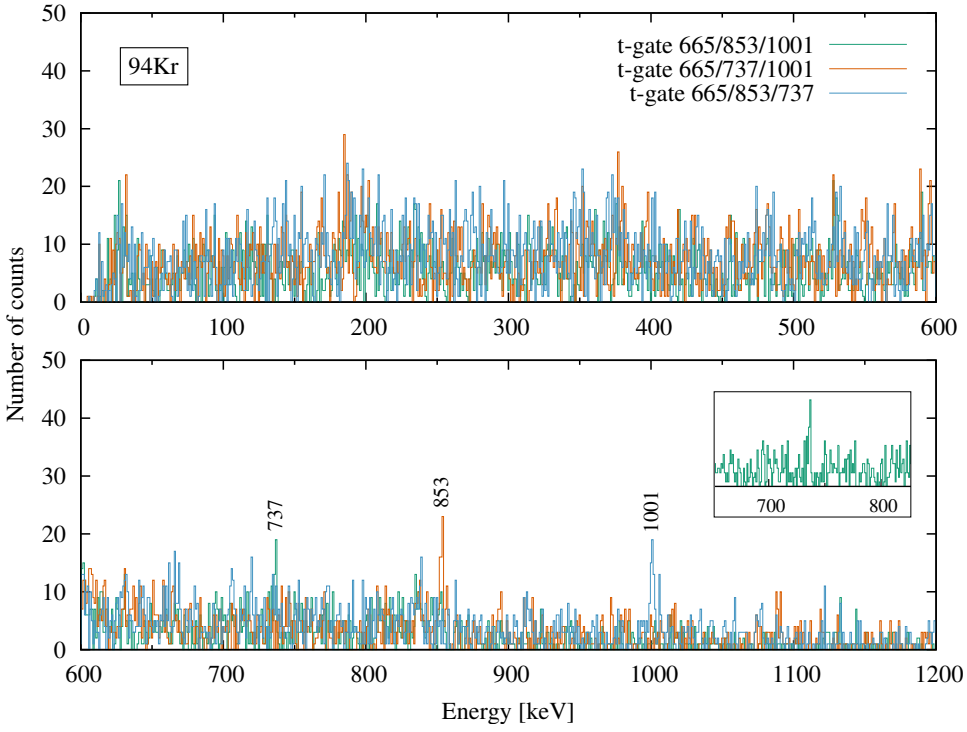

Figure 3.10: Triple coincidence spectra of ^{94}Kr within the ^{235}U(n, f) reaction. See text for further explanations.

They introduce a possible rotational band consisting of three transitions of 1001 keV, 853 keV and 666 keV. In fact also within this work for neutron induced fission of ^{235}U the spectroscopic analysis is challenging due to the low production yield. A coincidence analysis however confirms the existence of these states as well as a possible new transition of 737 keV which is feeding the cascade from above. The results are presented in figure 3.10 as well as tabulated in table 3.3.

Table 3.3: Energies assigned to ^{94}Kr within this work.

$\mathbf{E_{level}}$	$\mathbf{J_\Pi}^\dagger$	$\mathbf{E_\gamma}$	**Final level**	
keV		**keV**	**keV**	$\mathbf{J_\Pi}^\dagger$
0	0^+			0^+
665.8(1)	(2^+)	665.8(1)	0	2^+
1519.5(1)	(4^+)	853.7(1)	665.8(1)	(4^+)
2520.8(2)	(6^+)	1001.3(1)	1519.5(1)	(6^+)
3257.8(4)		737.0(3)	2520.8(2)	

† Spin and parity assignment is taken from [69]

3.2 Zirconium

3.2.1 ^{101}Zr

The zirconium isotope ^{101}Zr was analyzed with regard to the determination of lifetimes from the FATIMA data set. Particular interest was given to three coexisting substructures of collective behavior as they were proposed by G. Lhersonneau *et al.* [73] and W. Urban *et al.* [21]. According to the Nilsson model these substructures are denoted as the $\nu 3/2[411]$, $\nu 5/2[532]$ and $\nu 9/2[404]$. Figure 3.11 illustrates this situation for the $9/2^+$ (left side), the $3/2^+$ ground state (middle) and the $5/2^-$ (right side) band heads of ^{101}Zr.

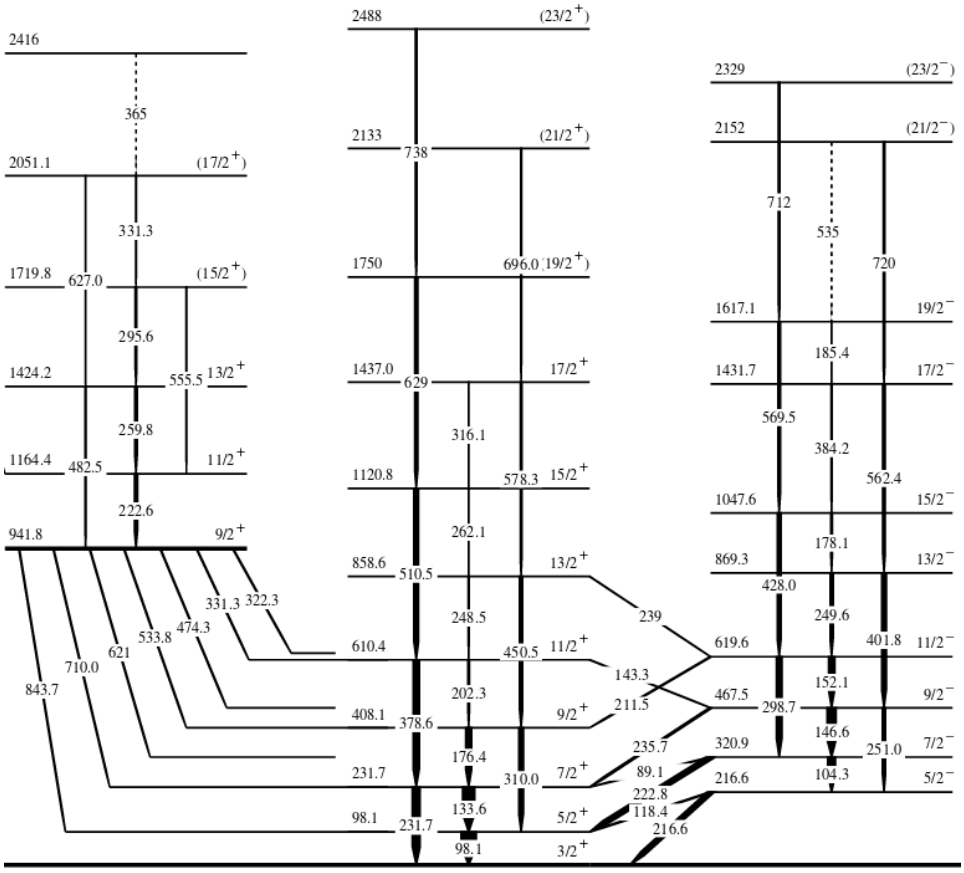

Figure 3.11: Partial level scheme of ^{101}Zr like it was determined by W. Urban *et al.* from spontaneous fission of ^{248}Cm (from [21]).

$5/2_1^+$ (98 keV) :

The half-life of the first excited $5/2^+$ state at 98.1 keV was earlier determined by Ohm *et al.* [74] to $T_{1/2} = 0.9(3)$ ns and by G. Lhersonneau *et al.* [73] to $T_{1/2} = 0.39(18)$ ns, both in β^--decay studies of ^{101}Y. Since ^{101}Zr is among the most strongly produced isotopes in neutron induced fission of ^{235}U, for the purpose of lifetime determination with delayed coincidences and with regard to fig. 3.11 this state offers several pairs of energy gates to be determined in lifetime. However, since these transitions are close in energy and all far below 1 MeV, which increases the effect of background contributions, a suitable pair of gates has to be chosen and interpreted carefully. In order to verify for the cleanliness of the associated transitions and to check for possible contributions of fission partners a coincidence plot for the consecutive ground state transitions 133.6 keV and 98.1 keV was performed.

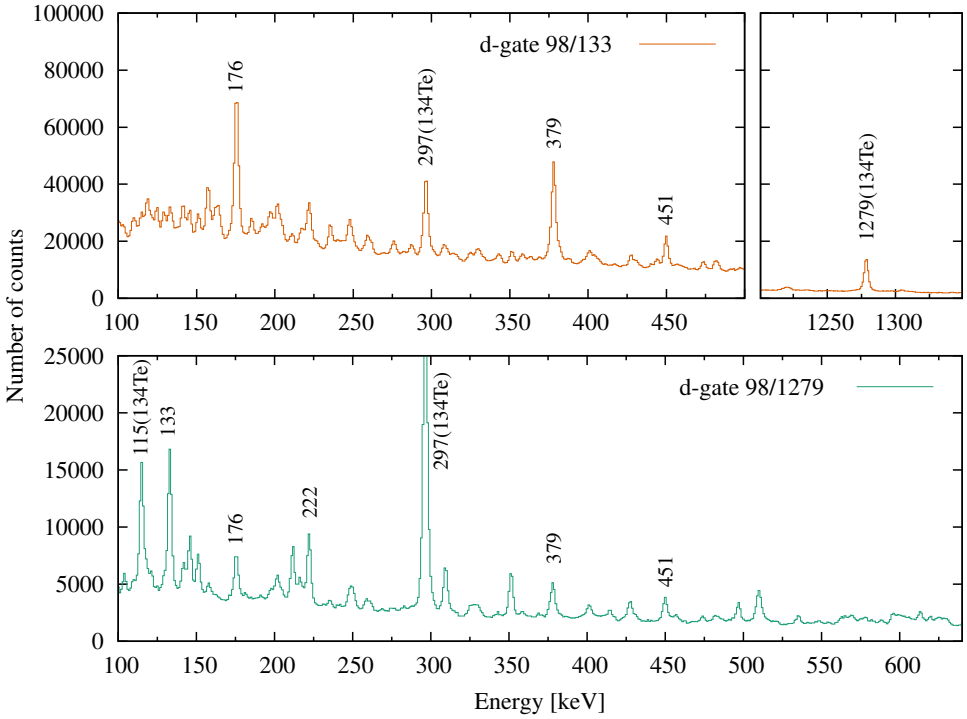

Figure 3.12: Upper panel: Coincidence spectrum with the 98 keV and the 133 keV transition in ^{101}Zr. Lower panel: Coincidence spectrum with the "mixed" transition pair of 98 keV from ^{101}Zr and 1279 keV from ^{134}Te. See text for further explanations.

The upper panel of fig. 3.12 shows the strongly pronounced feeding transitions at 176 keV, 379 keV and 451 keV of ^{101}Zr as well as the transitions at 297 keV and 1279 keV from the the fission partner ^{134}Te resulting from the 1n channel. It is interesting to mention that other tellurium partners such as ^{133}Te and ^{132}Te from the generally more probable 2n respectively 3n channels are barely visible. The lower panel of fig. 3.12 shows a "mixed" coincidence plot of 98 keV from ^{101}Zr and 1279 keV from ^{134}Te. Special attention was given to the strong ^{134}Te transition at 115 keV. For the later lifetime determination using LaBr spectra the gate limits for 98 keV were chosen more narrow in order to avoid overlaps with the 115 keV transition from ^{134}Te. However, different gate variations do not show a significant influence which can be easily deduced from the energy peak position, the FWHM but also by comparing with the associated HPGe coincidence spectra of higher energy resolution. Motivated by the earlier determined lifetimes in the subnanoseconds range - in a first attempt - the slope method which is generally feasible for this order of lifetime was applied to time spectra for different sets of gate triplets. However, the results of this measurement shows minor inconsistencies in lifetime so that a more precise analysis of the background became necessary. Figure 3.13 shows exemplary the results of this analysis. The LaBr projection of a 4 keV wide LaBr gate on the 133 keV transition and a selective Ge gate on 378 keV is shown in the upper panel. One can clearly see a well pronounced peak at 98 keV, which is however superimposed with a large Compton background. The spectra below show the time distributions for different 4 keV wide LaBr gates around 98 keV (referring to the color code of the upper panel) with the above mentioned configuration. Here, the 133 keV feeder served as the LaBr stop signal and the indicated gates served as the LaBr start signal. In the case of the 98 keV gate the start signal is in fact given by the 98 keV decay transition (and its background contributions) and thus showing a delayed portion (i.e. slope) on the left hands side (cf. fig. 3.13 c). By fitting eq. (2.5) to the exponential part of the slope (resp. the linear part in the logarithmic representation), this leads to a mean lifetime of $\tau = 659(22)$ ps. However, it is not obvious that the corresponding time distributions of the background gated start signals behave in the same way, hence showing similar lifetimes (cf. fig. 3.13a,b,d,e). It is thus misleading to use the slope method for a lifetime study of this state since it is of major importance to correct for the underlying background. In a further centroid shift analysis this issue was investigated in more detail. The results of this analysis are shown in fig. 3.14. The upper panel is showing the LaBr-projection for the 378 keV Ge gate (blue) and the 133 keV LaBr gate (orange).

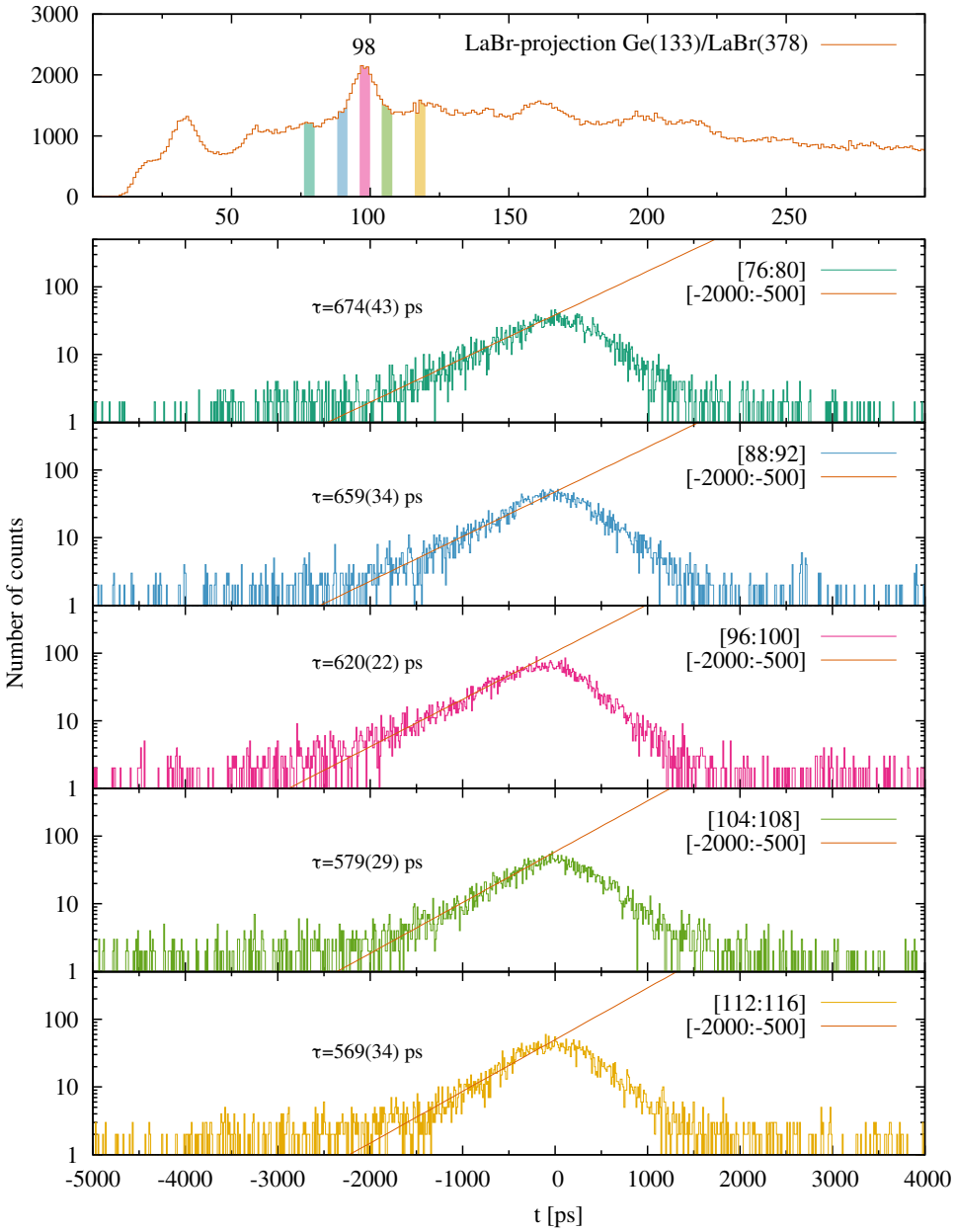

Figure 3.13: Slope fit time measurement for the 98-133 keV transition pair (in red) in ^{101}Zr and for different background-133 keV transition pairs. Note that the resulting time distributions result in comparable lifetimes. See text for further information.

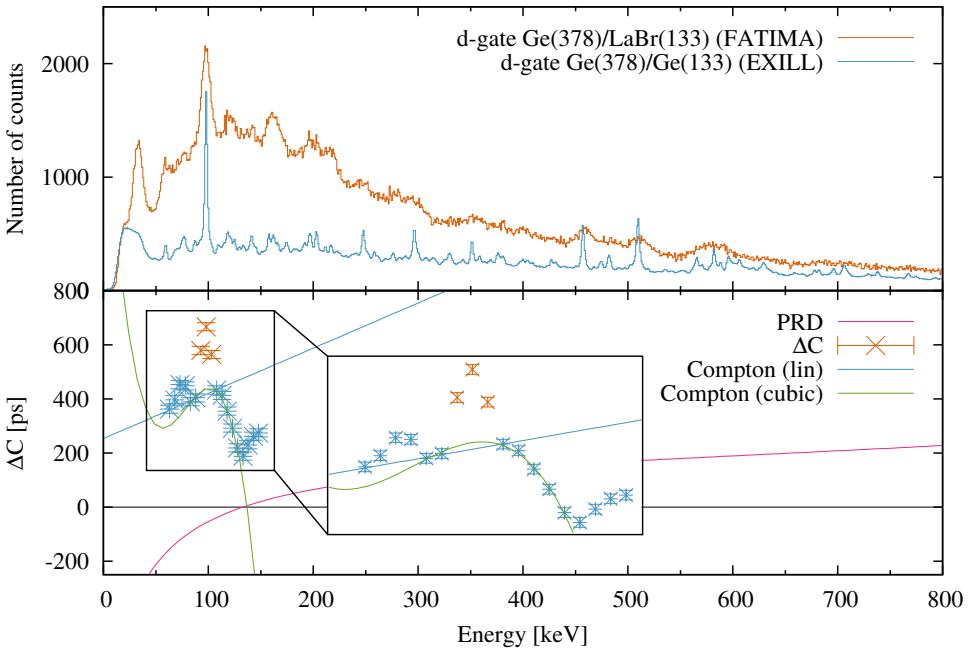

Figure 3.14: Lifetime determination of the $5/2^+$ state at 98 keV in ^{101}Zr using the GCDM. The reference energy is set on the feeding transition of 133 keV. Upper panel: LaBr- and Ge-projection of the 378 keV and 133 keV double gated spectrum. Lower panel: Centroid difference representation of the different MSDM components. The Compton background centroid difference for 98 keV was approached with a cubic fit for the surrounding background data points. For comparison a linear fit is also indicated. See text for further information.

As can be seen in the underneath Ge-projection the 98 keV peak is well separated from other transitions. For the lifetime analysis two matrices were built with the reference energy on 133 keV and a selective Ge gate on 378 keV in a way that the 133 keV feeding transition is serving as the LaBr start or the LaBr stop signal. Practically, the according centroid shifts with their associated gates were deduced from 5 keV wide gates, extending from 60 keV to 150 keV, where the time distribution was integrated over a given time interval. As can be seen in the lower panel of fig. 3.14 the centroid shifts belonging to the 98 keV peak clearly differ from the centroid shifts from the surrounding background. It is also worth to mention that the background associated centroid shifts show a rather smooth evolution in energy. This behavior is of importance since it is confirming the insensitivity towards

certain systematic errors (cf. also evolution of the 98 keV peak). Based on this time shift evolution of the background two functions were considered to determine the background contribution to the 98 keV peak; a linear function which was fitted to the three closest surrounding background points and a polynomial function of third order which was mainly fitted to the down-sloping part on the right hands side. Both approaches seem reasonable so that a mean value was taken for the background. With a centroid shift $\Delta C = 681(20)$ ps, a $\Delta C_{Compton} = 428(20)$ ps, a PRD = -58 ps and a peak-to-background ratio P/BG = 0.526(26) the mean lifetime calculates with eq. 2.25 to $\tau = 610(37)$ respectively $T_{1/2} = 423(26)$ ps. This is in good agreement with the result of G. Lhersonneau *et al.* [73] of $T_{1/2} = 0.39(18)$ ns.

$7/2_1^+$ (232 keV) :

The lifetime of the first excited $7/2^+$ state at 232 keV was also earlier determined by G. Lhersonneau *et al.* [73]. In a least-squares analysis of centroid shifts deduced from β-γ-t coincidences they indicate a half-life of $T_{1/2}$ = -0.02(9) leading to an upper limit of $T_{1/2} \leq 0.07$ ns[1].

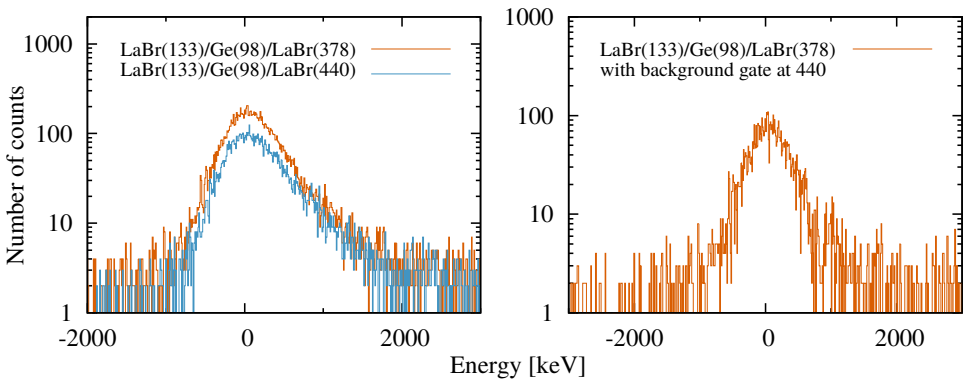

Figure 3.15: Qualitative representation of the background contribution for the 133-378 keV transition pair in ^{101}Zr. Left figure: Time distribution of the 133-378 keV transition pair (in orange), and a 133-background(440 keV) pair (in blue). Both spectra show a comparable slope component. Right figure: Time distribution of the 133-378 keV transition pair with an active background subtraction. Note that the long lifetime component is highly reduced.

[1] note the conflicting lifetime $\tau \geq 0.01$ ns differing by a factor of 10 in [75] which is referring to [73].

After the analysis of the previous $5/2^+$ state at 98 keV it is not surprising anymore that the background contributions have a major impact on the lifetime determination. The time spectra of figure 3.15(left panel) illustrate this for the delayed $LaBr_{start}(378)/LaBr_{stop}(133)$ pair (orange) respectively the $LaBr_{start}(378)/LaBr_{stop}(440)$ pair (blue) where the 440 keV corresponds to a wide start gate set in the background. By comparing these two spectra one can clearly see a second more prompt component in the lifetime distribution of the actual $LaBr_{start}(378)/LaBr_{stop}(133)$ combination whilst the background gated $LaBr_{start}(378)/LaBr_{stop}(440)$ pair is showing a more linear slope which is matching with the slower time component of $LaBr_{start}(378)/LaBr_{stop}(133)$. This gives evidence of a shorter lifetime component convoluted with a more delayed background.

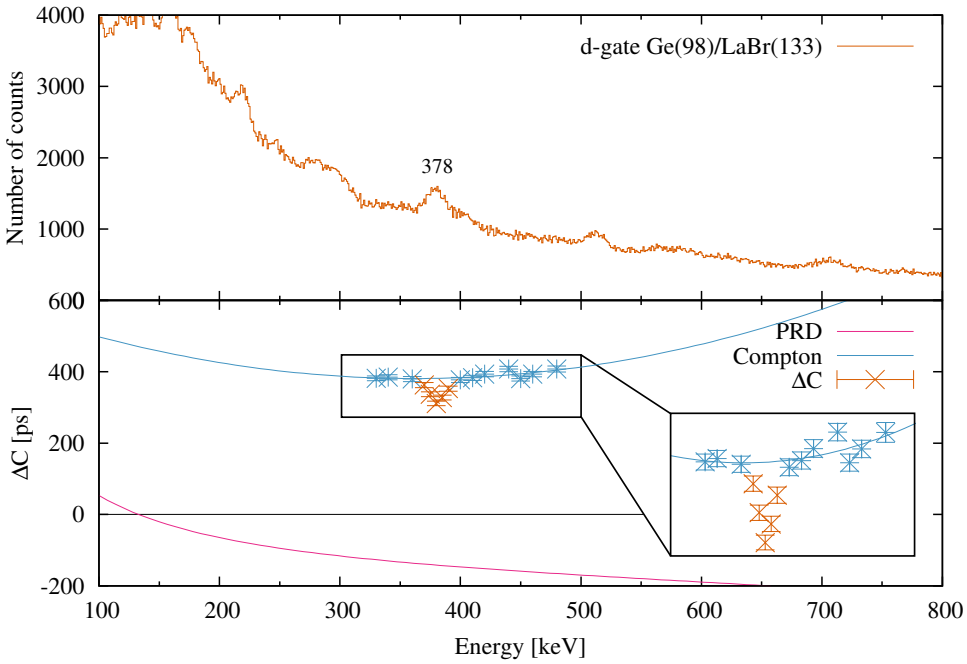

Figure 3.16: Lifetime determination plot for the $7/2^+$ state at 232 keV in ^{101}Zr using the GCDM. The reference energy is set on the decaying transition of 133 keV. The germanium selection gate is set on 98 keV.

The right panel of figure 3.15 is showing the time spectrum of the $LaBr_{start}(378)/LaBr_{stop}(133)$ with a subtracting background gate around 440 keV which subsequently removes the background and exposes the prompt time component. However, the resulting time spectra are highly depending

on the chosen background gates so that the state was analyzed more carefully using the GCD method. The results are presented in figure 3.16 for the 133 keV reference energy which is depopulating the $7/2^+$ state. The 98 keV ground state transition is serving as selective Ge gate and the 378 keV feeding transition was used as the corresponding LaBr start/stop signal. It is important to emphasize that the 378 keV peak related centroid shifts are appearing below the background related centroid shifts, thus faster. This comes from the above mentioned situation that the lifetime of the actual transition is in fact shorter than the surrounding background. A complete analysis for this state with a centroid shift $\Delta C = 310(10)$ ps, a $\Delta C_{Compton} = 380(20)$ ps, a PRD = -142(10) ps and a peak-to-background ratio P/BG = 0.262(13), the mean lifetime calculates with eq. 2.25 to $\tau = 92(32)$ ps or $T_{1/2} = 64(22)$ ps. Together with the results from [73] this leads to a possible half-life range of $42\,\text{ps} \leq T_{1/2} \leq 70\,\text{ps}$.

$5/2^-$ (217 keV) :

The $5/2^-$ state at 217 keV in ^{101}Zr was determined for the 104-217 keV transition pair. From the spectroscopic analysis these two transitions were the most suited for a lifetime analysis due to their intensity. Consequently the from above feeding 146 keV transition serves as selective germanium gate with a narrow gate width of 4 keV. The results of this analysis are presented in figure 3.17. The analysis for this state with a centroid difference $\Delta C = 141(40)$ ps, a $\Delta C_{Compton}$ = -397(50) ps, a PRD = 121(10) ps and a peak-to-background ratio P/BG = 0.75(7) the mean lifetime calculates with eq. 2.25 to $\tau = 370(68)$ ps or $T_{1/2} = 257(47)$ ps.

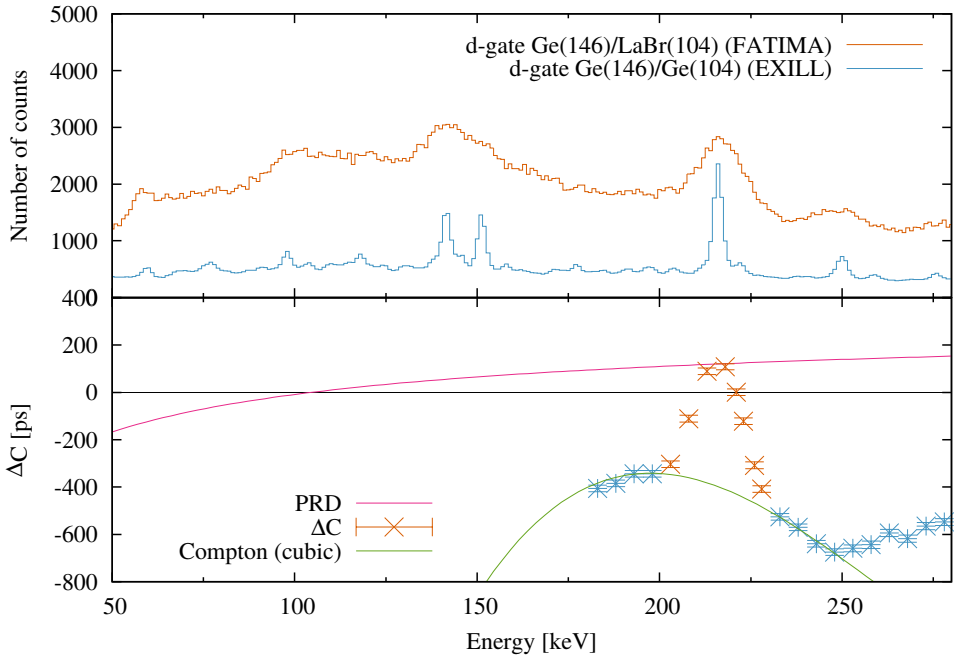

Figure 3.17: Lifetime determination plot for the $5/2^-$ state at 217 keV in ^{101}Zr using the GCDM. The reference energy is set on the feeding transition of 104 keV. The germanium selection gate is set on 146 keV. The Compton background was fit with a cubic function to the Compton data points.

Chapter 4

Summary

Nuclei in the mass region between neutron number $N = 50 - 60$ and above show interesting features which help experimentalists and theoreticians likewise to understand certain structural phenomena according to their microscopic and macroscopic description, respectively. Especially, the origin and the evolution of deformation in this region is often discussed controversially. The same is true for the origin of shape coexistence phenomena in this region. Experimental observables such as lifetimes of excited nuclear states can provide useful information to clarify still open questions.
A neutron induced fission experiment for the actinide targets ^{235}U and ^{241}Pu has been carried out in order to produce nuclei in this region and to detect their radiation with a γ efficient germanium array. Additional experiments were performed with a combined germanium-/$LaBr_3$(Ce) setup for the measurement of short lifetimes of excited states. In total 26 nuclei in this region have been considered in spectroscopic or lifetime analysis respectively. A summary of the these nuclei can be found in table 4.1. However, for the majority of the nuclei no, or no new information could be gathered. One reason for this was clearly the low production yield in certain regions. This is especially true for the Zn and Ga nuclei at the very neutron-rich side around $N = 50$.
Another problem was the identification of fission fragments. The enormous amount of simultaneously emitted γ radiation and the absence of additional fission fragment identification detectors made a proper assignment particularly difficult. Even when γ transitions could be identified as being emitted within a known fission event, the process is always accompanied with radiation from the respective complementary partner fragments. A method for the beneficially use of the constant γ yield ratio in partner fragments

Table 4.1: Nuclei which were considered within this work. NO indicates that no γ transitions were observed which could be assigned to this nucleus. In most of the cases this was due to a low production yield. X indicates that the nucleus was not analyzed within the respective experiment. O indicates that only already known γ transition were observed. NI means new information for the nucleus were found.

	EXILL		**FATIMA**
Nuclei	$^{235}\mathbf{U}(\mathbf{n},\mathbf{f})$	$^{241}\mathbf{Pu}(\mathbf{n},\mathbf{f})$	$^{235}\mathbf{U}(\mathbf{n},\mathbf{f})$
$^{79-81}$Zn	NO	NO	X
$^{80-82}$Ga	NO	NO	X
^{81}Ge	O	NO	X
^{82}Ge	O	O	NO
$^{83-84}$Ge	NO	NO	X
^{85}As	X	X	NO
^{83}Se	O	NO	X
$^{84-85}$Se	O	O	X
^{87}Kr	O	O	X
^{89}Kr	O	O	X
^{92}Kr	X	X	NI
^{93}Kr	X	X	NI
^{94}Kr	NI	O	X
^{96}Kr	NO	NO	X
^{95}Rb	X	X	X
^{96}Rb	X	X	X
^{89}Sr	O	O	X
^{98}Sr	O	O	X
^{101}Zr	X	X	NI
^{102}Nb	X	X	NO

could be successfully applied to well produced nuclei, but it certainly had its limitations for weakly produced transitions.
Lifetimes have been measured within the frame of fast-timing analyses. Results for the ^{92}Kr, ^{93}Kr and ^{101}Zr have been presented in chapter three. The values of the deduced half-life are presented in table 4.2 and compared with values from literature.

Table 4.2: Values for the half-life $T_{1/2}$ deduced from the GCDM and the slop fit method, respectively, for the nuclei ^{92}Kr, ^{93}Kr and ^{101}Zr produced in neutron-induced fission of ^{235}U.

Nuclei	**this work**	**literature**
^{92}Kr		
2_1^+ @ 769 keV	20(14) ps	$6.2^{1.8}_{1.0}$ ps [66]
^{93}Kr		
$(5/2)^+$ @ 98 keV	1.02(13) ns	$\leq$ 4 ns [70]
$(7/2)^+$ @ 355 keV	6.3(10) ns	10(2) ns [70]
		22(12) ns [71]
^{101}Zr		
$(5/2)^+$ @ 98 keV	423(26) ps	0.9(3) ns [74]
		0.39(18) ns [73]
$(5/2)^-$ @ 217 keV	257(47) ps	0.33(12) ns
$(7/2)^+$ @ 232 keV	64(22) ps	$\leq$ 0.07 ns [73]

Synthèse de la partie *Fragments de fission dans la région N=50-60* : Les noyaux dans la région de masse A ~ 100 possédant un nombre de neutrons $N = 50 - 60$ montrent des caractéristiques particulièrement intéressantes, notamment en ce qui concerne leurs formes et leurs évolutions le long d'une chaîne isotopique ou isotonique. La description microscopique des noyaux de cette région de la carte de Segré permettant de mieux comprendre à la fois l'origine de cette déformation et son évolution est encore très controversée. Les observables expérimentales telles que les durées de vie moyenne des états nucléaires excités peuvent fournir des informations particulièrement utiles pour clarifier les questions encore ouvertes. Une expérience de fission induite par des neutrons sur les cibles d'actinides ^{235}U et ^{241}Pu a été réalisée afin de produire des noyaux dans cette région et de détecter leurs rayonnements avec le spectromètre germanium EXILL (EXOGAM à l'ILL). Des expériences complémentaires ont été réalisées avec une configuration associant EXOGAM et des détecteurs rapides au /$LaBr_3$(Ce) pour la mesure des durées de vie moyenne courtes des états excités. Au total, 26 noyaux dans cette région ont été considérés dans l'analyse spectroscopique. Un résumé de ces noyaux peut être trouvé dans la table 4.1. Cependant, pour la majorité des noyaux aucune ou peu nouvelle information pourrait être recueillie. Une des raisons était le faible rendement de produits de fission dans certaines régions. Cela est particulièrement vrai pour les noyaux riches en neutrons les plus légers autour de $N = 50$ comme le Zn et le Ga.
Un autre problème était l'identification des fragments de fission. L'énorme quantité de rayonnements γ émis simultanément et l'absence de détecteurs d'identification de fragments de fission en coincidence compliquent l'affectation non ambigüe des rayonnements gamma observés à un fragment de fission donné. Même si des transitions γ peuvent être attribuées à un événement de fission, le processus de fission est toujours accompagné de rayonnements provenant des fragments complémentaires. Il est possible d'utiliser une méthode fondée sur les rapports d'intensité de transition γ dans les fragments de fission complémentaires pour lever des ambigüités -méthode explicitée en détail dans cette partie- mais celle-ci requiert une production suffisamment abondante et elle trouve ses limites pour les transitions les moins intenses et/ou les noyaux les moins produits. Les durées de vie moyenne de certains états excités ont été mesurées. Les résultats pour ^{92}Kr, ^{93}Kr et ^{101}Zr ont été présentés au chapitre trois.

Part II

A Fission Event Tagger for FIPPS

Chapter 5

Introduction

The detection of γ radiation originating from excited atomic nuclei is a relatively easy task. Its assignment to a nucleus or even to the corresponding deexcitation process of the nucleus however can become rather challenging. This is particularly true for fission experiments where several hundreds of nuclei are produced at the same time, but also for reactions on stable targets which can involve γ transitions from contaminations or from nuclei which are directly involved in the excitation process. For neutron induced fission reactions it was already demonstrated in the previous part of this thesis that the assignment of γ transitions is in most of the cases not a "straightforward" procedure, especially for the class of "naked" germanium arrays such as EXILL, Gammasphere, EUROGAM etc. which don't provide additional systems for particle identification. This lack of information restricts γ assignment to fundamental nuclear observables which are experimentally deduced by techniques such as the Rydberg–Ritz combination principle, the coincidence technique or the angular correlation method. However, all of which are based on the knowledge of some initial information about the nucleus. For instance, the use of any γ coincidence analysis needs the information of at least one γ transition which is already assigned to a nucleus. Thus, for nuclei for which no or only little information is available a proper γ assignment becomes often impossible. Indirect methods for the identification of nuclei like the previously introduced one (see section 2.2.3) for fission fragments can bypass this problematic but are however not very sensitive to weakly produced γ transitions. Additionally, this method does not distinguish between the actual fission event transitions, i.e. prompt-γs and those which are produced in β-decay, i.e. delayed-γs which is adding an additional systematic error. The awareness of this problematic in γ-spectroscopy led

to the combination of complementary identification systems in the past, for γ detection on the one hand, and particle detection on the other hand. A recent example of this combination is the *AGATA-VAMOS* collaboration at GANIL combining a high efficiency germanium array with a large-angle acceptance mass spectrometer.
With special regard to the EXILL array and the acquired knowledge of the corresponding campaign this chapter introduces a new spectrometer for γ detection and particle identification for fission reactions induced by thermal neutrons. The purpose, the performance and the partially conceptual design of this spectrometer is discussed in the first part of this chapter. A complementary device which is serving as a fission event tagger is introduced and discussed with respect to its compatibility in the second part of this chapter.

5.1 The FIPPS Spectrometer

As a follow-up instrument of the temporarily installed EXILL array the *FIssion Product Prompt γ-ray Spectrometer* FIPPS has been constructed as a permanent instrument as a part of the ILL's modernization program "Endurance" [76]. As is already derivable from the acronym, the FIPPS instrument is predominately designed for the identification of prompt γ transitions of fission products. Following the above introduction a distinction of prompt-γs with respect to delayed-γs is not possible without any additional information about the fission process, e.g. a fission event time tagging. Moreover, a proper fission product identification would highly increase the reliability of the γ assignment to a nucleus.
As of today, the FIPPS spectrometer is still under development. However, the main concept of its design can be subdivided into two parts: 1) an EXILL-like high efficiency germanium detector array for the detection of γ radiation and 2) a mass-spectrometer for the identification of fission fragments based on a gas-filled magnet. Projectwise, both parts are being realized within two phases which are discussed below.

5.1.1 FIPPS Phase I - The Germanium Array

Similar to the main plane ring of the EXILL array, the today's FIPPS germanium detector array consists of 8 germanium clover detectors arranged in a plane perpendicular to the neutron beam direction where each clover detector is positioned in an angle of 45° to the neighboring one. For the purpose of maximizing the γ efficiency the clover detectors were mounted as close as possible in order to cover a maximized solid angle resulting in a

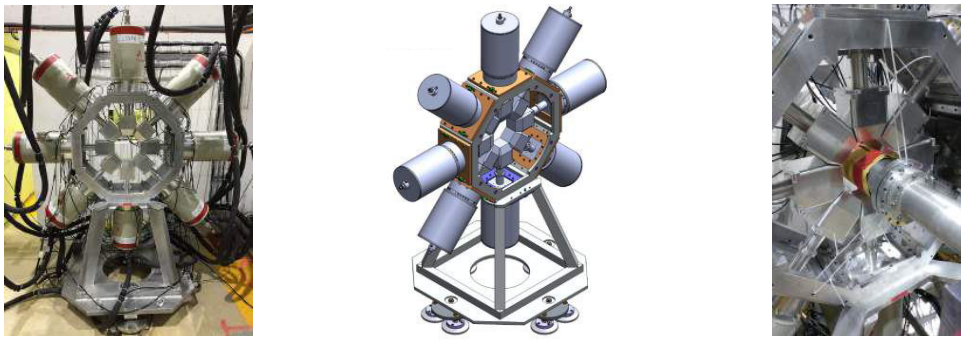

Figure 5.1: The FIPPS (phase I) array in 2017. Left: Front view (against beam direction). Middle: Schematic view. Right: Close-up view with the beam tube.

detector-/focal-point distance of 9 cm. However, unlike the EXILL array the FIPPS instruments is installed at the thermal[1] neutron beam line H22 (see also figure 2.3). There, the initial outgoing neutron flux is $7 \cdot 10^8\,\mathrm{cm}^{-2}\mathrm{s}^{-1}$. An about 2 m long collimation system which is installed in a secondary casemate before the actual germanium array is collimating the neutron beam to 15 mm in diameter providing a flux of $1 \cdot 10^8\,\mathrm{cm}^{-2}\mathrm{s}^{-1}$ in the target position. In this configuration a first (n,γ) campaign on various stable targets was held for one reactor cycle, i.e. 50 days in January-March 2017 performing with an energy resolution of 2 keV at 1.3 MeV for ^{60}Co and an (n,γ) efficiency for $^{205}\mathrm{Ti}(\mathrm{n},\gamma)$ at 1.4 MeV of 4%. An illustration of the FIPPS phase I configuration is shown in figure 5.1.
The FIPPS main detector ring can be extended with two additional endframes in a way that an EXILL-like rhombicuboctahedron geometry is formed. This allows the assembly of 4 additional germanium detectors at each side or supplementary detector systems like $La_3Br(Ce)$ scintillators for fast-timing studies. This modular geometry makes the FIPPS array much more flexible in use and adaptable to different experimental conditions.
Moreover, the complete experimental casemate of FIPPS was recently covered in a hermetic housing operating slightly below atmospheric pressure which allows the use of transuranium targets such as ^{239}Pu, ^{241}Pu, ^{243}Cm, ^{245}Cm, ^{247}Cm, ^{249}Cf or ^{251}Cf [76].

[1] in contrast to the EXILL's cold neutron beam line at PF1B.

5.1.2 FIPPS Phase II - The Mass Spectrometer

Complementary to the phase I germanium array the second phase of the FIPPS project foresees an extension with a system for the identification of fission fragments. Different configurations were already proposed in [76] and [77].
The main component of the FIPPS phase II project is a gas filled magnet (GFM). Accordingly, the identification of fission fragments is referring to a method which is known as the *Gas Filled Magnet Separation Method* which was developed at the Oak Ridge National Laboratory in 1958 [78] and which was used since then for the construction of recoil separators such as the *Jülich Online SEparator for Fission products* JOSEF [79] or the *TransActinide Separator and Chemistry Apparatus* TASCA for super-heavy element studies at GSI [80].

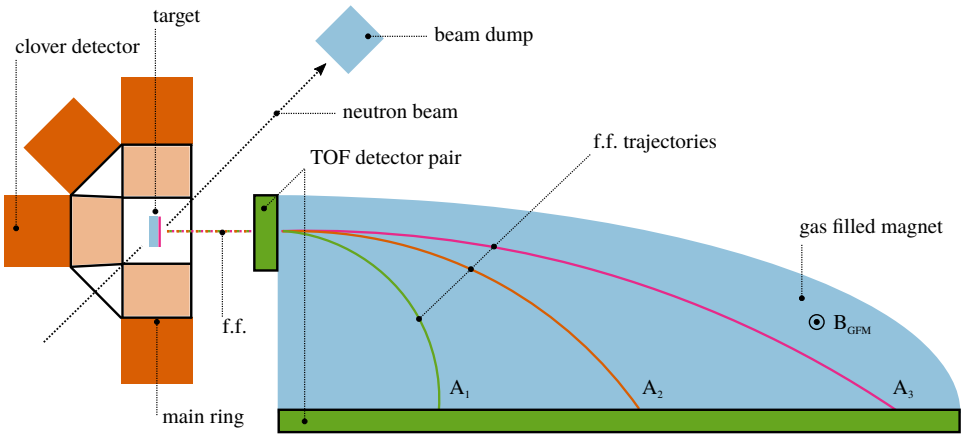

Figure 5.2: Schematic illustration of a potential design for FIPPS (phase II) from the top view perspective. Left side: The FIPPS germanium array. Neutrons are penetrating the actinide target. Fission fragments which are ejected to the left side are being stopped in a thick backing. Right side: The Gas Filled Magnet (GFM). Fission fragments which are ejected to the right side enter the GFM. Fragments are being separated according to their mass.

A dipole magnet under vacuum conditions separates fission fragments according to their p/Q ratio where $p = mv$ is the fragment's momentum and Q the ionic charge. In a gas filled magnet however, charged particles interact with the gas through charge exchange. This means, that if the mean

free path between two charge exchange collisions is small enough, then the separation is performed according to Q as a function of Z and v. To first order v cancels out and the magnetic rigidity Bρ is proportional to A/Z$^{\alpha}$ where A and Z are the fragments mass and charge respectively and α is a parameter given by the type of gas and its pressure.
In the simplified configuration shown in figure 5.2 the neutron beam is penetrating the fission target under 45° with respect to the entry window of the GFM. Assuming a fission target which is capable to release those fission fragments which are exiting into the direction of the GFM (e.g through a thin layer cover on the right side) and to stop those fission fragments which are moving to the left side (e.g into a thick backing). A single fission event can then be identified with respect to the observables of the two fragments within a coincidence measurement. While the "right" fission fragment is identified by the GFM according to its mass, its complementary fission partner emitted to the left side, is stopped in the target's thick backing. The emission of γ radiation is then detected with the Ge array.

5.2 A Conceptual Fission Event Tagger for FIPPS

As mentioned above, a fission event tagger could serve as an intermediate solution for the identification of fission events before the realization of FIPPS phase II. Additionally, such an event tagger could also be used additionally to the GFM, e.g as a fission start detector for the TOF measurement. However, the main purpose of such a device is the capability of identifying signals which are induced by fission events from other signals which accompany this reaction such as alpha emission or β-decay. Especially β-delayed γ-rays induce a large perturbation to the detection of fission γ radiation as learned from the results of the EXILL campaign. The reason for this originates from the γ multiplicity of prompt events and β-delayed events respectively[2]. The average energy which is carried away by prompt γ emission in thermal neutron induced fission of ^{235}U is about 7 MeV accounting for about 7-8 γ quanta while the energy of β-delayed γ radiation is about 6 MeV with an average multiplicity of about 5 γ transitions [81–86]. For a single fission event which is followed by about 6 β-decays in average, this implies an average delayed-γ multiplicity of about one quantum per β-decayed nucleus.

[2]Note that there are varying notations in literature concerning the definition of delayed γ transitions in fission (e.g. by time). In the frame of this discussion a delayed γ transition (or β-delayed γ transition) accounts for those transitions which are emitted by a nucleus after undergoing β-decay, hence after electron emission. Prompt γ transitions in contrast are emitted directly after fission or prompt neutron emission respectively.

In contrast to the 3-4 prompt γ transitions per nucleus it becomes evident that β-delayed γ transitions are less suitable for coincidence analysis, especially for the use in higher fold (e.g triple or quadruple) coincidences. The presence of β-delayed γ transitions in the data is thus worsening the peak to background ratio of prompt produced γ transitions which is especially affecting weakly populated states or states of isotopes far from the valley of stability.
With regard to a fission event tagger device the above discussed differentiation of prompt- and delayed-γ radiation can be achieved by the detection of a fission event and its distinction from β events. Different types of fission event tagging detectors can be considered with individual advantages and drawbacks. Depending on the design the fission event tagger has to fulfill certain requirements to assure compatibility with the γ spectroscopy at FIPPS. This includes the capability of sustaining high count rates, the resistance against radiation damage, a small thickness and a low neutron capture cross section in order to minimize additional (n, γ) background when exposed to the neutron beam. In the following, different fission event tagger designs based on a silicon detector, a gas detector, a liquid scintillator and a solid scintillator are briefly discussed with regard to their feasibility with FIPPS.

5.2.1 Silicon Detector

The use of a silicon semi-conducting detector has an advantage due to its simple installation. Moreover, silicon detectors usually provide a good energy resolution with regard to the detection of fission fragments. On the other hand however silicon detectors are not very resistant to radiation and limited in count rate. Usual Si detectors start to degrade after exposure to a fission fragment dose of a few 10^8 per cm^2 [87]. Thus, with an intended fission rate of about 100 kHz for FIPPS a close-by Si detector would only survive for a few hours.

5.2.2 Gas Detector

A gas-based detector, e.g. a Parallel Plate Avalanche Counter (PPAC) type [88] has a high count rate capability and is not prone to radiation damages. However, a gas detector has a long free flight path for one fission fragment leading to prolonged stopping times and hence, significant Doppler broadening of gammas from states with lifetimes of 0.01 to 1 ns. In addition such a detector requires a complex gas handling system. In a long term view such a detection system could be considered being installed at FIPPS,

e.g. in phase II. However, for the purpose of feasibility within phase I a simpler design is favored.

5.2.3 Active Target based on a Liquid Scintillator

The possibility of using liquid scintillating targets was proposed by Belier *et al.* [89]. This kind of active target is based on an organic liquid scintillator containing the dissolved actinide. The main advantages for this kind of detection system are the high detection efficiency and a good time resolution. The radiation resistance of such scintillating targets was already tested in previous experiments at Neutrograph and PF1B. With regard to scattering of the incident neutron beam the use of liquid scintillators requires the development towards deuterated solvents. The production and the feasibility of such an active target is discussed in detail in chapter 6.2. A schematic design is shown in figure 5.3.

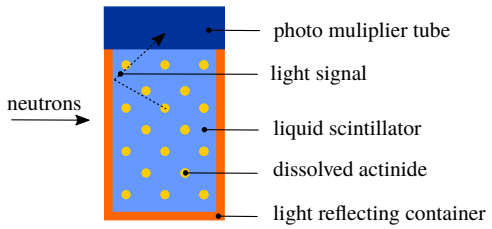

Figure 5.3: Schematic design of a potential active target fission event tagger. Incoming neutrons induce the fission process. The energy loss of the fission fragment in the liquid scintillator is inducing the emission of photons which are detected by the photo multiplier tube. The light reflecting container vessel is increasing the light collection.

5.2.4 Solid Plastic Scintillator

The main advantage for the use of a solid plastic scintillator is its capability of sustaining high count rates. A thick scintillator could be used for a complete stopping of the fission fragments. Alternatively a thin layer could provide a trigger signal for fission fragments which pass the scintillator before being stopped in an additional backing. This is for example required for nuclear moment measurements by perturbed angular correlation where the fragments are stopped in Cu or Ni layers.
Thin-Film scintillator Detectors (TFD) [90, 91] were used earlier for fission fragment detection, however for FIPPS the main challenge is an efficient light

collection in lateral direction without interfering with the neutron beam. In principle this is possible with a frame-like guide as interface between scintillator and photo-multiplier. However a too bulky light guide might cause false triggers from interaction of beta particles. A test of such a thin scintillating foil was performed at the Lohengrin instrument. A detailed discussion of a thin plastic scintillator is presented in chapter 6.1. Different schematic designs based on a solid plastic scintillator are shown in figure 5.4.

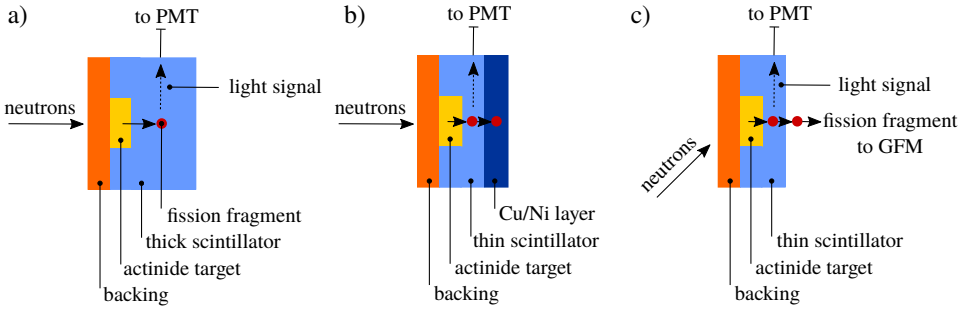

Figure 5.4: Schematic illustrations of different designs for a fission event tagger based on a solid plastic scintillator. a) Based on a thick scintillator. The fragment is depositing all its energy in the scintillator. b) Based on a thin scintillator with Cu/Ni backing. c) Based on a thin scintillator without backing for the use of additional identification in a GFM.

Chapter 6

Applied Experimental Methods

This chapter introduces the experimental methods which were employed for the production and for the testing of scintillator based fission event taggers. The first part of this chapter is related to fission event taggers based on thin scintillating layers. Their performance was tested at the Lohengrin spectrometer which is briefly introduced. The second part of this chapter is related to active actinide targets based on liquid organic scintillators.

6.1 Thin Plastic Scintillating Layers

6.1.1 Production of a Thin Plastic Scintillator

Thin plastic scintillating layers were produced with the spin coating technique (see e.g. [92]). Usually used for the deposition of thin uniform films on flat substrates, the procedure was carried out for the production of self-supporting scintillating layers. Therefore a small amount of the scintillating fluid was deposited in the center position of a $\approx 4\,\mathrm{cm}$ glass pane. In order to prevent the scintillating layer to stick to the glass pane after the actual coating process, the glass was previously coated with a weak soap solution which serves as an intermediate layer. The glass pane with the scintillating fluid was then mounted to the spin coater where it was undergoing short runs of several seconds with a rotational speed of 500-2000 rpm, depending on the used fluid and the intended thickness. Within this process the fluid spreads on the glass pane due to the centrifugal force (excess fluid is ejected

from the substrate), thus forming a homogeneous layer on the substrate[1]. An ab initio calculation for the intended thickness is often complicated to realize, since it depends on various parameters such as viscosity, concentration and volatility of the used solvent. The aimed thickness was therefore estimated empirically according to existing data for the viscosity of the solvent ($\approx 100 - 200\,\mathrm{g/l}$) and the rotational speed of the spin coater. The final thickness was then determined in a second stage, after the layer was completely cured, with an electronic depth profile device to a precision of $0.1\,\mu$m throughout the entire surface.
Two sets of plastic scintillators of different thickness were produced with this technique. A polystyrene based scintillator (F55), and a polyvinyl toluene based scintillator (EJ-296) [94]. Additionally, an industrially produced plastic scintillator of $25\,\mu$m thickness based on polyvinyl toluene with a 500 Å thick aluminum coating was used (EJ-212) [95]. All of these scintillators are based on a xylene solvent. A tabulated summary of the produced scintillating layers is shown in table 6.1.

Table 6.1: List of film scintillators produced with the spin coating technique.

scintillator	**thickness [μm]**	**quantity**	**comments**
EJ-212[†]	25	1	with 500 Å Al backing
EJ-296	4	4	
	6.7-6.8	4	
	12.7	4	
F55	2.5	4	
	4.1	4	

[†] This scintillator was commercially bought and it was the only one which was already tested at Lohengrin.

[1] In fact, this method can lead to inhomogeneous thickness at the edges of the substrate, often denoted as the *"coffee ring effect"* [93]

6.1.2 The Lohengrin Spectrometer

The Lohengrin spectrometer is a recoil mass separator which is installed in the ILL's reactor hall (see figure 2.3). It was designed for the study of the fission process but serves also for nuclear spectroscopy of neutron-rich isotopes produced during the fission process [96–98].
With regard to figure 6.1 fission fragments are produced close to the reactor core as a result of a fission reaction induced by a high thermal neutron flux which is impinging on a fissile target. At this point the neutron flux is $\approx 5 \cdot 10^{14}\,\mathrm{cm}^{-2}\mathrm{s}^{-1}$. Fission fragments are emitted isotropically from the target position. A collimator system which is installed along the beam tube lets pass a small portion of the fission fragments which are emitted towards the spectrometer. After leaving the target the fission fragments are not fully ionized but accumulate statistically an ionic charge after passing through a thin Ni layer leading to a mean q of ≈19-21 for light fission fragments and ≈22-24 for heavy fission fragments.

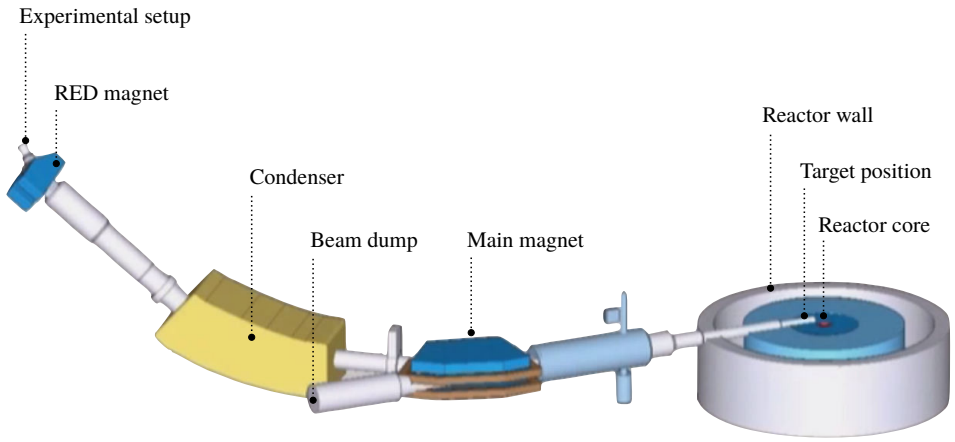

Figure 6.1: Schematic illustration of the Lohengrin mass separator. The separation of fission fragments according to their mass over ionic charge ratio is carried out by a combination of a magnetic field and an electric field. Note the 3-dimensional character of the illustration accounting for the bended trajectories. See text for further information.

The actual separation is achieved afterwards by a combination of a magnetic and an electric field provided by the main magnet and a condenser, respectively. In a first step the main magnet deflects fragments into hor-

izontal direction, with a constant magnetic field B which is perpendicular to the fragments momentum, according to the momentum over ionic charge ratio p/q. The successive electric field deflects the fragments into vertical direction according to their E_{kin}/q ratio. The combination of both fields forces fragments of the same A/q ratio to distribute on parabolas where the fragment velocity determines the position within the parabolas. An additional focusing magnet, the *Reverse Energy Dispersion* dipole magnet or RED magnet at the end of the Lohengrin spectrometer offers the possibility of increasing the particle density in focal position by up to a factor of about seven by collecting fragments of the same A/q but different velocities [98]. Mathematically, the above described technique for the separation of fission fragments with respect to their mass over ionic charge ratio A/q can be deduced from the Lorentz force law for a charged particle of mass A and velocity v moving in a magnetic and an electric field, respectively. Since both fields are perpendicular to each other a decoupled non-vectorial description is adequate leading to equations (6.1) and (6.2):

$$qvB = \frac{Av^2}{r_{mag}}, \tag{6.1}$$

$$qE = \frac{Av^2}{r_{con}}. \tag{6.2}$$

Here, r_{mag} and r_{con} are the radii of the circular trajectories that the charged particle, i.e. the fission fragment, describe in the magnetic field B and electric field E. From equations (6.1) and (6.2) it follows expression (6.3) for the velocity as a function of the magnetic and the electric field and the corresponding radii:

$$v = \frac{r_{con}E}{r_{mag}B}, \tag{6.3}$$

$$E_{kin} = \frac{A}{2}v^2, \tag{6.4}$$

$$E = \frac{U}{d}. \tag{6.5}$$

Together with equation (6.4) and (6.5) for the kinetic energy of the fragment E_{kin} and the electric field of the condenser E as a function of the electrostatic potential U and the plate distance d the following focusing conditions are derived:

$$\frac{\mathrm{A}}{\mathrm{q}} = \frac{1}{\chi}\frac{\mathrm{B}^2}{\mathrm{U}},$$

$$\frac{\mathrm{E}}{\mathrm{q}} = \phi \mathrm{U},$$

with the spectrometer parameters

$$\phi = \frac{\mathrm{r_{con}}}{2\mathrm{d}}, \qquad \chi = \frac{2\phi}{\mathrm{r_{mag}^2}}.$$

6.1.3 The Experimental Setup

The EJ-212 thin film plastic scintillator was tested at the Lohengrin instrument in October 2016. Therefore the scintillating layer was coupled to the entry window of a photomultiplier tube. An optical silicon grease which was applied in between the plastic layer and the PMT window was used for a proper light transport and additionally insured the physical connectivity between both. The whole apparatus (i.e. the PMT with the plastic scintillator) was mounted into a small housing which was directly connected to the exit window of the Lohengrin spectrometer in a way that the fission fragments penetrate the scintillator under an angle of 90°. The thin aluminum layer which was coated to one side of the scintillator was facing in the direction of the arriving fission fragments in order to reflect the light leaving the scintillator opposite the PMT. However, such a "dead layer" can affect the performance of the scintillator's resolution when the fragments deposit a part of their energy in it. Its effect is discussed in the following chapter. A schematic illustration of this setup is shown in figure 6.2.
In this configuration different energy scans of 2-5 min were performed with Lohengrin. In order to account for the whole fission fragment distribution, i.e. the light and the heavy fragments, energy scans were performed with light masses around A=90 and heavy masses around A=136.
Such a scintillator is not capable to resolve each mass which is provided for a given E and A/q. Therefore, a complementary experiment under the same conditions, but with a high energy resolution Si detector was performed. Thus, in direct comparison, the observed masses with the Si detector were projected to the weaker resolved scintillator mass distributions.

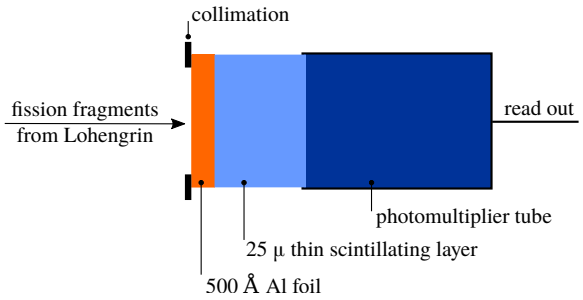

Figure 6.2: Schematic illustration of the experimental setup for the thin film fission tagger tested at the Lohengrin instrument. See text for further information.

6.2 Active Scintillating Liquid Targets

Preliminary tests on an active scintillating target were performed in February 2017 at the CEA/DAM Ile-de-France in Bruyère-les-Châtel. The use for such a target in in-beam experiments for FIPPS requires some properties which were intended to be evaluated within these tests (a brief introduction was already given in the previous chapter). This includes the compatibility of the liquid scintillator with the actinide with respect to its discrimination performance. But it concerns also the compatibility of the active scintillating target solvent with the used material for the vessel in which the solvent is stored. The following section briefly reports on this.

6.2.1 Vessel Capability

A suitable vessel for an active scintillating target as it is foreseen for in-beam experiments at FIPPS has to fulfill some requirements which are particularly crucial to neutron exposure. Depending on the design of the vessel two components are of special importance: 1) the fission fragment entry and exit windows, and 2) the transmission window which is coupled to the PMT.
The entry window which will be exposed to the neutron beam should have a low neutron capture cross section in order to prevent unwanted (n, γ) background. Also a low neutron scattering cross section is beneficial to minimize scatter neutrons which could cause (n, γ) background in the surrounding. For the same reason such an entry and exit window material should be as thin as possible.

Table 6.2: Calculated neutron scattering and neutron capture rates for the tested vessel materials assuming a thickness of 1 mm. Al is listed for comparison. The values for the neutron cross sections were taken from [99].

material	**density** $\mathbf{g/cm^3}$	$\sigma_{\mathbf{scatter}}$ **[b]**	$\sigma_{\mathbf{capture}}$ **[b]**	**n scattered** $\mathbf{[n/s]^\dagger}$	**n captured** $\mathbf{[n/s]^\dagger}$
MgO	3.60	7.94	0.063	$4.3{\cdot}10^6$ (4.3%)	$3.4{\cdot}10^4$ (0.03%)
MgF_2	3.15	11.75	0.082	$3.6{\cdot}10^6$ (3.6%)	$2.5{\cdot}10^4$ (0.02%)
ZrO_2	5.68	14.92	0.185	$4.1{\cdot}10^6$ (4.1%)	$5.1{\cdot}10^4$ (0.05%)
CF_2(FEP)	2.12	13.59	0.023	$3.5{\cdot}10^6$ (3.5%)	$5.9{\cdot}10^3$ (0.006%)
Al	2.25	1.50	0.231	$7.5{\cdot}10^5$ (0.8%)	$1.2{\cdot}10^5$ (0.11%)

† Assuming a neutron flux of $1{\cdot}10^8\,\mathrm{cm^{-2}s^{-1}}$.

The transmission window on the other hand should guarantee an optimal light transport to the photomultiplier. This also concerns its reactivity with the potential solvent, which could cause "blindness" of the window or even degrading it.
Several vessel materials were considered for the use with an active scintillating target with respect to the required characteristics listed above. Samples of magnesium oxide (MgO), magnesium fluoride (MgF_2), zirconium oxide (ZrO_2), and fluorinated ethylene propylene (CF_2) were tested for their reactivity with the liquid scintillators and for their light transmission. Their calculated neutron scatter- and capture probabilities are listed in table 6.2.

For the light transmission test, a 1 pW LED was coupled to a photomultiplier tube placed in a housing which was impervious to background light. The light yield was then measured with and without the sample which was placed in between. The results of the light transmission measurement can be found in table 6.2.

6.2.2 Production of Active Scintillating Liquid Targets

Active scintillating targets based on different liquid scintillators were produced. All of those targets were based on a ^{235}U solution. Therefore, an amount of approximately 0.1 g of uranium nitrate ($UO_2(NO_3)_2$) was diluted into 2.5 ml of a 1 M nitric acid solution (HNO_3) and additionally diluted with the same amount of water, leading to an uranium concentration of about 10 mg/ml. An extraction of 2.5 ml of this solution was then added to 0.5 ml of the respective liquid scintillator. Typically, these two components do not mix but are separated in a suspension. This suspension had therefore to be centrifuged for several minutes until they mix to a homogeneous emulsion.
With regard to the above discussion about the vessel material, neutron capture reactions and neutron scattering account also for the liquid scintillator and other involved components of the active target. As mentioned earlier, especially the presence of hydrogen is crucial to in-beam use, due to its high neutron scattering cross section of 82 b.
In consequence, three hydrogen-absent scintillators were considered for a potential use within an active target: hexafluorobenzene (C_6F_6)(EJ-313 [100]), deuterated benzene (C_6D_6)(EJ-315 [101]) and deuterated toluene (C_7D_8)[2]. Their neutron scattering and capture characteristics are listed in table 6.3. For their characterization the produced active target scintillators were filled into test tubes. The tubes were then inserted in an ORDELA 8100AB PERALS spectrometer [102]. This system is based on a PMT, a shaper and a zero crossing time circuit. These last 2 circuits provide respective signals to measure the energy of the particle and to perform a pulse shape analysis of the fluorescence signal. The data acquisition was performed with the FASTER [103] acquisition system.

[2]The test was however performed with hydrogen based toluene because of unavailability of deuterated toluene

Table 6.3: Calculated neutron scattering and neutron capture rates for the tested liquid scintillators assuming a thickness of 1 mm. Deuterated toluene (C_7D_8) was not tested but is listed for comparison.

scintillator	**density** $\mathbf{g/cm^3}$	$\sigma_{\mathbf{scatter}}$ **[b]**	$\sigma_{\mathbf{capture}}$ **[b]**	**n scattered** $\mathbf{[n/s]^\dagger}$	**n captured** $\mathbf{[n/s]^\dagger}$
C_6D_6	0.95	79.15	0.024	$5.4{\cdot}10^6$ (5.4%)	$1.6{\cdot}10^3$ (0.002%)
C_6F_6	1.61	57.41	0.079	$3.0{\cdot}10^6$ (2.9%)	$4.1{\cdot}10^3$ (0.004%)
C_7H_8 (toluene)	0.87	695.10	2.689	$3.9{\cdot}10^7$ (39.3%)	$1.5{\cdot}10^5$ (0.15%)
C_7D_8 (deut. tol)	0.94	99.98	0.287	$5.7{\cdot}10^6$ (5.7%)	$1.6{\cdot}10^3$ (0.001%)

† Assuming a neutron flux of $1{\cdot}10^8\,\mathrm{cm^{-2}s^{-1}}$.

Chapter 7

Results

This chapter reports on the results of the experiments which were performed for preliminary tests of a potential fission event tagger for FIPPS. The first part of this chapter refers to a fission event tagger based on a thin plastic scintillating layer, and the second part to an active target based on a liquid organic scintillator.

7.1 A Thin Plastic Scintillating Layer

Following the description of the experimental methods in section 6.1 a polyvinyl toluene based, 25 μm thick scintillation foil (EJ-212) coupled to a photomultiplier was tested at the Lohengrin spectrometer.

7.1.1 Scintillator Response

In order to evaluate the response and the discrimination capability of this scintillator an energy scan for fission fragment energies of $\approx 50 - 100$ MeV was performed with an A/q-ratio of 5. With respect to the Lohengrin acceptance this ratio leads to a strong fission fragment yield accounting for the light fission fragment distribution in neutron induced fission of ^{235}U. As demonstration of the discrimination performance a single energy spectrum for an E/q-ratio of 5 MeV is shown in figure 7.1. Typically, such a setting allows the observation of fission fragments with the masses A=85, 90, 95, 100, 105. However, in figure 7.1, two distributions were observed. A high energy Gaussian-like distribution which arises from the fission fragments and a low energy one which is associated with the electrons arising from β-decay.

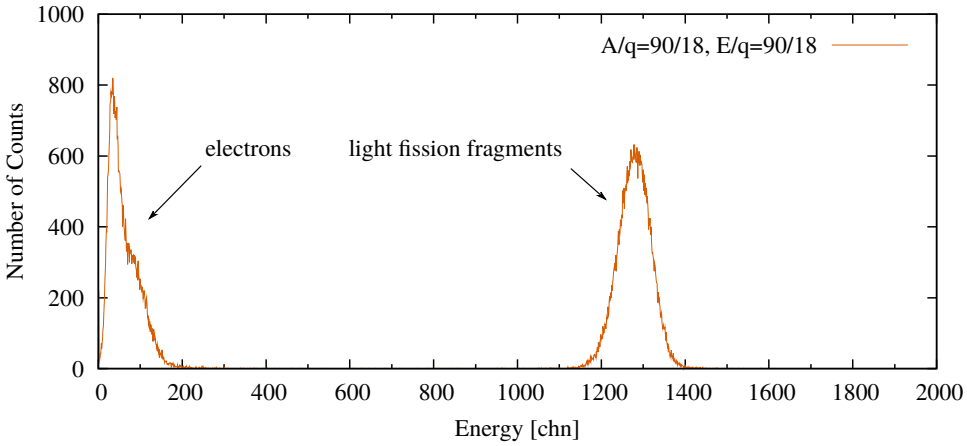

Figure 7.1: Pulse height spectrum for the energy deposition of fission fragments in a 25 μm thick scintillation foil coupled to a photomultiplier. The detected fission fragments satisfy an A/q=5 and an E/q-ratio of 5 MeV. The "left" distribution originates from electrons emitted in β decay, the "right" distribution from the fission fragments.

Thus, for these particular fission fragment masses and energies the scintillator is capable to discriminate electrons and fission fragments from each other. However, the resolution is too low for the differentiation of the corresponding masses and energies.
A complementary measurement was performed under the same Lohengrin conditions but with a Si detector replacing the scintillator. The results of this measurement are shown in the upper panel of figure 7.2. The improved resolution of the Si detector is capable to discriminate fission fragments with respect to the given setting. By this it was possible to project the identified masses and energies to the fission fragment distribution of the scintillator measurement. Therefore the integrated yield of all single peaks of the Si-spectrum was normalized to the distribution of the scintillator spectrum. Each peak was then reconstructed with a Gaussian distribution according to its particular relative yield as shown in the lower panel of figure 7.2.

In order to account for a broader spectrum of fission fragment masses and energies an additional energy scan was performed for an A/q-ratio of 136/21 which is representative of heavy fission fragments. This measurement was performed for an energy range between 30-75 MeV. All measurements, the light fission fragments scan and the heavy fission fragments scan, are summarized in figure 7.3.

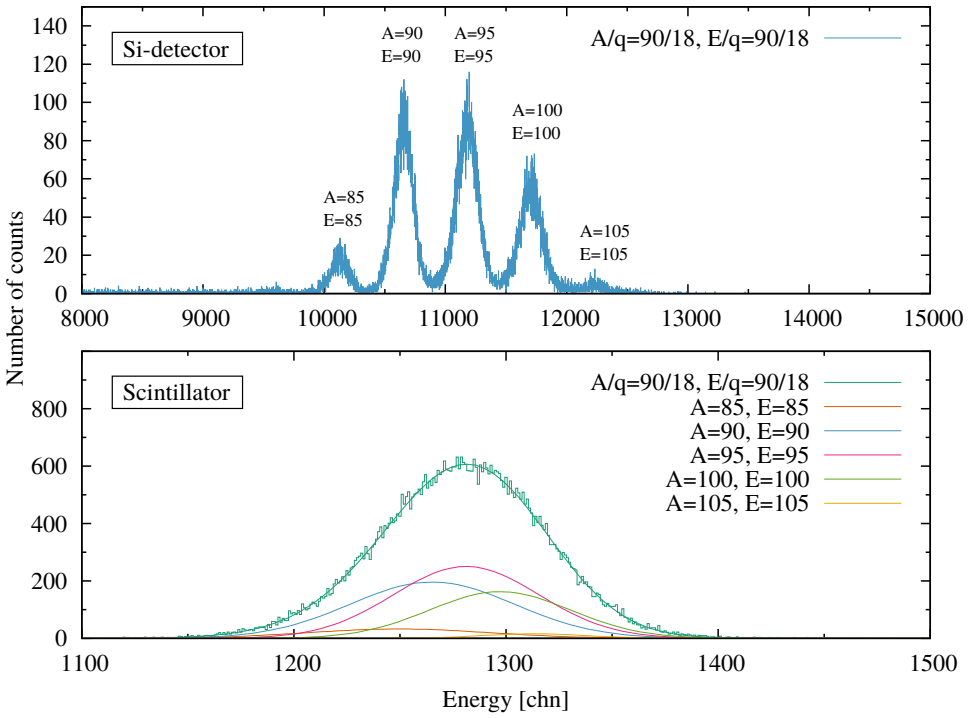

Figure 7.2: Pulse height spectrum for the energy deposition of fission fragments with an A/q=5 and an E/q-ratio of 5 MeV. Upper panel: Measured with a Si-detector. Lower panel: Measured with a 25 μm thick scintillation foil coupled to a photomultiplier. The inner Gaussian distributions were reconstructed from the Si-spectrum.

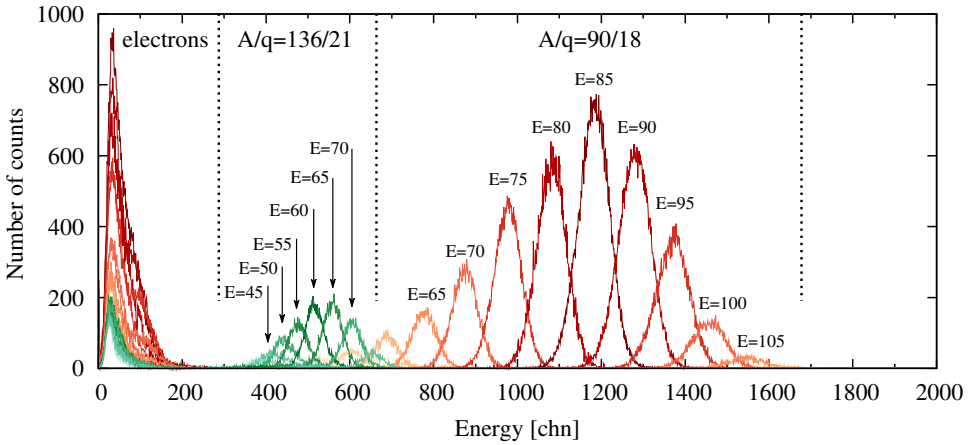

Figure 7.3: Pulse height spectrum for the energy deposition of light fission fragments with an A/q=5 and an E/q-ratio of 5 MeV, and heavy fission fragments with an A/q-ratio of 136/21 in neutron induced fission of ^{235}U measured with a 25 μm thick scintillation foil coupled to a photomultiplier.

7.2 Active Scintillating Liquid Targets

With respect to the description of the experimental methods in section 6.2 preliminary tests for the use of an active scintillating target for FIPPS were performed. These tests addressed the compatibility of the liquid scintillator with the vessel material, and the compatibility of the liquid scintillator with ^{235}U and its discrimination performance in a pulse shape analysis.

7.2.1 Vessel Compatibility

Different vessel material samples were tested with respect to their compatibility with different liquid organic scintillators, as well as their light transmission. In terms of compatibility of the scintillator and the container vessel, none of the tested vessel materials of table 7.1 showed any observable reaction with respect to dissolution or opacity within one week of exposure. The luminosity tests led to results of a light transmission between 93-100%. However, this result is strongly depending on the thickness of the samples. The results are summarized in table 7.1.

Table 7.1: Vessel compatibility with respect to dissolution and light transmission for the vessel materials MgO, MgF_2, ZrO_2 and CF_2(FEP) tested with the liquid scintillators C_7H_8, C_6D_6 and C_6F_6.

	C_7H_8	**C_6D_6**	**C_6F_6**	**light transmission (sample thickness)**
MgO	OK	NT	OK	95% (0.5 mm)
MgF_2	OK	NT	NT	99% (0.5 mm)
ZrO_2	OK	NT	OK	93% (1 mm)
CF_2(FEP)	OK	OK	OK	100% (some μm)

OK = vessel material and scintillator are compatible.
NT = not tested.

7.2.2 Particle Discrimination Performance

Different active targets were produced and tested with regard to their particle discrimination performance. The fabrication did not show any specific peculiarities concerning texture or solubility. All of the produced targets showed a homogeneous green uranyl color throughout the entire sample and the various components mixed to a homogeneous emulsion.
The discrimination characteristics for these targets were evaluated within the pulse shape discrimination technique. Figure 7.4 shows a two-dimensional distribution of the PSD value over the particle's energy for the C_6D_6 based active target. Two different distributions were observed which could be assigned to alpha particles and electrons respectively.
The C_6F_6 based active scintillating target however shows inferior discrimination properties compared to the C_6D_6. Its spectrum is shown in figure 7.5. The β-decay line strongly overlaps the alpha distribution. A clean α-β discrimination for this scintillator and for the applied PSD settings was thus not possible. A projection of this distribution leads to a peak-to-background ratio of 0.9 within a 2σ environment.

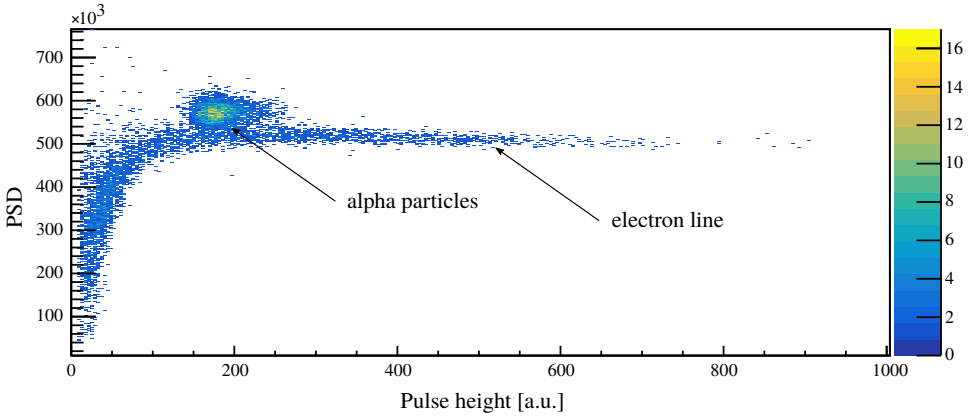

Figure 7.4: Pulse shape discrimination spectrum as a function of the pulse height for an ^{235}U active target based on the liquid scintillator C_6D_6.

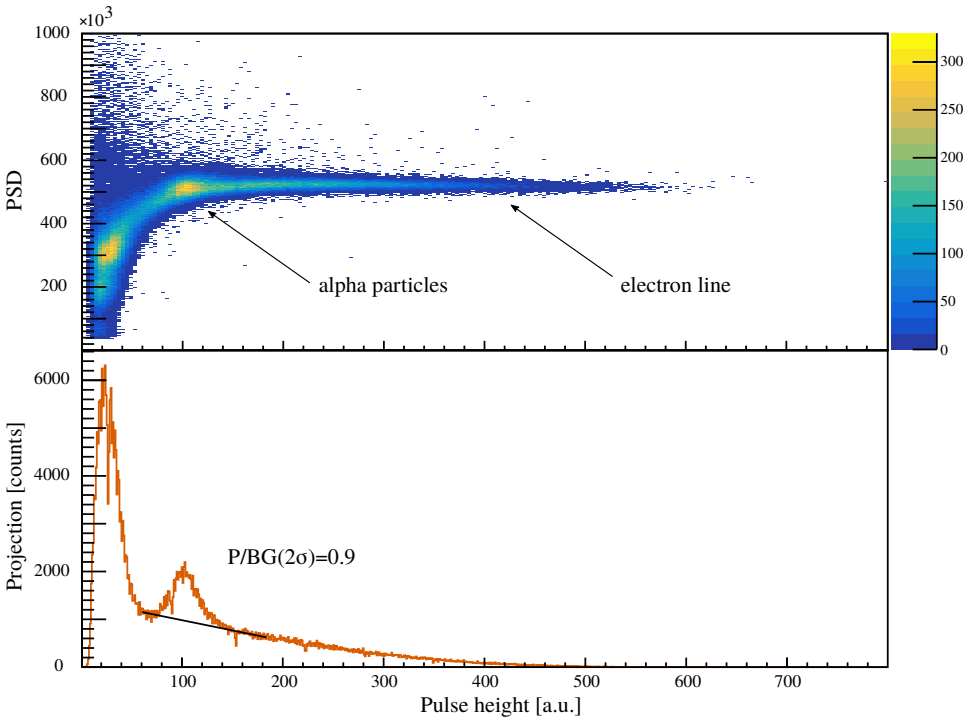

Figure 7.5: Top panel: Pulse shape discrimination spectrum as a function of the pulse height for an ^{235}U active target based on the liquid scintillator C_6F_6. Bottom panel: Projection onto the x-axis.

Chapter 8

Discussion

One major issue in the gamma spectroscopic analysis of fissile nuclei with large germanium detector arrays is the correct identification of fission events. In addition to these "useful" events the data stream contains a lot of gamma rays from neutron capture on the target nucleus or its backing, and from beta decay of the fission products accumulated in the backing. The perturbation by these events within the EXILL campaign was discussed and explored accordingly, and was the primary reason for the development of ancillary identification systems.
The recently developed FIPPS instrument at the ILL will provide a gas filled magnet for the identification of fission fragments. Combining such a setup with a fast detector which is discriminating fission events from other accompanying events is crucial for the realization of coincidence circuits with a germanium array. Moreover, it could be used as a stand-alone version for the tagging of fission events.
A preliminary conceptual design study of such a fission event tagger for the use under neutron exposure was subject of this thesis. Therefore, two main designs have been considered: a liquid scintillator based active target fission event tagger, and a solid plastic film based fission event tagger. The main focus for the consideration of such a tagger was on the neutron scattering characteristics of the involved components and the detection properties regarding the discrimination of fission events.
All commercially available solid plastic scintillators contain hydrogen which scatters and absorbs neutrons. However, the thickness of such a scintillator can be considerably reduced to a few micrometer, and the overall effective neutron capture and neutron scattering rates reduce accordingly. Moreover, the production of such homogeneous films from e.g. liquid deuterated scin-

tillators with the spin-coating technique was shown to be feasible. A 25 μm thick solid plastic scintillator based on polyvinyltoluene was tested at Lohengrin with regard to its discrimination characteristics. Within an energy range between 40-105 MeV accounting for light fission fragments and heavy fission fragments respectively the scintillator is suitable for the separation of fission events from electrons and hence capable of tagging fission events without any significant background. However, depending on the design of such a solid plastic scintillator fission event tagger the overall efficiency might suffer from the energy loss of fission fragments within the target and the dead-layer, i.e. aluminum coating respectively. For a simple ad hoc design as shown figure 8.1 this energy loss becomes evidently larger for small angles under which the fragments are emitted. Hence, assuming a required minimal energy deposition in the scintillator of 20 MeV to account for fission fragment discrimination, and a $^{235}UO_2$ target thickness of 1 mg/cm^2, the mean total fission event tagging efficiency calculates to $\approx 92\,\%$ corresponding to a solid angle acceptance of 80-85°.

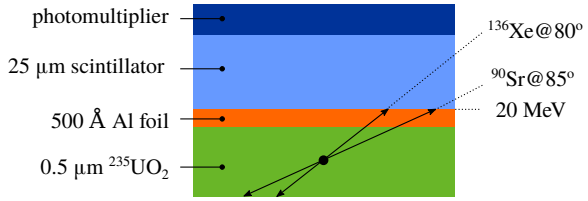

Figure 8.1: Simplified fission event tagger based on a solid plastic scintillator illustrating the limitations of fission fragment discrimination efficiency. Fission fragments being emitted under small angles lose too much energy in the target and the aluminum layer respectively. The calculation was done with *LISE++*.

Different "active targets" based on organic liquid scintillators have been produced and tested. Regarding the design of such an active fission event tagger the effective thickness which is exposed to the neutron beam might be significantly larger than for a solid plastic scintillator. Thus, a proper selection of suitable involved materials is essential in order to minimize neutron scattering and neutron absorption.
All of the tested vessel material show similar properties regarding their interaction with neutrons. A practical active scintillating target could consist of a liquid layer of ≈1 mm incorporated in an inorganic container vessel with a neutron entry window and a neutron exit window of 0.5 mm thickness each.

Alternatively a fluorinated ethylene propylene based vessel could be even manufactured much thinner which suggests the use of FEP as vessel material. Moreover, none of the tested samples show any significant chemical reaction with the used liquid scintillators.
Three potential liquid scintillators have been tested with respect to their particle discrimination properties with ^{235}U: C_6D_6, C_6F_6 and C_7H_8. With respect to their interaction with neutrons C_6D_6 and C_6F_6 show similar capture and scattering properties. However, the discrimination of alpha particles with C_6D_6 is superior since the beta line for C_6F_6 is overlapping the alpha distribution. Unfortunately, it was not possible to evaluate the discrimination characteristics for fission fragments, but as demonstrated in [89] a clear separation may be possible. C_7H_8 (toluene) shows also excellent discrimination properties but is unsuitable due to its huge neutron scattering cross-sections. The use of deuterated toluene should be considered.
In conclusion, both fission event tagger designs, based on a solid plastic scintillating layer or based on an organic liquid scintillator, have their benefits and drawbacks according to their application. When used as fission veto in order to perform (n, γ) spectroscopy a liquid scintillator is preferred since the veto efficiency is close to unity and additionally beta decays can partially be vetoed too. However, actinide nuclides have a high level density with many converted low-energy transitions. Therefore, care has to be taken to avoid falsifying intensity ratios when true conversion electrons trigger the veto. Moreover, a liquid scintillator based fission event tagger would not be feasible in combination with the gas filled magnet at FIPPS. Fission fragments would completely deposit their energy within the scintillator or the vessel window respectively, and thus not be available for further identification.
A solid plastic scintillator based fission event tagger on the other hand could be designed in a way that fission fragments pass through a thin layer without significant energy loss and being identified afterwards within the GFM. Moreover, its discrimination properties allow a clean separation of electrons and fission fragments throughout a large range of masses and energies. However, the fission fragment detection efficiency is inferior with respect to a liquid scintillator based fission tagger.

Synthèse de la partie *Un marqueur d'événement de fission pour FIPPS* : Comme mentionné dans la première partie de cette thèse, un problème majeur dans l'analyse par spectroscopie gamma des noyaux fissiles avec de grands multidétecteurs de germanium est l'identification correcte des événements de fission. En effet, aux rayonnements gamma émis par les événements de fission des cibles d'actinides, se superposent ceux issus de la capture des neutrons par la cible et les matériaux de structure l'environnant, ainsi que ceux provenant de la décroissance bêta des produits de fission qui s'accumulent dans la cible et son support. La perturbation causée par ces événements au sein de la campagne EXILL a été discutée et explorée en conséquence, et a été la principale raison du développement des systèmes d'identification auxiliaires.

L'instrument FIPPS (FIssion Prompt Product γ-ray Spectrometer) qui en cours de développement à l'ILL fournira un aimant rempli de gaz pour l'identification des fragments de fission. La combinaison d'un tel spectromètre avec un détecteur rapide qui différencie les événements de fission d'autres événements est cruciale pour réaliser ensuite une coïncidence avec un spectromètre de germanium. De plus, il pourrait être utilisé comme une version autonome pour le marquage des événements de fission.

Une étude conceptuelle préliminaire d'un tel marqueur d'événement de fission pour l'utilisation sous exposition neutronique a fait l'objet de cette thèse. Deux conceptions principales ont été considérées: un marqueur d'événement de fission de cible active basé sur un scintillateur liquide et un marqueur d'événement de fission à base d'un film plastique solide. L'objectif principal de la considération d'un tel marqueur était les caractéristiques de diffusion neutronique des composants impliqués et les propriétés de détection concernant la discrimination des événements de fission.

Tous les scintillateurs en plastique solide disponibles dans le commerce contiennent de l'hydrogène, élément qui disperse et absorbe les neutrons. L'épaisseur d'un tel scintillateur est donc un paramètre critique mais elle peut être considérablement réduite jusqu'à quelques micromètres, et les taux globaux effectifs de capture neutronique et de diffusion neutronique diminuent en conséquence. De plus, la production de tels films homogènes à partir, par exemple, de scintillateurs liquides deutérés avec la technique d'induction centrifuge se sont révélés réalisables. Un

scintillateur en matière plastique solide à base de polyvinyltoluène de 25 μm a été testé à *Lohengrin* en ce qui concerne ses caractéristiques de discrimination. Dans un domaine d'énergie entre 40 et 105 MeV, représentant des fragments de fission légers et des fragments de fission lourds, nous avons montré que le scintillateur est approprié pour la séparation entre événements de fission et électrons, et donc capable de marquer les événements de fission sans une contribution de β significative. Cependant, le rendement global pourrait souffrir de la perte d'énergie des fragments de fission dans la cible et la couche morte, à savoir le revêtement d'aluminium. Pour une conception ad hoc simple comme le montre la figure 8.1, cette perte d'énergie devient évidemment plus importante pour les petits angles sous lesquels les fragments sont émis. Par conséquent, en supposant un dépôt d'énergie minimal requis dans le scintillateur de 20 MeV nécessaire pour la discrimination des fragments de fission, et une épaisseur de cible de 1 mg/cm^2, alors l'efficacité de marquage d'événement de fission totale moyenne atteint $\approx 92\,\%$ correspondant, à une acceptance en angle solide de 80-85°.
Différentes cibles actives basées sur des scintillateurs liquides organiques ont été produites et testées. En ce qui concerne la conception d'un tel marqueur d'événement de fission actif, l'épaisseur effective qui est exposée au faisceau de neutrons peut être significativement plus grande que pour un scintillateur en plastique solide. Ainsi, une sélection appropriée des matériaux impliqués est essentielle afin de minimiser la diffusion et l'absorption des neutrons. Tous les matériaux utilisés comme contenant du scintillateur liquide qui ont été testés présentent des propriétés similaires en ce qui concerne leur interaction avec les neutrons. Une cible scintillatrice active pratique pourrait consister en une couche liquide de ≈1 mm incorporée dans un récipient contenant une fenêtre d'entrée de neutrons et une fenêtre de sortie de neutrons de 0,5 mm d'épaisseur chacune. Une alternative pourrait être un récipient à base d'éthylène et de propylène fluoré pouvant même être fabriqué beaucoup plus mince, ce qui suggère l'utilisation de FEP comme matériau de récipient. De plus, aucun des échantillons testés ne montre de réaction chimique significative avec les scintillateurs liquides utilisés.
Trois scintillateurs liquides potentiels ont été testés en ce qui concerne leurs propriétés de discrimination des particules avec ^{235}U: C_6D_6, C_6F_6 et C_7H_8. En ce qui concerne leur interaction avec les neutrons, C_6D_6 et C_6F_6 montrent des propriétés similaires de capture et de diffusion. Cependant, la discrimination des particules alpha avec C_6D_6 est inférieure

puisque la ligne bêta pour C_6F_6 chevauche la distribution alpha. Malheureusement, il n'a pas été possible d'évaluer les caractéristiques de discrimination pour les fragments de fission, mais comme démontré dans [89], une séparation claire peut être possible. C_7H_8 (toluène) montre également d'excellentes propriétés de discrimination mais est inadapté en raison de sa grande section efficace de diffusion des neutrons. L'utilisation de toluène deutéré devrait être envisagée.
En conclusion, les deux conceptions de marqueurs d'événements de fission, basées sur une couche de scintillation en plastique solide ou à base d'un scintillateur liquide organique, présentent leurs avantages et leurs inconvénients en fonction de leur application. Lorsqu'on l'utilise comme veto de fission pour effectuer la spectroscopie (n, γ), on préfère un scintillateur liquide car l'efficacité du veto est proche de l'unité et en outre les désintégrations bêta peuvent aussi être partiellement rejetées. Cependant, les noyaux d'actinides ont une densité élevée avec beaucoup de transitions converties à basse énergie. Par conséquent, il faut prendre soin d'éviter d'affecter les rapports d'intensité lorsque de véritables électrons de conversion déclenchent le veto. De plus, un marqueur d'événement de fission à base d'un scintillateur liquide n'est pas réalisable dans le cas d'une utilisation avec un aimant rempli de gaz comme à FIPPS. Les fragments de fission déposeraient complètement leur énergie dans le scintillateur ou dans la fenêtre du récipient, et seraient donc perdus pour une identification ultérieure. D'autre part, un marqueur d'événement de fission à base de scintillateur en plastique solide pourrait être conçu de manière à ce que les fragments de fission traversent une couche mince sans perte d'énergie significative et soient ensuite identifiés dans l'aimant rempli de gaz. Ses propriétés de discrimination permettent une séparation nette des électrons et des fragments de fission à travers une large gamme de masses et d'énergies. Cependant, l'efficacité de détection des fragments de fission est inférieure à celle d'un marqueur de fission à base de scintillateur liquide.

Part III

Production of the isomer ^{195m}Pt

Chapter 9

Introduction

9.1 ^{195m}Pt for Medical Use

Every year more than 8 million people worldwide die from cancer[1] [104]. Due to the variety of different types of cancer a specific adjusted treatment has thus to be applied accordingly. However, the treatment of cancer is often a combination of different therapeutic methods such as surgery, radiation therapy etc. This combinatorial treatment especially applies to so called non-disseminated tumors, i.e. primary solid tumors which can be accessed locally through surgery or external radiation therapy are often followed by a secondary treatment. For disseminated cancer types however, such as leukemia, or cancer in an advanced state where already metastases are build these locally accessible techniques are often not applicable anymore. These types of cancer require a global treatment such as chemotherapy. Unfortunately, chemotherapy often comes along with some major drawbacks since it is affecting normal cells and cancer cells at the same time due its cytotoxic nature. In most of the cases this is causing serious side effects such as nausea, vomiting, hair loss, bone marrow suppression and kidney damage. In addition to that not every patient responds to such a treatment but most of them will suffer from these side effects.
In the past years other promising methods were developed which bypass this global cell damage but address only cancer cells instead. In a general sense of meaning these techniques are often referred to as *targeted methods*. Especially radioisotopes have become more and more important in these kind

[1] At an average death rate of about 55 million deaths per year this implies every 7^{th} person dying as a result of cancer.

of applications. In the following sections some basic concepts for the use of radioisotopes in medicine are briefly sketched and applied to ^{195m}Pt.

9.1.1 Radioisotopes in Medicine

There is a variety of methods and techniques used in nuclear medicine which have their origin in the development of fundamental concepts in nuclear physics and radio chemistry. All of which involve the atomic nucleus or its radiation as a source of cell damage causing force for therapeutic issues, or for diagnostics when the radiation is penetrating the patients body without any serious cell damaging effect for the localization of specific structures within the body.

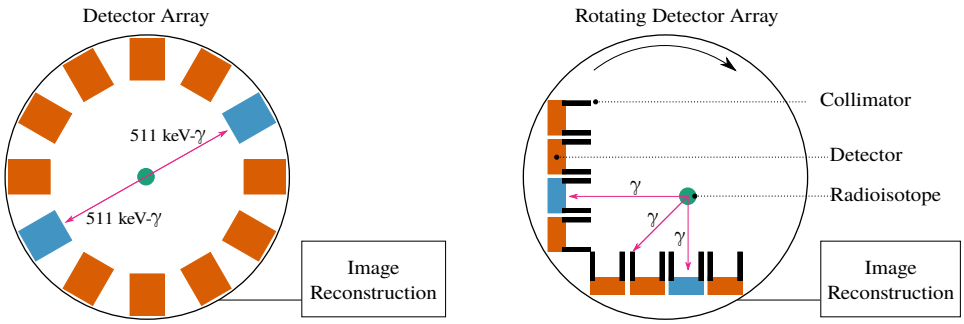

Figure 9.1: Schematic illustration of medical imaging techniques based on γ detection. Left: Positron emission tomography (PET). A static axially symmetric detector array detects two 511 keV photons created in positron-electron annihilation which propagate in opposite directions. Right: Single photon emission computed tomography (SPECT). The detection of single emitted photons is restricted by a collimation system. The origin of emission is reconstructed by computation of a rotating detector array.

Since the 1950s, with the first use of ^{131}I for the diagnosis and treatment of thyroid cancer, the demand for radioisotopes is steadily increasing for therapeutic and diagnostic applications, in-vitro or in-vivo. Today, as of 2016, the annual frequency of diagnostic nuclear medicine is about 2%, whereof about a tenths is used for therapeutic purposes, or in other words, 90% of all radioisotopes used in nuclear medicine are for diagnosis[2], and it is interesting to mention that about 80% of all diagnostic procedures world-

[2]The available statistical data is slightly varying

wide account for ^{99}Tc [105].

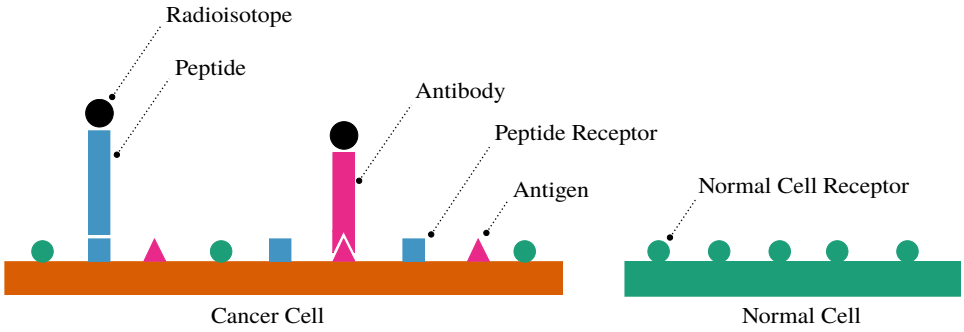

Figure 9.2: Schematic picture illustrating the basic idea behind targeted systems with radioisotopes for the radioimmunotherapy (RIT) and the peptide receptor radio therapy (PRRT). See text for further information.

The use of radioisotopes for diagnostic purposes requires however some specific properties. An ideal diagnostic radioisotope should minimize its interaction with the surrounding tissue. This implies the absence of any cell damage causing radiation such as electrons or α-particles. Also too low energy γ or X-ray emission is of disadvantage due to attenuation within the body. However, with special regard to the detection technique, it is γ emission which is tracing the location. Today there are mainly two imaging procedures adopted to γ emission which are commonly used, the *Positron emission tomography (PET)* and the *Single Photon Emission Computed Tomography (SPECT)* and its predecessor, the gamma camera, respectively (cf. figure 9.1). PET imaging requires the positron-electron-annihilation, leading to the subsequent creation of two 511 keV γ-rays which are emitting in opposite directions. Therefore, only neutron deficient nuclei which are decaying through β^+ emission are suitable radioisotopes for this imaging technique. SPECT on the other hand uses rotating collimated gamma detectors, i.e. gamma cameras for detection. Thus, there are basically no restrictions concerning the decay path or energy range of the γ-rays to be detected. However, due to the above mentioned attenuation probability of low energy photons and a technical collimation constraint for high energy photons, most of the currently used radioisotopes decay within the energy window of 60-300 keV (e.g. ^{99m}Tc decays via the emission of 140 keV photons) to which the medical and technical environment, i.e. detectors etc. is adjusted to.

Evidently the requirements for radioisotopes change for therapeutic use. Also referred to as *radionuclide therapy (RNT)*, cell damage is the main objective of this application. As already mentioned above, the emission of short-range radiation such as electrons or α-particles is therefore essential. However, for monitoring issues therapeutically used radioisotopes may also emit detectable γ radiation. Such a currently commonly used RNT agent is the beta emitter ^{177}Lu.
The medical in-vivo use of radioisotopes, whether for diagnostic or therapeutic purposes is however very diversified and depending on various parameters regarding the patient, the type of cancer etc. Some in-vivo radioisotope applications highlight an organ's malfunction which develops the tendency of an either increased or decreased uptake of a certain isotope. Other cancer cells over express certain receptors with regard to normal cells.
In so called "targeted systemic therapies" the radioisotope is therefore coupled to a bioconjugate. Based on the nature of the bioconjugate these therapies refer to *radioimmunotherapy (RIT)* when antibodies are used as bioconjugate or *peptide receptor radio therapy (PRRT)* when peptides are used. A RIT bioconjugation binds to its corresponding antigen and a PRRT bioconjugation to its corresponding peptide receptor, respectively (cf. figure 9.2). A crucial aspect for the choice of a suitable radioisotope for in-vivo procedures is the actual half-life of the radioisotope. On one hand, the lifetime has to be long enough to ensure sufficient time for the production of the radioisotope, i.e. the activation of the radioisotope, the shipping to the hospital, the process of conjugation and the actual time for efficiently "working" in the patients body. On the other hand, radioisotopes whose half-life is too long might cause serious damage to the patients body. The typical half-live for in-vivo used radioisotopes for targeted systems is of the order of a few days.

9.1.2 ^{195m}Pt for Medical Use

The platinum isotope ^{195}Pt is an interesting candidate for the use in nuclear medicine. Its $13/2^+$ high spin isomeric state ^{195m}Pt combines some unique properties which can be used for both, diagnostic and therapeutic purposes. The half-life is 4.01 days which makes it suitable for in-vivo use. The energy of this state is at 259 keV from where it depopulates via the emission of conversion electrons and low energy γ transitions into the ground state of ^{195}Pt.
With special regard to figure 9.3 which is representing the isomeric level scheme of ^{195m}Pt, the deexitation process from the $13/2^+$ isomer into the

$1/2^-$ ground state is predominantly passing via two other states, the $5/2^-$ state at 129.8 keV and the $3/2^-$ state at 98.9 keV involving four γ transitions, 129.5 keV, 30.9 keV, 129.7 keV and 98.9 keV as shown in figure 9.3. Originating from $13/2^+$, ^{195m}Pt decays with a relative intensity of almost 100% directly into the $5/2^-$ state at 129.8 keV. However, the involved 129.5 keV transition of mulipolarity M4 has a very low transition probability which is the actual reason for the spin-isomeric character of the $13/2^+$ state. Subsequently only a very small portion of the $(13/2^+)\rightarrow(5/2^-)$ decay is releasing its energy via γ emission (less than 1%). The main part is released via internal conversion, thus the emission of conversion electrons and as a results also the emission of corresponding X-rays and Auger electrons. From there the $5/2^-$ state either decays directly into the ground state (8%), or with a transition probability of 92% via a 30.9 keV-98.9 keV two-step cascade. With regard to the γ and X-ray emission the overall relative intensities are to 98.9 keV (11.7%), 129.7 keV (2.8%) and $K_\alpha + K_\beta$ (87.2%). A complete list is summarized in table 9.1.

Table 9.1: Isomeric transitions of ^{195m}Pt taken from [106]. The intensity is indicated as relative γ intensity.

Nature	$\mathbf{E_{transition}}$ **[keV]**	**Intensity [%]**
$\gamma_{(5/2^-\rightarrow3/2^-)}$	30.9	2.4
K_{α_2}	65.1	21.9
K_{α_1}	66.8	37.2
K_{β_3}	75.4	4.4
K_{β_1}	75.7	8.6
K_{β_2}	77.8	3.1
$\gamma_{(3/2^-\rightarrow1/2^-)}$	98.9	11.7
$\gamma_{(13/2^+\rightarrow5/2^-)}$	129.5	0.09
$\gamma_{(5/2^-\rightarrow1/2^-)}$	129.7	2.9

Overall, ^{195m}Pt emits 29 conversion and Auger electrons per decay on average [107, 108] which is more than any other radioisotope presently con-

sidered for such application. Additionally, low γ and X-ray transitions can be used in diagnostics for imaging with SPECT or gamma cameras.
Moreover, in chemotherapy platinum compounds such as cisplatin or carboplatin play an important role because of their cytotoxic effect on cancer cells. Therefore, by linking the ^{195m}Pt isomer to a cytotoxic platinum complex, it could also be used for a combined chemo-radionuclide therapy. Since not every patient responds to such a chemotherapy this could additionally provide a useful tool to test a patients uptake on chemotherapeutics before the actual treatment is performed.

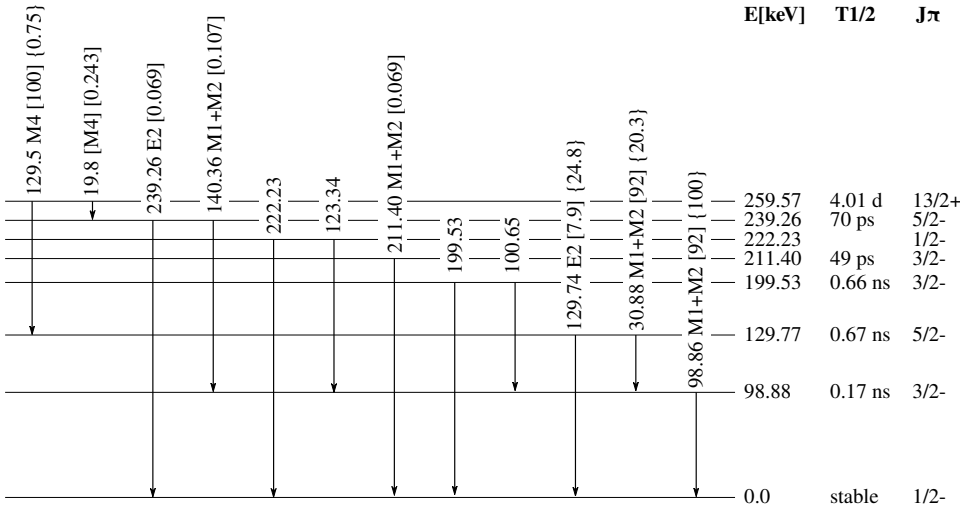

Figure 9.3: Level scheme of ^{195m}Pt. The values given in square brackets indicate the relative combined γ and internal conversion intensity normalized to the 129.5 keV $(13/2^+)\rightarrow(5/2^-)$ transition. The values in curved brackets are indicating the relative γ intensity normalized to the 98.86 keV transition (from [109]).

9.1.3 Production Routes

The above discussion for the use of radioisotopes in nuclear medicine was bypassing an important aspect so far: the actual production of radioisotopes. Today most of the available radioisotopes are produced in nuclear reactors and medical cyclotrons. Depending on the medical purpose (e.g. SPECT imaging) neutron-rich radioisotopes are generally produced via neutron capture in nuclear reactors, whereas neutron deficient radioisotopes used e.g.

for PET imaging, tend to be most easily produced in proton accelerators. In the case of the 6 hours ^{99m}Tc radioisotope the main production route goes via the indirect production of its 66 hours parent nuclide ^{99}Mo in nuclear reactors followed by a local extraction in so called technetium-99m generators.

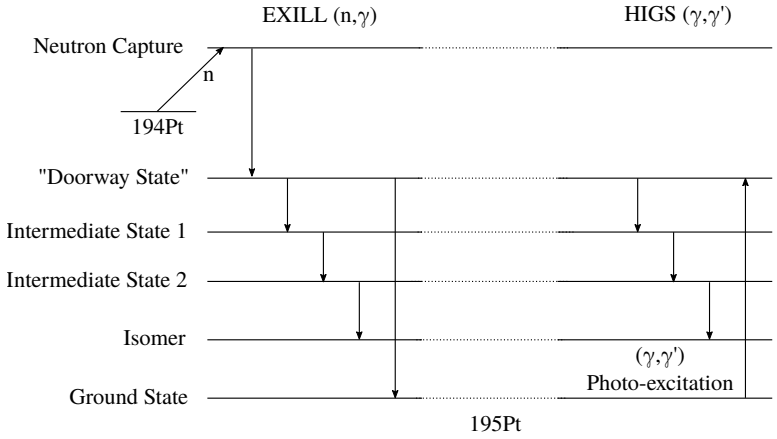

Figure 9.4: Schematic illustration of the basic idea behind the two experiments. Left: The EXILL experiment. From neutron capture on ^{194}Pt the excited neutron capture state is populated from where ^{195}Pt is decays through other states into the ground state. Probably a doorway state is populated which decays via intermediate states into the isomer and at the same time directly into the ground state. Right: The HIGS experiment. The activation of the isomer may be initiated with the population of higher lying doorway states via (γ, γ') photo-excitation from the ground state of ^{195}Pt.

For ^{195m}Pt it was already shown that the neutron capture reaction ^{194}Pt(n, γ)^{195}Pt leads to the population of the $13/2^+$ isomer ^{195m}Pt. However, the specific activity is far too low for its immediate use in medical applications. Other production routes which lead to a high specific activation of this isomer have to be found in order to make ^{195m}Pt a suitable medical radioisotope for in-vivo applications. A possibly elegant method which was proposed by D. Habs *et al.* [110] suggests a direct activation via (γ,γ') photo-excitation from the ground state with Compton backscattered laser light. Hence, the ^{195}Pt compound in its ground state is irradiated with a narrow-band γ beam of a given energy in order to excite a specific state - in the following called doorway state - which 1) decays directly into the

ground state of ^{195}Pt and 2) decays into the isomer (possibly via multiple γ deexcitations). This method however requires a ground state - doorway state linkage which wasn't observed yet for ^{195}Pt. A possible way for the observation of such a linkage is via a coincidence analysis of the neutron capture reaction $^{194}\mathrm{Pt}(\mathrm{n},\gamma)^{195}\mathrm{Pt}$ which deexcites from the high lying neutron capture state via the isomeric state into the ground state of ^{195}Pt. An illustration of both production routes is schematically presented in figure 9.4. Both experiments were performed within the scope of this thesis. A more detailed description of the experimental techniques and the analysis methods is given in the following chapter.

Chapter 10

Applied Experimental Methods

This chapter is subdivided into two parts. The first part reports on the neutron capture experiment with EXILL. The second part refers to the photo-excitation experiment with HIGS and the experimental procedures which were carried out for the production of the isomer ^{195m}Pt.

10.1 The EXILL Experiment

The neutron capture experiment using the reaction $^{194}\mathrm{Pt}(\mathrm{n},\gamma)^{195}\mathrm{Pt}$ was performed within the neutron capture sub-campaign of the EXILL experiment. Accordingly, the following discussion regarding the experimental setup, the data acquisition etc. is directly referring to the corresponding sections in the first part of this thesis (see sections 2.1.1 and 2.1.2). However, from the experimental as well as from the analysis point of view neutron capture reactions provide some specific characteristics which are presented in the following section and adapted to the discussion of ^{195}Pt.

10.1.1 Neutron Capture

According to reaction (10.1), neutron capture describes the process of a nucleus with the mass A absorbing a neutron n and thus forming an excited nucleus of the mass A+1

$$ {}^{\mathrm{A}}_{\mathrm{Z}}\mathrm{X}_{\mathrm{N}} + \mathrm{n} \rightarrow {}^{\mathrm{A+1}}_{\mathrm{Z}}\mathrm{X}^{*}_{\mathrm{N+1}}. \tag{10.1} $$

Since a neutron has no electric charge it can easily approach the nucleus. Therefore, at low energies the neutron capture cross section, i.e. the capture probability driven by the nuclear force becomes larger with the time the neutron spends in the vicinity of the nucleus. In this low-energy range the capture cross section is inversely proportional to the velocity of the neutron (1/v dependence) which is thus implying a higher neutron cross section for lower neutron energies[1].
Energetically this process is generally possible for all nuclei for which the sum of the total nuclear binding energy and the kinetic energy of the free neutron is still smaller than the binding energy B of the formed A+1 nucleus[2]

$$\mathrm{B(N,Z)} + \mathrm{E_n} < \mathrm{B(N+1,Z)}. \tag{10.2}$$

In other words, the excitation energy $\mathrm{E_x}$ of the A+1 nucleus is given by the sum of its neutron separation energy $\mathrm{S_n}$ and the kinetic energy of the neutron $\mathrm{E_n}$. Typically, $\mathrm{S_n}$ is of the order of 5-10 MeV. Thus, for thermal neutrons (25 meV) or even cold neutrons the energy of the neutron capture state is completely defined by the neutron separation energy $\mathrm{S_n}$.
However, from the nuclear structure point of view neutron capture becomes impossible when violating the selection rules. This becomes especially evident with regard to the conservation of angular momentum. Considering I to be the spin of the ground state of the A nucleus, or target nucleus respectively, and I′ to be the spin of the neutron capture state of the A+1 nucleus, then I′ is given by equation (10.3) where l is the angular momentum of the neutron and s is the spin of the neutron, with the relation for the corresponding parities presented in equation (10.4)

$$\mathrm{I'} = \mathrm{I} + \mathrm{l} + \mathrm{s}, \tag{10.3}$$

$$\pi' = \pi(-1)^{\mathrm{l}}. \tag{10.4}$$

At low energy however, neutrons carry to first order no angular momentum l but only a spin s which is either $\frac{1}{2}$ or $-\frac{1}{2}$, leading to a capture process which is known as s-wave neutron capture. Thus, for a given spin I of the

[1] Usually the neutron cross section (if not indicated otherwise) is given for thermal neutrons of 25 meV.

[2] In its limiting case where B(N,Z) = B(N+1,Z) (more accurate B(N,Z) = B(N-1,Z)) the neutron drip line is defined

target nucleus the spin I′ of the capturing state of the A+1 nucleus is already restricted to be $I' = I \pm \frac{1}{2}$. This restriction provides a useful input for the determination of the spin of the neutron capture state as shown below for ^{195}Pt.

Neutron Capture on ^{194}Pt

With respect to the objective of this work introduced in section 9.1.3 the production of the $13/2^+$ high spin isomer in ^{195}Pt is achieved via neutron capture on ^{194}Pt. In its ground state ^{194}Pt has a spin of 0^+. Applying eq. (10.3) and eq. (10.4) it follows immediately that the neutron capture state of ^{195}Pt has a spin of $1/2^+$. The energy of this state was determined earlier to 6105 keV [111, 112]. Principally, originating from this highly excited state, any other state can be accessed through the deexcitation process, only limited by the selection rules.

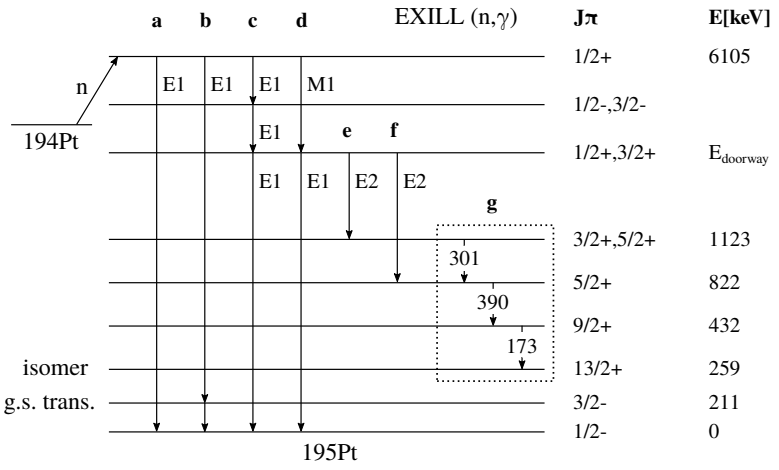

Figure 10.1: Schematic representation of expected γ transitions in ^{195}Pt excited via neutron capture. a) Direct E1 transition from the n.c.s. to the g.s., b) E1 transition into states of g.s. bands (e.g. into the $3/2^-$ state at 211 keV), c) E1 transition from the n.c.s. into a $1/2^-$ or $3/2^-$ state, and a subsequent E1 transition into a $1/2^+$ or $3/2^+$ doorway state, d) Direct M1 transition from the n.c.s. into a $1/2^+$ or $3/2^+$ doorway state, e,f) E2 transitions into $3/2^+$ or $5/2^+$ states of the "Warner cascade" g) The "Warner cascade". Other deexcitation paths are possible.

However, electric dipole radiation E1 is highly favored and the first γ decay, often referred to as *primary transition*, is most preferentially decay-

ing into $1/2^-$ states of ^{195}Pt. Considering a higher level density at higher energies and with regard to the E_γ^3 dependence for the energy of electric dipole radiation this process tends to maximize its energy, thus predominately decaying into the lowest of such $1/2^-$ states. Therefore (n,γ) primary transitions are usually of high energy[3].

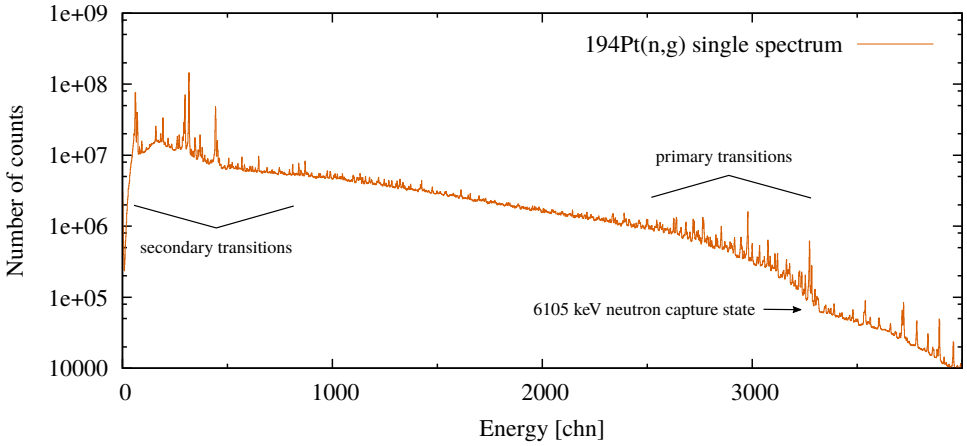

Figure 10.2: Full energy range single spectrum for the ^{194}Pt(n,γ) reaction as measured with EXILL in a logarithmic representation. One can clearly see the pronounced primary transitions depopulating the neutron capture state as well as the secondary transitions in the low energy range. Note the abrupt decrease in count rate after the 6.1 MeV neutron capture state.

The subsequent decays are often denoted as *secondary transitions*, regardless of their position within the cascade. Since the excitation energy of the nucleus for those transitions is much lower they are thus more governed by the actual nuclear structure properties at lower level density. This applies especially to the population of the $13/2^+$ high spin isomer in ^{195}Pt. As mentioned above it was already shown that the ^{194}Pt(n,γ) reaction leads to the population the ^{195m}Pt isomer [113] which is not necessarily obvious considering the change in spin from $1/2^+$ for the neutron capture state to the $13/2^+$ of the isomer. However, in 1982 D. Warner *et al.* observed a strong cascade of an isolated set of three transitions as the only isomer feeding path via neutron capture (see figure 10.1g) following the inverted spin sequence $(3/2^+,5/2^+)\rightarrow(5/2^+)\rightarrow(9/2^+)\rightarrow(13/2^+)$ which is thus suggesting a possible linkage with the $1/2^+$ neutron capture state via E2 transitions

[3] usually 3-10 MeV depending on the neutron separation energy

when coupled to a $1/2^+$ or a $3/2^+$ state. For the reason of better comprehensibility a selection of potential deexcitation paths is presented in figure 10.1. The cumulative spectrum of all transitions originating from the ^{195}Pt neutron capture state is shown in figure 10.2.

Experimental Conditions

The ^{194}Pt(n, γ) experiment was the first experiment of the EXILL campaign performed in October/November 2012. Within a total beam time of about 71 hours ($\approx$ 3 days) three different target configurations for ^{194}Pt were measured including two solid, heavier targets for the purpose of an optimized γ count rate, and a fine powder target to correct for self-attenuation effects. A compilation of these targets is listed in table 10.1. The latter is especially important with respect to the correction of low energy γ transitions of the Warner cascade.

Table 10.1: Target configuration for the different subsets of the ^{194}Pt(n, γ) experiment (upper part), and the different target compositions (lower part).

target	**measuring time [h]**	**file size [GB]**
GSI	15	65
GSI+LMU	12	58
GSI+LMU+TU	40	210
TU	4	some MB

target	**mass [mg]**	**composition Pt [%] (194, 195, 196, others)**
^{194}Pt bullets (LMU)[1]	140	95.95, 3.34, 0.64, 0.07
^{194}Pt foil (GSI)[2]	200	96.45, 2.46, 0.87, 0.22
^{194}Pt powder (TU)[3]	70	95.54, 3.23, 0.96. 0.27

[1] Provided by Ludwig-Maximilians-Universität München.
[2] Provided by Gesellschaft für Schwerionenforschung.
[3] Provided by Technische Universität München.

Under experimental conditions all targets were packed into teflon bags. Neutron capture on these bags does not significantly contribute due to its low cross section. These bags were installed in the center position of the EXILL array (see also section 2.1.2). However, with regard to the target composition and the involved neutron cross sections, the presence of γ transitions other than from ^{195}Pt are expected. ^{194}Pt has a combined thermal neutron cross section of 1.2 b (1.1 b leading to the production of ^{195g}Pt in its ground state, and $\leq$0.1 b into the metastable isomer ^{195m}Pt) and ^{195}Pt has a thermal neutron cross section of 28 b [114]. Exemplary for the GSI+LMU+TU main data set the effective capture rate for this target configuration[4] calculates to $N_{\mathrm{capt.},^{194}\mathrm{Pt}\rightarrow^{195g}\mathrm{Pt}} = 1.3 \cdot 10^5$ for the production of the ground state of ^{195}Pt, $N_{\mathrm{capt.},^{195}\mathrm{Pt}\rightarrow^{196}\mathrm{Pt}} = 1.0 \cdot 10^5$ for the production of ^{196}Pt and $N_{\mathrm{capt.},^{194}\mathrm{Pt}\rightarrow^{195m}\mathrm{Pt}} < 1.2 \cdot 10^4$ for the production of the isomeric state in ^{195}Pt. This implies an expected relative ^{195g}Pt production of 54% while 41% lead to the transmutation into ^{196}Pt and $<$ 5% to the production of the isomeric state ^{195m}Pt. With an effective production of 0.04% ^{197}Pt is negligible.

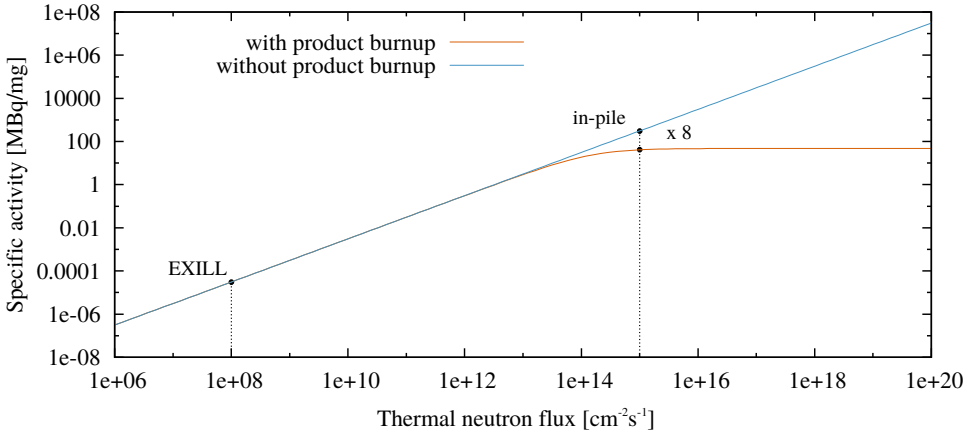

Figure 10.3: Calculation of the specific activity for the production of ^{195m}Pt in neutron capture as a function of the neutron flux and the effect of product burn-up.

It is also interesting to mention that the thermal neutron capture cross section of the isomeric state is of 13000 b often referred to as burn-up cross section [115]. Principally, this could seriously affect the overall production

[4]Note that it differs only marginal from the other configurations.

of ^{195m}Pt when capturing an additional neutron. For a high neutron flux this would lead to a saturation of the specific activity in which the product burn-up is in equilibrium with the the decay half-life. For the production in a high flux reactor at a neutron flux of about $10^{15}\,\mathrm{cm}^{-2}\mathrm{s}^{-1}$ this would already lower the specific activity by a factor of 8 with respect to a zero burn-up cross section[5]. Practically however, this effect is negligible for the used neutron flux of $10^{8}\,\mathrm{cm}^{-2}\mathrm{s}^{-1}$ as illustrated in figure 10.3.

10.1.2 Data Processing

The total amount of recorded raw data for the 3 days ^{194}Pt(n, γ) experiment is about 333 GB divided into subfiles (i.e. runs) of about 2 GB each. The data preprocessing was performed with the *Ana* code [116] and the *Soco V2* code [64]. All runs of each detector were gain matched and energy calibrated to internal transitions of the actual in-beam experiment.

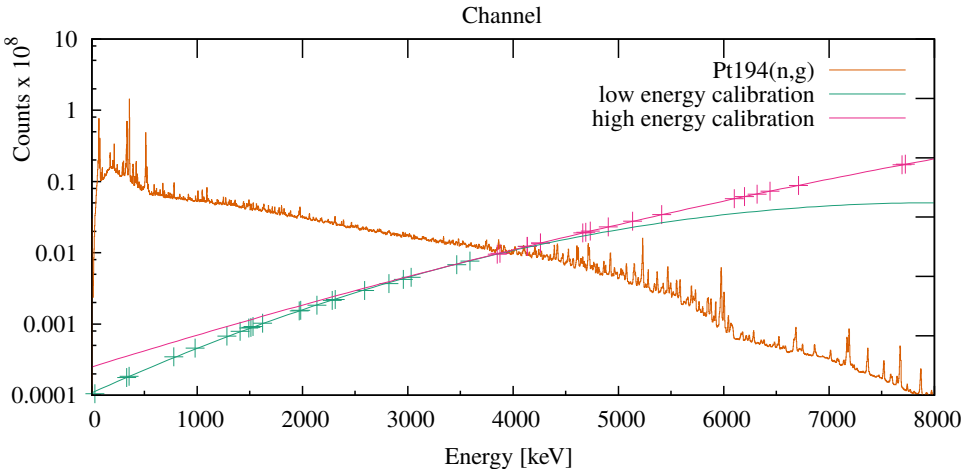

Figure 10.4: Energy calibration for the EXILL array using known internal transitions of ^{196}Pt and ^{28}Al. For the matter of precision two energy calibration were performed, one for the low energy range and one for the high energy range, respectively, in order to achieve a proper alignment of primary transitions.

Due to the large neutron capture cross section of ^{195}Pt it was therefore practical to use γ transitions which are produced via the deexcitation

[5] e.g. the in-pile neutron flux of the ILL reactor

of ^{196}Pt and which are well known throughout a large energy range[6]. Additionally, γ rays originating from the aluminum beam tube were used as calibration points. The overall energy calibration is shown in figure 10.4. With special regard to the assignment of high energy primary transitions there is a particular interest in a proper energy calibration in the high energy range up to 6.1 MeV. Therefore, the low and the high energy range was calibrated separately with two polynomials of second order.
For the coincidence analysis mainly two matrices were used. One γ-γ matrix with a coincidence window of 200 ns for the use of single gates, and a 3-dimensional γ-γ-γ matrix, i.e., cube, with a coincidence window of 400 ns for the analysis of triple γ events, i.e., double gates. Both matrices were corrected for Compton and add-back events (see also section 2.2).

[6] ^{196}Pt was well studied in neutron capture, thus providing γ transitions up to the neutron separation energy of 7.923 MeV.

10.2 The HIGS Experiment

The following section introduces the methods which were carried out for the photo-excitation of ^{195}Pt. In this frame the following section reports on the free electron laser facility HIGS and the method of Compton backscattering.

10.2.1 The HIGS Facility

The High Intensity Gamma-ray Source HIGS is a Free Electron Laser (FEL) based Compton backscattering γ-ray source. Operated by the Triangle Universities Nuclear Laboratory (TUNL) the corresponding HIGS facility is located on the campus of Duke university in Durham, North Carolina, USA. Historically, the use of such storage ring driven FEL for the production of γ radiation through Compton backscattering was proposed by Sandorfi *et al.* in 1983 as a next generation LEGS facility (Laser+Electron Gamma Source) [117].

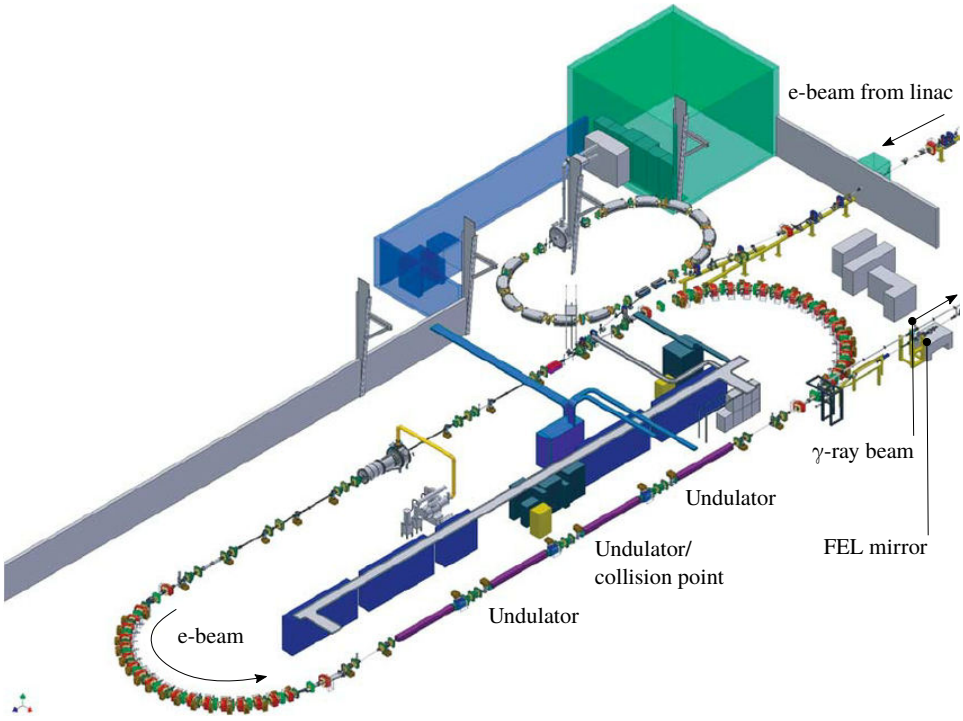

Figure 10.5: Schematic top view of the HIGS facility with the electron storage ring and the free electron laser unit (from [118]).

However, the idea for the production of γ beams via Compton scattering of laser light against high energy electrons was already pointed out by R. Milburn [119] and F.R. Arutyunian and V.A. Tumanian [120] in 1963. In both cases the main concept of these techniques is based on the Compton interaction of a photon with a relativistic electron. In a head-on collision with the electron (i.e. a relative angle of 180°) the (low energy) photon is being scattered in backward direction inside a narrow cone with increased energy [121–123]. A more detailed description is given in the next section.
At HIGS electrons are provided by a linear accelerator injecting electron bunches into a storage ring. In a complementary configuration the direct injection is bypassed and the electrons are being pre-accelerated in a first synchrotron, the booster injector, before injection into the storage ring. This allows for an injection energy range of about 200 MeV to 1.2 GeV.
Once injected into the storage ring, electrons are kept circulating on a 108 m path with two straight sections of about 35 m. The actual FEL is installed at one of these sections consisting of two electromagnetic undulators and a ≈ 54 m long optical cavity forming an optical klystron FEL (OK FEL). While passing through this section electrons are periodically, marginal deflected according to the adjusted frequency of the alternating magnets of the undulators. This acceleration forces the electrons to emit electromagnetic radiation, i.e. photons in forward direction with the electron beam, allowing photon energies of about roughly 1-10 eV. The resulting photons are subsequently captured in the optical cavity of a length equal to one half of the storage ring, i.e. ≈ 54 m. For the electrons which are nearly moving at the speed of light, this design accounts for a "natural" production of stimulated radiation when the electron bunch and the photons are traveling in the same direction which is thus amplifying the FEL's photon beam. The actual Compton backscattering process would not occur in this single electron bunch mode since electrons and photons always "meet" in forward moving direction. However, operating with two electron bunches separated by one half of the the storage ring circumference allows for head-on collisions of the second electron bunch with photons produced by the first electron bunch and being reflected by optical cavity mirrors. Thus, HIGS can produce γ-rays with about 2 to 100 MeV[7]. In the directional extension to the optical cavity a collimation system for the γ beam is installed, leading to the target and/or detection area. A schematic illustration of the HIGS facility is shown in figure 10.5.

[7]The optical cavity mirror is "transparent" for these energies.

10.2.2 Compton Backscattering

As introduced above, the creation of an intense high energetic photon beam at HIGS is based on two main principles:
The intensity amplification of low energetic photons by stimulated emission when electrons and photons are traveling in the same direction. And the amplification in energy in the Compton backscattering process when moving in opposite directions (see figures 10.6 and 10.7). The latter can be directly deduced from a relativistic representation of the Compton formula eq. (10.5):

$$\mathrm{E}'_\mathrm{p} = \mathrm{E}_\mathrm{p} \frac{1 - \beta \cos\Omega}{(1 - \beta \cos\Omega') + \frac{\mathrm{E}_\mathrm{p}}{\gamma \mathrm{m}_0 \mathrm{c}^2}(1 - \cos\phi)}, \tag{10.5}$$

with the energies E_p and E'_p of the photon before and after the scattering process, $\beta = \frac{\mathrm{v}}{\mathrm{c}}$ where v is the velocity of the electron and c the speed of light, the angle Ω and Ω' between photon and electron before and after scattering, the angle ϕ of the photon trajectory before and after scattering, the mass of an electron at rest m_0, and the Lorentz factor $\gamma = \frac{1}{\sqrt{1-\beta^2}}$. Note that in the rest system of the electron $\beta = 0$ and $\gamma = 1$ which leads to the classical Compton scattering representation (eq. (10.6)) and thus a loss of energy for the photon

$$\mathrm{E}'_\mathrm{p} = \frac{\mathrm{E}_\mathrm{p}}{1 + \frac{\mathrm{E}_\mathrm{p}}{\mathrm{m}_0 \mathrm{c}^2}(1 - \cos\phi)}. \tag{10.6}$$

According to eq. (10.5), and for an electron energy of 1 GeV (i.e. $\beta = 0.999999869$ and $\gamma = 1957$), and assuming an ideal scattering angle of $\Phi = 180°$ an incident photon of 8.2 eV results in a high energy photon of 112 MeV.

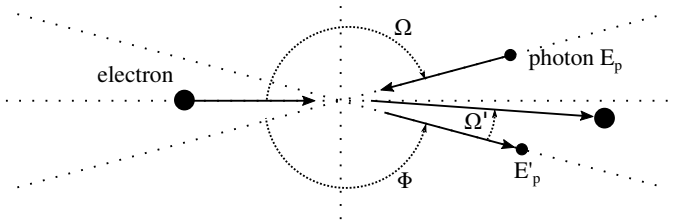

Figure 10.6: Diagram of the Compton scattering process according to eq. (10.5): Ω and Ω' are referring to the angle between electron an photon before and after scattering, respectively. Φ is the angle between the incoming and the outgoing photon. All angles are related to the relative movement of the corresponding particles. Note the particular relation under ideal Compton backscattering in one dimension. See text for further information.

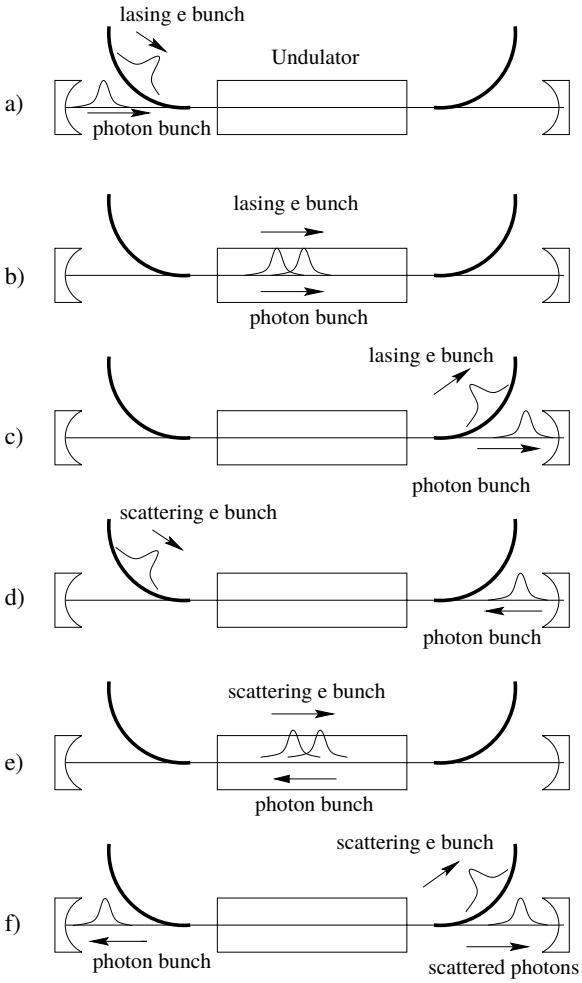

Figure 10.7: Schematic illustration of the intercavity FEL production and the Compton backscattering process (top view)(from [124] and [125]): a) The relativistic (lasing) electron bunch from the storage ring is entering the optical cavity section. The previously created low energy photon bunch reflected by the left mirror is entering the cavity at the same time. b) Electrons in the undulator amplify the photon pulse by stimulated emission. c) Electron bunch and amplified photon bunch leave the undulator section. d) Photon bunch reflects at the right mirror and reenters undulator. Second (scattering) electron bunch enters the undulator section with opposite direction to the photon bunch. e) Photon bunch and electron bunch collide in head-on Compton scattering and produce gamma rays. f) Gamma rays are being backscattered and leave the optical cavity.

10.2.3 Experimental Conditions

The activation experiment following the reaction $^{194}\mathrm{Pt}(\gamma,\gamma')^{195}\mathrm{Pt}$ was performed during 1 week in October 2016 at the HIGS facility in Durham, North Carolina, USA.
In the EXILL campaign several potential doorway states for the population of of $^{195\mathrm{m}}\mathrm{Pt}$ could be identified, which are described in detail in section 11.1.2. The aim of the HIGS measurement was to explore the possibility of a resonant production/population of these states with γ-ray beam. For this reason the HIGS beam was adjusted to these energies accordingly.
With regard to the possible doorway states observed in the (n,γ) EXILL experiment, the HIGS γ beam was set to these energies accordingly. In activation runs between 3 and 18 hours natural platinum foils[8] in stacks of 4-5 round foils (22 mm in diameter, 0.05 mm thickness, 99.99% purity) were irradiated. In order to monitor the photon flux a scintillating detector[9] was installed in upstream direction before the target position. Its calibration was performed towards a NaI detector for each energy during a given time interval in supplementary measurements without targets.
An additional HPGe detector which was installed under 0° with respect to the strongly attenuated γ beam, downstream of the target, was used for the determination of the energy distribution of the γ beam.

[8] i.e. 33% ^{194}Pt, 34% ^{195}Pt, 25% ^{196}Pt, 7% ^{198}Pt.
[9] often denoted as the photon flux paddle.

Chapter 11

Results

This chapter reports on the results of the experiments carried out for the production of the isomer ^{195m}Pt. Therefore, the first part of this chapter is dedicated to the neutron capture experiment at EXILL and the search for suitable doorway states and the second part to their selective activation via photoexcitation with HIGS.

11.1 ^{194}Pt(n,γ) with EXILL

Following the discussion about target impurities and neutron cross sections introduced in section 10.1 the ^{194}Pt(n,γ) reaction has rather to be considered as $^{194/195}$Pt(n,γ) reactions with transmutation probabilities as indicated in eq. (11.1)

$$\begin{aligned} ^{194}\mathrm{Pt} + \mathrm{n} &\rightarrow {}^{195g}\mathrm{Pt} \quad (54\%), \\ ^{194}\mathrm{Pt} + \mathrm{n} &\rightarrow {}^{195m}\mathrm{Pt} \quad (< 5\%), \\ ^{195}\mathrm{Pt} + \mathrm{n} &\rightarrow {}^{196}\mathrm{Pt} \quad (41\%). \end{aligned} \tag{11.1}$$

With regard to figure 11.1 the single spectrum of these reactions is showing the expected results: the strong 333 keV and 356 keV transitions from ^{196}Pt are dominating the low energy range of the spectrum while the ^{195}Pt assigned transitions appear to be less well pronounced. The indicated 173 keV transition and the 390 keV transition of the Warner cascade will be subject of the following discussion about the isomer populating transitions.

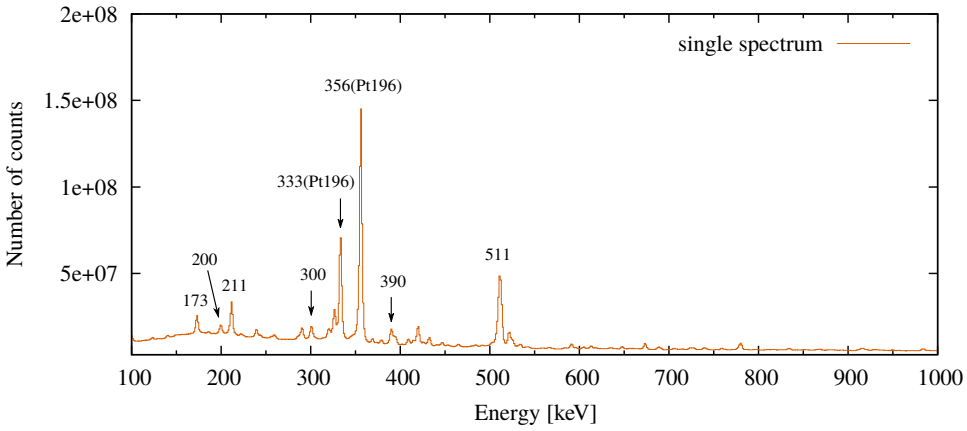

Figure 11.1: Single spectrum of the low energy range for the neutron capture reaction on a highly enriched ^{194}Pt target, detected with the EXILL array. The isomer feeding transitions of the Warner cascade are indicated (i.e. 173, 390 and 300 keV), as well a the strong ground state band transitions 200 keV and 211 keV. The presence of γ transitions from ^{196}Pt comes from the residual target contamination of ^{195}Pt with a high neutron cross section.

11.1.1 Isomer Populating Transitions

As of today four states are known which directly populate the high spin isomer of ^{195}Pt: The $9/2^+$ state at 432 keV, the $(11/2^+)$ state at 547 keV, the $(17/2^+)$ state at 628 keV and the $(15/2^+)$ state at 758 keV [126, 127]. The latter two states were observed in 2011 via the ^{192}Os(^{7}Li, p3nγ) reaction but could not be identified within this work. It was neither possible to observe the assigned γ transitions connected with the $(11/2^+)$ state at 547 keV. The $9/2^+$ state at 432 keV however, was, as mentioned earlier, already observed by D. Warner *et al.* [111] as a constituent of a strong isolated set of three transitions (i.e 173, 390 and 301 keV) as the only isomer feeding transitions for ^{195}Pt in neutron capture on ^{194}Pt. Thus, since the observation of γ transitions above the isomer using common coincidence techniques with transitions depopulating the isomer is highly unfeasible due to the 4 days lifetime, this 173 keV transition was the starting point for the investigation of isomer populating transitions within this work. A single gated coincidence spectrum for this transition is shown in figure 11.2.

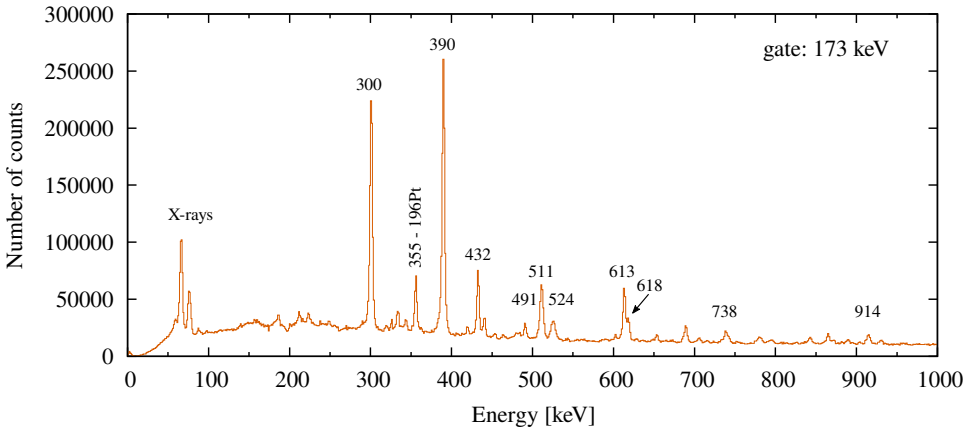

Figure 11.2: Single coincidence spectrum of the 173 keV transition. See text for further explanations.

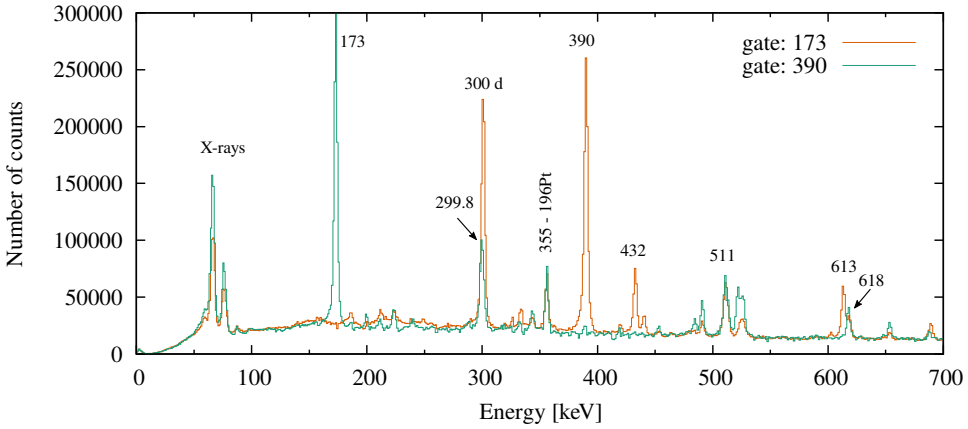

Figure 11.3: Comparison of coincidence spectra with gates on 173 keV and 390 keV in the low energy range. The 432 keV transition appears to be coincident with the 173 keV peak but not with 390 keV. Note also that the 300 keV transitions are not aligned, indicating a doublet (d) at 300 keV. See text for further information.

With regard to D. Warner *et al.* [111] and figure 11.2 the 300 keV and the 390 keV transitions appear to be in strong coincidence with 173 keV. Additionally, other higher lying peaks in the low energy region up to 1 MeV could be observed which are indicated in figure 11.2. However, as can be deduced from the remaining presence of the 355 keV $(2^+)\rightarrow(0^+)$ transition

from ^{196}Pt as random coincidence peak, these transitions have to undergo further analysis. With the second constituent of the Warner cascade, a gate was set on the 390 keV transition (cf. figure 11.3). In comparison one can already conclude that certain transitions like the 618 keV transition which is in coincidence with both has to feed the $5/2^+$ state at 822 keV from which the 390 keV is depopulating from above. It is also interesting to mention that the 432 keV peak appears in the coincidence spectrum of 173 keV but not in coincidence with 390 keV. In fact, D. Warner *et al.* already observed this strong 432 keV transition in coincidence with 173 keV but were not able to place it within the level scheme, and thus assuming that it has to feed the Warner cascade from above[1].

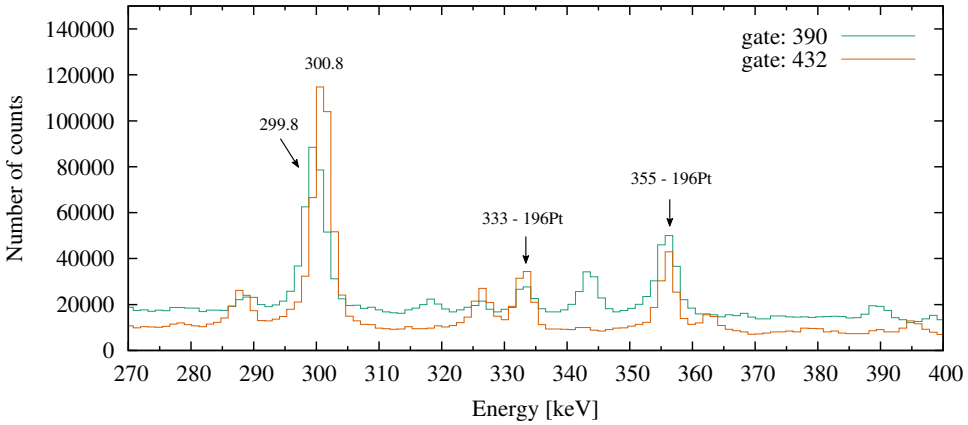

Figure 11.4: Comparison of coincidence spectra with gates on 390 keV and 432 keV in the low energy range. The 300 keV doublet appears as two transitions: A 299.8 keV peak in coincidence with 432 keV and a 300.8 keV peak which is in coincidence with the 390 keV transition. For verification note also the good alignment of the 333 keV and the 355 keV peaks from ^{196}Pt.

It is also remarkable that the 300 keV peaks in fig. 11.3 seem not to be aligned in energy with regard to the chosen gate. In a further coincidence analysis with single gates set on 390 keV and 432 keV, respectively, presented in figure 11.4, this effect became even more pronounced, leading to the conclusion that the 300 keV peak is a doublet of a 299.8 keV and a 300.8 keV

[1] "The 432 keV coincident transition cannot be placed in the scheme [...] but presumably feeds the cascade from above" [111]p.26.

transition. With special regard to the well aligned ^{196}Pt transitions a systematic error could be excluded. Morever, an additional double coincidence gate involving the 173 keV and the 432 keV transition gives rise to the assumption that the actual Warner cascade splits up above the 173 keV state into two different branches. With regard to fig. 11.5 this particular set of gates seems to be only in coincidence with the 300.8 keV transition in the low energy range.

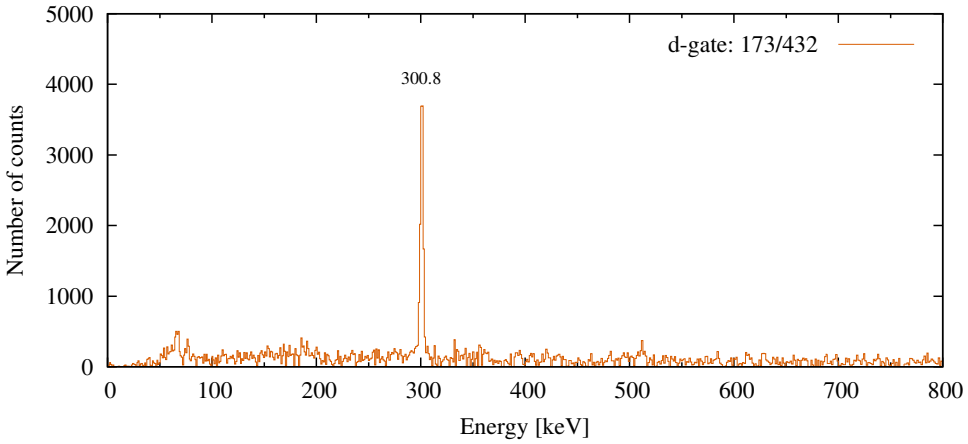

Figure 11.5: Double coincidence spectrum of the 173 keV transition and the 432 keV, transition showing only the clean,intense 300.8 keV peak in the low energy range.

On the other hand, by setting a double coincidence on the 173 keV and the 390 keV transition the previous 300.8 keV seems not to be in coincidence anymore. Instead the 299.8 keV transition from the Warner cascade appears (cf. fig. 11.6), but in comparison with fig. 11.6 at much lower intensity. Moreover, the double gated 173/390 keV spectrum is much more fragmented implying that the 822 keV state is populated by more transitions than the previously reported 299.8 keV. A more detailed analysis of these above feeding transitions is given in the following section.

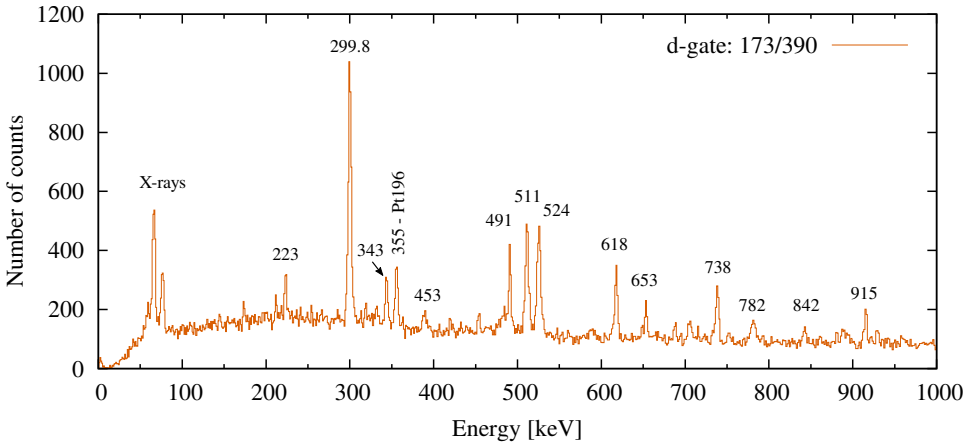

Figure 11.6: Double coincidence spectrum of the the 173 keV and the 390 keV transition as the lower two transitions of the Warner cascade.

11.1.2 Doorway States

The search for doorway states was initiated with a coincidence analysis of high energy primary transitions. The high energy region of the spectrum was thus systematically "scanned" by gating on present transitions. The resulting coincidence spectra were subsequently analyzed for transitions which populate a state which is connected with the isomer (see above) or which sum up to the energy corresponding to such a state accordingly. As a result no other transition than the already established 173 keV transition could be found that directly populates the isomer. This implies that each primary transition which leads to the population of the isomeric state has to be in coincidence with 173 keV. Thus, by gating on 173 keV, all of those primary transitions should be observable in principle. A spectrum of the high energy range of such a coincidence analysis is shown in figure 11.7. A double coincidence analysis with 173 keV and the respective primary transition was then carried out to assign the intermediate transitions, i.e. those transitions which depopulate the doorway state and which subsequently decay into the isomer.

Representative for the identified states, a coincidence analysis for the 2352 keV state is illustrated in figure 11.8. This state is directly populated by a primary transition of 3553 keV (see also figure 11.7). By gating on this primary transition all directly depopulating and consecutive transitions are visible in coincidence. As shown in the upper panel of figure 11.8 the direct ground state transition of 2352 keV is clearly visible. However, by studying the

higher energy range of this spectrum one can see that this state predominantly decays via states which are assigned to the ground state such as 200, 211, 420 keV etc. The only transition which could be found to have an isomer linkage was the 1187 keV transition which is decaying into the 1165 keV state. This linkage could be verified within a double coincidence analysis of the primary transition and the consecutive 1187 keV transition as shown in the lower panel of figure 11.8. The resulting spectrum shows the three strong transitions of the modified "Warner cascade", 433, 301, and 173 keV originating from the 1165 keV state.
A proposed level scheme for the isomer related transitions as well as the associated table are presented in figure 11.9 and table 11.1, respectively. It should be mentioned, however, that a proper assignment of the direct ground state transitions originating from the respective doorway states could not be done in a distinct way for all identified states. The ground state transitions are therefore not listed in table 11.1 and denoted with dashed lines in the level scheme in figure 11.9.

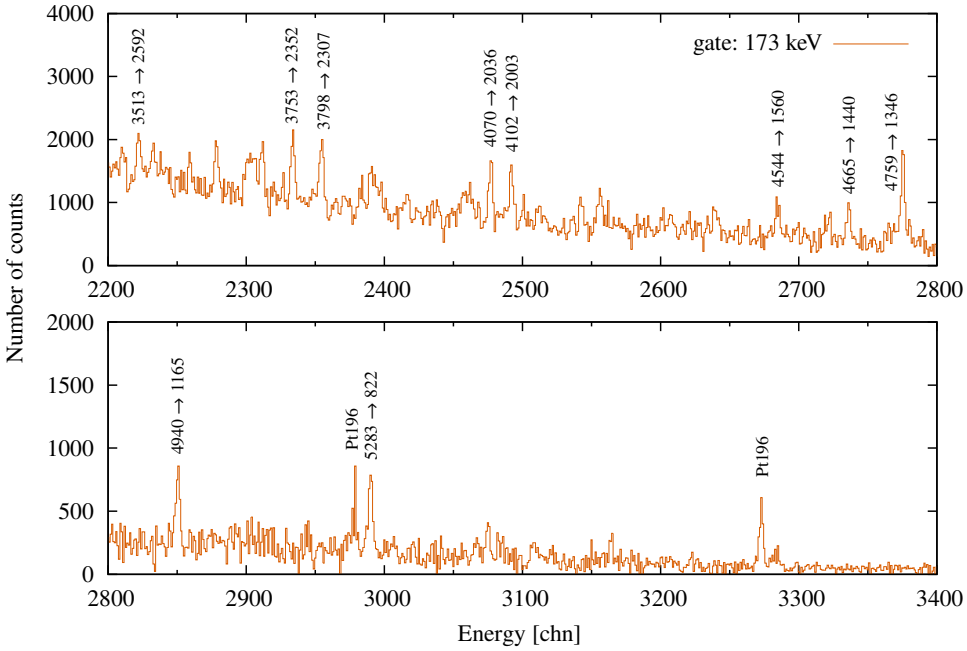

Figure 11.7: Coincidence spectrum gated on the 173 keV transition showing primary transitions and the state they are decaying to denoted as (primary)→(state).

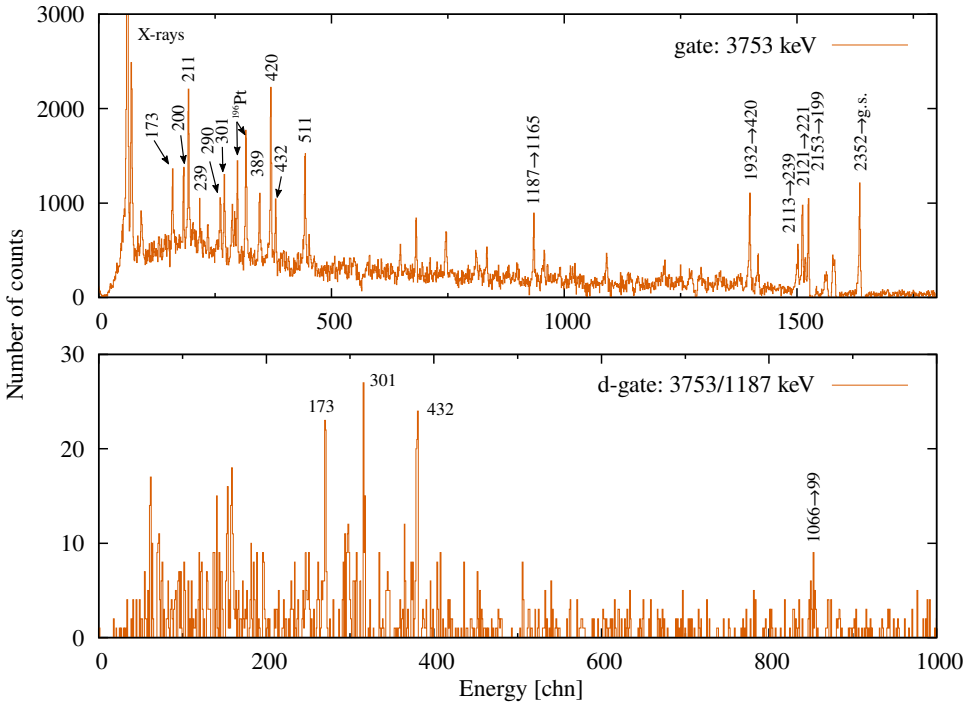

Figure 11.8: Coincidence spectra of the 2352 keV state. Upper panel: Single gated on the primary transition of 3753 keV. The peaks in the spectrum are denoted by their energy and the state they decay to according to (transition)→(state). Lower panel. Double coincidence spectrum of the 3753 keV and the 1187 keV transition showing the strong transitions of the modified Warner cascade.

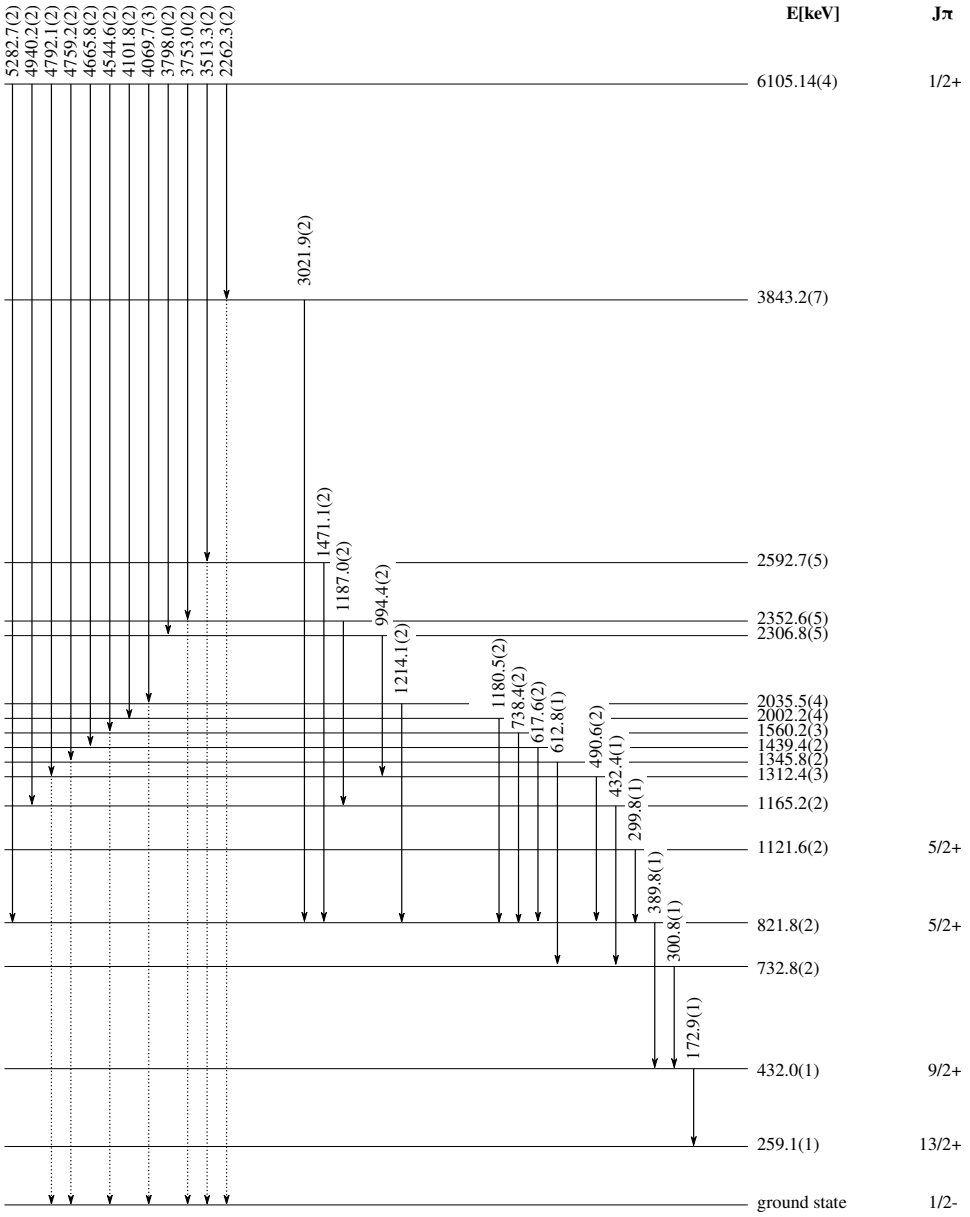

Figure 11.9: Proposed level scheme of isomer feeding transitions in ^{195}Pt populated in cold neutron capture on ^{194}Pt.

Table 11.1: Table of proposed isomer related states in ^{195}Pt populated in cold neutron capture on ^{194}Pt.

$\mathbf{E_{level}}$	$\mathbf{J_\Pi}^\dagger$	$\mathbf{E_\gamma}$	**Final level**	
keV		**keV**	**keV**	$\mathbf{J_\Pi}^\dagger$
432.0(1)	9/2+	172.9(1)	259.9(1)	13/2+
732.8(2)		300.8(1)	432.0(1)	9/2+
821.8(6)	5/2+	389.8(1)	432.0(1)	9/2+
1121.6(2)	5/2+	299.8(1)	821.8(2)	5/2+
1165.2(2)		432.4(1)	732.8(2)	
1312.4(3)		490.6(2)	821.8(2)	5/2+
1345.8(2)		612.8(1)	732.8(2)	
1439.4(2)		617.6(2)	821.8(2)	5/2+
1560.2(3)		738.4(2)	821.8(2)	5/2+
2002.2(4)		1180.5(2)	821.8(2)	5/2+
2035.5(4)		1214.1(2)	821.8(6)	5/2+
2306.8(5)		994.4(2)	1312.4(3)	
2352.6(8)		1187.0(2)	1165.2(2)	
2592.7(5)		1471.1(2)	821.8(2)	
3843.2(7)		3021.9(2)	821.8(2)	

† Spin and parity assignment is taken from [128]

11.2 ^{195}Pt(γ,γ') with HIGS

Regarding the experimental results of the proposed doorway states presented in the first part of this chapter the HIGS experiment was performed in order to specifically populate these states via photoexcitation. Such an experiment is mainly subdivided into two parts: the activation process of the ^{195}Pt samples and the subsequent activity measurement. Accordingly, the first part of this section reports on the activation process and the second part on the measurement of the platinum samples at Ge-detectors.

11.2.1 Irradiation Process

Following the experimental methods introduced in chapter 10.2 stacks of 4 platinum foils were irradiated in a γ-beam collimated to 1 inch (25.4 mm) with different energies. However, the production of a such a γ-beam at HIGS via Compton backscattering leads to an energy spread which is in first order depending on the collimation width and the resulting energy, i.e. the higher the energy the larger is the energy spread. This affects especially the low energy side of the beam's energy distribution which develops a pronounced tail with increasing energy. In order to perform a calculation of the γ-density for a given energy the beam energy distribution has to be determined. Experimentally, this was done by measuring the backscattered γ-beam under 0° with respect to the beam axis in a germanium detector.

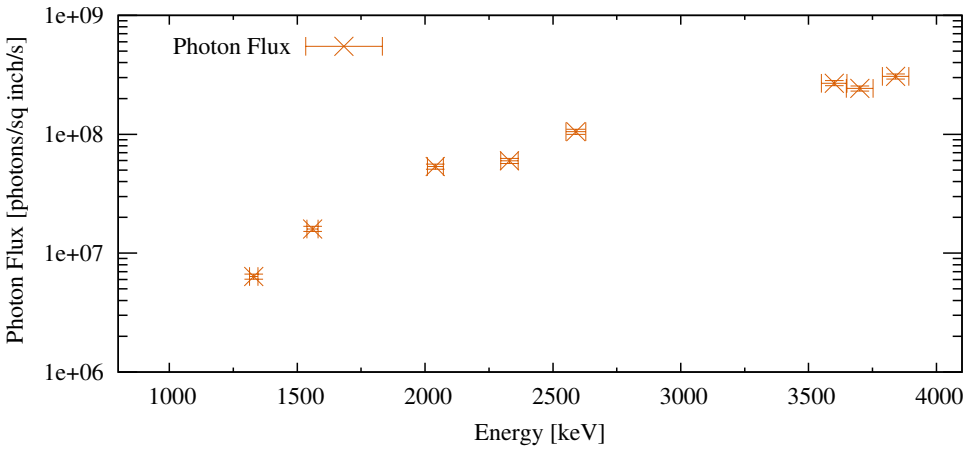

Figure 11.10: γ-flux in photons per seconds as a function of energy for the measured energies. See text for further information.

For γ energies up to 2 MeV the energy spread had only a minor effect on the profile and an almost Gaussian energy distribution was observed. However, for higher beam energies the effect of Compton scattering within the Ge-detector dominates the spectrum, making a proper, direct extrapolation of the actual energy profile impossible. For this reason the detected spectrum was deconvoluted with the response function of the Ge-detector and fitted to a log-normal function (see fig. 11.11 and fig. 11.12). The respective center positions resulting from these fits are listed in table 11.2 and put into context with the potential doorway states, the irradiation time and the γ-flux for this energy. As introduced earlier, the γ-flux was measured with a scintillator paddle in upstream direction. The flux density is energy dependent and hence, with respect to a comparable activation at different energies, the irradiation time was adapted accordingly (see also fig. 11.10).

Table 11.2: Experimental conditions for the irradiation of the platinum samples. The deconvoluted energy beam profile was fitted to a log-normal function whose center value is denoted as E_{Beam}.

$\mathbf{E_{Beam}}$,($\mathbf{E_{States}}$) [keV]	$\mathbf{FWHM_{log-normal}}$ [keV]	Irr. time [h]	Gamma flux Photons/s
1331, (1313,1346)	43	17.5	$6.36 \cdot 10^6$
1559, (1560)	59	16.7	$1.60 \cdot 10^7$
2032, (2035)	79	6.7	$5.34 \cdot 10^7$
2319, (2352)	80	13.6	$5.98 \cdot 10^7$
2578, (2592)	114	5.4	$1.05 \cdot 10^8$
3568†	180	9.8	$2.69 \cdot 10^8$
3662†	172	19.5	$2.43 \cdot 10^8$
3801, (3843)	189	2.7	$3.06 \cdot 10^8$

† No doorway states were proposed for these irradiation energies.

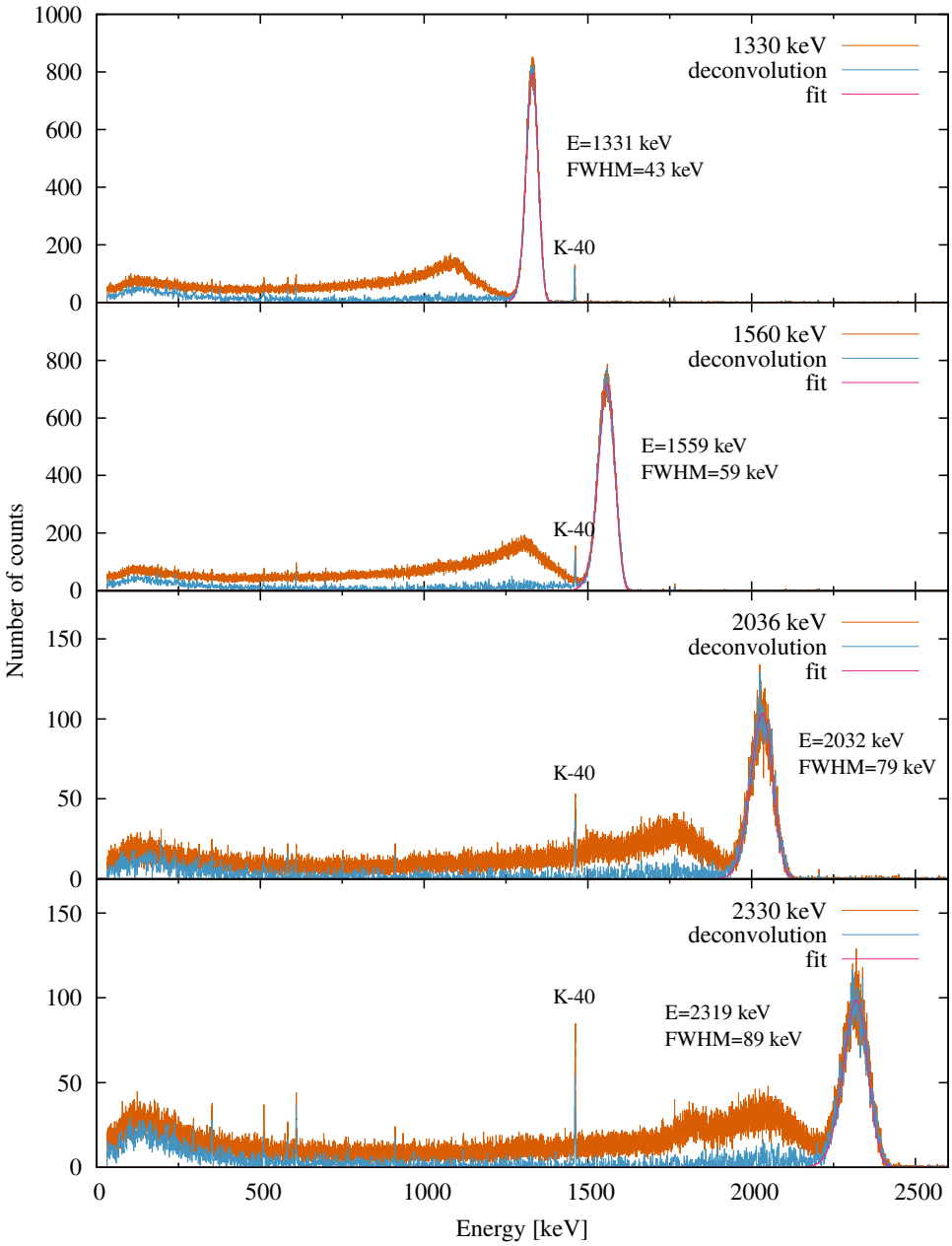

Figure 11.11: Energy spectra of the HIGS γ-beam for different energies measured with a HPGe detector under 0° with respect to the beam direction. The beam profile was fitted to a log-normal function. Note that the Compton spectrum on the left side is induced by Compton scattering within the detector. See text for further information.

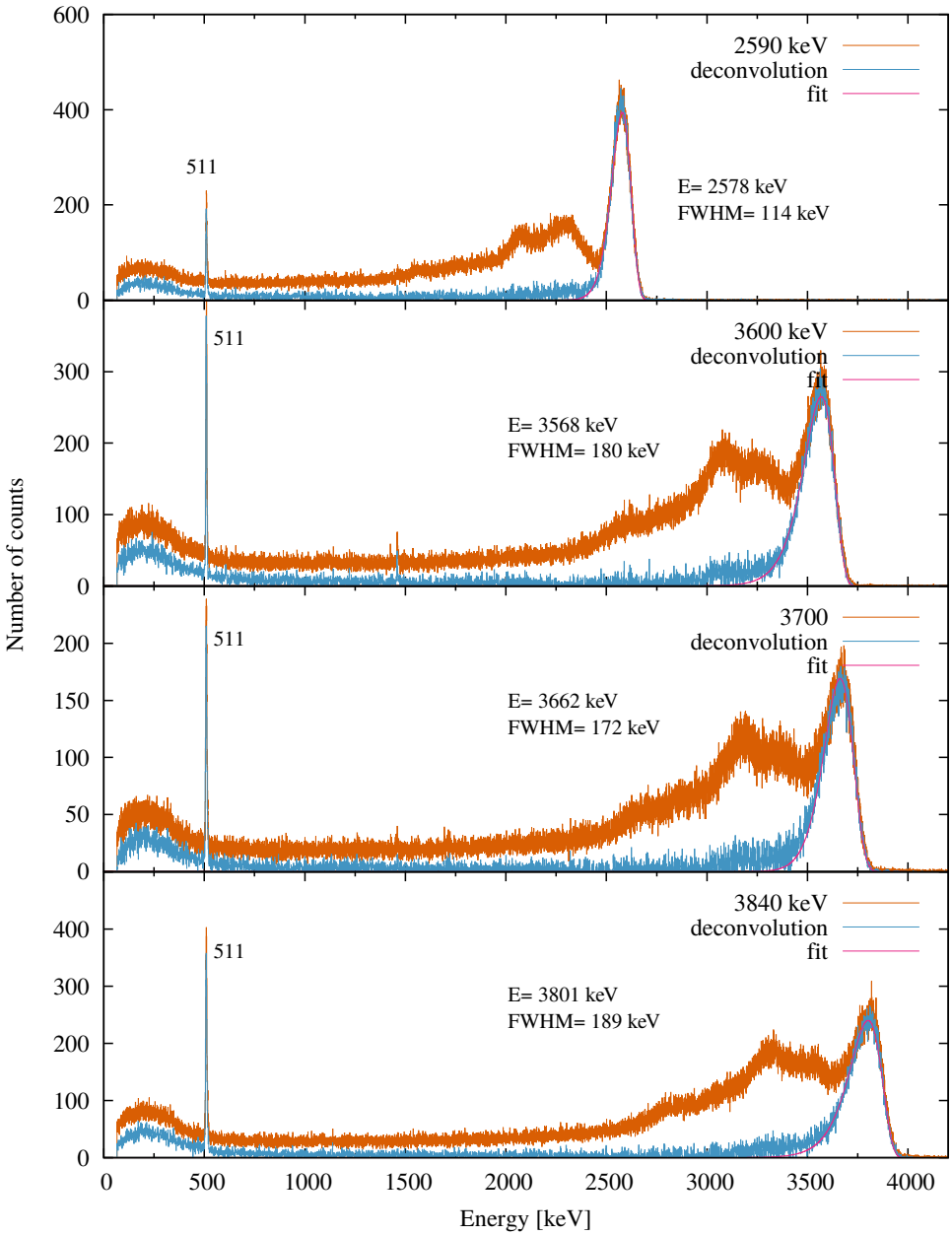

Figure 11.12: Energy spectra of the HIGS γ-beam for different energies measured with a HPGe detector under 0° with respect to the beam direction. The beam profile was fitted to a log-normal function. Note that the Compton spectrum on the left side is induced by Compton scattering within the detector. See text for further information.

11.2.2 Activity Measurement

After the irradiation of the platinum samples the activity was measured with different lead shielded germanium detectors in order to reach an optimal background suppression. Considering the limited irradiation time, resulting in an expected low activity, and the limited available measuring time, three sample foils for each were measured simultaneously by placing them head-to-head in a "flower-like" configuration on the face of the germanium detector capsule. The efficiency calibration was therefore also adopted to this particular configuration with an active source placed in off-center position.
Since the isomer depopulating transitions are all of low energy (see table 9.1 and figure 9.3) the calibration was performed with a mixed source of different well defined γ transitions in the region of interest. A plot of the efficiency calibration for the used detectors is shown in figure 11.13.

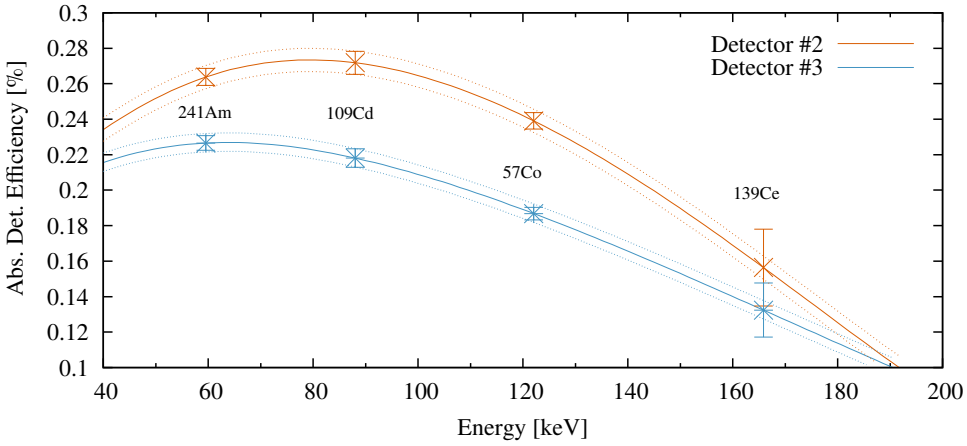

Figure 11.13: Efficiency calibration of the low energy range for the detectors used for activation measurements. The data points refer to known decays of a mixed calibration source.

For the purpose of demonstration a recorded activation spectrum of a platinum foil which was irradiated for 19.5 h with a γ-beam energy of 3.7 MeV is shown in fig. 11.14. With respect to the decay scheme presented in fig. 9.3 it was possible to observe the expected isomeric lines for the ^{195m}Pt isomer at 65.1 keV, 66.8 keV (X-rays) and 98.9 keV (γ-ray). Additionally, other background transitions were detected which were polluting the spectrum, but which could be beneficially used for proper calibration of

the energy and resolution.
The remaining spectra of the activity measurements for the respective beam energies can be found in the appendix D.3-D.2.

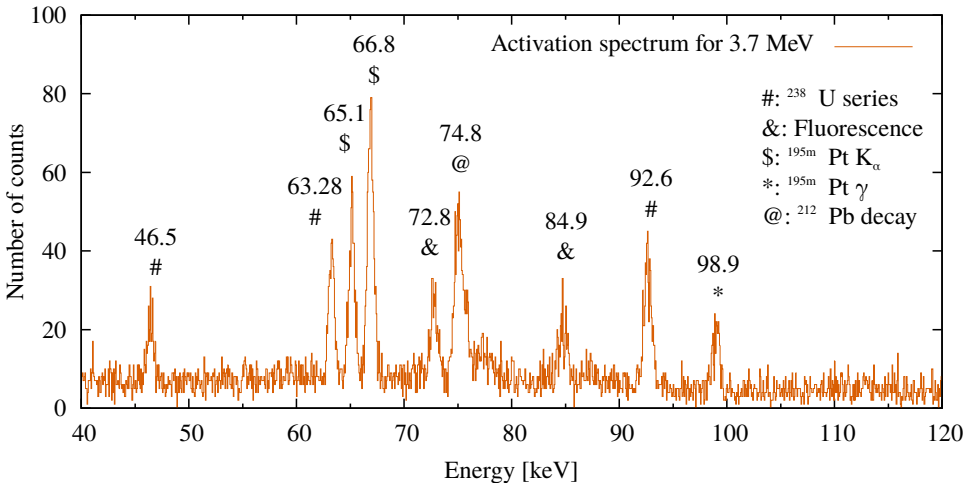

Figure 11.14: Activation spectrum of a platinum foil with natural isotopic composition irradiated for 17.5 h with a γ-beam of 3.7 MeV. The origin of the present transitions is indicated. See text for further information.

With respect to the measured count rates of the 98.9 keV γ transition and the 65 keV and 67 keV X-ray transitions respectively, the activity of the end of the irradiation process A_{EOI} was calculated according to equation (11.2):

$$A_{EOI} = A \cdot e^{d/\tau} \cdot F_m, \tag{11.2}$$

where A is the measured activity per Pt disk, corrected for the abundance of the respective transition and the detector's efficiency, d is the delay time between the end of the irradiation and the start of the activation measurement, τ is the lifetime of ^{195m}Pt, and F_m a factor correcting for the decay during the measurement. The measured activities per disk for each irradiation energy are summarized in table 11.3. It is important to notice that these activities correspond to the respective irradiation time, γ-flux density and beam distribution, respectively.
Moreover, the integrated cross-sections of the proposed doorway states were calculated in the units of eV · b. Generally, an indication of the actual cross-section, i.e. in units of b, would be favored but such a calculation requires

additional information about the width Γ of the irradiated state. Thus, the integrated cross-section $\sigma\Gamma$ was calculated for $\Gamma = 1\,\mathrm{eV}$ according to equation (11.3):

$$\sigma\Gamma = \frac{\mathrm{A_{EOI}}}{\mathrm{N_{^{195}Pt} S_{irr} F_\gamma}}, \tag{11.3}$$

where $\mathrm{N_{^{195}Pt}}$ is the number of ^{195}Pt atoms in the the sample, $\mathrm{S_{irr}}$ is a factor accounting for the saturation, i.e. the decay during irradiation, and $\mathrm{F_\gamma}$ is the γ-flux density deduced from the beam energy distribution at the respective energy for $\Gamma = 1\,\mathrm{eV}$. The calculated integrated cross-sections for the proposed doorway states are summarized in table 11.3.

Table 11.3: Measured activation and the deduced integrated cross-section for the different irradiation energies. See text for further information

$\mathbf{E_{B,(S)}}$ [keV]	Irr. time [h]	Spec. γ-flux density [$\mathbf{cm^{-2}s^{-1}eV^{-1}}$]	$\mathbf{A_{EOI}}$ [mBq/disk]	Int. σ [eV.b]
1331	17.5	28	19(4)	
(1313)		18		10.7(20)
(1346)		19		10.0(19)
1559	16.7	51	37(6)	
(1561)		51		7.6(13)
2032	6.7	126	27(6)	
(2035)		125		5.3(12)
2319	13.6	127	25(7)	
(2352)		83		4.1(11)
2578	5.4	175	33(6)	
(2592)		167		6.1(11)
3568	9.8	293	99(9)	
3662	19.5	269	150(13)	
3801	2.7	319	55(8)	
(3843)		270		12.4(17)

For the given values of the integrated cross-section it is even more important to emphasize that the calculation is based on the assumption that only the considered state is contributing to the activation. However, with special regard to the energy beam distribution, the width becomes larger with increasing energy which is subsequently increasing the possibility for the irradiation of more than only one state within this region. Moreover, since the spectral γ-flux density decreases from the peak to the wings of the Gaussian-like distribution, states in the wings which potentially contribute to the activation but which are irridiated with only a fraction of the expected flux would be highly overestimated with respect to their cross-section. Accordingly, the presented values rather represent a lower limit than the actual integrated cross-section for the activation of the isomeric state.
To account for this particular situation the integrated cross-sections as a function of energy were considered in an exclusion plot which is presented in figure 11.15.

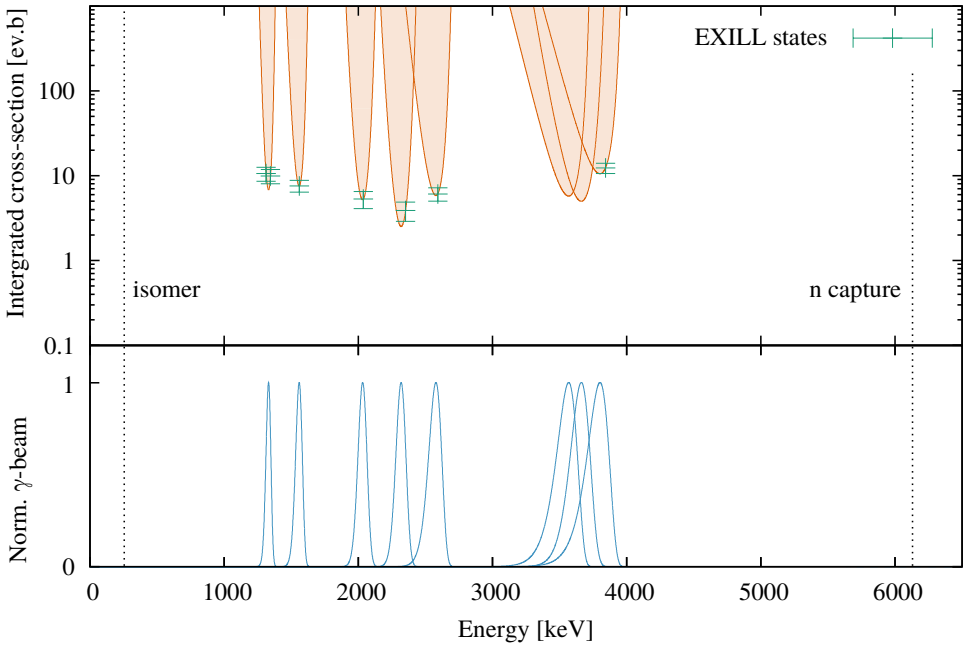

Figure 11.15: Exclusion plot for the experimentally deduced integrated cross-sections as a function of the energy (upper panel), and the normalized beam energy distribution(lower panel). The isomeric state at 259 keV and the neutron capture state at 6.1 MeV are indicated.

Chapter 12

Discussion

Traditional anti-cancer drugs target generic characteristics of cancer cells which are overexpressed with respect to normal cells. The treatment with chemotherapeutics for instance targets the disproportionate cell devision of cancer cells over normal cells. However, such approaches always affect cancer cells and normal cells at the same time and thus, patients often suffer from undesirable side effects.

In the last decades the development of cancer selective drugs has become an important field. In so called targeted therapies only cancer cells are addressed. This approach is based on the overexpression of certain receptors on cancer cells to which a respective counterpart, i.e. antibodies or peptides etc. can bind to. Labeling these agents with a radionuclide which decays via the emission of electrons or α particles can cause massive damage to the cell's DNA which is subsequently leading to the cell death. A radionuclide which is compatible with this method has to fulfill certain properties, such as a suitable half-life for in-vivo use, a sufficient amount of short-range radiation for cell damage, and possibly also low energy transitions for imaging. With a half-life of 4 days, an average electron release of 29 electrons per decay, and an intense 99 keV γ transition, the platinum isomer ^{195m}Pt is a potentially adequate candidate. However, the production of this isomer with a high specific activity is infeasible with common techniques.

Photo-excitation with intense γ beams could principally lead to such a high specific activity of the isomer, but this method requires a linkage between the ground state and the isomer which was not observed yet for ^{195}Pt.

The general idea of this work was the search for these linkages, i.e. states above the isomer which partly decay into the ground state and partly decay into the isomer. Thus, by irradiating platinum with an intense γ beam with

an energy corresponding to these doorway states a substantial activity of the isomer could be produced.
In order to identify these states a neutron capture experiment following the reaction $^{194}\mathrm{Pt}(n,\gamma)$ was performed within the frame of the EXILL campaign and analyzed accordingly. Several new states could be assigned to ^{195}Pt which clearly lead to the population of the isomer and which additionally show evidence of a respective ground state linkage.
In a follow-up experiment platinum samples were irradiated for these energies with a γ beam produced via Compton backscattering at HIGS, and subsequently measured with respect to their accumulated activity. The experiment verified the general possibility of activating the $13/2^+$ isomer in ^{195}Pt via photo-excitation from the ground state. However, the measured activities and the deduced integrated cross-sections for the respective doorway states seem to be too low for medical usability. The deduced values for the integrated cross-sections are plotted in figure 12.1 and compared with previous experiments at HIGS, and with simulations performed with the Talys code [129].

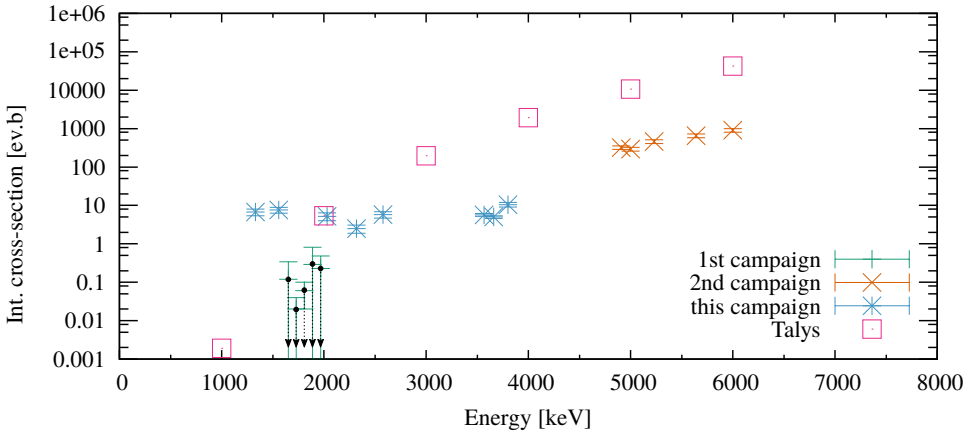

Figure 12.1: Integrated cross-sections for the population of the 13/2+ isomer in ^{195}Pt as a function of energy. Green: Experimental results in the low energy range from the first HIGS campaign. Note that the deduced values represent a detection limit. Orange: Experimental results in the high energy range from the second HIGS campaign. Blue: Experimental results for the irradiation of "doorway states" from this work. Pink: Talys calculation for the cross-section normalized to the HIGS γ-flux and to an effective linewidth of 1 eV.

A first campaign had been performed in 2011 to cover the range from 1.54 to 2.05 MeV with seven activations equally spaced in energy. The activated platinum foils had been rapidly shipped to France and measured in the low level gamma spectrometry labs of LPSC Grenoble and LSM Modane. Only tight upper limits resulted from this campaign, showing that a direct systematic search for doorway states by scanning in small steps would require very long beam time.
A second campaign had been performed in 2012 where platinum foils could be activated in a "parasitic" beam time upstream to another experiment. The main experiment required higher energies, ranging from 4.8 to 9.7 MeV. The activated platinum foils were measured at Duke University and at ILL Grenoble and LPSC Grenoble. All samples showed a clear activation. However, due to the high level density at such high excitation energies likely many doorway states are covered by every activation, therefore the observed activation cannot be attributed to single doorway states. For the activation at 9.7 MeV above the neutron binding energy of ^{196}Pt, there is certainly also an important contribution from $^{196}\mathrm{Pt}(\gamma,\mathrm{n})^{195\mathrm{m}}\mathrm{Pt}$ reactions in the foil with natural isotopic composition [130, 131].
Theses first two campaigns had shown that this type of activation experiments are indeed feasible at HIGS but that a continuous "brute-force" search is too time consuming.
In direct comparison, following the evolution of the experimentally deduced integrated cross-section with energy and the evolution of the integrated cross-section of the Talys calculation, the present results show no significant evidence for excitation pathways. However, since the Talys calculation is globally overestimating the cross-section for those energies which were randomly irradiated, but consistently following a global trend, cf. the results from the first and the second campaign, the irradiated energy regions around 1330 keV, 1560 keV and 2035 keV could be interpreted as low cross-section doorway pathways.

Synthèse de la partie *La production de l'isomère Pt-195m* :
Les médicaments anticancéreux traditionnels ciblent les caractéristiques génériques des cellules cancéreuses qui sont surexprimées par rapport aux cellules saines. Le traitement avec des agents chimiothérapeutiques, par exemple, cible la division cellulaire disproportionnée des cellules cancéreuses par rapport aux cellules normales. Malheureusement, de telles approches affectent non seulement les cellules cancéreuses mais aussi les cellules saines, les patients souffrant alors souvent d'effets secondaires indésirables. Au cours des dernières décennies, le développement de médicaments sélectifs contre le cancer est devenu un domaine important. Dans les thérapies ciblées, seules les cellules cancéreuses sont affectées. Cette approche est basée sur la surexpression de certains récepteurs sur des cellules cancéreuses auxquels une contrepartie (ou agent), c'est-à-dire des anticorps ou des peptides, peut se lier. Le marquage de ces agents avec un radionucléide qui se désintègre par l'émission d'électrons ou de particules α peut causer des dommages massifs à l'ADN de la cellule, ce qui entraîne sa mort. Un radionucléide compatible avec cette méthode doit remplir certaines propriétés, telles qu'une demi-vie appropriée pour une utilisation in vivo, une quantité suffisante de rayonnement à courte portée pour endommager les cellules et aussi des transitions à faible énergie pour l'imagerie. Avec une demi-vie de 4 jours, une libération moyenne d'électrons de 29 électrons par désintégration et une transition γ intense de 99 keV, l'isomère du platine ^{195m}Pt est un candidat potentiellement adéquat. Cependant, la production de cet isomère avec une activité spécifique élevée est infaisable avec des techniques courantes. La photo-excitation avec des faisceaux intenses de γ pourrait conduire à une activité spécifique de l'isomère très élevée, mais cette méthode nécessite une liaison entre l'état fondamental et l'isomère qui n'a pas encore été observée pour ^{195}Pt.
L'idée générale de ce travail était la recherche de ces liaisons, c'est-à-dire des états au-dessus de l'isomère qui décroîteraient au moins partiellement vers l'état isomérique. Ainsi, en irradiant du platine avec un faisceau intense de gamma avec une énergie correspondant à ces états particuliers, une activité substantielle de l'isomère pourrait être produite. Afin d'identifier ces états, une expérience de capture de neutrons $^{194}\mathrm{Pt}(n,\gamma)$ a été réalisée dans le cadre de la campagne EXILL. Plusieurs nouveaux états appelés états d'entrée (dans le schéma de niveaux) ont pu être assignés à ^{195}Pt, dont les décroissances montrent clairement

une alimentation de l'état isomérique d'intérêt, et également un rapport d'embranchement vers l'état fondamental.
Au vu de ces résultats prometteurs, cette première expérience s'est poursuivi par une expérience dans laquelle des échantillons de platine ont été irradiés avec un faisceau γ produit par rétrodiffusion Compton à HIGS, faisceau dont l'énergie a été ajusté successivement à celles des états excités mesurés précedemment. L'activité accumulée durant ces différentes activations a ensuite été mesurée. L'expérience a montré qu'il était possible d'activer l'isomère $13/2^+$ dans ^{195}Pt par photo-excitation à partir de l'état fondamental. Cependant, les activités mesurées et les sections efficaces intégrées déduites pour les états d'intérêts semblent être trop faibles pour permettre une utilisation médicale. Les valeurs déduites pour les sections efficaces intégrées sont représentées dans la figure 12.1 et comparées aux expériences précédentes à HIGS, et avec des simulations effectuées avec le code Talys : une première campagne a été réalisée en 2011 pour couvrir la gamme de 1,54 à 2,05 MeV avec sept activations également espacées en énergie. Les feuilles de platine activées à HIGS ont été rapidement expédiées en France et mesurées dans les laboratoires de spectrométrie gamma de du LPSC Grenoble et du LSM Modane. Seules des limites supérieures ont résulté de cette campagne, montrant qu'une recherche systématique des états d'entrée par balayage avec des petits pas en énergie nécessiterait un temps de faisceau très longs.
Une seconde campagne a été réalisée en 2012 où des feuilles de platine pouvaient être activées dans un faisceau parasite en amont d'une autre expérience, l'expérience principale nécessitant des énergies plus élevées, allant de 4,8 à 9,7 MeV. Les feuilles de platine activées ont été mesurées à l'Université de Duke et à l'ILL et au LPSC de Grenoble. Tous les échantillons ont montré une activation. Cependant, en raison de la forte densité de niveau à de telles énergies d'excitation élevées, de nombreux états d'entrée sont couverts par chaque irradiation, l'activation observée ne pouvant donc pas être spécifique et attribuée à un état d'entrée unique. Pour l'activation à 9,7 MeV au-dessus de l'énergie de liaison neutronique de ^{196}Pt, il y a certainement aussi une contribution importante de la réaction $^{196}\mathrm{Pt}(\gamma, \mathrm{n})^{195\mathrm{m}}\mathrm{Pt}$, puisque la cible utilisée était une feuille de platine naturel.
Ces deux premières campagnes ont montré que ce type d'expérience d'activation est en effet faisable avec un faisceau γ comme celui de HIGS mais qu'une recherche insuffisamment ciblée prend trop de temps.

D'après l'évolution de la section efficace intégrée en fonction de l'énergie déduite expérimentalement et l'évolution de la section efficace intégrée du calcul de Talys, les résultats obtenus ne montrent pas de signes convaincants de chemin d'excitation spécifique permettant de peupler l'isomère. Cependant, puisque le calcul de Talys surestime globalement la section efficace tout en suivant systématiquement une tendance globale, cf. les résultats de la première et de la deuxième campagne, les régions d'énergie autour de 1330 keV, 1560 keV et 2035 keV -pour lesquelles les valeurs de sections efficaces mesurées sont supérieures aux calculs Talys- pourraient être interprétées comme des états d'entrée peuplés avec une section efficace faible.

Chapter 13

Final Conclusions

This thesis presented three topics embedded within the scope of *"Nuclear structure studies with neutron-induced reactions"*:

1) *Fission fragments in the* $N = 50 - 60$ *region*,
2) *A fission event tagger for FIPPS*, and
3) *Production of the isomer* ^{195m}Pt.

With respect to the enclosing main title of this work, the 2012/13 EXILL campaign can be considered as the connecting element between the various parts: The neutron-rich region around neutron number $N = 50 - 60$ was investigated within the framework of neutron-induced fission experiments of the EXILL campaign. Experimental boundaries of this campaign concerning the identification of fission fragments in particular, led to the idea of a complementary particle detector in the form of a fission event tagger. And finally, the discussion of the production of the isomer ^{195m}Pt, which was initiated with a neutron capture experiment of the EXILL campaign.
The study of fission fragments in the $N = 50 - 60$ region was presented in the first part of this thesis. The main interest for the investigation of this region was motivated by the appearance of effects like deformation and shape coexistence. Experimentally, these nuclei were produced via neutron-induced fission of ^{235}U and ^{241}Pu. The analysis of excited states was carried out in a γ-spectroscopic framework for the assignment of γ transitions and the analysis of lifetimes, respectively. However, the large amount of simultaneously produced γ transitions made a proper assignment to the respective nucleus particularly challenging. This was especially evident for the analyzed nuclei, which were predominately produced apart from high production yields. The availability of the two data sets, i.e. ^{235}U and ^{241}Pu, was generally helpful regarding the identification of fission fragments, but for poorly produced

nuclei the benefit of the ^{241}Pu data set for nuclei lighter than mass number A ≈ 100 was rather little with respect to ^{235}U. It would be however interesting to consider other fissile targets for the access of this mass region. In this context the the uranium fissile isotope ^{233}U could be an interesting candidate due to its shifted light fission fragment distribution towards lighter nuclei. Such a fissile target could be considered in future experiments with the EXILL array. Moreover, originating from the experiences of the EXILL campaign, these kind of experiments would most probably essentially profit from ancillary detectors for particle identification.

Such a fission event tagger was discussed in the second part of this thesis. Foreseen for the use at the *FIssion Product Prompt γ-ray Spectrometer* FIPPS at the Institut Laue-Langevin, it has to fulfill specific requirements concerning the application under neutron exposure. The performed experiments aimed to specify these requirements and to propose a preliminary design for this detector. The discussion was concentrating on two different concepts for scintillator based fission event taggers: The first one was a fission event tagger which is based on a scintillating foil which is connected to a photomultiplier tube. Within the scope of this work a 25 μm thick scintillating foil has been tested with regard to its particle discrimination properties at the ILL's mass spectrometer *Lohengrin*. The second design of a fission event tagger was based on an organic liquid scintillator deposited into an inorganic container vessel. To be used as an "active target", different scintillating liquids have been incorporated with a solution of ^{235}U. Both, different scintillating liquids and different vessel materials have therefore been considered with regard to their neutron scattering and absorption cross section. Moreover, the vessel materials have been tested with respect to their chemical compatibility with the respective liquids. Three active targets based on different liquid scintillators have been tested for their α-β particle discrimination characteristics. In comparison, both designs exhibit suitable properties for the use as a fission event tagger at FIPPS, albeit practical for different purposes. A liquid scintillator based fission event tagger has a very high detection efficiency. Thus, when used as a fission veto detector it could be applied to (n, γ) spectroscopy for the respective actinide target which is dissolved in the scintillating liquid. The scintillating foil based fission event tagger on the other hand can be designed in way that fission fragments pass through a thin layer without significant energy loss which makes it compatible with the gas filled magnet which is foreseen in the second phase for FIPPS. However, both designs and the respective tests were carried out on a very preliminary stage, and therefore further investigation is clearly necessary.

The production of the isomer ^{195m}Pt was presented in the third part of this thesis. Motivated by its potential use as a radioisotope in nuclear medicine, two experiments were performed which intended, as final goal, to find a production route which is leading to a high specific activity of this isomer. In the first experiment, ^{195}Pt was produced via neutron capture on a stable enriched ^{194}Pt target in the frame of the EXILL campaign. This experiment aimed to assign new states to ^{195}Pt which populate the isomer, and additionally decay into the ground state. In the context of this thesis these states were denoted as *doorway states*. Such potential doorway states were found. The second experiment was performed at the *High Intensity Gamma-ray Source* (HIGS) of the TUNL facility. Platinum samples of natural isotopic composition were irradiated with a γ-beam tuned for the energies of the potential doorway states which were identified before. The subsequent measurement of particular γ- and X-ray transitions which are associated with the isomer led to an estimation of the integrated cross section for the population of the isomer ^{195m}Pt via the respective doorway state by photonuclear reactions. The results of these measurements demonstrated that the population of the isomer via "indirect" pathways is feasible. However, a high specific activation through a single resonant state could ultimately not be proven. Rather it seems that several states contribute to the activation of ^{195m}Pt at the same time. Unfortunately, the relatively broad energy distribution of the HIGS beam does not allow to verify to which part a particular state contribute to the activation of the isomer. This could be however tested with the much more narrow γ-beam like it is provided by the *Extreme Light Infrastructure* facility ELI-NP in a potential follow-up experiment.

Conclusions Finales

Dans ce travail de thèse trois sujets connexes ont été intégrés dans le cadre commun et générique d' *"Études de structure nucléaire avec des réactions induites par des neutrons"*. Ces trois sujets sont:

1) *La spectroscopie de fragments de fission dans la région* $\mathrm{N} = 50 - 60$,
2) *La conception d'un marqueur d'événement de fission pour FIPPS*, et
3) *L'étude de la production de l'isomère* $^{195\mathrm{m}}\mathrm{Pt}$.

La campagne EXILL qui s'est déroulée en 2012-13 est à la fois le cadre et le lien unifiant les différentes parties de ce travail: les noyaux riches en neutrons autour du nombre de neutrons $\mathrm{N} = 50 - 60$ ont été produits par des réactions de fission induites par les neutrons lors de la campagne EXILL. Les limites expérimentales de cette campagne concernant l'identification des fragments de fission en particulier, ont conduit à l'idée d'un détecteur de particules complémentaire sous la forme d'un marqueur d'événement de fission. Enfin, la discussion de la production de l'isomère $^{195\mathrm{m}}\mathrm{Pt}$, qui a été initiée avec une expérience de capture de neutrons de la campagne EXILL. L'étude des fragments de fission dans la région $\mathrm{N} = 50 - 60$ a été présentée dans la première partie de cette thèse. L'intérêt principal pour l'étude de cette région était motivé par des variations brutales de l'énergie de liaison des deux derniers neutrons (S2n), concomittantes avec un changement brutal des rayons carrés moyens. Les nombreuses études sur le sujet indiquent des effets importants de déformation et de coexistence de formes, accessibles notamment par spectrosopie gamma. Expérimentalement, ces noyaux ont été produits par fission induite par des neutrons provenant du réacteur à haut flux de l'ILL, refroidis et collimatés sur les cibles d'actinides de $^{235}\mathrm{U}$ et $^{241}\mathrm{Pu}$. L'analyse des états excités a été effectuée par des méthodes de spectroscopie γ pour l'attribution des transitions γ, la construction des schémas de niveaux et l'analyse des durées moyenne de vie. Cependant, la grande quantité de transitions γ produites simultanément dans les réactions de fission a rendu l'affectation correcte des transitions à un noyau donné

particulièrement difficile. Cela était particulièrement évident pour les noyaux analysés, dont les taux de production étaient particulièrement faibles. L'utilisation des deux cibles de fission à savoir ^{235}U et ^{241}Pu, a été utile pour l'identification des fragments de fission dans la mesure où, pour un noyau d'intérêt les fragments complémentaires sont différents d'une cible à l'autre. Toutefois, les noyaux légers de masse A $\approx$ 100 ont été faiblement produits dans la fission de ^{241}Pu par rapport à ^{235}U, ce qui a limité l'application de cette technique. Il serait cependant intéressant d'envisager d'autres cibles fissiles pour l'accès à cette région de masse. Dans ce contexte, l'isotope fissile de l'uranium ^{233}U pourrait être un candidat intéressant en raison de sa distribution de fragments de fission légère qui est décalée vers des noyaux plus légers. Une telle cible fissile pourrait être considérée dans de futures expériences avec le spectromètre EXILL. Ce type d'expérience bénéficierait très probablement de détecteurs auxiliaires tel le marqueur de fission pour l'identification des particules. Un tel marqueur d'événement de fission a été discuté dans la deuxième partie de cette thèse. Prévu pour l'utilisation au FIPPS à l'Institut Laue-Langevin, il doit répondre à des exigences spécifiques concernant l'application sous exposition neutronique. Les expériences réalisées visaient à préciser ces exigences et à proposer une conception préliminaire pour ce détecteur. La discussion s'est concentrée sur deux concepts différents pour les matériaux scintillants. Le premier était un marqueur d'événement de fission basé sur une feuille scintillante connectée à un tube photomultiplicateur. Dans le cadre de ce travail, les propriétés de discrimination des particules d'une feuille scintillante d'une épaisseur de 25 μm a été testée auprès du spectromètre de masse *Lohengrin* de l'ILL. La deuxième conception d'un marqueur d'événements de fission était basée sur un scintillateur liquide organique déposé dans un récipient inorganique. Pour être utilisés comme cible active, plusieurs liquides scintillants ont été incorporés avec une solution de ^{235}U. Différents matériaux pour le contenant de cette solution ont été considérés notamment pour mesurer les sections efficaces de diffusion et d'absorption de neutron. De plus, les matériaux du récipient ont été testés pour leur compatibilité chimique avec les liquides respectifs. Au final, trois cibles actives basées sur différents scintillateurs liquides ont été évaluées pour leurs caractéristiques de discrimination des particules α et β. Les deux conceptions présentent des propriétés compatibles avec l'utilisation en tant que marqueur d'événements de fission auprès FIPPS, avec des toutefois des avantages et des inconvénients spécifiques en fonction de leur usage. Un marqueur d'événement de fission à la base d'un scintillateur liquide a une efficacité de détection très élevée. Ainsi, pour une utilisation en tant que rejet d'évènements de fission comme dans le cas de

la sélection des réactions de capture radiative (n, γ) une cible active liquide doit être privilégiée pour son éfficacité proche de 100%. Toutefois une telle cible est incompatible avec l'utilisation d'un spectromètre tel que FIPPS. Pour la spectroscopie et l'étude des fragments de fission en revanche, un scintillateur solide suffisamment fin, permet la transmission des fragments sans perte significative d'énergie et l'analyse en masse et en charge par un spectromètre rempli de gaz, tel celui prévu pour l'ILL. Cependant, si les deux conceptions et les tests qui ont été effectués ont montré la faisabilité d'un marqueur d'évènements de fission, ils en sont restés à un stade très préliminaire, et des études plus approfondies sont nécessaires.

La production de l'isomère ^{195m}Pt a été présentée dans la troisième partie de cette thèse. Motivées par son utilisation potentielle en tant que radio-isotope en médecine nucléaire, deux expériences ont été réalisées dans le but final de trouver une voie de production conduisant à une activité spécifique élevée de cet isomère. Dans la première expérience, ^{195}Pt a été produit par capture de neutrons sur une cible stable et enrichie de ^{194}Pt dans le cadre de la campagne EXILL. Cette expérience visait à chercher des nouveaux états (dits états d'entrée ou doorway states en anglais) à ^{195}Pt peuplant l'isomère, qui décroit ensuite vers l'état fondamental. De tels états ont été trouvés. La deuxième expérience a été réalisée à l'installation *High Intense Gamma-ray Source* (HIGS) de l'institution TUNL. Des échantillons de platine de composition isotopique naturelle ont été irradiés avec un faisceau γ, dont l'énergie était successivement ajustée sur celle des états d'entrée identifiés durant la campagne EXILL. La mesure des transitions γ associées à la décroissance de l'isomère a permis d'estimer la section efficace intégrée de population de l'isomère dans ^{195m}Pt en fonction de l'état d'entrée sur lequel l'énergie du faisceau γ de HIGS était réglée.

Les résultats de ces mesures ont démontré que la population de l'isomère via les voies indirectes ouvertes par ces états d'entrée est réalisable. Cependant, il n'a pas été possible de démontrer que l'alimentation de l'isomère par un seul état bien identifié permettait d'atteindre une activation spécifique suffisamment élevée pour une utilisation potentielle en médecine nucléaire. Il semble plutôt que plusieurs états contribuent simultanément à l'activation de ^{195m}Pt. Malheureusement, la distribution en énergie relativement large du faisceau fourni par HIGS ne permet pas de déterminer les contributions individuelles de chaque état d'entrée à l'activation de l'isomère. Cette étude pourra être poursuivie avec l'objectif de lever ces incertitudes avec le faisceau γ de haute résolution en énergie qui sera fourni par l'installation *Extreme Light Infrastructure* ELI-NP dans un avenir proche.

Appendix A

Light Fission Fragment Distribution

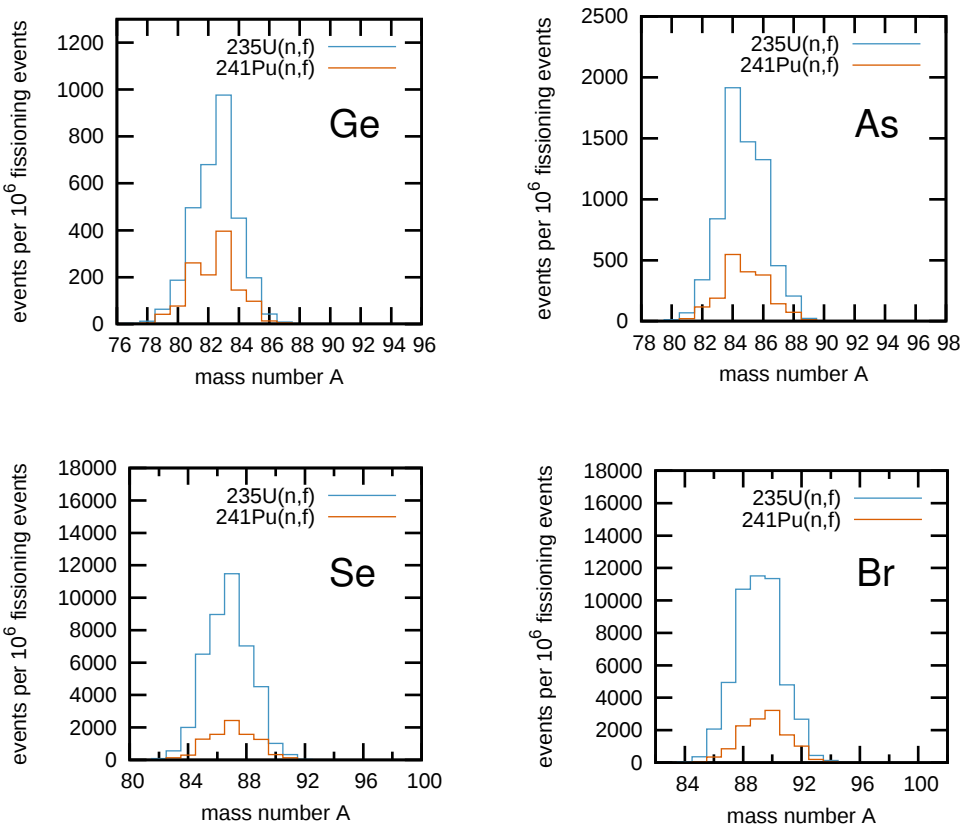

Figure A.1: Productions yields of the Z=32-41 nuclei in neutron induced fission of ^{235}U and ^{241}Pu respectively.

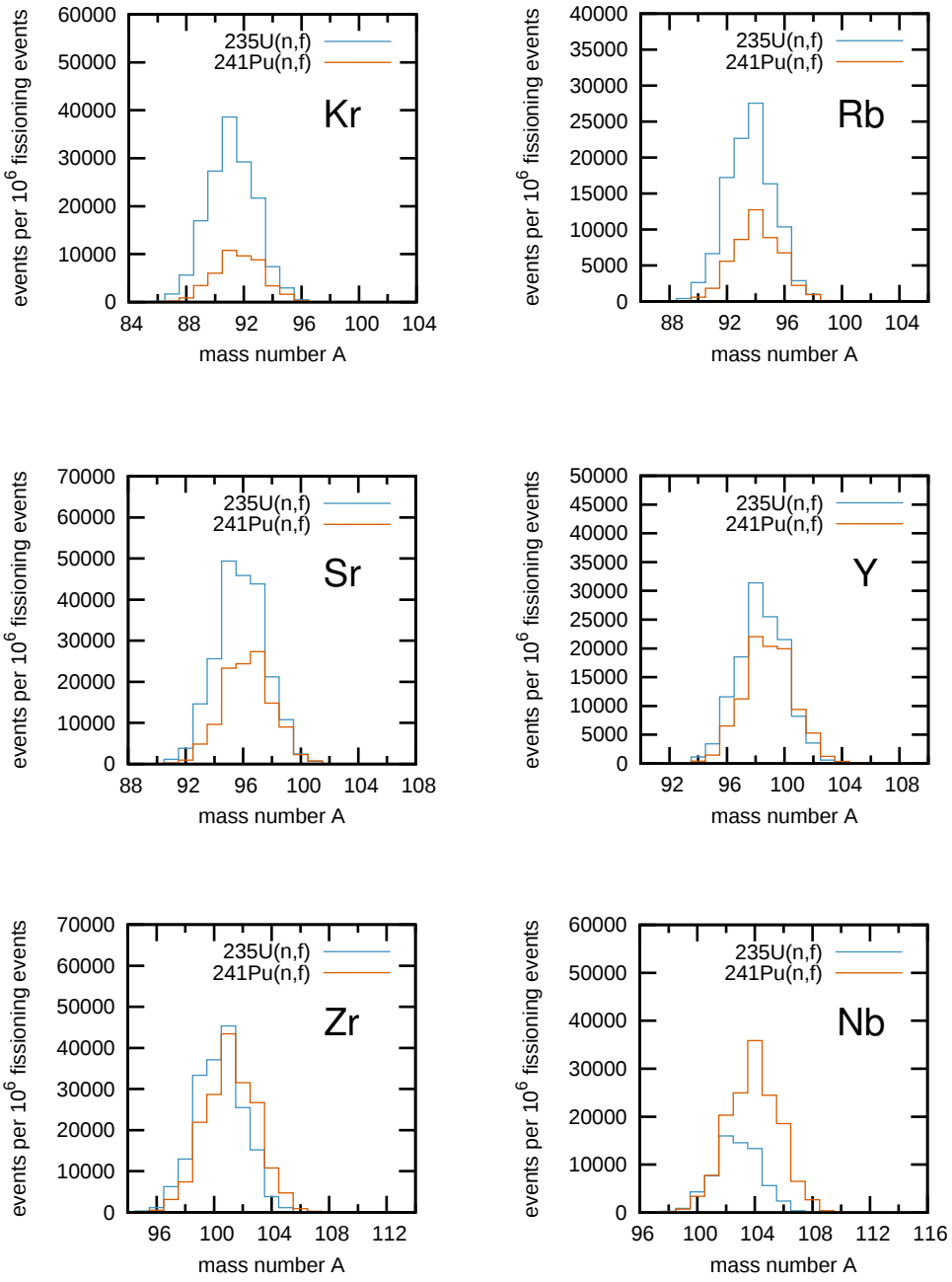

Figure A.2: *Continue.* Productions yields of the Z=32-41 nuclei in neutron induced fission of ^{235}U and ^{241}Pu respectively.

Appendix B

Selenium Analysis for (n,fission) with EXILL

B.1 Selenium

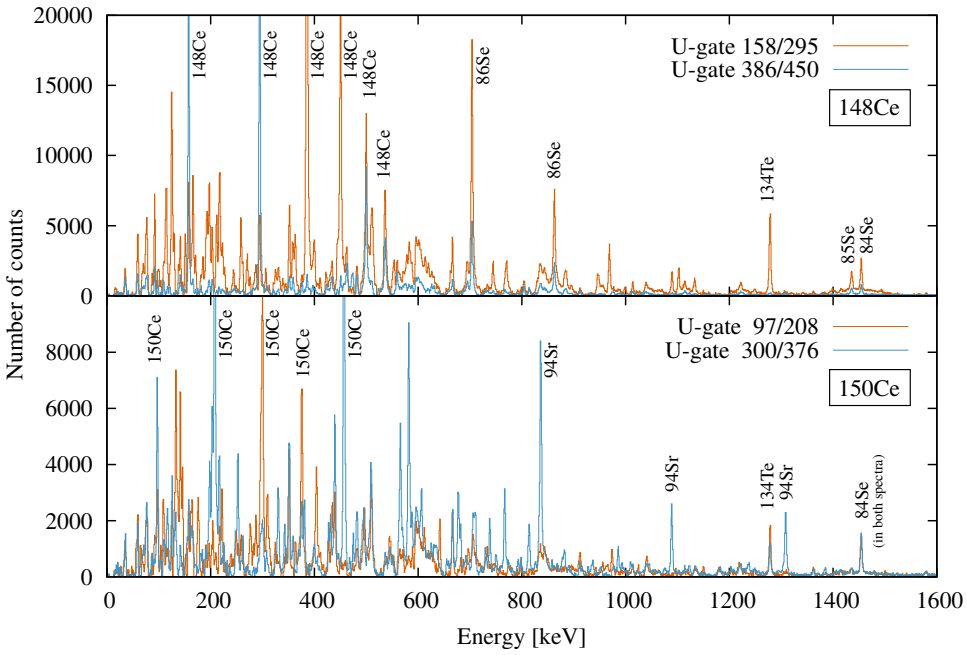

Figure B.1: γ-coincidence spectra using double gates in the complementary partner isotopes of selenium within the ^{235}U(n, f) reaction. Upper panel: Coincident transitions of ^{148}Ce. Lower panel: Coincident transitions of ^{150}Ce. See text for further explanations.

The selenium isotopes 83,84 and 85 were analyzed. In order to estimate their yield and to identify distinctive γ-transitions for an analysis the complementary partner cerium for the ^{236}U fissioning system were considered to be interpreted within a coincidence analysis. Therefore, the intense yrast transitions of ^{148}Ce (see e.g. [132]) and ^{150}Ce [133] were used as gates. For ^{148}Ce this implies the 5n-channel for ^{83}Se, respectively 4n for ^{84}Se and 3n for ^{85}Se. For ^{150}Ce the associated neutron emission is (in this order) 3n, 2n, 1n for ^{83}Se, ^{84}Se, ^{85}Se. The choice of taking ^{148}Ce and ^{150}Ce for the identification of ^{83,84,85}Se was justified with its prominent occurrence in the selenium spectra. To verify selenium transitions from unwanted random coincidences two independent γ-transition sets of the yrast band of each cerium isotope were taken into account. The results are shown in fig. B.1; the upper panel is showing the coincident transitions belonging to ^{148}Ce. Moreover ^{86}Se is present due to the likeliness of the 2n decay as well as the 1438 keV ground state transition of ^{85}Se and the 1455 keV ground state transition of ^{84}Se. The 1279 keV line was assigned to ^{134}Te which is predicted the most produced isotope in cold neutron induced fission of ^{235}U and is thus a result of random coincidences. The lower panel is showing, besides ^{150}Ce, the 1455 keV line of ^{85}Se. The 1438 keV transition is not visible here which may be due to the reduced probability of a 1n decay. The ^{94}Sr transitions appear to be in coincidence with the 300/376 keV gates which are also members of ^{94}Sr.

B.1.1 ^{83}Se

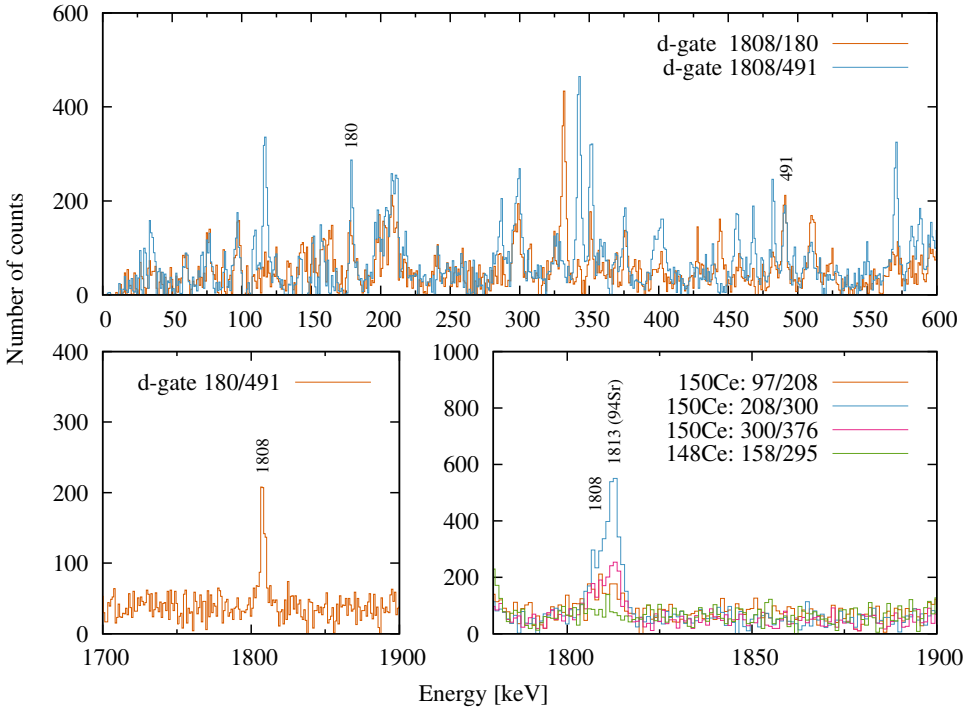

Figure B.2: Double gated γ-coincidence spectra of the ^{235}U(n, f) reaction. Upper panel: 1808 and 180 resp. 1808 and 491 keV gates of ^{83}Se. Lower-right panel: 180 and 491 keV gates coincident with 1808 keV transition in ^{83}Se. Lower-right panel: ^{148,150}Ce partner coincidences of ^{83}Se. See text for further explanations.

From the analyzed selenium isotopes, 83 is clearly produced the weakest. The low production yield makes a certain identification difficult at best. However, starting from the most recent γ-spectroscopic results on ^{83}Se by Fotiades *et al.* [134] and Porquet *et al.* [135] populated in fusion-fission reaction of a ^{18}O beam on a ^{208}Pb target, both assign a strong 1808 keV ground state transition to ^{83}Se. In fact this transition appears to be coincident with the selenium partner ^{150}Ce but not with other cerium isotopes, however, it is not inconsistent due to a preferred 3n emission; a variation in ^{150}Ce gates confirms this assumption (see fig. B.2 lower-right panel). The same figure also illustrates very well the limits of selectivity in double coincidence measurements. Although three different sets of double gates in ^{150}Ce were

chosen to verify the 1808 keV transition another peak at 1813 keV was seen which belongs to ^{94}Sr and which is "randomly" coincident with the energies 97, 208, 300 and 376 keV which also appear in ^{94}Sr and in its partners (notice the missing transitions in ^{148}Ce). Both, Fotiades and Porquet *et al.* also saw two cascading transitions of 491 and 180 keV populating the 1808 keV state. Coincidence plots of these transitions are shown in fig. B.2 (upper and lower-left panel). The energies deduced from these plots are presented in table B.1. It is interesting to mention that both, the 180 as well as the 491 keV transition, can be seen in both spectra of fig. B.2 (upper panel). However, the clear 1808 keV peak in fig. B.2 (lower-left panel) and the determined energies which are in good agreement with previously published results imply that these transitions populating the 1808 keV state. No other transitions could be clearly assigned to ^{83}Se.

Table B.1: Energies assigned to ^{83}Se within this work.

$\mathbf{E_{level}}$	$\mathbf{J_\Pi}^\dagger$	$\mathbf{E_\gamma}$	**Final level**	
keV		**keV**	**keV**	$\mathbf{J_\Pi}^\dagger$
0	$9/2^+$			
1808.5(2)	$13/2^+$	1808.5(2)	0	$9/2^+$
2299.6(2)	$15/2^+$	491.2(1)	1808.5(2)	$13/2^+$
2479.2(2)	$(17/2^+)$	179.6(1)	2299.6(2)	$15/2^+$

† Spin and parity assignment is taken from [134]

B.1.2 ^{84}Se

The even-even ^{84}Se at N=50 decays with an intense transition of 1455 keV into its ground state. Its affiliation to the seleniums can already be concluded with the results of fig. B.1. A coincidence plot of this transition with the 208 resp. 300 keV transition from ^{150}Ce is shown in B.3. Besides the coincident ^{150}Ce lines it also shows a couple of peaks in the mid-energy range of 1-2 MeV as well as a strong transition of 667 keV. Various experiments already showed that the 667 keV is depopulating the 4^+ state of ^{84}Se and decaying into the 1455 keV 2^+ state (cf. [136]). However, by comparing the intensities of these two transitions by gating on its fission partners this assignment could

be confirmed (see fig B.4); the intensity ratio for the 667 and the 1455 keV peak is constant in coincidence with ^{148}Ce, ^{149}Ce and ^{150}Ce, other than the ratio of ^{85}Se or ^{86}Se (cf. fig. B.4). Finally, fig. B.5 shows those transitions populating the 4^+ or states above. The results are summarized in table B.2.

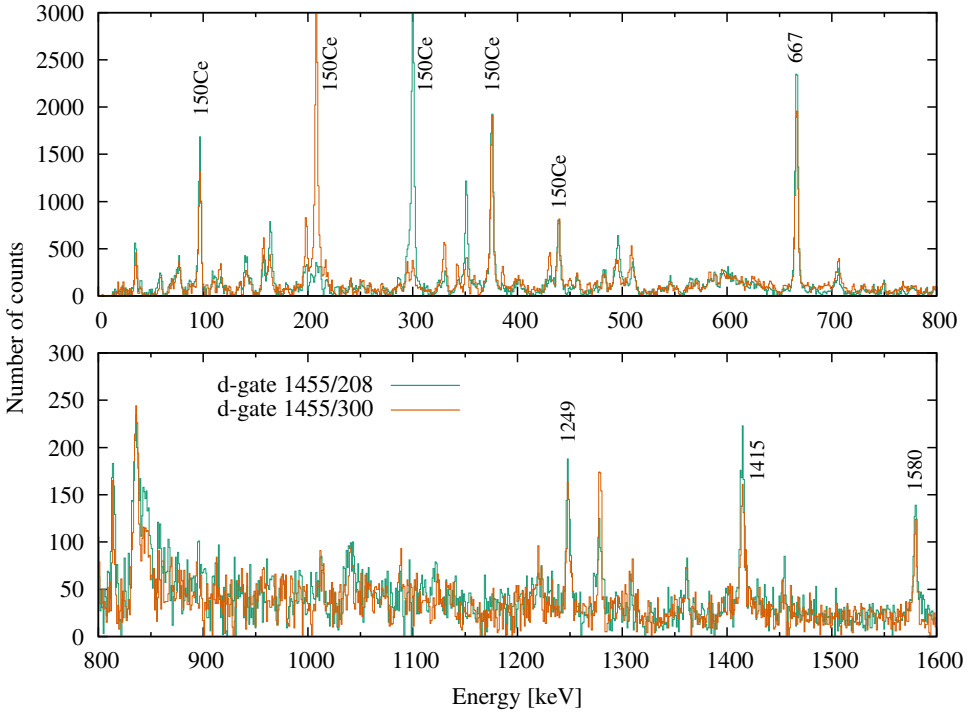

Figure B.3: Mixed coincidence spectra from ^{235}U(n, f). Orange: 1455 and 208 keV transition from ^{84}Se resp. ^{150}Ce. Green: 1455 and 300 keV transition from ^{84}Se resp. ^{150}Ce. See text for further information.

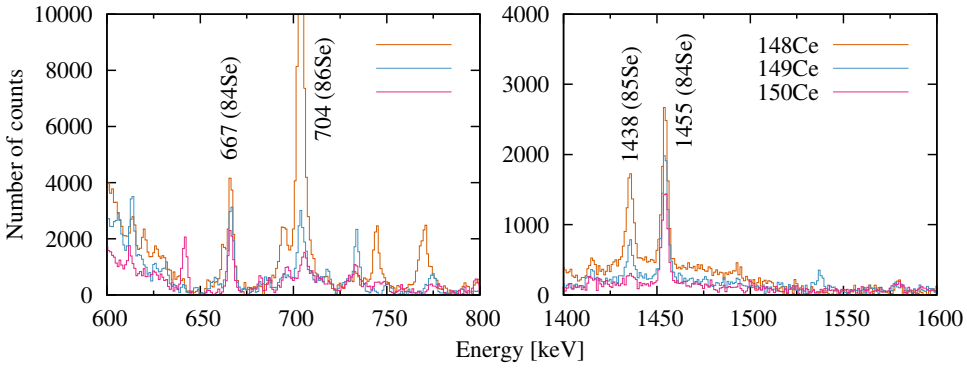

Figure B.4: Comparison of the intensity ratio for ^{84}Se, ^{85}Se and ^{86}Se by gating on the fission partner ^{148}Ce, ^{149}Ce and ^{150}Ce in the ^{235}U(n, f) reaction. See text for further explanations.

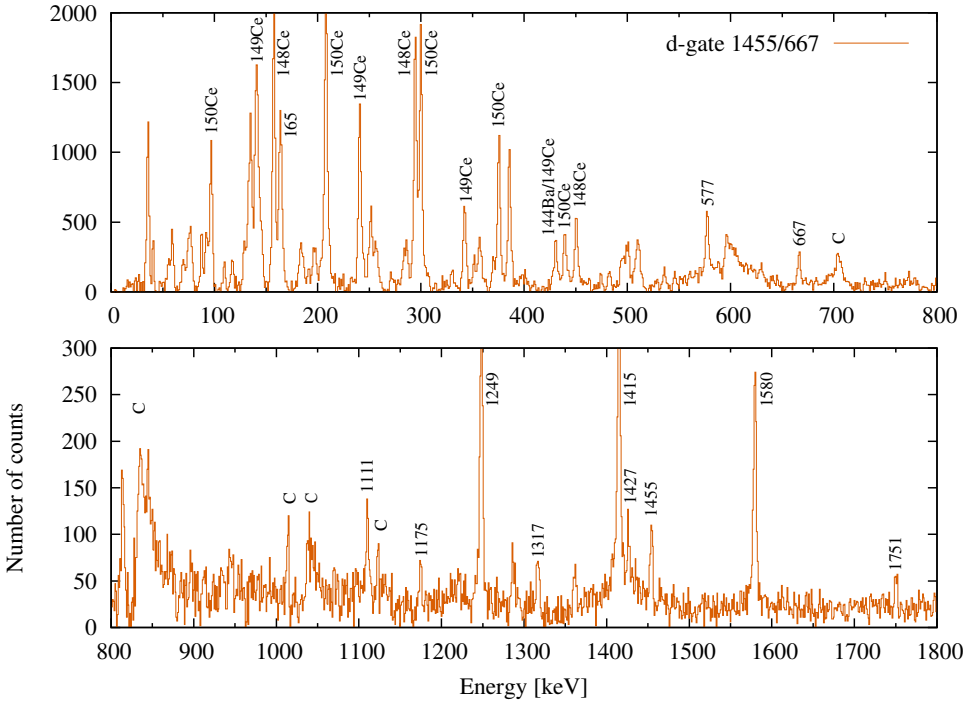

Figure B.5: Double coincidence spectra of the two cascading transitions 1455 and 667 keV in ^{84}Se. Contaminations or peaks which could not be assigned to a nucleus are labeled with C. See text for further explanations.

Table B.2: Energies assigned to ^{84}Se within this work.

E_{level} keV	J_Π †	E_γ keV	Final level keV	Final level J_Π †
0	0^+			
1454.9(1)	2^+	1454.9(1)	0	0^+
2121.9(1)	4^+	666.0(1)	1454.87(3)	2^+
2699.7(1)	(2,3,4)	577.9(1)	2121.86(5)	4^+
		1249.0(1)	1454.9(1)	2^+
3232.7(3)		1110.9(3)	2121.9(1)	4^+
3297.2(3)		1175.4(3)	2121.9(1)	4^+
		1843.7(2)	1454.9(1)	2^+
3370.8(1)		1248.9(1)	2121.9(1)	4^+
3409.4(5)		1287.7(5)	2121.9(1)	4^+
3439.0(4)		1317.1(4)	2121.9(1)	4^+
3537.3(3)		1415.4(2)	2121.9(1)	4^+
3542.3(4)		2087.4(4)	1454.9(1)	2^+
3548.7(3)		1426.8(2)	2121.9(1)	4^+
3701.9(1)		1580.1(1)	2121.9(1)	4^+
		164.5(1)	3537.3(3)	
3872.6(3)		1750.7(3)	2121.9(1)	4^+

† Spin and parity assignment is taken from nndc.

B.1.3 ^{85}Se

The N=51 ^{85}Se was most recently analyzed by Porquet *et al.* [135] in prompt gamma coincidences from spontaneous fission of ^{248}Cm and ^{252}Cf; they built the level scheme on the 1436 keV transition which is decaying into the ground state. In fact, this is the only transition of ^{85}Se which could be identified via its complementary fission partner ^{146}Ce, ^{148}Ce and ^{150}Ce within this work. Thus, mixed coincidence gates of 1436 keV and 295 respectively 158 keV of

the even-even ^{146}Ce, decaying with the emission of 3 neutrons, were used to build the level scheme above; a coincidence plot is shown in fig. B.6. It is conspicuous that some transitions from other nuclei, in particular ^{138}Ba and ^{134}Te, appear to be coincident with the chosen gates. For ^{138}Ba it is the 1435.8 keV ground state transition which is "polluting" the analysis, in the case of ^{134}Te a 1438.1 keV transition. Hence, the krypton fission partner of ^{138}Ba and the zirconium partner of ^{134}Te are present in a coincidence measurement as well which made the analysis more complex. However, three transitions were seen which could not be assigned to any other nucleus than ^{85}Se, 398, 540 and 883 keV. Figure B.7 shows the coincidence spectra of these transitions with the 1436 keV line. Both, the 540 and the 398 keV transition were observed in coincidence with each other but not with 883 keV. Thus, the assignment proposed by Porquet *et al.* seems consistent with the observations made in this work so that the 883 keV transition populates the 1436 keV state, and the 398 keV and the 540 keV transitions decay subse-

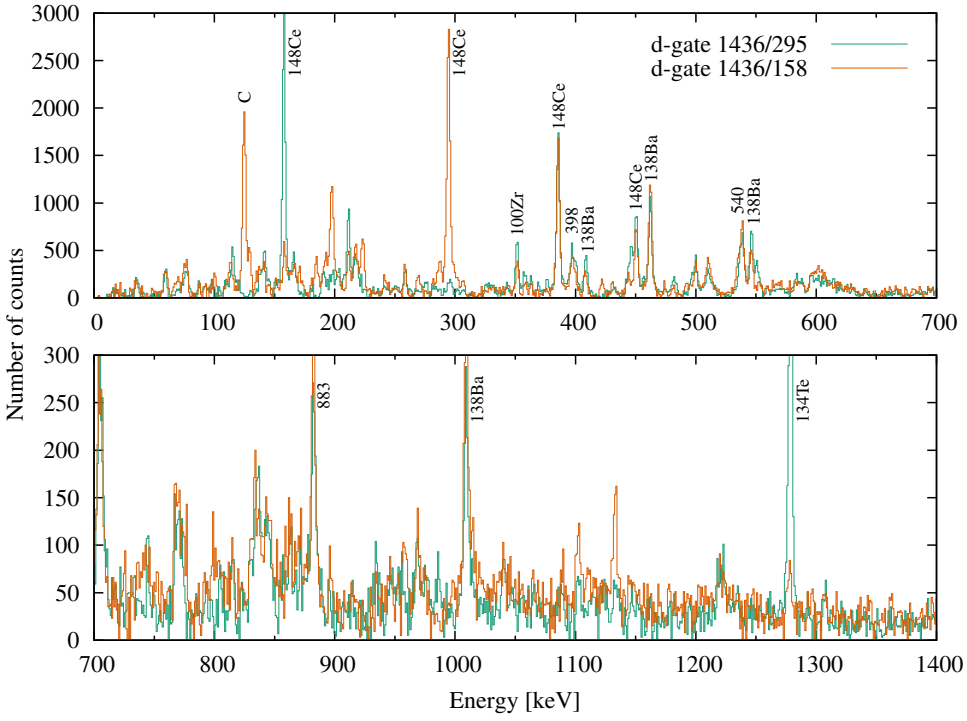

Figure B.6: Mixed double coincidence spectra within ^{235}U(n, f). 1436 keV transition from ^{85}Se gated with 295 keV resp. 158 keV from ^{148}Ce. See text for further explanations.

quently into it. This is also in agreement with the results of Kurpeta *et al.* [137]. The 444 keV transition proposed by Porquet *et al.* to depopulate the (17^+) state at 4254 keV is present in all spectra of fig. B.7. Also the prominent appearance of the discussed transitions of ^{85}Se in coincidence measurements with 444 keV give rise to the assumption that it is populating ^{85}Se from above. The 1436 keV peak in fig. B.7 might be a possible link between the corresponding states but the contamination of this transition discussed earlier made a proper assignment rather insecure. The results are presented in table B.3.

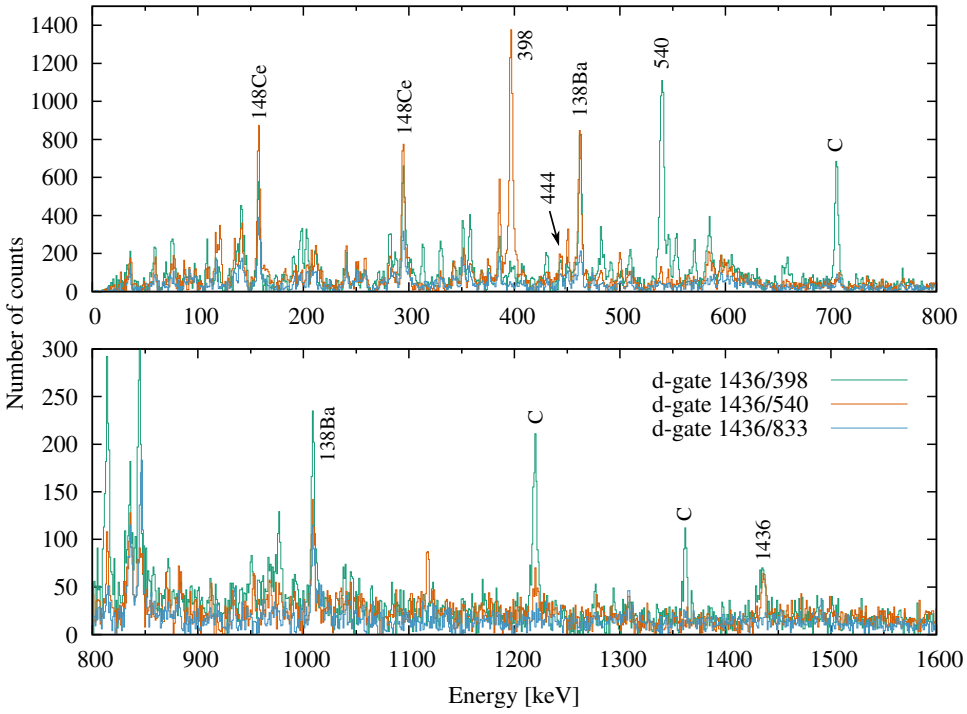

Figure B.7: Double coincidence spectra within ^{235}U(n, f). 1436 keV from ^{85}Se gated with 398, 540 and 883 keV. See text for further explanations.

Table B.3: Energies assigned to ^{85}Se within this work. The 444.3 keV transition could not be assigned with a state. See text for further explanations.

$\mathbf{E_{level}}$ keV	$\mathbf{J_\Pi}^\dagger$	$\mathbf{E_\gamma}$ keV	**Final level** keV	$\mathbf{J_\Pi}^\dagger$
0	$5/2^+$			
1435.7(1)	$(9/2^+)$	1435.7(1)	0	$5/2^+$
1976.4(1)	$(11/2^+)$	540.7(1)	1435.7(1)	$(9/2^+)$
2319.0(1)	$(11/2^+)$	883.3(1)	1435.7(1)	$(9/2^+)$
2373.8(1)	$(13/2^+)$	397.4(1)	1976.4(1)	$(11/2^+)$
		444.3(2)		

† Spin and parity assignment taken from [137].

Appendix C

Tabulated Spectroscopic n,fission Results with EXILL

Table C.1: Spectroscopic results from the γ coincidence analysis. The presented results for each nuclei do not claim to be complete within the feasibility of the EXILL data.

Nucleus	$\mathbf{E_{level}}$ **keV**	$\mathbf{J_\Pi}$	$\mathbf{E_\gamma}$ **keV**	**Final level** **keV**	$\mathbf{J_\Pi}$
^{82}Ge[(1)]	0	0+			
	1348.1(1)	2+	1348.1(1)	0	0+
	2286.5(2)	4+	938.4(2)	1348.1(1)	2+
	2932.9(3)	(5+,6+)	646.4(2)	2286.5(2)	4+
	3226.3(2)	(6+)	939.8(1)	2286.5(2)	4+
			1175.8(3)		
			359.5(2)		

(1) Spin and parity assignment is taken from [128]

Nucleus	E_{level} keV	J_Π	E_γ keV	Final level keV	Final level J_Π
$^{83}Se^{(2)}$	0	9/2+			
	1808.5(2)	13/2+	1808.5(2)	0	9/2+
	2299.6(2)	15/2+	491.2(1)	1808.5(2)	13/2+
	2479.2(2)	(17/2+)	179.6(1)	2299.6(2)	15/2+
$^{84}Se^{(3)}$	0	0+			
	1454.9(1)	2+	1454.9(1)	0	0+
	2121.9(1)	4+	667.0(1)	1454.9(1)	2+
	2699.7(1)	(2,3,4)	577.9(1)	2121.9(1)	4+
			1249.0(1)	1454.9(1)	2+
	3232.7(3)		1110.9(3)	2121.9(1)	4+
	3297.2(3)		1175.4(3)	2121.9(1)	4+
			1843.7(2)	1454.9(1)	2+
	3370.8(1)		1248.9(1)	2121.9(1)	4+
	3409.4(5)		1287.7(5)	2121.9(1)	4+
	3439.0(4)		1317.1(4)	2121.9(1)	4+
	3537.3(1)		1415.4(1)	2121.9(1)	4+
	3542.3(4)		2087.4(4)	1454.9(1)	2+
	3548.7(2)		1426.8(3)	2121.9(1)	4+
	3701.9(1)		1580.01(1)	2121.9(1)	4+
			164.5(1)	3537.3(1)	
	3872.57(25)		1750.7(3)	2121.9(1)	4+
$^{85}Se^{(4)}$	0	5/2+			
	1435.7(1)	(9/2+)	1435.7(1)	0	5/2+
	1976.4(1)	(11/2+)	540.7(1)	1435.7(1)	(9/2+)
	2319.0(1)	(11/2+)	883.3(1)	1435.7(1)	(9/2+)
	2373.8(1)	(13/2+)	397.4(1)	1976.4(1)	(11/2+)
			444.3(2)		

(2) Spin and parity assignment is taken from [134]
(3) Spin and parity assignment is taken from [138]
(4) Spin and parity assignment is taken from [137]

Nucleus	E_{level} keV	J_Π	E_γ keV	Final level keV	Final level J_Π
^{87}Kr[5]	0	5/2+			
	1419.7(1)	(7/2+)	1419.7(1)	0	5/2+
	1475.8(1)	3/2+,5/2+	1475.8(1)	0	5/2+
	1577.7(1)	9/2+	1577.7(1)	0	5/2+
	1841.4(1)	(9/2+)	421.7(1)	1419.7(1)	(7/2+)
	2071.7(1)		230.2(1)	1841.4(1)	(9/2+)
	2105.4(1)	11/2+	264.0(1)	1841.4(1)	(9/2+)
	2258.8(1)	11/2-	681.1(1)	1577.7(1)	9/2+
			417.0(5)	1841.4(1)	(9/2+)
	2451.5(1)		610.1(1)	1841.4(1)	(9/2+)
	2614.8(2)	(13/2+)	509.4(2)	2105.4(1)	11/2+
	3525.5(1)	(15/2-)	1266.8(1)	2258.8(1)	11/2-
	3526.2(2)		911.4(1)	2614.8(2)	(13/2+)
	4088.6(2)		563.1(1)	3525.5(1)	(15/2-)
	4416.9(2)		2575.4(2)	1841.4(1)	(9/2+)
	4595.9(2)		2754.5(2)	1841.4(1)	(9/2+)
	4668.0(4)		2826.5(4)	1841.4(1)	(9/2+)
	4711.1(2)		2869.7(2)	1841.4(1)	(9/2+)
	4785.2(4)		2943.8(4)	1841.4(1)	(9/2+)
	4859.0(4)		3017.6(3)	1841.4(1)	(9/2+)
	5382.5(4)		3541.1(4)	1841.4(1)	(9/2+
^{89}Kr[6]	0	3/2(+)			
	28.6(1)*	5/2+		0	3/2(+)
	982.2(1)	9/2+	953.6(1)	28.6(1)	5/2+
	1772.4(1)	11/2-	790.1(1)	982.2(1)	9/2+
	2278.1(1)		1295.9(1)	982.2(1)	9/2+
	2647.1(3)		874.8(3)	1772.4(1)	11/2-
	3214.5(1)		936.4(1)	2278.1(1)	
	4374.6(1)		1160.0(1)	3214.5(1)	

[5] Spin and parity assignment is taken from [138]

[6] Spin and parity assignment is taken from [139]

* This state was not observed within this work. The value was taken from [139]

Nucleus	E_{level} keV	J_Π	E_γ keV	Final level keV	Final level J_Π
^{92}Kr[7]	0	0+			
	768.4(2)	2+	768.4(2)	0	0+
	1803.1(2)	4+	1034.7(2)	768.4(2)	2+
	1984.2(3)		181.1(1)	1803.1(2)	4+
	2065.8(2)	4	1297.4(1)	768.4(2)	2+
	2077.0(2)		1308.7(1)	768.4(2)	2+
	2491.6(3)		507.4(1)	1984.2(3)	
			688.29(5)	1803.1(2)	4+
	2834.5(3)		1031.4(2)	1803.1(2)	4+
	3035.7(3)		1232.6(1)	1803.1(2)	4+
	3171.8(3)		1368.7(1)	1803.1(2)	4+
	3178.1(3)		1112.3(1)	2065.8(2)	4
	3593.9(4)		759.5(2)	2834.5(3)	
	3627.4(4)		1135.9(1)	2491.6(3)	
			455.5(1)	3171.8(3)	
	3845.4(4)		809.8(1)	3035.7(3)	
	4175.7(4)		548.3(1)	3627.4(4)	
	4980.3(4)		804.6(1)	4175.7(4)	
^{93}Kr[8]	0	1/2+			
	117.4(1)	(3/2+)	117.4(1)	0	1/2+
	354.7(2)	(7/2+)	237.3(1)	117.4(1)	(3/2+)
	982.8(2)	(11/2+)	628.1(2)	354.7(2)	(7/2+)
	1516.4(3)	(15/2+)	533.7(1)	982.8(2)	(11/2+)
	2187.4(3)		671.0(1)	1516.4(3)	(15/2+)
	2401.4(3)	(19/2+)	885.0(1)	1516.4(3)	(15/2+)
	3199.6(3)	(23/2+)	798.2(2)	2401.4(3)	(19/2+)

[7] Spin and parity assignment is taken from [69]
[8] Spin and parity assignment is taken from [70]

Nucleus	E_{level} keV	J_Π	E_γ keV	Final level keV	Final level J_Π
^{94}Kr[9]	0	0p			0+
	665.8(1)	(2+)	665.8(1)	0	2+
	1519.5(1)	(4+)	853.7(1)	665.82(11)	(4+)
	2520.8(2)	(6+)	1001.3(1)	1519.54(14)	(6+)
	3257.8(4)		737.0(3)	2520.81(18)	
^{95}Rb[10]	0	5/2-			
	619.3(1)	(7/2-)	619.3(1)	0	5/2-
	810.6(1)	(9/2+)	810.6(1)	0	5/2-
			191.1(1)	810.6(1)	(9/2+)
	1399.7(2)		589.1(1)	810.6(1)	(9/2+)
	1567.2(2)		167.5(1)	1399.7(2)	
	1567.4(2)		757.0(3)	810.6(1)	(9/2+)
^{89}Sr[11]	0	5/2+			
	1031.9(1)	1/2+	1031.9(1)	0	5/2+
	1473.2(2)	(7/2)+	1473.2(2)	0	5/2+
	1939.5(2)	5/2+	466.3(1)	1473.2(2)	(7/2)+
	2006.9(3)	3/2+	2006.9(3)	0	5/2+
	2280.0(1)	11/2-	1248.1(1)	1031.9(1)	1/2+
			272.5(3)	2006.9(3)	3/2+
	2569.9(1)	(3/2)-	289.9(3)	1473.2(1)	11/2-
			1538.0(1)	1031.9(1)	1/2+
	3227.6(1)	(3/2)-	657.8(1)	1473.2(1)	(3/2)-
			2196.0(4)	1031.9(1)	1/2+
		(3/2)-	947.7(1)	1473.2(2)	11/2-

[9] Spin and parity assignment is taken from [69]
[10] Spin and parity assignment is taken from [138]
[11] Spin and parity assignment is taken from [138]

Nucleus	E_{level} keV	J_Π	E_γ keV	Final level keV	Final level J_Π
$^{91}Sr^{(12)}$	0	5/3+			
	94.0(1)	(3/2)+	94.0(1)	0	5/3+
	439.4(1)	(+)	345.4(1)	94.0(1)	(3/2)+
	1042.2(1)		602.8(1)	439.4(1)	(+)
	1230.9(2)		1136.9(1)	94.0(1)	(3/2)+
	2065.0(2)		1625.6(1)	439.4(1)	(+)
	2159.3(3)		1719.9(1)	439.4(1)	(+)
	2658.0(1)		1615.9(1)	1042.2(1)	
	3312.0(3)		2872.6(2)	439.4(1)	(+)
	3364.8(1)		2925.3(1)	439.4(1)	(+)
	3386.6(3)		2344.4(2)	1042.2(1)	
	3446.3(2)		3006.8(2)	439.4(1)	(+)
	3532.4(2)		3092.9(2)	439.4(1)	(+)
	3547.2(2)		3107.8(2)	439.4(1)	(+)
	3567.9(3)		3128.5(3)	439.4(1)	(+)
	3586.8(2)		3147.4(2)	439.4(1)	(+)
	3646.1(6)		3206.7(6)	439.4(1)	(+)
	3662.4(3)		3223.0(3)	439.4(1)	(+)
	3695.1(6)		3255.6(6)	439.4(1)	(+)
	3723.0(6)		3283.6(6)	439.4(1)	(+)
	3736.8(2)		2505.9(8)	1230.9(2)	
	3776.3(5)		3336.9(5)	439.4(1)	(+)
	4043.1(2)		3603.7(2)	439.4(1)	(+)
	4078.3(2)		2847.2(1)	1230.9(2)	
			3639.0(2)	439.4(1)	(+)
	4189.2(2)		3147.0(1)	1042.2(1)	
	4265.7(2)		3223.5(2)	1042.2(1)	
	4239.9(3)		3800.5(3)	439.4(1)	(+)
	4327.4(2)		3887.9(2)	439.4(1)	(+)
			3285.2(5)	1042.2(1)	

(12) Spin and parity assignment is taken from [138]

Nucleus	E_{level} keV	J_Π	E_γ keV	Final level keV	Final level J_Π
^{98}Sr[13]	0	0+			
	144.3(1)	2+	144.3(1)	0	0+
	433.5(2)	4+	289.2(2)	144.3(1)	2+
	866.7(2)	6+	433.2(1)	433.5(2)	4+
	1433.0(2)	8+	566.3(1)	866.7(2)	6+
	1837.5(2)	(3+)	1693.1(1)	144.3(1)	2+
	1978.0(2)	(4+)	140.5(2)	1837.5(2)	(3+)
	2043.3(3)		1609.8(2)	433.5(2)	4+
	2121.6(3)	(10+)	688.7(2)	1433.0(2)	8+
	2152.6(2)	(5+)	174.6(1)	1978.0(2)	(4+)
			315.1(1)	1837.5(2)	(3+)
	2359.9(3)	(6+)	207.2(1)	2152.6(2)	(5+)
			382.0(1)	1978.0(2)	(4+)
	2431.1(4)		1997.1(3)	433.5(2)	4+
			1564.9(1)	866.7(2)	6+
	2533.0(2)	(6+)	1666.3(1)	866.7(2)	6+
	2601.2(3)	(7+)	241.2(1)	2359.9(3)	(6+)
			448.9(1)	1837.5(2)	(3+)
	2770.5(3)		237.5(2)	2533.0(2)	(6+)

[13] Spin and parity assignment is taken from [140]

Appendix D

Activity Measurement Spectra from HIGS

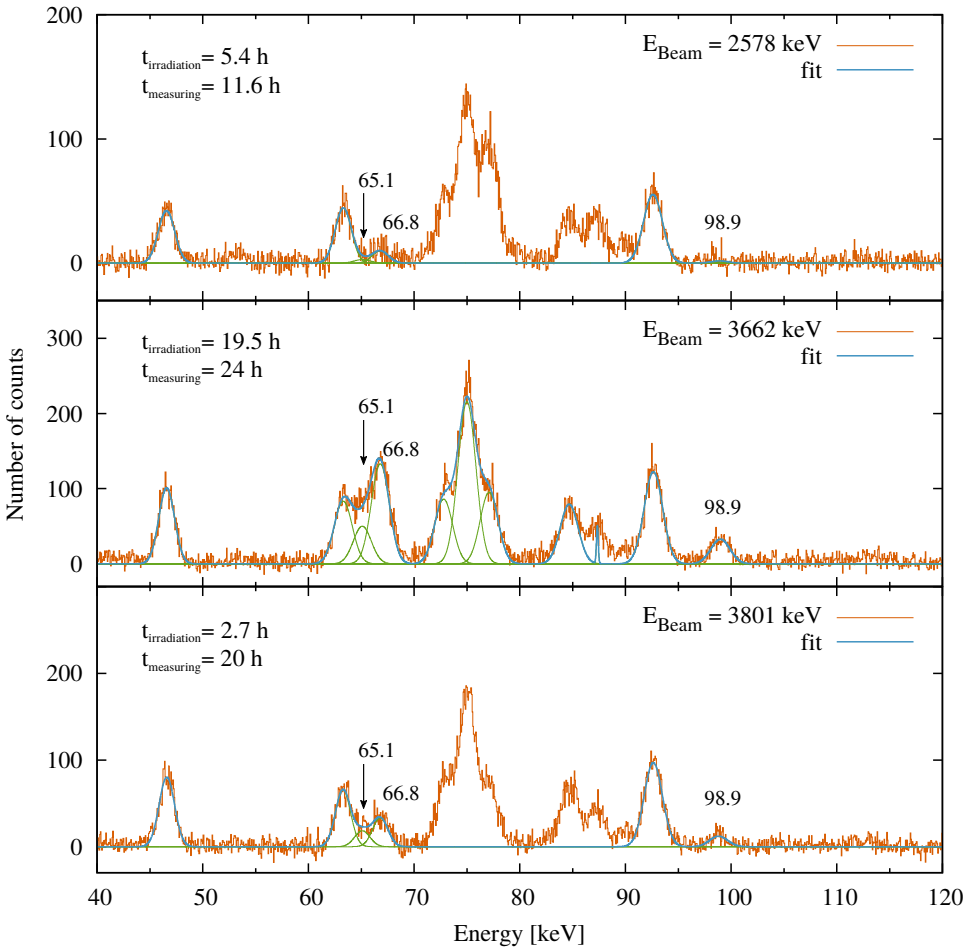

Figure D.1: Activation spectra of nat. platinum foils irradiated with a γ-beam of 2.58, 3.66 and 3.80 MeV, respectively. The irradiation and measurement time are indicated.

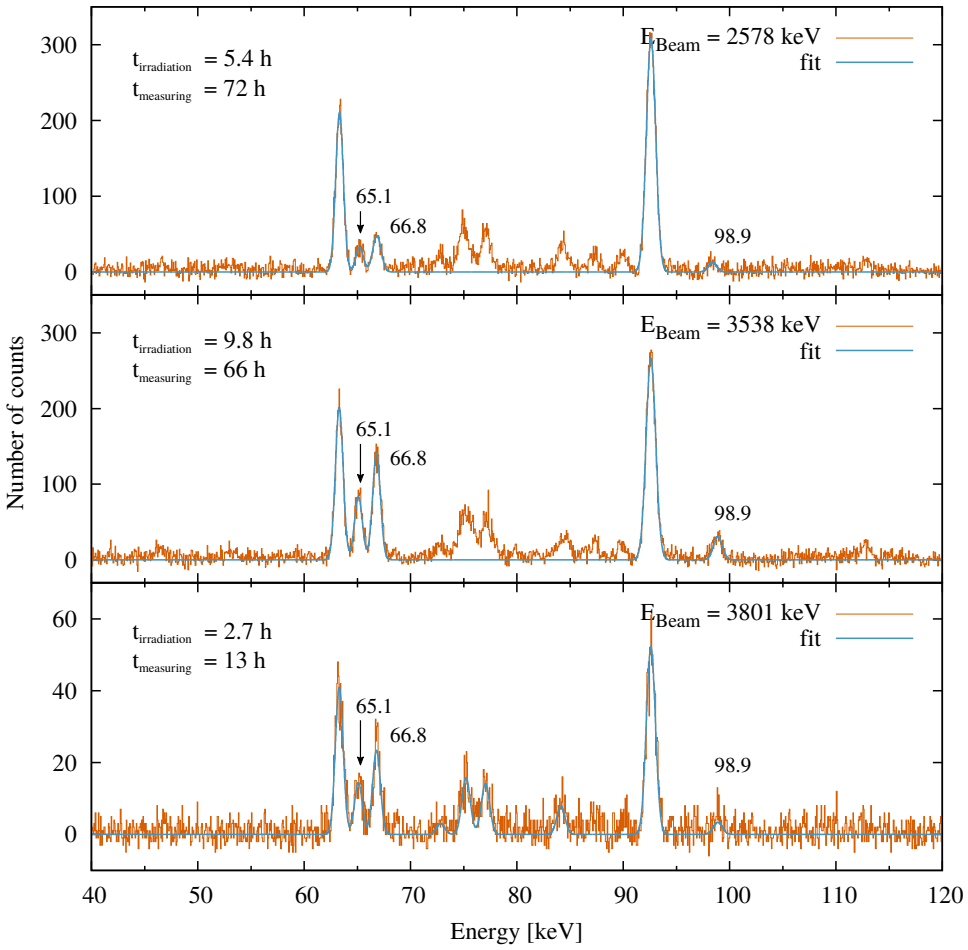

Figure D.2: Activation spectra of nat. platinum foils irradiated with a γ-beam of 2.58, 3.54 and 3.80 MeV, respectively. The irradiation and measurement time are indicated.

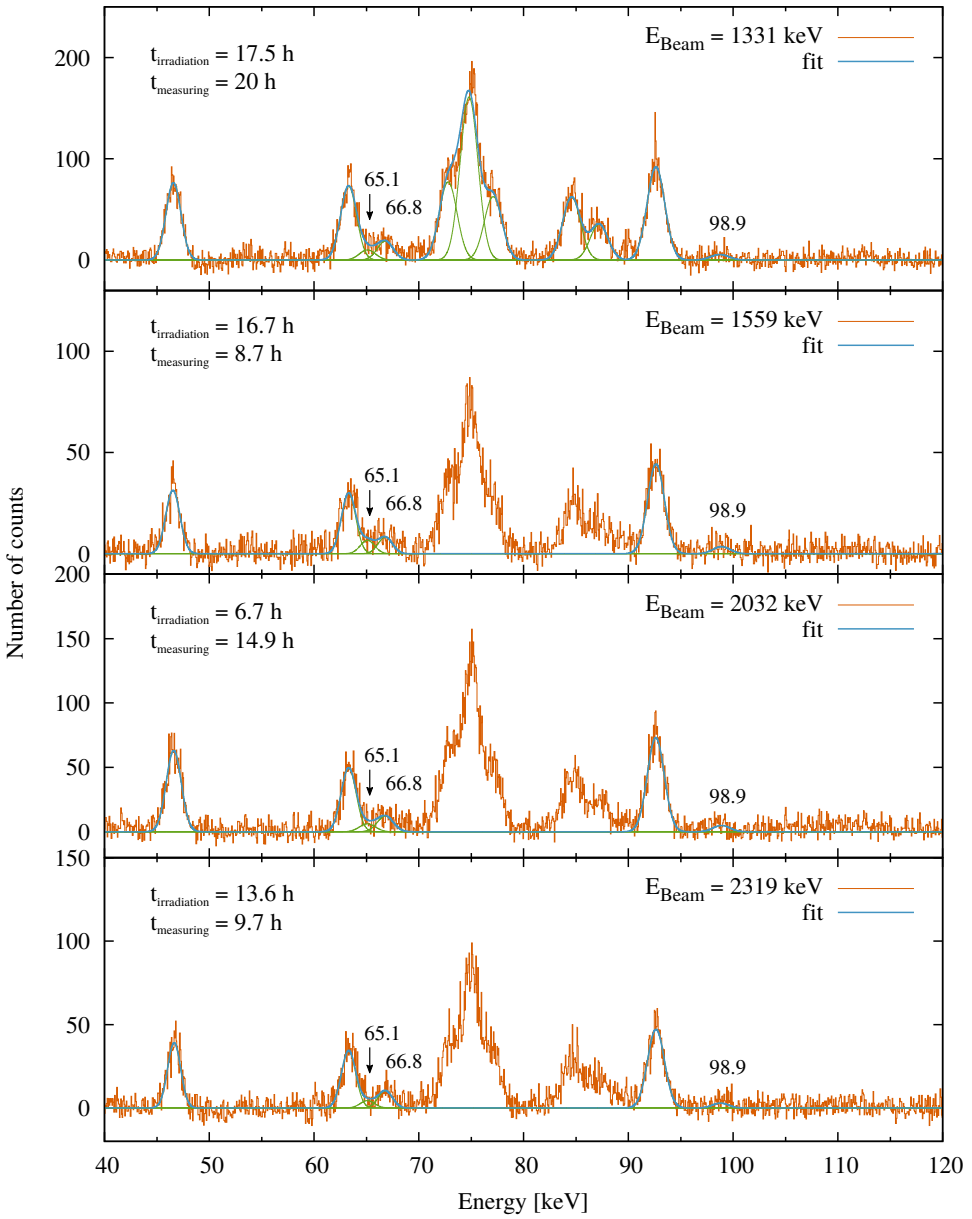

Figure D.3: Activation spectra of nat. platinum foils irradiated with a γ-beam of 1.33, 1.59, 2.03 and 2.32 MeV, respectively. The irradiation and measurement time are indicated.

Acknowledgement

In retrospect, I have to say, that I was very lucky to work with the people I finally worked with during the last three years. I am honestly grateful for this opportunity. This thesis would not have been possible without the help and the support of these people to which I would like to express my deepest gratitude:

Gilles de France, who, as the director of my thesis, supervised me during the past three years of my PhD. I am very grateful for the confidence he was having into me and my work at each moment of this period, giving me the freedom to work independently and at the same time being always informed about the progress of my work to keep me on the right track.

Ulli Köster, for almost everything concerning this thesis, and beyond. I truly don't know where to start, nor where to stop. But this thesis would not have been possible without him.

Jean-Marc Régis for his enormous help on the analysis of lifetime measurements, which he was willing to discuss with me in an uncountable amount of emails.

Waldemar Urban, for all the work he invested into the data processing of the $^{194}\mathrm{Pt}(\mathrm{n},\gamma)$ experiment and his profound expertise helping me with its analysis.

Jan Jolie, who, as my former PhD supervisor, gave me the opportunity to continue my work within this GANIL-ILL collaboration in the first place.

The group of the TUNL facility, especially Werner Tornow, Sean Finch, Krishichayan and Megha Bhike for a very fruitful collaboration at HIGS and the following support within a great communication.

Gilbert Bélier, for inviting me to the CEA Bruyères-le-Châtel, and the support in the experiments we performed for the realization of a fission event tagger for the ILL. In this context I would also like to thank Jean Aupiais for the production of the active targets and Martine Millerioux for showing me the art of spin coating.

Felix Kandzia, for accurately reviewing my thesis in the last moment but also for his company at the ILL. I hope you can use at least a bit from this work on the fission tagger.

Gary Simpson, for his interest in my work and all the suggestions and help he was offering me during the time at the ILL.

Christelle Schmitt, for patiently introducing me to the use of the GEF code.

Nima Saed-Samii, for his IT support over all these years.

Matthias Rudigier, for the insightful discussions on the fast-timing technique and much more.

Caterina Michelagnoli, for her help on the EXILL experiments and for her company at GANIL and ILL.

The GANIL group, especially Piet van Isacker, Emmanuel Clément, François de Oliveira, Xavier Ledoux, Dieter Ackermann and Beyhan Bastin, and

the ILL group, especially Aurélien Blanc, Michael Jentschel, Torsten Soldner, Oliver Zimmer and Kim Yung hee for the help which they offered to me in the last years and the very welcoming and familiar atmosphere.

Also I would like to thank the students and people I met during the last years for all the discussions inside, but also outside work: Bartholomé Cauchois, Mathieu Babo, Coralie Lederoff, Lucas Schwob, Quentin Fable, Pierre Chauveau, Florent Boulay, José Luis, Arkadiusz Mika, Benoit Mauss, Richard Wagner, Florian Rumenapp and Philipp Gausmann.

Especially, I would like to thank my parents, my brother and his family, my grandmother and Pascale Randriantiana for their support in all respects.

Bibliography

[1] E. Cheifetz, R. C. Jared, S. G. Thompson and J. B. Wilhelmy, Experimental Information Concerning Deformation of Neutron Rich Nuclei in the $A \sim 100$ Region, *Phys. Rev. Lett.* 25, 38–43 (1970)

[2] P. Federman and S. Pittel, Towards a unified microscopic description of nuclear deformation, *Physics Letters B* 69, 385 - 388 (1977)

[3] P. Federman and S. Pittel, Unified shell-model description of nuclear deformation, *Phys. Rev. C* 20, 820–829 (1979)

[4] F.C. Charlwood, K. Baczynska, J. Billowes et al., Nuclear charge radii of molybdenum fission fragments, *Physics Letters B* 674, 23 - 27 (2009)

[5] M. Keim, E. Arnold, W. Borchers et al., Laser-spectroscopy measurements of 72–96kr spins, moments and charge radii, *Nuclear Physics A* 586, 219 - 239 (1995)

[6] C. Thibault, F. Touchard, S. Büttgenbach et al., Hyperfine structure and isotope shift of the, *Phys. Rev. C* 23, 2720–2729 (1981)

[7] F. Buchinger, E. B. Ramsay, E. Arnold et al., Systematics of nuclear ground state properties in $^{78^{-}100}$Sr by laser spectroscopy, *Phys. Rev. C* 41, 2883–2897 (1990)

[8] P. Lievens, R.E. Silverans, L. Vermeeren et al., Nuclear ground state properties of 99sr by collinear laser spectroscopy with non-optical detection, *Physics Letters B* 256, 141 - 145 (1991)

[9] B. Cheal, M.D. Gardner, M. Avgoulea et al., The shape transition in the neutron-rich yttrium isotopes and isomers, *Physics Letters B* 645, 133 - 137 (2007)

[10] P. Campbell, H. L. Thayer, J. Billowes et al., Laser spectroscopy of cooled zirconium fission fragments, *Phys. Rev. Lett.* 89, 082501 (2002)

[11] U. Hager, A. Jokinen, V.-V. Elomaa et al., Precision mass measurements of neutron-rich yttrium and niobium isotopes, *Nuclear Physics A* 793, 20 - 39 (2007)

[12] U. Hager, T. Eronen, J. Hakala et al., Publisher's Note: First Precision Mass Measurements of Refractory Fission Fragments [Phys. Rev. Lett. 96, 042504 (2006)], *Phys. Rev. Lett.* 96, 069901 (2006)

[13] S. Rinta-Antila, T. Eronen, V. V. Elomaa et al., Decay study of neutron-rich zirconium isotopes employing a penning trap as a spectroscopy tool, *The European Physical Journal A* 31, 1–7 (2007)

[14] A. Kankainen, L. Batist, S. A. Eliseev et al., Mass measurements of neutron-deficient nuclides close to a = 80 with a penning trap, *The European Physical Journal A - Hadrons and Nuclei* 29, 271–280 (2006)

[15] S. Rahaman, U. Hager, V. V. Elomaa et al., Precise atomic masses of neutron-rich br and rb nuclei close to the r-process path, *The European Physical Journal A* 32, 87–96 (2007)

[16] G. Audi, A.H. Wapstra and C. Thibault, The ame2003 atomic mass evaluation: (ii). tables, graphs and references, *Nuclear Physics A* 729, 337 - 676 (2003)

[17] Richard F. Casten, *Nuclear Structure from a Simple Perspective*, Oxford Science Publications 2nd edition (2001)

[18] Kris Heyde and John L. Wood, Shape coexistence in atomic nuclei, *Reviews of Modern Physics* 83, 1467–1521 (2011)

[19] W. Urban, J.L. Durell, A.G. Smith et al., Medium-spin structure of 96,97Sr and 98,99Zr nuclei and the onset of deformation in the A$\sim$100 region, *Nuclear Physics A* 689, 605 - 630 (2001)

[20] W. Urban, J.A. Pinston, T. Rzaca-Urban et al., First observation of the $\nu\,9/2[404]$ orbital in the $A \sim 100$ mass region, *Eur. Phys. J. A* 16, 11-15 (2003)

[21] W. Urban, J. a. Pinston, J. Genevey et al., The $\nu 9/2$ [404] orbital and the deformation in the A$\sim$100 region, *European Physical Journal A* 22, 241 - 252 (2004)

[22] G. Bocchi, S. Leoni, B. Fornal et al., The mutable nature of particle-core excitations with spin in the one-valence-proton nucleus ^{133}Sb, *Physics Letters B* 760, 273 - 278 (2016)

[23] J. Jolie, J.-M. Régis, D. Wilmsen et al., The (n,γ) campaigns at EXILL, *EPJ Web of Conferences* 93, 01014 (2015)

[24] M. Jentschel, A. Blanc, G. de France et al., Exill - a high-efficiency, high-resolution setup for gamma-spectroscopy at an intense cold neutron beam facility, *Journal of Instrumentation* 12, P11003 (2017)

[25] G. de France, A. Blanc, F. Drouet et al., The EXILL campaign, *Pramana Journal of Physics* 85, 467 - 478 (2015)

[26] ILL webpage, https://www.ill.eu/about/what-is-the-ill/ (online accessed on April 22, 2017)

[27] ILL webpage, https://www.ill.eu/instruments-support/instruments-groups/instruments/pf1b/description/instrument-layout/ (online accessed on April 22, 2017)

[28] C.W. Beausang, S.A. Forbes, P. Fallon et al., Measurements on prototype Ge and BGO detectors for the Eurogam array, *Nuclear Instruments and Methods in Physics Research Section A: Accelerators, Spectrometers, Detectors and Associated Equipment* 313, 37 - 49 (1992)

[29] J. Simpson, The Euroball Spectrometer, *Zeitschrift für Physik A Hadrons and Nuclei* 358, 139 - 143 (1997)

[30] I-Yang Lee, The GAMMASPHERE, *Nuclear Physics A* 520, 641 - 655 (1990)

[31] J. Simpson, F. Azaiez, G. De France et al., The EXOGAM array: A radioactive beam gamma-ray spectrometer, *Acta Physica Hungarica, Series A: Heavy Ion Physics* 11, 159 - 188 (2000)

[32] J.-M. Régis, G.S. Simpson, A. Blanc et al., Germanium-gated g–g fast timing of excited states in fission fragments using the EXILL/FATIMA spectrometer, *Nuclear Instruments and Methods in Physics Research Section A: Accelerators, Spectrometers, Detectors and Associated Equipment* 763, 210 - 220 (2014)

[33] D. Bazzacco et al., The GASP experiment: Project report of a gamma spectrometer, *INFN-BE-90-11* (1990)

[34] J. M. Régis, H. Mach, G. S. Simpson et al., The generalized centroid difference method for picosecond sensitive determination of lifetimes

of nuclear excited states using large fast-timing arrays, *Nuclear Instruments and Methods in Physics Research, Section A: Accelerators, Spectrometers, Detectors and Associated Equipment* 726, 1 - 12 (2013)

[35] webpage, https://www.nobelprize.org/nobel_prizes/physics/laureates/1954/bothe-bio.html (online accessed on April 22, 2017)

[36] webpage, https://forge.epn-campus.eu/projects/lstdataprocess/files (online accessed on April 22, 2017)

[37] webpage, https://github.com/rlica/gaspware (online accessed on April 22, 2017)

[38] Kenneth S. Krane, *Introductory Nuclear Physics*, John Wiley and sons 3rd edition (1987)

[39] K.-H. Schmidt, B. Jurado, C. Amouroux and C. Schmitt, General Description of Fission Observables: GEF Model Code, *Nuclear Data Sheets* 131, 107 - 221 (2016)

[40] James Terrell, Distributions of fission neutron numbers, *Physical Review* 108, 783 - 789 (1957)

[41] James Terrell, Fission neutron spectra and nuclear temperatures, *Physical Review* 113, 527 - 541 (1959)

[42] James Terrell, Neutron yields from individual fission fragments, *Phys. Rev.* 127, 880 - 904 (1962)

[43] V.F. Apalin, Yu.N. Gritsyuk, I.E. Kutikov, V.I. Lebedev and L.A. Mikaelyan, On the number of neutrons emitted by ^{235}U fission fragments, *Nuclear Physics* 55, 249 - 256 (1964)

[44] R. B. Leachman, Emission of Prompt Neutrons from Fission, *Phys. Rev.* 101, 1005 - 1011 (1956)

[45] M. S. Zucker and N. E. Holden, Energy dependence of the neutron multiplicity in fast neutron induced fission of ^{235}U, ^{238}U and ^{239}Pu, *report BNL–38491* (1986)

[46] E. J. Axton, *Nucl. Stand. Ref. Data* 214 (1985)

[47] M. A. C. Hotchkis et al., Rotational bands in the mass 100 region, *Nucl. Phys.* A530, 111-134 (1991)

[48] M. A. C. Hotchkis, J. L. Durell, J. B. Fitzgerald et al., New neutron-rich nuclei ^{103,104}Zr and the A∼100 region of deformation, *Phys. Rev. Lett.* 64, 3123 - 3126 (1990)

[49] W. Urban, A. Korgul and T. Rzaca-Urban, First observation of excited states in ^{137}Te and the extent of octupole instability in the lanthanides, *Physical Review C* 61, 137 - 140 (2000)

[50] A. Astier, M. G. Porquet, T. Venkova et al., High-spin structures of five N=82 isotopes: ^{136}Xe, ^{137}Cs, ^{138}Ba, ^{139}La, and ^{140}Ce, *Physical Review C - Nuclear Physics* 85, 1 - 17 (2012)

[51] A. Astier, T. Konstantinopoulos, M.-G. Porquet et al., High-spin structures of $^{138}_{57}\mathrm{La}_{81}$, *Phys. Rev. C* 89, 034310 (2014)

[52] P J Nolan and J F Sharpey-Schafer, The measurement of the lifetimes of excited nuclear states, *Reports on Progress in Physics* 42, 1 (1979)

[53] Glenn F. Knoll, *Radiation detection and measurement*, John Wiley and sons 3rd edition (2000)

[54] H. Mach, R. L. Gill and M. Moszynski, A method for picosecond lifetime measurements for neutron-rich nuclei. Outline of the method, *Nuclear Inst. and Methods in Physics Research, A* 280, 49 - 72 (1989)

[55] L. Boström, B. Olsen, W. Schneider and E. Matthias, Numerical analysis of the time spectrum of delayed coincidences, I, *Nuclear Instruments and Methods* 44, 61 - 64 (1966)

[56] B. Olsen and L. Boström, Numerical analysis of the time spectrum of delayed coincidences, II, *Nuclear Instruments and Methods* 44, 65 - 72 (1966)

[57] Z. Bay, Calculation of Decay Times from Coincidence Experiments, *Phys. Rev.* 77, 419 - 419 (1950)

[58] H. Mach, F.K. Wohn, G. Molnár et al., Retardation of B(E2; $0_1^+ \rightarrow 2_1^+$) rates in $^{90-96}$Sr and strong subshell closure effects in the A∼100 region, *Nuclear Physics A* 523, 197 - 227 (1991)

[59] M. Moszyński and H. Mach, A method for picosecond lifetime measurements for neutron-rich nuclei, *Nuclear Instruments and Methods in Physics Research Section A: Accelerators, Spectrometers, Detectors and Associated Equipment* 277, 407 - 417 (1989)

[60] J.-M. Régis, G. Pascovici, J. Jolie and M. Rudigier, The mirror symmetric centroid difference method for picosecond lifetime measurements via γ-γ Coincidences using very fast LaBr 3(Ce) scintillator detectors, *Nuclear Instruments and Methods in Physics Research, Section A: Accelerators, Spectrometers, Detectors and Associated Equipment* 622, 83 - 92 (2010)

[61] J.-M. Régis, M. Rudigier, J. Jolie et al., The time-walk of analog constant fraction discriminators using very fast scintillator detectors with linear and non-linear energy response, *Nuclear Instruments and Methods in Physics Research Section A: Accelerators, Spectrometers, Detectors and Associated Equipment* 684, 36 - 45 (2012)

[62] J.-M. Régis, J. Jolie, N. Saed-Samii et al., $B(E2; 2_1^+ \rightarrow 0_1^+)$ value in ^{90}Kr, *Phys. Rev. C* 90, 067301 (2014)

[63] J Régis, J Jolie, H Mach et al., The Generalized Centroid Difference method for lifetime measurements via γ - γ coincidences using large fast-timing arrays, *EPJ Web of Conferences* 93 (2015)

[64] N. Saed-Samii, *SocoV2* (private communication)

[65] S. Mukhopadhyay, L. S. Danu, D. C. Biswas et al., Prompt γ spectroscopic studies of fragment nuclei in thermal neutron induced fission of ^{235}U, *Phys. Rev. C* 85, 064321 (2012)

[66] M. Albers, K. Nomura, N. Warr et al., Shape dynamics in neutron-rich Kr isotopes: Coulomb excitation of ^{92}Kr, ^{94}Kr and ^{96}Kr, *Nuclear Physics A* 899, 1 - 28 (2013)

[67] B. Pfeiffer, Private Communication (2000)

[68] M. Graefenstedt, U. Keyser, F. Münnich and F. Schreiber, Experimental beta-decay energies of ^{91,92}Br, *Nuclear Physics A* 491, 373 - 382 (1989)

[69] T. Rzaca-Urban, W. Urban, a. Kaczor et al., Shapes of the neutron-rich $^{88-94}$Kr nuclei, *The European Physical Journal A* 9, 165 - 169 (2000)

[70] J. K. Hwang, A. V. Ramayya, J. H. Hamilton et al., High spin states in ^{151,153}Pr, ^{157}Sm, and ^{93}Kr, *Phys. Rev. C* 82, 034308 (2010)

[71] G. Lhersonneau, A. Wöhr, B. Pfeiffer, K.-L. Kratz and the ISOLDE Collaboration, First decay study of the very neutron-rich isotope ^{93}Br, *Phys. Rev. C* 63, 034316 (2001)

[72] S. J. Zhu, J. H. Hamilton, A. V. Ramayya, E. F. Jones and Hwang, Octupole correlations in neutron-rich ^{143,145}Ba and a type of superdeformed band in ^{145}Ba, *Phys. Rev. C* 60, 051304 (1999)

[73] G. Lhersonneau, H. Gabelmann, M. Liang et al., Level scheme of Zr101 and structure of the N=61 Sr, Zr, and Mo isotones, *Physical Review C* 51, 1211 - 1225 (1995)

[74] H. Ohm, G. Lhersonneau, U. Paffrath, K. Shizuma and K. Sistemich, The Deformation of ^{101}Zr, *Z.Phys.* A326, 233 (1987)

[75] R. Orlandi, A. G. Smith, D. Patel et al., Single-particle and collective degrees of freedom in ^{101}Zr and ^{103,105}Mo, *Physical Review C - Nuclear Physics* 73, 1 - 12 (2006)

[76] A. Blanc, A. Chebboubi, G. de France et al., From EXILL (EXogam at the ILL) to FIPPS (FIssion Product Prompt gamma-ray Spectrometer), *EPJ Web of Conferences* 93, 01015 (2015)

[77] A. Blanc, A. Chebboubi, H. Faust et al., FIssion Product Prompt gamma-ray spectrometer: Development of an instrumented gas-filled magnetic spectrometer at the ILL, *Nuclear Instruments and Methods in Physics Research Section B: Beam Interactions with Materials and Atoms* 317, 333 - 337 (2013)

[78] Bernard L. Cohen and Clyde B. Fulmer, Fission-fragment mass separator and the nuclear charge distribution of fission fragments of a single mass, *Nuclear Physics* 6, 547 - 560 (1958)

[79] H. Lawin, J. Eidens, J.W. Borgs et al., The Jülich on-line separator for fission products "JOSEF", *Nuclear Instruments and Methods* 137, 103 - 117 (1976)

[80] J. Even, J. Ballof, W. Brüchle et al., The recoil transfer chamber: An interface to connect the physical preseparator TASCA with chemistry and counting setups, *Nuclear Instruments and Methods in Physics Research Section A: Accelerators, Spectrometers, Detectors and Associated Equipment* 638, 157 - 164 (2011)

[81] A. Oberstedt, T. Belgya, R. Billnert et al., New Prompt Fission Gamma-ray Spectral Data and its Implication on Present Evaluated Nuclear Data Files, *Physics Procedia* 47, 156 - 165 (2013)

[82] A. Oberstedt, P. Halipré, F.-J. Hambsch et al., Prompt Fission Gamma–ray Spectra Characteristics - Systematics and Predictions, *Physics Procedia* 64, 91 - 100 (2015)

[83] S. Oberstedt, R. Billnert, A. Gatera et al., Prompt Fission Gamma–ray Spectra Characteristics - A First Summary, *Physics Procedia* 64, 83 - 90 (2015)

[84] J.-M. Laborie, G. Belier and J. Taieb, Measurement of Prompt Fission Gamma-ray Spectra in Fast Neutron-induced Fission, *Physics Procedia* 31, 13 - 20 (2012)

[85] Pleasonton, Frances and Ferguson, Robert L. and Schmitt, H. W., Prompt Gamma Rays Emitted in the Thermal-Neutron-Induced Fission of ^{235}U, *Phys. Rev. C* 6, 1023-1039 (1972)

[86] G. Rimpault, D. Bernard, D. Blanchet et al., Needs of Accurate Prompt and Delayed Gamma-spectrum and Multiplicity for Nuclear Reactor Designs, *Physics Procedia* 31, 3 - 12 (2012)

[87] K. Livingston and P.J. Woods and T. Davinson and A.C. Shotter, Heavy ion radiation damage in double-sided silicon strip detectors, *Nuclear Instruments and Methods in Physics Research Section A: Accelerators, Spectrometers, Detectors and Associated Equipment* 370, 445 - 451 (1996)

[88] C.Y. Wu, R.A. Henderson, R.C. Haight et al., A multiple parallel-plate avalanche counter for fission-fragment detection, *Nuclear Instruments and Methods in Physics Research Section A: Accelerators, Spectrometers, Detectors and Associated Equipment* 794, 76 - 79 (2015)

[89] Gilbert Belier, Jean Aupiais, Cyril Varignon and Sylvain Vayre, Characterization and development of an active scintillating target for nuclear reaction studies on actinides, *Nuclear Instruments and Methods in Physics Research Section A: Accelerators, Spectrometers, Detectors and Associated Equipment* 664, 341 - 346 (2012)

[90] Luis Muga, Response of thin-film scintillator detectors to high-energy argon and krypton ions, *Nuclear Instruments and Methods* 124, 541 - 546 (1975)

[91] N.N. Ajitanand and K.N. Iyengar, On the technique of preparation of high quality thin film scintillators, *Nuclear Instruments and Methods* 133, 71 - 74 (1976)

[92] L. E. Scriven, Physics and applications of dip coating and spin coating, *MRS Proceedings* 121 (1988)

[93] James Cawse, Daniel Olson, Bret Chisholm et al., Combinatorial chemistry methods for coating development V: Generating a combinatorial array of uniform coatings samples, *Progress in Organic Coatings* 47, 128-135 (2003)

[94] EJ webpage, http://www.eljentechnology.com/index.php/products/plastic-scintillators/ej-296 (online accessed on September 30, 2017)

[95] EJ webpage, http://www.eljentechnology.com/products/plastic-scintillators/ej-200-ej-204-ej-208-ej-212 (online accessed on September 30, 2017)

[96] P. Armbruster, M. Asghar, J.P. Bocquet et al., The recoil separator Lohengrin: Performance and special features for experiments, *Nuclear Instruments and Methods* 139, 213 - 222 (1976)

[97] G. Fioni, H.R. Faust, M. Gross et al., Reduction of energy dispersion on a parabola mass spectrometer, *Nuclear Instruments and Methods in Physics Research Section A: Accelerators, Spectrometers, Detectors and Associated Equipment* 332, 175 - 180 (1993)

[98] ILL webpage, https://www.ill.eu/instruments-support/instruments-groups/instruments/pn1/description/instrument-layout/ (online accessed on September 30, 2017)

[99] webpage, https://www.ncnr.nist.gov/resources/n-lengths/ (online accessed on September 30, 2017)

[100] EJ webpage, http://www.eljentechnology.com/products/liquid-scintillators/ej-313 (online accessed on September 30, 2017)

[101] EJ webpage, http://www.eljentechnology.com/products/liquid-scintillators/ej-315 (online accessed on September 30, 2017)

[102] webpage, http://www.amale.com/new/ORDELA/perals/Default.htm (online accessed on September 30, 2017)

[103] webpage, http://faster.in2p3.fr/ (online accessed on September 30, 2017)

[104] webpage, http://www.cancerresearchuk.org (online accessed on June 8, 2017)

[105] webpage, http://www.world-nuclear.org/information-library/non-power-nuclear-applications/radioisotopes-research/radioisotopes-in-medicine.aspx (online accessed on June 8, 2017)

[106] Huang Xiaolong and Kang Mengxiao, *Nuclear Data Sheets* 121:395 (2014)

[107] Boon Q. Lee, Hooshang Nikjoo, Jörgen Ekman et al., A stochastic cascade model for Auger-electron emitting radionuclides, *International Journal of Radiation Biology* 92, 641-653 (2016)

[108] B. Q. Lee, A. E. Kibedi and K. A. Stuchbery, Atomic Radiations in the Decay of Medical Radioisotopes: A Physics Perspective, *Computational and Mathematical Methods in Medicine* 2012, 651475 (2012)

[109] J. K. Poggenburg, Private Communication (1972)

[110] D. Habs and U. Köster, Production of medical radioisotopes with high specific activity in photonuclear reactions with γ-beams of high intensity and large brilliance, *Applied Physics B* 103, 501–519 (2011)

[111] D. D. Warner, R. F. Casten, M. L. Stelts, H. G. Börner and G. Barreau, Nuclear structure of ^{195}Pt, *Phys. Rev. C* 26, 1921-1935 (1982)

[112] G. Audi, A.H. Wapstra and C. Thibault, The AME2003 atomic mass evaluation, *Nuclear Physics A* 729, 337 - 676 (2003)

[113] A. de Shalit, O. Huber and H. Schneider, On the Decay of Some Odd Isotopes of Pt, Au, and Hg, *Helv.Phys.Acta* 25, 279 (1952)

[114] D.J.H. Schwarz and R.B. Schwartz, Neutron cross sections, *Brookhaven National Laboratory. Report BNL 325* (1958)

[115] J.D. Hoeschele, T.A. Butler, J.A. Roberts and C.E. Guyer, Analysis and refinement of the microscale synthesis of the sup(195m) Pt-labeled antitumor drug, cis-Dichlorodiammineplatinum(II), cis-DDP, *Radiochimica Acta* 31, 27-36 (1982)

[116] W. Urban, *Ana* (private communication)

[117] A. M. Sandorfi, M. J. LeVine, C. E. Thorn et al., High Energy Gamma Ray Beams from Compton Backscattered Laser Light, *IEEE Transactions on Nuclear Science* 30, 3083-3087 (1983)

[118] webpage, http://www.tunl.duke.edu/images/higs/ (online accessed on October 16, 2017)

[119] Richard H. Milburn, Electron Scattering by an Intense Polarized Photon Field, *Phys. Rev. Lett.* 10, 75-77 (1963)

[120] F.R. Arutyunian and V.A. Tumanian, The Compton effect on relativistic electrons and the possibility of obtaining high energy beams, *Physics Letters* 4, 176 - 178 (1963)

[121] J. Madey, The duke fel light source facility, In *Proceedings of the 1997 Particle Accelerator Conference* volume 1, 24-28 (1997)

[122] V. N. Litvinenko, B. Burnham, M. Emamian et al., Gamma-ray production in a storage ring free-electron laser, *Phys. Rev. Lett.* 78, 4569-4572 (1997)

[123] C. Sun, J. Li, G. Rusev, A. P. Tonchev and Y. K. Wu, Energy and energy spread measurements of an electron beam by compton scattering method, *Phys. Rev. ST Accel. Beams* 12, 062801 (2009)

[124] Annalisa D'Angelo, Review of Compton scattering projects, *Particle accelerator. Proceedings, 6th European conference* (1998)

[125] T. Scott Carman, Vladimir Litveninko, John Madey et al., The TUNL-FELL inverse Compton gamma-ray source as a nuclear physics facility, *Nuclear Instruments and Methods in Physics Research Section A: Accelerators, Spectrometers, Detectors and Associated Equipment* 378, 1-20 (1996)

[126] J. F. W. Jansen, A. Faas and W. J. B. Winter, Excited States in ^{195}Pt from the Decay of 2.3 h ^{195}Ir-g, 3.7 h ^{195}Ir-m and 183 d ^{195}Au, *Z.Phys.* 261, 95 (1973)

[127] Y. D. Fang, Y. H. Zhang, X. H. Zhou et al., Identification of high-spin states in the stable nucleus ^{195}Pt, *Phys. Rev. C* 84, 017301 (2011)

[128] T. Rzaca-Urban, W. Urban, J. L. Durell, A. G. Smith and I. Ahmad, New excited states in ^{82}Ge: Possible weakening of the $N = 50$ closed shell, *Phys. Rev. C* 76, 027302 (2007)

[129] webpage, https://tendl.web.psi.ch/ (online accessed on October 21, 2017)

[130] U. Köster and M. Günther and D. Habs, Production of radioisotopes with high specific activity by photonuclear reactions: From a "wild idea" to reality, *Radiotherapy and Oncology* 102, S102 (2012)

[131] U. Köster and M. Günther, private communication

[132] S. J. Zhu, M. Sakhaee, J. H. Hamilton et al., Observation of new levels and proposed octupole correlations in neutron-rich ^{150}Ce, *Physical Review C - Nuclear Physics* 85, 1 - 8 (2012)

[133] B. R. S. Babu, S. J. Zhu, A. V. Ramayya et al., Identification of gamma transitions in Nd, *Physical Review C* 54, 568 - 571 (1996)

[134] N. Fotiades, A. F. Lisetskiy, J. A. Cizewski et al., First observation of high-spin states in ^{83}Se, *Phys. Rev. C* 74, 034308 (2006)

[135] M.-G. Porquet, A. Astier, Ts. Venkova et al., High-spin excitations of ^{81,82,83,85}Se : Competing single-particle and collective structures around N = 50, *European Physical Journal A* 39, 295 - 306 (2009)

[136] E. F. Jones, P. M. Gore, J. H. Hamilton et al., Identification of ^{88}Se and new levels in ^{84,86}Se, *Physical Review C - Nuclear Physics* 73, 86 - 89 (2006)

[137] J. Kurpeta, W. Urban, T. Materna et al., Low-spin structure of ^{85}Se and the βn branching of ^{85}As, *Phys. Rev. C* 85, 027302 (2012)

[138] M. Wang, G. Audi, A. H. Wapstra et al., The AME2012 atomic mass evaluation (II). Tables, graphs and references, *Chin.Phys.C* 36, 1603 (2012)

[139] J. K. Hwang, A. V. Ramayya, J. H. Hamilton et al., Identification of levels in ^{159}Sm and high spin states in ^{89,91}Kr, *Phys. Rev. C* 78, 017303 (2008)

[140] J. L. Durell, T. J. Armstrong and W. Urban, Two-quasiparticle bands in neutron-rich nuclei, *European Physical Journal A* 20, 97 - 100 (2004)

Abstract

Within the scope of atomic nuclear structure studies with neutron-induced reactions, this work presents the results of a fission fragment study in the N=50-60 region, the development of a fission event tagger, and the production of the isomer ^{195m}Pt. Each of the different sub-topics has its origin in the 2012/13 EXILL campaign, where nuclear structure studies were carried out with neutron-induced reactions, and explored with a γ-efficient detector array. In the first part of this thesis, the neutron-rich region around neutron number N=50-60 was investigated with neutron-induced fission reactions on the fissile targets ^{235}U and ^{241}Pu. Gamma spectroscopy methods were applied for the identification of the respective fission fragments, the assignment of γ transitions, and the analysis of lifetimes of excited states. The slope fit method as well as the recently developed *generalized centroid difference method* were used for the analysis of lifetimes in the low picoseconds to sub-nanoseconds range. Lifetimes for the nuclei ^{92}Kr, ^{93}Kr and ^{101}Zr are presented. In the second part, first results of the development of a new detector for the discrimination of fission fragments are presented. This fission event tagger is intended to be used at the *FIssion Product Prompt γ-ray Spectrometer* (FIPPS) at the Institut Laue-Langevin. Within the scope of this study, two different detector designs, based on a solid plastic scintillator and an organic liquid scintillator, respectively, were tested. In the third part the possibility of the specific population of the spin-isomer in ^{195}Pt is discussed with special regard to its use as radioisotope in nuclear medicine. Such a specific activation could be realized via certain “doorway states” in photo-excitation reactions. The search for these doorway states was initiated within a neutron capture experiment at EXILL where potential states were found. The activation of the isomer via these states was tested afterwards with photonuclear reactions using the high intense γ-beam HIGS of the TUNL facility.

Key words: Nuclear physics, nuclear structure, gamma spectroscopy, nuclear fission, lifetime measurement, EXILL, fission event detector, active targets, FIPPS, radioisotopes, radionuclides, nuclear medicine, targeted radionuclide therapy, photonuclear excitation.

Resumé

Ce travail s'inscrit dans le cadre d'études de structures nucléaires réalisées en utilisant des réactions de fission induites par neutrons froids. Il décrit successivement les résultats d'une étude sur des noyaux ayant un nombre de neutrons N=50-60, sur le développement d'un marqueur d'événements de fission et enfin sur la production de l'isomère ^{195}Pt. Chacun des différents sous-thèmes trouve son origine dans la campagne EXILL qui s'est déroulée en 2012-2013 et durant laquelle un spectromètre de grande efficacité pour la détection des rayonnements *γ* (EXOGAM) a été utilisé auprès du réacteur à haut flux de neutrons de l'Institut Laue-Langevin (ILL). Dans la première partie de cette thèse, les noyaux d'intérêt ont été produits par fission induites par des neutrons sur les cibles fissiles ^{235}U et ^{241}Pu. Des méthodes de spectroscopie *γ* ont été appliquées pour l'identification des fragments de fission, l'attribution des transitions *γ* à un noyau et l'analyse des durées de vie moyenne des états excités. L'analyse des durées de vie moyenne des états excités dans la plage de quelques picosecondes à quelques nanosecondes a été réalisée en utilisant deux méthodes complémentaires. Dans les deux cas, il s'agit de réaliser un spectre en temps construit à partir de la coincidence entre une transition qui alimente le niveau mesuré et une transition qui le désexcite. Les durées de vie moyenne pour les noyaux ^{92}Kr, ^{93}Kr et ^{101}Zr sont présentées. Dans la seconde partie, les premiers résultats du développement d'un nouveau détecteur pour la discrimination des fragments de fission sont présentés. Ce marqueur d'événements de fission est destiné à être utilisé sur le spectromètre *FIssion Prompt Product γ-ray Spectrometer* (FIPPS) de l'ILL. Dans le cadre de cette étude, deux conceptions de détecteurs différentes, basées sur un scintillateur en plastique solide et un scintillateur liquide organique, ont été testées. Dans la troisième partie, la possibilité de la population spécifique de l'isomère de spin dans ^{195}Pt est examinée au regard particulièrement de son utilisation en tant que radio-isotope en médecine nucléaire. Une telle activation spécifique pourrait être réalisée grâce à l'existence d'états excités dont la structure permettrait une population ciblée dans le cas de l'utilisation de réactions de photo-excitation. La recherche de tels états a été initiée lors d'une expérience de capture de neutrons à EXILL dans laquelle des états potentiels ont été identifiés. L'activation de l'isomère par ces états a ensuite été testée avec des réactions photonucléaires à l'aide du faisceau haute intensité disponible auprès de l'installation *γ* HIGS de TUNL (Triangle Universities Nuclear Laboratory, Duke, USA).

Mots-clés : Physique nucléaire, structure nucléaire, spectroscopie gamma, fission nucléaire, mesure de durée de vie, EXILL, détecteur d'événements de fission, cibles actives, FIPPS, radio-isotopes, radionucléides, médecine nucléaire, thérapie ciblée par radionucléides, excitation photonucléaire.